# ULTRAFAST INTERFACIAL ELECTRON TRANSFER DYNAMICS IN DYE-SENSITIZED SEMICONDUCTOR NANO-MATERIALS

By

**SANDEEP VERMA**

**Bhabha Atomic Research Centre, Mumbai-85**

***A Thesis submitted to the***

***Board of Studies in Chemical Sciences***

***In partial fulfillment of requirements***

***For the Degree of***

**DOCTOR OF PHILOSOPHY**

***of***

**HOMI BHABHA NATIONAL INSTITUTE**

**OCTOBER 2011**

# Homi Bhabha National Institute

## Recommendations of the Viva Voce Board

As members of the Viva Voce Board, we certify that we have read the dissertation prepared by **Sandeep Verma** entitled "**Ultrafast Interfacial Electron Transfer Dynamics in Dye-Sensitized Semiconductor Nano-Materials**" and recommend that it may be accepted as fulfilling the dissertation requirement for the Degree of Doctor of Philosophy.

Tulsi Mukherjee ____________ Date: 10/5/2012
Chairman: Prof. T. Mukherjee

____________ Date: 10/05/2012
Guide/Convener: Asst. Prof. H. N. Ghosh

____________ Date: 10/05/2012
External Examiner: Prof. A. Samanta

____________ Date: 10/05/2012
Member 1: Prof. S. K. Sarkar

____________ Date: 10/05/2012
Member 2: Prof. D. K. Palit

____________ Date: 10/05/2012
Member 3: Assoc. Prof. A. K. Tyagi

Final approval and acceptance of this dissertation is contingent upon the candidate's submission of the final copies of the dissertation to HBNI. I hereby certify that I have read this dissertation prepared under my direction and recommend that it may be accepted as fulfilling the dissertation requirement.

Date: 10/05/2012
Place: BARC, Mumbai

# STATEMENT BY AUTHOR

This dissertation has been submitted in partial fulfillment of requirements for an advanced degree at Homi Bhabha National Institute (HBNI) and is deposited in the Library to be made available to borrowers under rules of the HBNI.

Brief quotations from this dissertation are allowable without special permission, provided that accurate acknowledgement of source is made. Requests for permission for extended quotation from or reproduction of this manuscript in whole or in part may be granted by the Competent Authority of HBNI when in his or her judgment the proposed use of the material is in the interests of scholarship. In all other instances, however, permission must be obtained from the author.

**(SandeepVerma)**

# DECLARATION

I, hereby declare that the investigation presented in the thesis has been carried out byme. The work is original and has not been submitted earlier as a whole or in part for a degree / diploma at this or any other Institution / University.

**(Sandeep Verma)**

# DEDICATIONS…

*To My Loving Parents*

# ACKNOWLEDGEMENTS

In the first place, I would like to express my deepest sense of gratitude and sincere thanks to my supervisor Dr. H. N. Ghosh for his guidance, encouragement and excellent support throughout this study. I am grateful to him for introducing me in ever exciting field of ultrafast spectroscopy and nanomaterials.

A very special thanks goes to Dr. Amitava Das (CSMCRI, Bhavnagar, India) for his continuous support in synthesis of tailor made molecular systems. I owe my deepest gratitude for his crucial contribution in improving the quality of my research work.

I wish to express my words of thanks to Dr. T. Mukherjee, Director, chemistry group (BARC, India) for providing me the facilities which are conducively favorable for carrying out my research work.

I am thankful to Dr. S. K. Sarkar, Head, Radiation and Photochemistry Division (BARC, India) for his constant support and encouragement to my scientific endeavors.

I am thankful to all my sample collaborators. To Dr. Prasenjit Kar and Dr. Amrita Ghosh who worked under supervision of Dr. Amitava Das (CSMCRI, Bhavnagar, India) I would like to thanks for providing all metal-polypyridyl complexes and porphyrin dye. I also thanks to Dr. J. K. Sainis and Alka Gupta (Molecular Biology Division, BARC, India) for extraction and purification of protein samples.

I am thankful to Dr. D. K. Palit, Head, Ultrafast and Discharge chemistry Section (BARC, India) for his support in ultrafast spectroscopy lab.

I am grateful to Dr. J. A. Mondal his help in initial phase of research work. His warm approach has helped me in difficult time of my research work. I take this opportunity to thanks him for all his kind gesture.

I wish to express my sincere thanks to Prof. Anindya Datta (IITB, India) for TCSPC measurements, Dr. Divesh Srivastava for recording TEM images (CSMCRI, Bhavnagar, India), Mr. Subhash Bihani (SSPD, BARC, India) for CD spectroscopy, all group members at NCFRR, Pune (India) for TCSPC and pulse radiolysis study and all group members in LINAC (BARC, India) for pulse radiolysis studies.

The discussion and coöperation with all my colleagues have contributed substantially to my research work. My special thanks to Sreejith for valuable discussions. I appreciate Sreejith and Sachin for sharing and cheer up many delightful moments during my thesis work. To Rajib, Chandralekha, Snehal, Mahendra and all members of the RPCD group, I am very grateful for the cooperative spirit and the excellent working atmosphere.

I thanks to all my friends for their unwavering support during my difficult time. Their friendship has provided a wonderful time along the way. Life would not have been the same without my batch mates -my friends in this institution (BARC). I greatly appreciate their belief in me that has strengthened my aspirations in pursuit of thesis work.

I am deeply and forever indebted to my parents for their love and encouragement throughout my entire life. I express my eternal gratitude to my brother and my sister-in-law for their constant emotional support. I owe special gratitude to my family for their moral support through thick and thin of life.

Last but not least, words fail me to express my appreciation to my wife Ananya whose dedication, love and persistent confidence in me, has taken the load off my shoulder. Without her vital caring on occasion, I would not have finished this thesis. I take this opportunity to express my profound gratitude to her.

B. A. R. C., Mumbai **Sandeep Verma**

October, 2011

# SYNOPSIS

Photodriven energy and electron transfer reactions play central role in chemical transformation of solar energy in light harvesting photosynthetic pigments. It stores solar energy in the form of biomass which has produced biofuels and fossil fuels reserves in nature. In an ever growing demand of energy, different energy resources such as fossil fuels, hydroelectric power and nuclear fuels are acquired at striking rate. As a result, the utility of such resources embarks on source availability as well as subsequent environmental impacts.[1] In recent times, renewable sources are being explored to meet global energy demand. The sun is abundant source of energy by means of solar radiation reaching on earth's surface. In an estimate, an hour of solar energy irradiation striking on earth surface is worth of one year global energy demand.[1] Thus, it justifies current mankind's intellect quest for light harnessing even in small portion. In fact in nature, it is not about the solar conversion efficiency, which is mere 0.1-1% in plants,[2]; rather it is about efficient solar radiation capture by widespread photosynthetic pigments as its bona fide testimony lies in opulent green color of earth's biosphere. In nature, the sophisticated light harnessing molecules evolve gradually with earth's life. So, it's a challenge for scientific fraternity to come up with energy efficient "solar-to-electricity" conversion devices at par of rapid human pace. In this scenario, chemists in particular have advanced in introducing different organic and inorganic material to mimic natural photosynthesis and thus fastened the solar energy perspectives in primary photoconversion processes.

The seminal work by Grätzel and Co-workers on "dye sensitized solar cell (DSSC)" led to paradigm shift in molecular photophysics and wide band gap semiconductor materials.[3] Unlike conventional single junction photocells in which photoinduced charge separation occur in single phase of semiconductor material, the DSSC involve light absorption and charge separation in different phases.[4] For this purpose, the wide band gap semiconductor material such as $TiO_2$, ZnO, $SnO_2$ *etc.* are used as mesoporous film and sensitized with suitable dye molecules. In a primary photoconversion process, the photoexcitation results an electron injection from surface adsorbed dye molecules into conduction band of $TiO_2$ electrode which leaves behind positively charge dye cation$^{+\bullet}$. The electron transfer from redox mediator ($I^-/I_3^-$) regenerates dye ground states. The photogenerated electrons and holes diffuse to FTO/$TiO_2$ and Pt/FTO electrodes which restore the system in original state with gain of photovoltaic power. The solar light to electricity conversion efficiency is about 8-11% in DSSC which is comparable to most of 1st and 2nd generation photovoltaic cells (6-24%).[5]

In absence of built-in electrical field, the success of DSSC cell is based on kinetic competition at interface of dye sensitized mesoporous $TiO_2$ film.[6] The key kinetics are electron injection (in $TiO_2$), recombination (electron and dye cation) and regeneration (electron transfer from $I^-/I_3^-$ to dye cation) which play pivotal role in DSSC performance. The driving force of each kinetics is governed by numerous molecular (dye) properties *viz.* HOMO-LUMO energetics, charge distribution, stability of redox states, surface linking groups, molecular orientation, aggregation *etc.*[4] Fortunately, the photophysical study of the half-cell assembly incasing the dye sensitized $TiO_2$ film is worthwhile in appraisal of interfacial charge separation phenomena as the kinetics are three order ($10^3$ -$10^5$ range) faster than regeneration kinetics due to redox electrolyte.[6] Therefore, it allows adjudging the prosperous sensitizer dye molecules based on certain kinetics parameters postulated in initial model studies.[6]

The advancements of direct detection techniques in time scale ranging from $10^{-15}$ to $10^{-3}$ seconds offers more reliable understanding of interfacial electron transfer kinetics. In particular, the transient absorption and emission measurements have come clean in cross correlating the kinetics control over device performance.[7] Besides kinetics factor, the dye spectral coverage in red region of solar spectra (650-950nm region) is a key to enhance photocurrent as electron thermalization trail is reduced to $TiO_2$ conduction band offset and heat dissipation is minimal. So, the calculated photocurrent accumulation,[4] is higher in red region of solar irradiance spectrum. Therefore, new sensitizer dye molecules should adore improved spectral and kinetics properties.

In this thesis work, newly synthesized organic and inorganic sensitizer molecules are used in spectral sensitization of $TiO_2$ and ZnO semiconductor nanomaterials. Different strategies are used to improve optical response of dye molecules. It includes molecular amendments either in improvements of established sensitizer such as Ruthenium polypyridyl complexes or in addressing the shortcoming of known sensitizer such as porphyrin dyes. In addition, the inspiration from natural photosynthetic antenna system is drawn in efficient spectral sensitization of ZnO quantum dots (QDs). In this thesis work, catechol moiety is used as linkage to metal oxide semiconductor surface except in photosynthetic antenna complex where naturally occurring carboxylate functionality is used. The molecular photophysics is explored by steady state and transient study of absorption and photoluminescence. Most of surface electron transfer reactions are studied on $TiO_2$ nanoparticles (NPs). The interfacial electron transfer dynamics of half-cell reaction in dye sensitized wideband gap semiconductor nanoparticle in solution and film phase are carried out using transient detection techniques such as femtosecond time resolved transient absorption spectroscopy and picosecond time resolved emission spectroscopy.

The main aim of these studies is to understand the fundamental aspect of interfacial charge separation using newly designed and synthesized sensitizer molecules. The efforts confide in electron injection and back electron transfer reactions to assess the molecular level modification for enhanced optical response of sensitizer molecules. The spectroscopic observables are used in detection of various transient species produced during interfacial charge transfer reactions. For examples, excited states of dye, conduction band electrons, cation formed after electron injection *etc.* have unique spectral absorbance in visible and near IR region. This allows cross correlation of electron transfer kinetics which validates the transient species. For instance, electron injection reaction from excited state of dye into semiconductor nanoparticles can be probed by measuring excited state absorbance decay, formation of cation absorbance or delocalized electron absorbance. Similarly, back electron transfer dynamics are correlated in decay of cation absorbance, ground state bleach recovery and decay of conduction band electron absorbance. All such kinetics studies show the feasibility of newer sensitizer molecules in primary photoconversion processes.

## CHAPTER 1: GENERAL INTRODUCTION

This chapter gives introduction about operating principle of dye sensitized solar cell in relevance to interfacial electron transfer dynamics. A brief history of photovoltaic cells and current standing of DSSC is described. The scope of improvement in DSSC efficiency is cited from literature. In this regards, the importance of kinetics factors in controlling the half-cell reaction (primary photoconversion process) at dye sensitized $TiO_2$ interface is discussed in details. It describes interfacial electron transfer reactions by semi classical theory of electron transfer which was originally developed by Marcus for donor-acceptor system in homogenous medium. A brief description of Gerischer model of heterogeneous electron transfer is used for semiconductor/electrolyte interface. By using either of fluctuating energy models,[8] mathematical formulation of kinetics rate expressions are derived for electron injection and back electron transfer reactions. The effect of electronic coupling strength (donor-acceptor) on electron transfer reaction is summarized in adiabatic and non-adiabatic limits.[9] The contribution of surface states (semiconductor material) in interfacial electron transfer and its rate expression is included from available literature reports. A brief background of optical and electronic property of semiconductor material has been included in this chapter. The energetics of charge carrier in semiconductor material is described in term of charge-carrier density, effective mass of charge carrier and size of nanomaterial. The photophysical aspects of sensitizer dye molecules are described in relevance to DSSC. This chapter gives brief introduction of various strategies adopted for molecular modification of existing dye molecules to get better optical response and/or kinetics control over interfacial charge separation. Finally, an overview and scope of this thesis work is entitled.

## CHAPTER 2: EXPERIMENTAL TECHNIQUES

A general outline of different experimental technique and instrumentation used in the present thesis work is given in this chapter. A brief description of nanomaterial characterization by transmission electron microscopy has been described. The principle of TEM image formation is included in the discussion. The basic principles of steady state absorption, emission and circular dichroism are described. The time resolved emission and absorption measurements are used to study excited state dynamics of various sensitizer molecules used in present thesis work. Time correlated single photon counting and streak camera imaging techniques are employed in detection of transient emission profile (temporal and spectral). The operating principle and instrumentation details of time resolved emission measurements are described in details. The nature of transient species generated in photoinduced reaction (including interfacial electron transfer reactions) is very diverse towards their optical photo-response,[10] and studied by more versatile technique- "a femtosecond time-resolved, two-colour pump-probe absorption spectroscopy". The principle of pump-probe study, generation and power amplification of ultrashort optical pulses, second harmonic generation of pump pulse (400nm) and white light continuum generation (470-1000nm) of probe pulses are described in details. Optical layout and instrumental detail of transient absorption spectrometer is given in this chapter. A brief detail about pulse radiolysis method for generation and detection of dye cation is described in this chapter.

## CHAPTER 3: INTERFACIAL ELECTRON TRANSFER DYNAMICS ON $TiO_2$ AND $ZrO_2$ NP SURFACE SENSITIZED BY CATECHOL FUNCTIONALIZED Os(II)-POLYPYRIDYL COMPLEXES: A CHARGE TRANSFER EMISSION STUDY.

The basic of charge transfer (CT) interaction in catechol assisted strongly coupled dye/$TiO_2$ system is addressed in this chapter. A replacement of Ru(II)- ion with Os(II)- ion in metal-polypyridyl complexes produces significant optical response in red region of visible light spectrum (i.e. 600-800nm).[11] Newly synthesized Os-polypyridyl complexes are examined for spectral sensitization of $TiO_2$ NPs in solution phase. In addition, $ZrO_2$ NPs are incorporated in photophysical study to understand the interplay of surface states in CT interactions. The CT interaction is evaluated in surface binding strength of catechol linkage, electron transfer emission quenching and CT luminescence. The CT luminescence corresponds to radiative recombination of conduction band electron ($TiO_2$) and oxidized Os(III)-bipyridyl complex. Thus, back electron transfer reactions are probed by monitoring CT luminescence in TCSPC measurements. These photophysical studies rationalize surface electron transfer reactions from singlet and triplet MLCT excited state manifolds of Os(II)-bipyridyl complexes on sensitized $TiO_2$ and $ZrO_2$ NPs.

## CHAPTER 4: HEAVY ATOM EFFECTS ON INTERFACIAL ELECTRON TRANSFER REACTION IN M(II)–POLYPYRIDYL (M=Ru/Os) COMPLEX SENSITIZED $TiO_2$ NP: AN ULTRAFAST TIME-RESOLVED ABSORPTION STUDY.

The heavy atom effects on interfacial electron transfer reaction of catechol functionalized $Ru^{II}$- and $Os^{II}$-polypyridyl complex sensitized $TiO_2$ NPs are presented in this chapter. The "singlet→triplet" intersystem,[11] crossing is more efficient in heavy metal ion Os(II)-bipyridyl complexes than their Ru(II)-analogues. The charge transfer interaction in catechol bridged dye/$TiO_2$ system assist in single exponential electron injection from unthermalized MLCT manifolds.[12] So, the question is whether strong electronic coupling always ensures a single exponential electron injection or the inter system crossing which redistribute the population in MLCT manifolds (singlet and triplet), determine the electron transfer dynamics. Furthermore, the large electronic coupling matrix ($H_{AB}$) of CT interactions has drawbacks of short lived interfacial charge separation despite of high electron injection yield. The electronic coupling varies on changing $\pi$-acceptor behavior of d$\pi$-orbital on replacing 4d transition metal ion ($Ru^{II}$) with 5d transition metal ion ($Os^{II}$). Thus, femtosecond time-resolved absorption studies divulge information on heavy atom effect on electron injection and back electron injection kinetics. These photophysical studies help to understand better perspective of Os(II)-bipyridyl complexes than its Ru (II)-analogues in term of spectral coverage and kinetics competition.

## CHAPTER 5: HOLE STABILIZATION BY LIGAND LOCALIZED CHARGE TRANSFER STATES IN Ru(II)–POLYPYRIDYL COMPLEX SENSITIZED $TiO_2$ NP FILM: AN ELECTRON DONOR ANTENNA EFFECT.

In an alternative approach to get kinetics favor in primary photoconversion process, bipyridyl ligands of Ru(II)-polypyridyl complexes are modified with secondary electron donating group such as amino derivatized bipyridyl ligands. The photophysical changes sought after ligand modification and its effect on interfacial charge separation is conferred in this chapter. A facile electron donor “N, N' -dimethylaminophenyl” moiety is appended on auxiliary bipyridyl ligand of catechol functionalized Ru(II)-polypyridyl complex which incorporates “ligand-to-ligand charge transfer (LLCT)” excited states into aboriginal MLCT excited state manifolds. The low energy LLCT optical transitions than that of MLCT states, are evidenced in steady state absorption, emission and transient emission measurements which are carried out under different conditions such as aerated vs. deaerated, protonated vs. de-protonated and ambient vs. low temperatures. The direct and indirect effect of LLCT transitions on interfacial electron transfer reaction are explored by comparing the interfacial electron transfer dynamics in ligand modified and non-modified Ru(II)-complex/$TiO_2$ NPs film. The transient absorption measurements which are performed with protonated and non-protonated sensitizer/$TiO_2$ film, establishes a connection between spatial charge separations and LLCT states. The LLCT states represent intramolecular charge separated states to which the catechol linkage offers CT interactions. Thus, the study explores the link which couples photo-induced intramolecular charge separation to surface electron transfer reactions.

## CHAPTER 6: EXCITON-COUPLED CHARGE-TRANSFER DYNAMICS IN PORPHYRIN J-AGGREGATE/ $TIO_2$ NP COMPLEX.

A poor electronic coupling is one of the reasons why the electron injection yield is low in porphyrin/$TiO_2$ system. Apart from this, non-specific aggregation and limited spectral coverage despite of high molar extinction coefficient are other inadequacies which deter sensitization study with porphyrin dyes. In this chapter, a well ordered J-aggregation approach is used in spectral broadening of porphyrins. A mono catechol derivative of tetraphenylporphyrin is used in “edge-to-edge” stacking pattern of J-aggregate formation. The J-aggregates embraces low energy “delocalized electronic states” also known as “exciton states”,[13] that broadens the spectral coverage. The temporal and spectral exciton properties are discussed in detail in this chapter. The exciton coherence encompasses on average ~14 porphyrin molecules which increases the electron donor strength of porphyrin-ensemble on account of congruent transition moments aligned in direction of $TiO_2$ acceptor states (conduction band). The strong CT interaction due to catechol binding on $TiO_2$ surface assists in exciton dissociation which has typically large binding energy for Frenkel excitons. Thus, interfacial charge separation can benefit from surface exciton dissociation. The exciton coupled charge transfer reactions in porphyrin-J-aggregate sensitized $TiO_2$ NPs are demonstrated using transient emission and absorption measurements. The working principle in such composite system enlighten the basic requirement of long range association of light absorbing chromophore groups to achieve energy directing antenna function

## CHAPTER 7: EMPLOYING A PHOTOSYNTHETIC ANTENNA COMPLEX TO INTERFACIAL ELECTRON TRANSFER ON ZnO QUANTUM DOT.

In this chapter, the antenna function of natural light harvesting “phycocyanin-allophycocyanin (PC-APC)” protein pigments is ascertained in ZnO sensitization study. In native PC-APC conjugates, the protein scaffolds serve as template for strong excitonic interaction and long range dipole-dipole interaction of carboxylate functionalized phycocyanobilin (PCB) chromophores.[14] It causes a gradual energetic shift of light absorbing PCB chromophores from peripheral PC unit to APC core region and constitutes the energy directing antenna function. The long range energy transfer function in native PC-APC conjugate and its possible use in ZnO semiconductor sensitization is addressed in this chapter. The ZnO QDs are used because of its pH compatibility to native PC-APC conjugates buffer solution. The streak camera transient emission measurement and femtosecond transient absorption measurements are used to explore the PC→APC energy transfer function. The carboxylate functionality of PCB chromophore (in PC and APC unit) attaches native PC-APC conjugate to ZnO QDs surface and the spectral sensitization is confirmed in photophysical study. The transient study explores various electron transfer pathways including electron injection and back electron transfer kinetics in native and denatured PC-APC/ZnO QDS system. This study displays the antenna function of energy efficient biomolecules in favor of better charge separation across the semiconductor interface.

## CHAPTER 8: INTERFACIAL ELECTRON TRANSFER DYNAMICS ON $TiO_2$ NP SURFACE SENSITIZED WITH POLYNUCLEAR Ru/Os POLYPYRIDYL COMPLEX: A MOLECULAR ANTENNA EFFECT ON EFFICIENT CHARGE SEPARATION.

In this chapter, energy and electron transfer pathways in polynuclear Ru/Os complex are explored. The “sequential electron and cation transfer” model is mimicked very effectively in polynuclear metal-polypyridyl complexes using “Ru(II)-complexes as ligands/Os(II)-complexes as metals" strategy. The spectral sensitization of $TiO_2$ NPs using trinuclear [$Ru^{II}$-complex (^ bridging ligand)$]_2Os^{II}$-complex is presented in this chapter. The excited state energy transfer from peripheral $Ru^{II}$-complex to core $Os^{II}$-complex in trinuclear $Ru_2$^$Os_1$ complex is investigated by transient absorption and emission studies. The role of supramolecular antenna function in interfacial electron transfer dynamics is explored by comparing transient studies in trinuclear $Ru_2$^$Os_1$ and mononuclear $Os_1$ complex sensitized $TiO_2$ NPs. This study provide fundamental information on how interfacial electron transfer dynamics changes on inclusion of individual component ($M^{II}$-complex) into larger assembly. It shows that large functional array of multicomponent "energy/electron" donor entities are very useful in spectral sensitization of $TiO_2$ semiconductor material on account of very large optical response (throughout 400-1000nm region) and efficient interfacial charge separation kinetics.

## CHAPTER 9: SUMMARY AND OUTLOOK.

In conclusion, present thesis work demonstrates various strategies to modify sensitizer dye molecules in order to get better optical response and kinetics control over interfacial charge separation on wide band gap semiconductor nanomaterial. All the molecular amendments are reflected in improved spectral response. The experimental findings offer better understanding of surface electron transfer reactions which are phenomenal to semiconductor material. In all the systems, strong electronic coupling is experienced which renders prolific charge separation at interface. In addition, the molecular modifications are fruitful in reducing the driving force for back electron transfer reactions which essentially increases the lifetime of charge separated species. Thus, fundamental aspects of interfacial electron transfer reaction are explored in present thesis work which has practical importance in DSSC and in biomimetic systems.

**REFERENCES:**

[1] Energy for the 21st century: A Comprehensive Guide to Conventional and Alternative Sources, 2nd edition, Author: R. L. Nersesian, Publisher: M. E. Sharpe, New York, 2010.

[2] N. S. Lewis, Science, 2007, 315, 798.

[3] B. O'Regan, M. Grätzel, Nature, 1991, 353, 737.

[4] A. Hagfeldt, G. Boschloo, L. Sun, L. Kloo, H. Pettersson, Chem. Rev. 2010, 110, 6595.

[5] M. A. Green, K. Emery, Y. Hishikawa, W. Warta, Prog. Photovolt.: Res. Appl., 2011, 19, 84.

[6] A. Listorti, B. O'Regan, J. R Durrant, Chem. Mater., 2011, 23, 3381.

[7] D. F.Watson, G. J. Meyer, Annu. Rev. Phys. Chem. 2005, 56, 119.

[8] Surface electron transfer processes, Author: R. J. D. Miller, G. L. McLendon, A. J. Nozik, W. Schmickler, F. Willig, Publisher: John Wiley & Sons, 1995.

[9] Electron Transfer in Chemistry, Edited: V. Balzani, Wiley-VCH, Weinheim, 2001.

[10] N. A. Anderson, T. Lian, Annu. Rev. Phys. Chem., 2005, 56, 491.

[11] Photochemistry and Photophysics of Coordination Compounds: Ruthenium (Volume-280, p.117), Osmium (Volume 281, p.101), Editors: V. Balzani, S. Campagna, Springer, Topics in Current Chemistry Series, 2007.

[12] W. R. Duncan, O. V. Prezhdo, Annu. Rev. Phys. Chem., 2007, 58,143.

[13] E. G. McRae, M. J. Kasha, in Physical Processes in Radiation Biology, Academic Press, New York, 1964, 23.

[14] R. Huber, Angew. Chem. Int. Ed. Engl., 1989, 28, 848.

# LIST OF ABBREVIATIONS:

APC : Allophycocyanin

BET : Back Electron Transfer

CB : Conduction Band

CD : Circular Dichroism

CT : Charge Transfer

DOS : Density of State

DSSC : Dye Sensitized Solar Cell

ES : Excited State

ESA : Excited State Absorption

ET : Electron Transfer

FC : Frank-Condon

FWHM : Full Width at Half Maximum

GS : Ground State

HEPES : 4-(2-Hydroxyethyl)-1-Piperazineethanesulfonic Acid

HOMO : Highest Energy Occupied Molecular Orbital

IC : Internal Conversion

IET : Interfacial Electron Transfer

ILCT : Intra-Ligand Charge Transfer

IR : Infra-Red

IRF : Instrument Response Function

ISC : Intersystem Crossing

L : Ligand

LCT : Ligand Localized Charge Transfer

LLCT : Ligand-Ligand Charge Transfer

LUMO : Lowest energy Unoccupied Molecular Orbital

MLCT : Metal to Ligand charge Transfer

NHE : Normal Hydrogen Electrode

NP : Nanoparticle

OD : Optical Density

PBS : Phycobilisome

PC : Phycocyanin

PCB : Phycocyanobilin

PES : Potential Energy Surface

PL : Photo-Luminescence

QD : Quantum Dot

QY : Quantum Yield

SAED : Selected Area Electron Diffraction

SCE : Saturated Calomel Electrode

SE : Stimulated Emission

TA : Transient Absorption

TCSPC : Time Correlated Single Photon Counting

TEM : Transmission Electron Microscopy

$TiO_2$ : Titanium dioxide

TPPcat : 5,10,15-trisphenyl- 20-(3,4-dihydroxybenzene) porphyrin

TS : Transition State

UV-Vis : Ultraviolet Visible

VB : Valence Band

ZnO : Zinc Oxide

$ZrO_2$ : Zirconium Oxide

**Miscellaneous**

bpy: 2,2'-bipyridine

dcbpy: 4,4'-dicarboxylic acid 2,2'-bipyridine

dpp: 2,3-bis(2’-pyridyl)pyrazine

cat: catechol

fs: femtosecond

ps: picosecond

ms: microsecond

ns: nanosecond

## CONTENTS:

**Page Number**

**List of figure** **1**

**List of schemes** **11**

**List of tables** **14**

**1. General Introduction** **15-52**

1.1 Solar energy and solar cell 15

1.2 Electron transfer: In relevance to DSSC 19

1.2.1 Mechanism of DSSC 19

1.2.2 Classical theory of electron transfer 22

1.2.3 Electron transfer in semiconductor/dye interface 30

1.3 Semiconductor material 38

1.4 Spectral sensitization using molecular system 44

1.5 Thesis overview 45

1.6 Scope of the thesis: DSSC and biomimetic systems 46

1.7 References 47

---

**2. Experimental Techniques** **53-96**

2.1 Introduction 53

2.2 Transmission electron microscopy (TEM) 53

2.2.1 Introduction 53

2.2.2 TEM layout 55

2.2.3 Image formation 57

2.3 Steady-state absorption, Circular dichroism and Fluorescence measurements 59

2.4 Time resolved emission measurements 62

- 2.4.1 TCSPC measurements 63
- 2.4.2 Streak camera measurements 66
- 2.4.3 Streak camera vs. TCSPC measurements 70

2.5 Time Resolved Absorption Measurements: Pump-Probe technique 71

- 2.5.1 Introduction 71
- 2.5.2 Requirement of amplifier laser system in pump-probe experiments 74
- 2.5.3 Amplifier laser system 76
- 2.5.3a Ultra-short pulse generation: Ti:sapphire oscillator 76
- 2.5.3b Amplification of ultra-short pulses: Chirped pulse amplification 79
- 2.5.3c Regen amplification and Multipass amplification 81
- 2.5.3d Pulse compressor 85
- 2.5.4 Pump pulse: Second harmonic generation 86
- 2.5.5 Probe pulse: Third order non-linear interaction 87
- 2.5.6 Pump-probe transient absorption spectrometer: Measurement set-up 88

2.6 Pulse Radiolysis 91

2.7 Materials 92

2.8 Reference 92

------------------------------------------------------------------------------------------------

**3. Interfacial Electron Transfer Dynamics on $TiO_2$ and $ZrO_2$ NP Surface Sensitized by Catechol Functionalized Os(II)-Polypyridyl Complexes: A Charge Transfer Emission Study 97-120**

3.1 Introduction 97

3.2 Materials 99

3.3 Synthesis of Complex-**1** and complex-**2** 99

3.3a. Synthesis of 4-(3, 4-Dimethoxy-phenyl)-(2, 2’bipyridinyl) ($Me_2L_1$) 99

3.3b. Synthesis of 4-[2,2’]Bipyridinyl-4-yl-benzene-1,2-diol ($L_1$) 100

3.3c. Complex -**1** 101

3.3d. Complex -**2** 102

3.4 Synthesis of $TiO_2$ Nanoparticles 102

3.5 Results and discussion 103

3.5.1 TEM of $TiO_2$ NPs 103

3.5.2 Cyclic voltammetry 103

3.5.3 Photophysical properties of Os-complexes 104

3.5.4 Dye binding with nanoparticles 106

3.5.5 Steady state emission of complex-**1** on $TiO_2$ and $ZrO_2$ NPs surface 109

3.5.6 Time-resolved emission studies in dye/semiconductor system 111

3.5.7 Electron transfer dynamics from CT emission 114

3.6. Conclusion 117

3.7 References 117

------------------------------------------------------------------------------------------------

**4. Heavy Atom Effects On Interfacial Electron Transfer Reaction In M(II)–Polypyridyl (M=Ru/Os) Complex Sensitized $TiO_2$ Nanoparticles: An Ultrafast Time-Resolved Absorption Study 121-142**

4.1 Introduction 121

4.2 Materials 124

4.2.1 Synthesis of complex-**1** 124

4.3 Results and discussion 125

4.3.1 Cyclic voltammetry 125

4.3.2 Spectroscopic properties: UV-vis absorption spectra 125

4.3.3 Excited state dynamics of free complex -**1** and -**2** in acetonitrile 127

4.3.4 Transient absorption measurements of complex-**1**/$TiO_2$ and complex-**2**/$TiO_2$ NPs 130

4.3.5 Interfacial electron transfer dynamics 135

4.4. Conclusion 139

4.5 References 140

---

**5. Hole Stabilization By Ligand Localized Charge Transfer States in Ru(II)–Polypyridyl Complex Sensitized $TiO_2$ NP Film: An Electron Donor Antenna Effect 143-183**

5.1 Introduction 143

5.2 Materials 145

5.2.1 Synthesis of Complexes -**2** and -**3** 145

5.3A Results and discussion 148

5.3.1 Cyclic voltammetry 148

**Part 5A: Photophysical Study of Ligand Localized Excited State in Ru(II)-Polypyridyl Complexes: A Combined Effect of Electron Donor-Acceptor Ligand 149**

5.3.2 Steady state absorption and emission spectra of **L1** and **L2** molecules 149

5.3.3 Steady state absorption spectra of complexes -**1**, -**2** and -**3** 150

5.3.4 Steady state PL spectroscopy of complexes -**1**, -**2** and -**3** 152

5.3.5 Effect of pH on 1:1:1 physical mixture of $Ru^{II}(bpy)_3$, **L1**, **L2** molecular species 154

5.3.6 Steady state PL studies at low temperature (77K) 156

5.3.7 Time resolved emission (TCSPC) studies of complexes -**1**, -**2** and -**3** 157

5.3.8 Time resolved emission studies (TCSPC) of complexes -**1**, -**2** and -**3** at low pH 162

5.4A Conclusion 163

**Part 5B: Efficient Charge Separation in Ru (II)-Polypyridyl Complex Sensitized $TiO_2$ Film: Hole Stabilization by LLCT states 165**

5.3B Results and discussion 166

5.3.9 $TiO_2$ film preparation and sensitization 166

5.3.10 Spectral sensitization of $TiO_2$ NPs: UV-vis absorption spectra 166

5.3.11 Excited state dynamics of free complex-**3** in acetonitrile 167

5.3.12 Transient absorption spectra of complex -**1**/$TiO_2$ film 170

5.3.13 Transient absorption spectra of complex -**3**/$TiO_2$ film 171

5.3.14 Interfacial electron transfer dynamics 172

5.4B Conclusion 176

5.5 References 177

---

**6. Exciton-Coupled Charge-Transfer Dynamics in Porphyrin J-Aggregate/ $TiO_2$ Complex 183-210**

6.1 Introduction 183

6.2 Materials 187

6.2.1 J-aggregate preparation 187

6.3 Results and discussion 187

6.3.1 J-aggregate formation: CD spectrum 187

6.3.2 Spectral sensitization of $TiO_2$ NPs: UV-VIS absorption spectrum 188

6.3.3 CT emission: J-aggregate/$TiO_2$ NPs vs. monomer/$TiO_2$ NPs 190

6.3.4 TCSPC measurements: Exciton coupled CT emission 191

6.3.5 Excited state relaxation dynamics: Monomer vs. J-aggregate TPPcat 193

6.3.6 Interfacial electron transfer dynamics: monomer/$TiO_2$ vs. J-aggregate/$TiO_2$ 197

6.4. Conclusion 205

6.5 References 206

---

## 7. Employing A Photosynthetic Antenna Complex To Interfacial Electron Transfer On ZnO Quantum Dot 211-232

7.1 Introduction 211

7.2 Materials 213

7.2.1 ZnO quantum dots preparation 213

7.3 Results and discussion 214

7.3.1 Photophysical properties of ZnO QDs 214

7.3.2 Photophysical properties of native PC-APC complex 215

7.3.3 Spectral sensitization of ZnO QDs: PC-APC/ZnO QDs 217

7.3.4 PC→APC energy transfer: Time resolved emission and absorption studies 219

7.3.5 Interfacial electron transfer on ZnO QDs: Native vs. denatured PC-APC complex 224

7.3.6 Role of antenna function of PC-APC conjugates on Interfacial electron transfer 229

7.4 Conclusion 230

7.5 References 231

---

**8. Interfacial Electron Transfer Dynamics on $TiO_2$ NP Surface Sensitized With Polynuclear Ru/Os-Polypyridyl Complex: A Molecular Antenna Effect on Efficient Charge Separation 233-258**

8.1 Introduction 233

8.2 Materials 237

8.2.1 Synthesis of trinuclear $Ru_2$^$Os_1$ complex 237

8.3 Results and discussion 239

8.3.1 Cyclic voltammetry 239

8.3.2 Spectral sensitization of $TiO_2$ NP: UV-vis absorption spectra 239

8.3.3 Intramolecular energy transfer in $Ru_2$^$Os_1$ complex: Transient Absorption study 242

8.3.4 Interfacial electron transfer dynamics in $Ru_2$^$Os_1$/$TiO_2$ system: Antenna effect 247

8.4. Conclusion 253

8.5 References 254

---

**9. Summary and Outlook 259-266**

9.1 Summary 259

9.2 Outlook 263

---

**List of publications 267-270**

# LIST OF FIGURE:

**Figure 1.1:** The potential energy curves of the reactant and product states in ET reaction. $\Delta G^0$ is the free energy change and $\Delta G^*$ is the free energy of activation.

**Figure 1.2:** ln($k_{et}$) *vs.* free energy plot. It shows the ET reactions occur in the normal region, barrier less, and in the inverted region when $-\Delta G^0 < \lambda$, $-\Delta G^0 = \lambda$, and $-\Delta G^0 > \lambda$,respectively.

**Figure 1.3**: Schematic representation of $H_{AB}$ electronic coupling matrix element for ET reaction.

**Figure 1.4:** PES for an electron-transfer reaction in inverted region, showing vibrational quantization, assuming the same vibrational frequency ($\nu$) in reactant and product states.

**Figure 1.5:** Gerischer diagram of semiconductor electrode/redox couple interface.

**Figure 1.6:** Marcus model of IET reaction. Electron injection occurs from an excited state to a continuum of conduction band. Bold arrow -1: barrier less forward ET from S* to matching acceptor states. Curved arrow -2: electron thermalization in C.B. of $TiO_2$ semiconductor. Dashed arrow -3: back electron transfer in Marcus inverted region.

**Figure 1.7:** PES of GS and ES.

**Figure 1.8:** Schematic presentation of DOS ($\rho(E)$), charge carrier densities ($n(E)$ & $p(E)$) as a function of energy (conduction and valence band). Total density of charge carrier ($n^0$ & $p^0$) is integral area of Fermi function weighted DOS (shown here as shaded area).

**Figure 1.9:** Size quantization effect: Discrete molecular energy levels gradually converging into energy bands with increasing particle size.

**Figure 1.10:** Direct bandgap and indirect bandgap transitions in ZnO and $TiO_2$ semiconductors.

**Figure 1.11:** Jablonski diagram depicting various excited state relaxation process. Radiative processes are shown by solid straight arrow (absorption and emission), non-radiative processes

are shown by curved arrow (internal conversion (IC), Vibrational relaxation (VR), Inter system crossing (ISC) and non-radiative decay). Typical time scales are shown in seconds (S).

----------------------------------------------------------------------------------------------------------

**Figure 2.1**: amplitude and phase modulation in light passing through specimen.

**Figure-2.2**: Schematic layout of transmission electron microscope. Ray diagram of (i) DP and (ii) Image mode TEM operation.

**Figure 2.3**: Block diagram of TCSPC set up.

**Figure 2.4**: streak projection of incident photons as function of time and position.

**Figure 2.5**: Schematic presentation of streak camera imaging technique.

**Figure 2.6:** block diagram of streak camera imaging of photoluminescence: (1) optical pulse splits, one part excite sample and other used in PD trigger signal. (2) Trigger signal fed to frequency divider which synchronizes sweep frequency rate. (3) The luminescence is collected at magic angle and the spectrograph project a stripe of wavelength dispersed PL spectrum on streak tube. (4) Synchronized sweep of “Photoelectron” stripe produces 2D image on CCD. (5) CCD readout displayed in computer and analyzed by “OptoAnalyse” software.

**Figure 2.7:** Optical layout of two colour pump-probe set-up.

**Figure 2.8:** Scheme of the states involved in a pump probe experiment in a dye solution. (A) Excited state absorption, (B) Bleaching, and (C) Stimulated emission.

**Figure 2.9:** spatial overlapping of pump-probe pulse.

**Figure 2.10**: Optical layout of Ti:sapphire oscillator used in present pump-probe set-up: Top panel: two prism pair for negative GVD; Bottom panel: chirped mirrors for negative GVD.

**Figure 2.11**: Box diagram showing chirped pulse amplification (CPA).

**Figure 2.12**: pulse stretching principles.

**Figure 1.13**: “Öffner stretcher” ray diagram.

**Figure 1.14**: Optical scheme of confocal multi-pass Ti: Sapphire amplifier. M1 and M2 are two confocal mirrors with two difference focal lengths.

**Figure 2.15**: Optical scheme of regen Ti: Sapphire amplifier. M1 and M2 are HR-mirrors.

**Figure 2.16**: Optical layout of combined regen/twopass Ti: Sapphire amplifier.

**Figure 2.17**: pulse compressor principles.

**Figure 2.18:** A schematic complete diagram showing the transient absorption spectrometer for detection in the visible region and near IR region.

----------------------------------------------------------------------------------------------------------

**Figure 3.1**. TEM image of $TiO_2$ NPs. Insides window shows HRTEM and SAED pattern of prepared $TiO_2$ NPs.

**Figure 3.2**. Optical absorption spectra of a) complex-**1** and b) compelx-**2**) in acetonitrile at 298 K. [Inset: Steady state emission spectra of complex-**1** at 298 K exciting at c) 450 nm, d) 650 nm and e) at 78K exciting at 450 nm]

**Figure 3.3:** Transient emission decay kinetics monitored at 670nm probing a) complex-**1** in acetonitrile, b) $[Os^{II}(bpy)_3]^{+2}$ in acetonitrile after 453 nm excitation.

**Figure 3.4**: Optical absorption spectra of complex-**1** (25 μM) in presence of various $TiO_2$ concentrations- 1) 0.0, 2) 0.29, 3) 0.43, 4) 0.59, 5) 0.79, 6) 1.04, 7) 1.5, 8) 2.0, 9) 2.8, 10) 3.7; 11) 5.0 $gL^{-1}$. 12) Normalized spectra of complex-**1**. 13) optical spectra of $TiO_2$ NPs (5 gm/L). (Inset: Benesi-Hildebrandt plot of the complex-**1** /$TiO_2$ complex monitored at 530 nm).

**Figure 3.5**: Optical absorption spectra of complex-**1** a) in water, b) on $ZrO_2$ NPs (20gm/L). c) normalized spectra of compelx-**1** and d) $ZrO_2$ NPs [complex-**1** concentration ~ 50 μM].

**Figure 3.6:** PL spectra of complex-**1** a) in water, b) on $TiO_2$ NPs (20gm/L) and (c) on $ZrO_2$ nanoparticle (20gm/L) surface. $\lambda_{ex}$ is 450 nm and optical density at excitation wavelength kept 0.3 for all the samples (Note: excitation intensity is same for all the three measurements). Inset: Excitation spectra complex-**1** d) in water ( $\lambda_{em}$ = 730nm) and e) on $TiO_2$ NPs surface ( $\lambda_{em}$ = 844nm).

**Figure 3.7**: Single-photon-counting studies of complex-1 in different media, a) in acetonitrile, b) in water, c) in $ZrO_2$ colloid (20.0 gm/L), d) in $TiO_2$ colloid (20gmm/L) after 453 nm excitation. Emission wavelength was kept for all the measurements at 670 nm**.**

----------------------------------------------------------------------------------------------------------

**Figure 4.1**: Optical absorption spectra of complex a) **-1** in water, b) **-2** in water; c) **-1** on $TiO_2$ nanoparticle surface and d) **-2** on $TiO_2$ nanoparticle surface dispersed in water (concentration of -**1** was kept ~38 μM and concentration of **-2** was kept ~30 μM).

**Figure 4.2**: Left Panel: Transient absorption spectra of complex-**1** in acetonitrile solution following excitation at 400nm laser pulse at 200 fs, 500 fs, 1 ps, 5 ps, and 10 ps time delays. Right Panel: a) ESA decay at 710 nm, b) bleach recovery at 470nm.

**Figure 4.3**: Left panel: The transient absorption spectra of complex-**2** in acetonitrile solution after 400nm photoexcitation at 200 fs, 500 fs, 1 ps, 5 ps, 10 ps, and 30 ps time delays. Right Panel: a) ESA deacy at 710 nm, b) bleach recovery at 490nm and c) 610nm.

**Figure 4.4**: The transient absorption spectra of oxidized a) complex-**1,** b) complex-**2, c)** Ligand **L1** in aqueous solution. (Y-axis is scaled a.u. for comparison purpose).

**Figure 4.5**: Left panel : Transient absorption spectra of complex-**1** sensitized $TiO_2$ nanoparticle, Right panel: Transient absorption spectra of complex **-2** sensitized $TiO_2$ nanoparticle, at 200 fs, 500 fs, 1 ps, 5 ps, 10 ps, and 50 ps time delays after excitation at 400 nm.

**Figure 4.6**: Left panel: TA kinetics of complex-**1** sensitized $TiO_2$ nanoparticle, Right panel: TA kinetics of complex-**2** sensitized $TiO_2$ nanoparticle, at 710nm, 790nm, 900nm and 1000nm probe wavelengths.

**Figure 4.7:** Bleach recovery kinetics at 490 nm in a) complex-**1**/$TiO_2$ system and b) complex-**2**/$TiO_2$ system. (Inset: bleach recovery in short time scale).

**Figure 4.8**. TA kinetic traces of conduction band electron monitored at 1000 nm in A) **1**/$TiO_2$ and B) **2**/$TiO_2$ systems after excitation at 400 nm.

---

**Figure 5.1**: Steady state absorbance spectra of (a) **L1** ligand and (b) **L2** ligand. Emission spectra of (c) **L1** ligand, (d) **L2** ligand with 300nm excitation (bold lines) and (e) **L2** ligand with 400nm excitation (short dash line) in neutral condition in acetonitrile solvent.

**Figure 5.2**: Optical absorbance spectra of (a) complex-**1**, (b) complex-**2** and (c) complex-**3** in neutral (bold lines) and (a') complex-**1**, (b') complex-**2** and (c') complex-**3** in acidic (dash-dot lines) condition in acetonitrile solvent (concentration of all complexes were kept same).

**Figure 5.3:** PL spectra of (a) complex-**1**, (b) complex-**2** and (c) complex-**3** in neutral (bold lines) and (a') complex-**1**, (b') complex-**2** and (c') complex-**3** in acidic (dash-dot lines) condition in acetonitrile solvent (All PL spectrum are recorded in aerated acetonitrile solvent and normalized with respect to same optical density at excitation wavelength).

**Figure 5.4:** Left Panels - **1:1:1** physical mixture of Ru(bpy)3 complex, **L1**, **L2** ligands ; Right Panels - **1:1** physical mixture of Ru(bpy)$_3$ complex, **L2** ligand; Top Panels – acetonitrile solvent; bottom panels- $HNO_3$-acetonitrile solvent. (a) Excitation spectra for 505 emission wavelength (actual intensity divided by 10 in panel-A), (b) excitation spectra for 615 emission wavelength,

(c) emission spectra at 400 excitation wavelength and (d) emission spectra at 460nm excitation wavelength.

**Figure 5.5:** Uncorrected PL spectra of (a) complex-**1**, (b) complex-**2** and (c) complex-**3** at 77K in ethanol methanol mixture (v/v 4:1).

**Figure 5.6:** PL-kinetics of (a) complex-**1**, (b) complex-**2** and (c) complex-**3** in aerated acetonitrile. ($\lambda_{\text{excitation}}$ = 406nm; laser source ~ 66ps FWHM).

**Figure 5.7**: PL-kinetics of protonated (a) complex-**1**, (b) complex-**2** and (c) complex-**3** at respective emission peak wavelengths in aerated acetonitrile with $HNO_3$ solvent. ($\lambda_{\text{excitation}}$ = 406nm; laser source ~ 66ps FWHM).

**Figure 5.8**: Optical absorption spectra of a) complex-**1** in water, b) complex-**3** in water; c) complex-**1** /$TiO_2$ and d) complex-**3**/$TiO_2$ nanoparticle surface dispersed in water.

**Figure 5.9**: Left Panel: TA spectra of complex-**3** in acetonitrile solution following excitation at 400nm laser pulse at 200fs, 500fs, 1ps, 3ps, 10ps, 20ps, 50ps, and 100 ps time delays. Right Panel: TA Kinetic trace of a) complex-**3** at 610 nm, b) complex-**1** at 610nm.

**Figure 5.10:** TA spectra of complex-**1**/$TiO_2$ film in presence of acetonitrile following excitation at 400nm laser pulse at 200 fs, 500 fs, 1 ps, 5ps, 10ps, 20ps, 50ps, and 100 ps time delays. [Inset shows the kinetic trace at 610 nm].

**Figure 5.11**: TA spectra of complex-**3** sensitized $TiO_2$ nanoparticle film in presence of acetonitrile at 200 fs, 1 ps, 5 ps, 10 ps, 50 ps and 100ps time delays after excitation at 400 nm. [Inset shows the kinetic trace at 610 nm].

**Figure 5.12**: BET kinetics monitored by bleach recovery at 480nm in (a) complex-**1**/$TiO_2$ and (b) complex-**3**/$TiO_2$ film following excitation with 400 nm laser pulse.

**Figure 5.13**: BET kinetics monitored by TA of $e^-$(C.B. $TiO_2$) at 900nm in (a) complex-**1**/$TiO_2$ and (b) complex-**3**/$TiO_2$ film; (1) Panel-A : in neutral condition (acetonitrile ); (2) Panel-B: in acidic condition ($HNO_3$ -acetonitrile).

------------------------------------------------------------------------------------------------------------

**Figure 6.1**: CD spectrum of 20μM TPPcat: (a) monomer, (b) J-aggregate.

**Figure 6.2:** Optical absorption spectra of TPPcat (20 μM) in different condition: (a) Monomer , (b) Monomer/$TiO_2$, (c) J-aggregate, (d) J-aggregate / $TiO_2$, (e) bare $TiO_2$.

**Fgure-6.3**: Q-band emission spectra of different systems: (A) Monomer, (B) Monomer / $TiO_2$, (C) J-aggregate, (D) J-aggregate / $TiO_2$.

**Figure 6.4:** Emission decay traces for the TPPcat (20μM) using 460nm (~39ps FWHM) excitation wavelength: (a) Monomer, (b) J-aggregate, (c) Monomer/$TiO_2$, (d) J-aggregate / $TiO_2$.

**Figure 6.5**: Transient absorption spectrum of monomer (Left Panel) and J-aggregated (right panel) TPPcat at different time delay after excitation at 400 nm.

**Figure 6.6**: Left Panel: Normalized TA Kinetic of monomer TPPcat (a) at 610nm and at (b) 650nm; Right Panel: TA Kinetic of J-aggregated TPPcat (a) 610nm, b) 730, c) 490nm.

**Figure 6.7**: Transient absorption spectra of Monomer /$TiO_2$ NP (Panel-A) and J-aggregate /$TiO_2$ NP (Panel-B) at different time delay after exciting at 400nm laser light. (Steady state absorption is shown for comparison (thin line)).

**Figure-6.8**: Normalized Kinetic decay traces of injected electron in CB of $TiO_2$ at 1000nm in (a) Monomer/$TiO_2$, (b) J-aggregate / $TiO_2$ system and normalized bleach recovery kinetics in (c) Monomer/$TiO_2$, (d) J-aggregate / $TiO_2$ at 670nm.

**Figure 6.9**: Kinetic decay traces monitored at 570nm (a) Monomer/$TiO_2$ (b) J-aggregate/$TiO_2$ systems.

**Figure 6.10**: CT kinetics of (a) Monomer-TPPcat/$TiO_2$, (b) J-aggregate-TPPcat / $TiO_2$ at 730nm.

-----------------------------------------------------------------------------------------------------

**Figure 7.1:** Absorption spectrum of a) zinc acetate and b) ZnO QD. c) Emission spectra of ZnO QD with photoexcitation at 290nm.

**Figure 7.2**: HR-TEM image of ZnO QD.

**Figure 7.3:** a) Steady state absorption spectra of PC-APC conjugate (~4.7μM); Emission spectrum of native PC-APC conjugate at b) 400nm excitation and c) 590nm excitation. (Inset: Excitation spectrum for 725nm emission wavelength).

**Figure 7.4:** Absorption spectra of PC-APC conjugate in a) native condition, b) denatured condition. (Concentration is kept same at 4.7μM).

**Figure 7.5:** Emission spectra of PC-APC conjugate in a) native condition, b) denatured condition. (Absorbance is kept same at $\lambda_{ex}$ 400nm).

**Figure 7.6**: CD spectra of PC-APC conjugate in a) native condition, b) denatured condition (8M urea).

**Figure 7.7.** Optical absorption spectra of a) native PC-APC conjugates b) PC-APC / ZnO QD; c) ZnO QD at different concentration (peak positions are indicated by arrow).

**Figure 7.8:** Emission spectra of PC-APC conjugate in a) absence and in b) presence of ZnO QD after photoexcitation at 400nm.

**Figure 7.9:** Transient emission spectra of native PC-APC conjugate in buffer solution at 8.0pH in 0-30 ps time scale by using laser pulse excitation at 400nm.

**Figure 7.10:** Transient emission decay kinetics of conjugated PC-APC complex at a) 615nm, b) 655nm and c) 675nm (Normalized for comparison purpose).

**Figure 7.11.** Transient absorption spectra of native PC-APC conjugates (Panel A) and denatured PC-APC complex (Panel B) recorded at 500 fs, 1 ps, 2 ps, 5 ps, 10 ps and 20 ps delay times after 400nm laser pulse excitation.

**Figure 7.12.** TA kinetics at 600nm and 660nm which respectively probes i) panel A: the PC and APC entity of native PC-APC conjugate, ii) panel B: denatured PC-APC complex.

**Figure 7.13.** Transient absorption decay kinetics at 720nm represents A) SE growth of native PC-APC conjugate, B) ESA decay of denatured PC-APC mixture.

**Figure 7.14.** Transient absorption spectra of native PC-APC conjugate sensitized ZnO QD (Panel A) and denatured PC-APC complex sensitized ZnO QD (Panel B) recorded at 500 fs, 1 ps, 2 ps, 5 ps, 10 ps and 20 ps delay times after 400nm laser pulse excitation.

**Figure 7.15:** Transient absorption spectra of [PC-APC conjugate]$^{\bullet+}$ cation.

**Figure 7.16:** Transient absorption spectra of [denatured PC-APC mixture]$^{\bullet+}$ cation.

**Figure 7.17.** TA kinetics at 1) Panel A: 690nm probing to (PC-APC)+• cation in a) native PC-APC/ZnO QD, b) denatured PC-APC/ZnO QD system. 2) Panel B: 850nm probing to e— CB (ZnO QD) in c) native PC-APC/ZnO system, d) denatured PC-APC/ZnO system.

---

**Figure 8.1**: Optical absorption spectra of ~30 μM $Os_1$ a) in water, b) on $TiO_2$ nanoparticle surface, c) Normalized absorption spectra of $Ru_1$ in water.

**Figure 8.2**: Optical absorption spectra of ~ 17μM $Ru_2$^Os a) in water, b) on $TiO_2$ nanoparticle surface, c) Normalized absorption spectra of $Ru_2$^$Ru_1$ in water.

**Figure 8.3**: Benesi-Hildebrandt plot of $Os_1/TiO_2$ system monitored at 530 nm.

**Figure 8.4:** Benesi-Hildebrandt plot of $Ru_2$^$Os_1/TiO_2$ system monitored at 600nm.

**Figure 8.5**: TA spectra of $Os_1$ complex in acetonitrile at different time delay after excitation at 400nm laser pulse.

**Figure 8.6**: TA spectra of $Ru_2$^$Os_1$ complex in acetonitrile at different time delay after excitation at 400nm laser pulse.

**Figure 8.7**: TA spectrum of $Ru_2$^$Ru_1$ complex at 20ps delay time [Inset: a) Bleach recovery kinetics (630nm), b) ESA kinetics (1000nm) of $Ru_2$^$Ru_1$ complex, c) ESA kinetics at 630nm for $Ru_1$ complex].

**Figure 8.8**: TA kinetics of $Ru_2$^$Os_1$ complex a) 500nm, b) 630nm and c) 900nm.

**Figure 8.9**: TA kinetics of $Os_1$ complex a) 610nm and b) 710nm.

**Figure 8.10**: TA spectra of $Os_1$ complex a) in absence of $TiO_2$ NPs b) in presence of $TiO_2$ NPs at 20ps time delay after excitation at 400nm laser pulse.

**Figure 8.11**: TA spectra of $Ru_2$^$Os_1$ /$TiO_2$ NPs at different time delay after excitation at 400nm laser pulse.

**Figure 8.12**: TA kinetics at 1000nm a) $Ru_2$^$Os_1$/$TiO_2$ NPs, b) $Os_1$/$TiO_2$ NPs.

**Figure 8.13**: TA kinetics of $Ru_2$^$Ru_1$/$TiO_2$ NPs at 950nm. (Inset: TA spectrum of $Ru_2$^$Ru_1$ complex a) in absence of $TiO_2$ NPs, b) in presence of $TiO_2$ NPs).

## LIST OF SCHEME:

**Scheme-1:** Basic electron transfer process in DSSC.

**Scheme-2**: State diagram showing key electron transfer kinetics of DSSC: The favorable kinetics are shown by green (solid) arrow whereas intercepting kinetics are shown by red (hash) arrow. The kinetics are numbered in order of relevant time scale.

------------------------------------------------------------------------------------------------------------

**Scheme 3.1:** Structure of complex-**1** and complex-**2**

**Scheme 3.2:** Reaction Scheme for the synthesis of the ligand $\mathbf{L_1}$.

**Scheme 3.3:** Mechanistic Scheme showing three-level model which consists of the ground state ($S_o$) state, the excited triplet state ($^3$MLCT) state and the excited singlet ($^1$MLCT) state of Os-cat1 (**I**) adsorbed on $TiO_2$ and $ZrO_2$ nanoparticles. Excitation of 453 nm inject electrons into the conduction band of $TiO_2$ and shallow surface states of $ZrO_2$ nanoparticles. Excitation of 589 nm excitation inject electron into the conduction band of $TiO_2$ and deeper surface states of $ZrO_2$ nanoparticles

------------------------------------------------------------------------------------------------------------

**Scheme 4.1**: Structure of complex-**1** and complex-**2.**

**Scheme 4.2**: Mechanistic scheme showing three-level model which consists of the ground state ($S_o$), excited triplet state ($^3$MLCT) and excited singlet ($^1$MLCT) state of complexes-**1** and **-2** adsorbed on $TiO_2$ nanoparticles

------------------------------------------------------------------------------------------------------------

**Scheme 5.1a**: Structure of complex-**1**, complex-**2** and complex-**3**.

**Scheme 5.1b**: Structure of complex-**1** and complex-**3.**

**Scheme 5.2:** Synthetic methodology adopted for the synthesis of **L2** and molecular structures of the different ligands.

**Scheme 5.3:** A simplified pictorial representation of different photophysical processes in complexes -**1** (blue), -**2** (green) and -**3** (red) (A common ground state ($S_0$), $^1$MLCT and $^3$MLCT states are shown for the sake of convenience only).

**Scheme 5.4:** Straight arrow (1) and (5) represent direct $S_0 \rightarrow$ MLCT and $S_0 \rightarrow$ LLCT transitions; curved arrow (2), (3) and (4) indicate radiationless transitions; bold arrow indicates dominant photo processes.

**Scheme 5.5**: Schematic representation of IET in complex -**3**/$TiO_2$ film.

-----------------------------------------------------------------------------------------------------------

**Scheme 6.1:** Schematic diagram of porphyrin-J-aggregate/$TiO_2$ composite. The "head-to-tail" stacking pattern of porphyrin molecules in J-aggregate introduces exciton absorption band (450-500nm and 700-800nm) in spectral sensitization of $TiO_2$ NP.

**Scheme 6.2**: J-aggregate-TPPcat.

**Scheme 6.3**: Excited and exciton relaxation pathways in monomer and J-aggregated TPPcat.

**Scheme 6.4**: Free charge carrier generation in frenkel exciton coupled J-aggregate-porphyrin / semiconductor ($TiO_2$) composite system accomplish via interfacial exciton dissociation process. The separated hole is delocalized through excitonic coherence of J-aggregate. The immobilized hole is spatially less accessible to electron injected in $TiO_2$ and hence leads to slower back electron transfer.

-----------------------------------------------------------------------------------------------------------

**Scheme-7.1.** A: The ring assembly of PC and APC unit for coherent and incoherent energy transfer. B: Phycocayanobilin-apoprotein sensitization of ZnO.

**Scheme-7.2:** Photophysical process in native-PC-APC conjugate/ ZnO system: (i) Primary electron injection from initially photo excited PC species. (ii) Sequential energy transfer directs captured photon energy from non-injecting PC to APC entity. (iii) Secondary electron injection accomplish from APC unit.

**Scheme-8.1**: Photoexcitation of chromophoric array followed by vectorial energy transfer towards reaction center (Rc).

**Scheme-8.2**: Left: Trinuclear "Ru$_2$^Os" complex **(-1)** ([Ru(bpy)$_2$(dpp)]$_2$Os(bpy-CH=CH-catechol)); Right: Mononuclear "Os$_1$" complex **(-2)** (Os(bpy)$_2$(bpy-CH=CH-catechol)).

**Scheme-8.3:** Synthetic methodology adopted for the synthesis of trinuclear Ru$_2$^Os$_1$ complex.

**Scheme-8.4** : Interfacial electron transfer mechanism in Ru$_2$^Os$_1$/TiO$_2$ system: (i) Primary electron injection from directly photoexcited core Os center, (ii) Vectorial energy transfer from peripheral Ru to Os center, (iii) Slow electron injection through space, (iv) Slow back electron transfer through space

## LIST OF TABLE:

**Table 3.1:** Emission life times of Os-cat1 (I) and Os-cat2 (II) in different media.

----------------------------------------------------------------------------------------------------------

**Table-5.1 :** Time resolved emission kinetics data of complex-**1**, **-2** and **-3** in different conditions.

**Table-5.2 :** Transient emission kinetics data of 1:1:1 physical mixture of $Ru^{II}(bpy)_3$, **L1** and **L2.**

----------------------------------------------------------------------------------------------------------

**Table-7.1**: Fitting parameter for time resolved emission traces of native PC-APC complex.

**Table-7.2:** Fitting parameter for transient absorption kinetics of PC-APC conjugate in native and denatured condition (instrument response function (IRF) ≤100fs).

**Table-7.3:** Fitting parameter for transient absorption kinetics of PC-APC conjugate in native and denatured condition in presence of ZnO QD (sensitized ZnO QD**).**

# CHAPTER 1

# GENERAL INTRODUCTION

## 1.1 Solar energy and solar cell:

The sun is the primary source of energy to the earth biosphere. In nature, the solar energy is stored as chemical energy through photoinduced energy- and electron- transfer reactions in light harnessing photosynthetic pigments.[1.1] The consumable chemical forms and compatible metabolisms have provided biomass energy to human society.[1.2] In an ever growing demand of energy, human race has acquired almost all energy resources such as biofuels, fossil fuels, hydroelectric power, nuclear fuels *etc.* at a very striking rate.[1.3] As a result, the utility of such resources embarks on availability and environmental issues. The global energy consumption will continue to rise as per demand of growing human race and alternative energy sources have become need of time.[1.4] The sun is abundant source of energy by means of solar radiation reaching on earth's surface. In an estimate, an hour of solar energy irradiation striking on earth surface is worth of one year global energy demand.[1.5] Thus, it justifies current mankind's intellect quest for light harnessing even in small portion. In fact in nature, it is not about the solar energy conversion efficiency, which is mere 0.1-1% in plants; rather it is about efficient solar radiation capture by widespread photosynthetic pigments as its bona fide testimony lies in opulent green color of earth's biosphere.[1.6] In nature, the sophisticated light harnessing molecules evolve gradually with earth's life. So, it's a challenge for scientific fraternity to come up with energy efficient "solar-to-electricity" conversion devices at par of rapid human pace. In this scenario, chemists in particular have advanced in introducing different organic and inorganic materials to mimic natural photosynthesis and thus fastened the solar energy perspectives in primary photoconversion processes.[1.7-1.9]

The physical phenomena of conversion of light to electricity was first observed by A. -E. Becquerel in 19th century using a photoelectrochemical cell made of metal electrodes and electrolyte.[1.10] The falling light photon ejected the electron from metal electrode surface and the photogalvanic effect was observed.[1.11] The photovoltaic (PV) power remains primitive until the use of semiconductor material.[1.12] The definite energy separation between conduction and valence bands in semiconductor, boost the electrical conductance from minority charge carriers.[1.13] The development in semiconductor technology has unleashed the key of electron mobility on exposure to visible solar irradiation. In the beginning of discrete cell technology, silicon semiconductor material seized the conversion efficiency more than 6% due to its ideal ~1.1eV energy band gap which covers a good portion of solar spectrum in visible and near IR region.[1.14] The 1st generation single crystal (c-Si) silicon solar cell embarks on cost effectiveness issue due to limited source availability/supply of highly purified c-Si wafers and the field seeks alteration despite of high 24.7% efficiency of c-Si solar cell on record.[1.15] The emergence of thin-film technology and better understanding of mesoscopic heterojunction semiconductors material rapidly shape up 2nd generation of cost-effective photocells and it projects a step closer to 3rd generation solar cell.[1.16] The 2nd generation photocells such as amorphous silicon, CdTe and CIGS (copper Indium Gallium Selenide) are examples of thin-film technological breakthrough with efficiency in 8-20% range.[1.17] Notwithstanding the environmental toxicity and low feedstock availability of CdTe material, low efficiency of amorphous Si cell and the cost of fabricating CIGS, the forefront is now zooming on multijunction III-V compound semiconductor (In, Ga, As, P *etc.*) photocells- a futuristic 3rd generation solar cell.[1.18] The multiple layer $A^3B^5$ type heterojunction surpasses the Shockley-Queisser limit (31%),[1.19] of single junction photocells (1st and 2nd generation) but needs to testify on reliability gesture.

In principle, the photoaction primarily conquers the energy-gap between electron (n-type) and hole (p-type) membrane and the built-in electrical field drives the photogenerated minority charge carriers avoiding recombination with majority charge carrier.[1.5,1.13,1.16,1.18] The chemical energy is stored in electron-hole pair production (Fermi energy differentiates for n- and p-type layer) which generates photo-voltaic effect. The more simplified form of which realized in a class apart, “dye-sensitized solar cell (DSSC)” when Grätzel and co-workers demonstrated 8-9% efficiency using metal-polypyridyl complexes for desired photoaction and mesoporous $TiO_2$ film and redox electrolyte ($I^-$ / $I_3^-$) in storing chemical energy at interface.[1.20,1.21] The low production cost, a moderate 9-11% efficiency,[1.22] and heterojunction assembly makes DSSC as emerging technology between 2nd and 3rd generation solar cell. The benefits of DSSC are many such as low production cost, ease of design, flexibility in assembling, large feedstock availability, non-toxicity of main component $TiO_2$, short energy payback time and suitable for indoor and diffuse light conditions.[1.17] Conceptually, DSSC mimic natural photosynthesis in which light absorption and charge carrier transport are separated in different phase i.e. sensitizing dye/redox couple and electron conducting $TiO_2$ film.[1.23,1.24] This way it relaxes stringent quality control as cost entailing factor of conventional p-n junction solar cell where both the function operates in one layer (at p-n junction).[1.25] The freedom of selecting different sensitizer molecules such organic dyes and organometallic complexes allows desirable spectral coverage and HOMO-LUMO control over interfacial charge separation process.[1.17,1.26-1.29] Furthermore, different wide band gap semiconductor materials such as ZnO, $TiO_2$, $SnO_2$ *etc.*, surface morphology, surface binding groups, hole conducting electrolytes *etc.* all provide an ample chance for DSSC makeover to achieve 15% energy efficient target. [1. 17,1.30-1.32]

In absence of built-in electrical field, the success of DSSC cell is based on kinetic competition at the interface of dye sensitized mesoporous $TiO_2$ film.[1.17,1.33-1.36] The key kinetics are electron injection, recombination and regeneration which play central role in DSSC performance. These factors are mainly dominated by sensitizer dye molecules because the driving force of each electron transfer process is related with HOMO-LUMO energetics, surface linking groups and molecular orientation.[1.33,1.37] Fortunately, the photophysical study of the half-cell assembly incasing the dye sensitized $TiO_2$ film is worthwhile in appraisal of interfacial charge separation phenomena as the kinetics involved are three order ($10^3$-$10^5$ range) faster than the impact of redox electrolyte bearings.[1.34] Therefore, it is sensible to adjudge the new sensitizer dye molecules by certain kinetics parameters postulated in initial model studies.

The advancement of direct detection techniques in the time scale ranging from $10^{-15}$ to $10^{-3}$ seconds offers more reliable understanding of interfacial electron transfer (IET) kinetics. In particular, the transient absorption and emission measurements have come clean in cross correlating the kinetics control over device performance.[1.38-1.40] Besides kinetic factors, the dye spectral coverage in red region of solar spectra (650-950nm region) is a key to enhance photocurrent as electron thermalization trail is reduced to $TiO_2$ conduction band offset and heat dissipation is minimal.[1.41] So, the calculated photocurrent accumulation is higher in red region of solar irradiance spectrum.[1.17] Therefore, new sensitizer dye molecules should endeavor high absorption coefficient throughout visible and near IR region. In addition, large functional arrays are beneficial for improved kinetics and spectral response. Various aspects of interfacial electron transfer, related materials and detection methods are described in this chapter.

## 1.2 Electron transfer: In relevance to DSSC

### 1.2.1 Mechanism of DSSC:

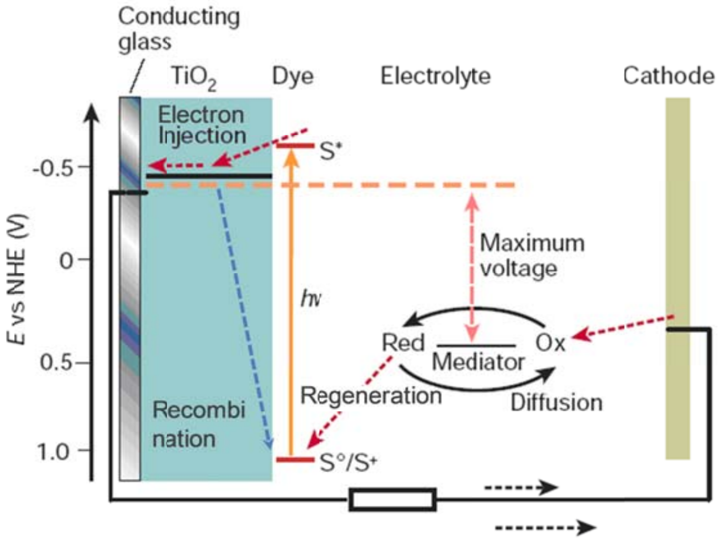

**Scheme 1.1:** Basic electron transfer process in DSSC

The core of DSSC comprises mesoporous nanocrystalline $TiO_2$ film for electron conduction, dye molecules for photoaction and redox electrolyte for hole transport enactments.[1.17,1.20,1.33] The mesoporous nature of $TiO_2$ nanoparticles (NPs) film has high surface area which enhances monolayer coverage of dye molecules.[1.42] Photoexcitation of surface adsorbed dye molecules results in electron injection into conduction band of $TiO_2$ electrode and leaves behind positively charge dye cation$^{+\bullet}$. The electron transfer from redox mediator ($I^-$ / $I_3^-$) regenerates dye in its ground state. Thus optical absorption and charge separation occur in separate phases which lead to efficacious primary energy conversion step (scheme-1.1). The photogenerated electrons and holes are diffused to fluorine-tin-oxide coated glass (FTO)/$TiO_2$ and Pt/FTO electrodes and restore the system in original state with gain of photovoltaic power.

Unlike p-n junction PV devices, the built-in electrical field is absent in DSSC as the nanocrystalline $TiO_2$ material does not support any band bending (conduction band) near interface, a phenomena,[1.43] that produces potential gradient after redistributing free charge carrier between two components of different electrochemical potential (Fermi level) *viz.* macrocrystalline $TiO_2$ and electrolyte solution.[1.44] In dark condition, the Fermi level of $TiO_2$ electrode stays in equilibrium with midpoint potential of redox electrolyte which lies deep within band gap of $TiO_2$ semiconductor material. So, net photocurrent and photovoltage is zero in dark. On matching dye excited state energetics above $TiO_2$ conduction band edge, the photoexcitation results electron injection into $TiO_2$ film. The rise in local concentration of electron on $TiO_2$ interface raises the Fermi level close to conduction band edge and flow the electron flux towards FTO contacts (Fermi level of FTO remain same as in dark condition). The hole transfer to fairly concentrate redox electrolyte have no effects on its chemical potential and remain same as that in dark condition. Thus, the photoexcitation energy is stored in the form of free energy of injected electrons which produces photo-voltage and the net electron and hole transfer to respective electrodes results in photocurrent.

The high efficiency (9-11%) of DSSC is results of favorable kinetic competition at interface.[1.34,1.45] Kinetic control is meaningful in terms of relative magnitude of intercepting processes rather than absolute magnitude of individual kinetics. The forward processes including electron injection (❷) and dye regeneration (❹), are faster than the intercepting processes including recapture of injected electron (❺,❼) and excited state decay (❸).The reason of kinetics favour lies in spatial and phase separation of photo generated charge-carriers which reduce the chances of interfacial charge transfer (❺,❼). Scheme-1.2 is event narrative of kinetic control in DSSC in which typical time scales are referred from transient studies reported in literature.[1.34,1.38,1.39,1.46-1.51] It is apparent from scheme-1.2 that excited state decay (❸) and interfacial charge recombination (❺) are competing loss path ways which intercept the

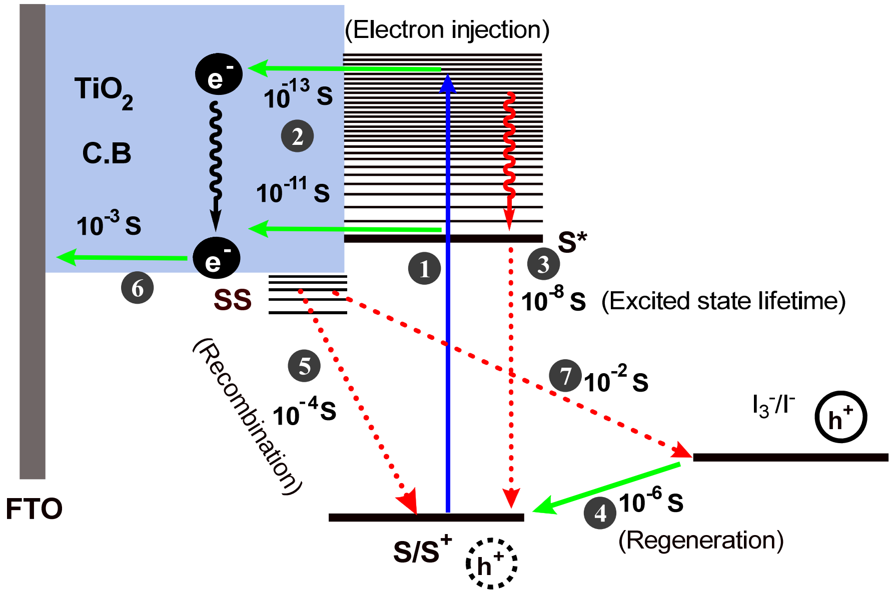

**Scheme 1.2:** State diagram showing key electron transfer kinetics of DSSC: The favorable kinetics are shown by green (solid) arrow whereas intercepting kinetics are shown by red (broken) arrow. The kinetics are numbered in order of relevant time scale.

forward gain process (❻) before recapture of electron by oxidized redox couple (❼). This makes rather easy to assess primary photoconversion process by using half-cell assembly *i.e.* dye sensitized $TiO_2$ film. Even, sometime more simplified approach using dye sensitized $TiO_2$ nanoparticle in solution phase can be a reasonable approximation due to flat band positioning of $TiO_2$ NP in solution and in film. In absence of redox electrolyte, though surface charging phenomena affect the interfacial charge recombination and electron conduction in $TiO_2$ film; nonetheless it shows the feasibility of new system. Therefore, these approaches are more popular in understanding basic electron transfer reaction using transient detection techniques.

From kinetic point of view, an ideal dye sensitized $TiO_2$ system should exhibits forwards processes more efficient than intercepting processes. For example,

1. Efficient primary charge separation demand electron injection kinetics- to be faster than decay of excited states: Step ❷ > Step ❸
2. Efficient interfacial charge separation demands cation transfer kinetics to be faster than recombination reactions of oxidized dye molecules: Step ❹ > Step ❺
3. Efficient charge collection requires electron transport to be faster than recapture with diffusing hole: Step ❻ > Step ❼

The aforementioned IET reactions can be controlled by careful design of sensitizer molecules. It includes an optimization of surface binding strength (electronic coupling matrix), energetics of sensitizer dye molecules (Gibbs free energy), structural orientation, inherent photoactive electronic transitions ($\pi \rightarrow \pi^*$, $n \rightarrow \pi^*$, MLCT) *etc*. A sequential gain of long lived and energetic charge separated species is possible through balancing strength of each factor. For example, a strong electronic coupling (binding strength) out-compete the excited state decay channel but also increase charge recombination process. Thus, high electron injection yield comes at cost of lifetime of charge separated states. Likewise, the decreased HOMO-LUMO gap results higher spectral coverage but it also reduces driving force for electron injection or regeneration of dyes. The dye molecules having $\pi \rightarrow \pi^*$ transition usually exhibits higher absorption coefficient than MLCT based dyes but lacks a long lived excited states and broad spectral coverage. Thus, the dye molecules comprising strong electronic coupling, broad spectral coverage and slow recombination dynamics would be an ideal photosensitizer.

### 1.2.2 Classical theory of electron transfer (ET):

The electron transfer theories in donor (D)-acceptor (A) system are based on fluctuating energy model originally developed by Marcus and applied to semiconductor/electrolyte interface by

Gerischer.[1.38,1.52,1.53] In such model, harmonic oscillator approximation is used to describe the fluctuating motion of nuclei in transition state (T.S.) formalism.[1.54] The electron transfer phenomena is defined by two intersecting parabolic energy diagram of reactant (D-A) and product ($D^+$-$A^-$) states.

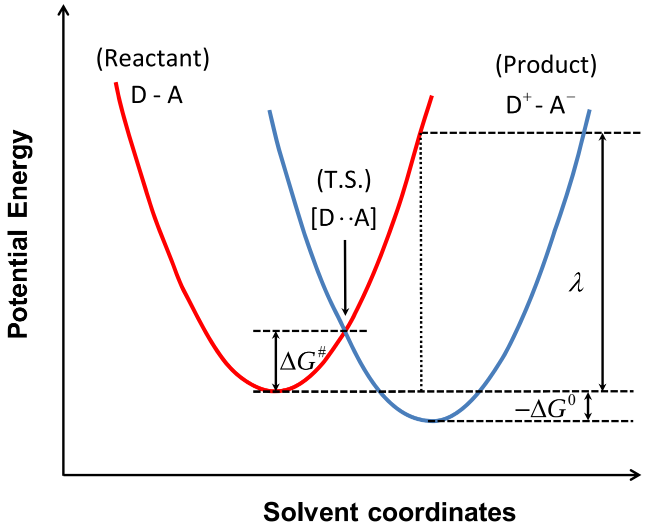

**Figure 1.1:** The potential energy curves of the reactant and product states in ET reaction. $\Delta G^0$ is the free energy change and $\Delta G^*$ is the free energy of activation.

Figure-1.1 shows schematic presentation of reactant's and product's potential energy surfaces (PES) with transition state forming at their intersection point. The electron transfer occurs at intersecting point (T.S.) where nuclear coordinates remains unchanged, a condition recognized as "Franck-Condon principle".[1.55] The Franck-Condon approximation is reasonable on ground of slow nuclear vibration ($\upsilon_n \sim 10^{11}$-$10^{13}$ $s^{-1}$) as compared to ultrafast electron transfer ($K_{et}$ ~$10^{15}$ $s^{-1}$) in transition state.[1.56] At the time of electron transfer, solvent coordinates changes and activation energy ($\Delta G^{\#}$) is needed in transforming the system from "reactant energy minima" to "product energy minima". According to classical theory of electron transfer, the crossing rate of

T.S. is Arrhenius function of activation energy ($\Delta G^{\#}$) along with pre-exponential factors which are frequency ($\upsilon_n$) of nuclear motion passing through transition state and crossover transmission probability ($\kappa_{\mathrm{t}}$). The activation energy is formulated in terms of driving force ($\Delta G^0$) and solvent reorganization energy (λ) by applying Gibbs free energy as quadratic function of solvent reaction coordinates. Rate of electron transfer is given by

$$k_{\mathrm{et}} = \kappa_{\mathrm{t}}\upsilon_n \exp\left(\frac{-\Delta G^{\#}}{K_B T}\right) \tag{1.1}$$

Where $\Delta G^{\#}$ is given by

$$\Delta G^{\#} = \left(\frac{\left(\Delta G^0 + \lambda\right)^2}{4\lambda}\right) \tag{1.2}$$

The reorganization energy ($\lambda$) is energy involved in relaxation process of solvation shell and comprises both intramolecular ($\lambda_{in}$) and solvent ($\lambda_{out}$) contributions. The $\lambda_{in}$ is given by

$$\lambda_{in} = \sum_j \frac{1}{2} f_j \left(\Delta Q_{e,j}\right)^2 \tag{1.3}$$

where, $\Delta Q_{e,j}$ is change in equilibrium values of $j^{\text{th}}$ bond coordinates in passing from reactant to product states and $f_j$ represents force constant of $j^{\text{th}}$ order bond.[1.55] For symmetrical molecules, like $\mathrm{Ru(bpy)_3}$ and simple aromatic molecules, which do not involve very distorted excited states, the inner sphere reorganization energy is low ~0.16eV.[1.57] The outer sphere reorganization ($\lambda_{out}$) energy corresponds to translational and orientational polarization of solvent molecules. The $\lambda_{out}$ term is formulated by assuming spherical reactants of radii $r_A$ and $r_B$ with centre to centre distance of $R_{AB}$ and solvent as dielectric continuum.

$$\lambda_{out} = \frac{(\Delta e^2)}{4\pi\varepsilon_o}\left(\frac{1}{\varepsilon_{op}} - \frac{1}{\varepsilon_s}\right)\left(\frac{1}{2r_A} + \frac{1}{2r_B} - \frac{1}{R_{AB}}\right) \tag{1.4}$$

where, $\varepsilon_{op}$ and $\varepsilon_s$ are optical and static dielectric constants of solvent medium.[1.58] The absolute value of λ distinguishes the energy- *vs*. electron- transfer mechanism. The reorganization energy ($\lambda_{out}$) is higher for electron transfer reactions (1-2eV) than energy transfer reaction (0.1-0.7eV) due to net charge transfer in former process.[1.17,1.58]

The relative magnitude of reorganization energy ($\lambda$) and driving force ($-\Delta G^0$) play decisive role in acceleration or retardation of electron transfer reaction. The essence of Marcus theory is realized in existence of inverted region in which rate of electron transfer decreases as the reaction becomes more exergonic ($-\Delta G^0$). Normally, the rate of electron transfer increases with increase in driving force (($-\Delta G^0$)) and reaches to maximum when $-\Delta G^0$ equalize to λ. At this point, the reorganization energy compensated by reaction energy ($-\Delta G^0$) and barrier less ($\Delta G^{\#} = 0$) charge separation occur. Past this point, the exergonicity ($-\Delta G^0$) exceeds reorganization energy (λ) and rate of ET reaction decreases with increasing activation energy ($\Delta G^{\#}$). The three regions are shown in figure-1.2. In ET reactions, the exergonic energy is used in vibrational excitation of ambient solvent molecules. In the case of barrier-less ET reaction, the resonant phonon coupling maximizes the reaction rate. As the reaction becomes more exergonic, the resonant phonon coupling deviates from ideal condition and slow down the ET reaction rate. The physical explanation of higher activation energy in Marcus inverted region is recognized as distortion of solvent environment prior to electron transfer reaction. The normal and inverted regions are more familiar in DSSC where small reorganization energy supports ultrafast electron injection ($\sim 10^{13}$ $s^{-1}$) at low driving force in normal region and large exergonicity ($-\Delta G^0 > 1.1$eV) of charge recombination reactions enforce slow kinetics in “inverted” region.[1.59-1.62] In classical Marcus theory, the activation energy ($\Delta G^{\#}$) dependent ET rate is given for non-

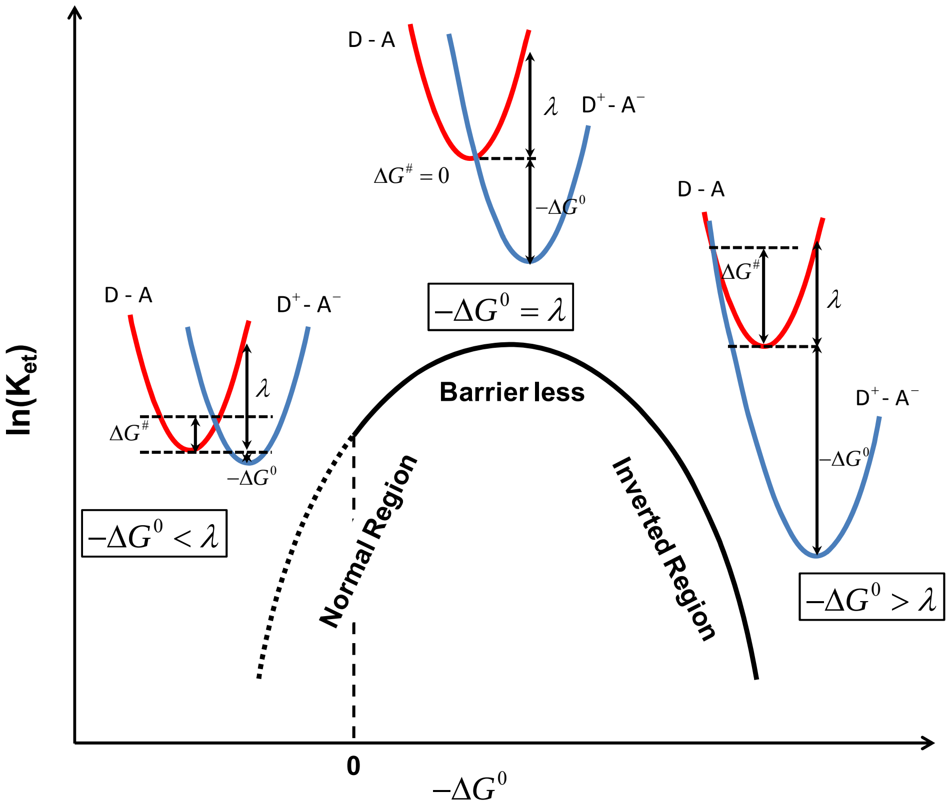

**Figure 1.2:** ln($k_{et}$) *vs.* free energy plot. It shows the ET reactions occur in the normal region, barrier-less, and in the inverted region when $-\Delta G^0 < \lambda$, $-\Delta G^0 = \lambda$, and $-\Delta G^0 > \lambda$,respectively.

adiabatic reactions in which electronic coupling is very weak in D-A system. The outer-sphere electron transfer reaction *viz.* electron transfer between metal-complexes, largely occurs in such non-adiabatic limit.[1.63] On the contrary, the inner sphere ET reactions as observed in reactant chemisorbed on electrode surface, is close to adiabatic limits.[1.55,1.63-1.66] In strongly coupled D-A system (Figure-1.3), the energy surface splits in crossing region which affects the transmission factor ($\kappa_t$). Landau and other give $H_{AB}$ parameter for energy separation between two surfaces.[1.67] In a quantum mechanical approach, Hush formulated the $H_{AB}$ parameter for mixing of initial ($\psi_R^0$) and final ($\psi_P^0$) states for adiabatic ET reactions.

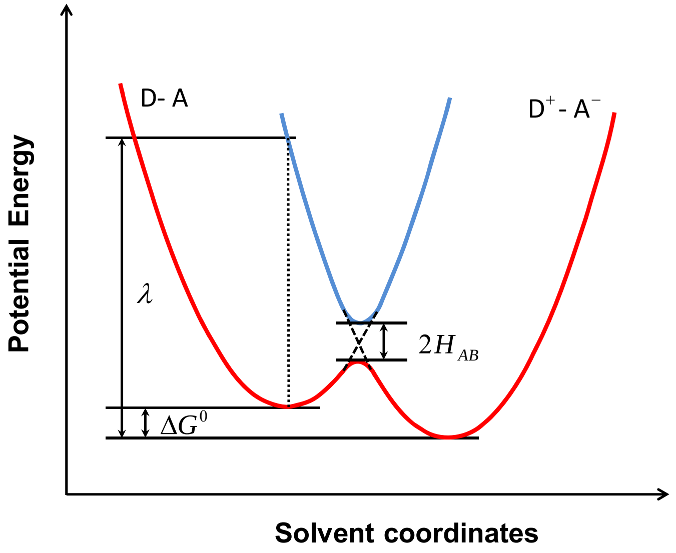

**Figure 1.3**: Schematic representation of $H_{AB}$ electronic coupling matrix element for ET reaction

The Marcus-Hush theory,[1.38] includes $H_{AB}$ electronic coupling in a classical electron transfer rate expression, given by:

$$k_{et} = \frac{2\pi}{\hbar}\left|H_{AB}^2\right|\frac{1}{\sqrt{4\pi\lambda K_B T}}\exp\left(\frac{-\left(\Delta G^0+\lambda\right)^2}{K_B T}\right) \qquad (1.5)$$

The significance of $H_{AB}$ parameter lies in strongly coupled quantum system where large coupling matrix separates energy surfaces and the reaction follows lower energy surface path. In adiabatic limit, the ET occurs every time the nuclear coordinates of transition states are formed and hence "frequency of nuclear motion ($\upsilon_n$)" is rate determining factor in adiabatic electron transfer reactions. In normal region, the nuclear tunneling is insignificant because of availability of ultrafast electron transfer route (~$10^{15}$ $s^{-1}$) in transition state. Nuclear tunneling is more relevant in inverted region as thermal activation barrier of transition state is considerably large.

In inverted region, electron transfer via nuclear tunneling requires almost no activation barrier in transition from donor to acceptor vibrational levels below classical crossing region/point and hence is more favorable.[1.68,1.69] In this condition, electron transfer can take place from any two vibrational levels of same energy as shown in figure-1.4.

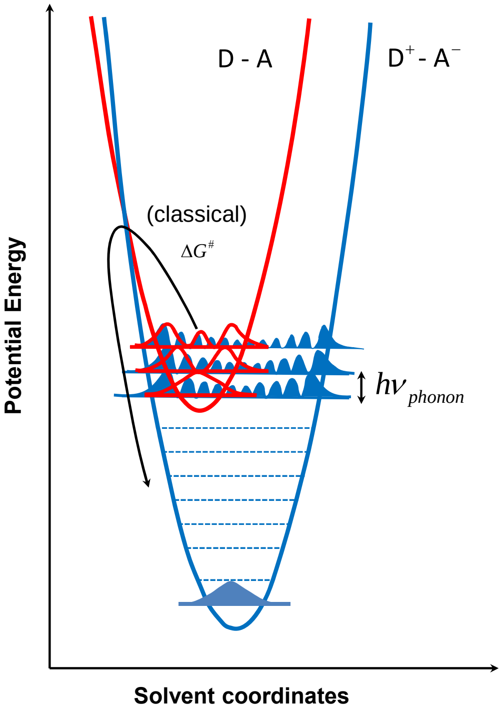

**Figure 1.4:** PES for an electron-transfer reaction in inverted region, showing vibrational quantization, assuming the same vibrational frequency (ν) in reactant and product states.

In further simplification, on average one high frequency mode ($nh\nu_{phonon}$) effectively contributes to electron transfer reaction, given by:

$$k_{\text{et}} = \frac{2\pi}{\hbar}\left|H_{AB}^{2}\right|\frac{1}{\sqrt{4\pi\lambda_{out}K_BT}}\times\sum_{n}\left[\frac{e^{-S}S^{n}}{n!}\right]\left[\exp\left(\frac{-\left(\Delta G^{0}+\lambda_{out}+nh\nu_{phonon}\right)^{2}}{K_BT}\right)\right] \tag{1.6}$$

where, $S = \dfrac{\lambda_{in}}{h\nu_{phonon}}$ is related to dimensionless quantity which represents electron-vibronic coupling. The sum $\sum_n \left[ \dfrac{e^{-S} S^n}{n!} \right]$ represents Franck-Condon factor for 0th and nth vibrational mode of reactant and product states, respectively. The summation is given for all coupled modes ("limit of n"). Each value of "n limit" represents a separate 0→n reaction channel. The sum is dominated by those channels which satisfy energy conservation rule: $-\Delta G^0 \approx \lambda_{out} + nh\nu_{phonon}$

Therefore, high frequency mode mainly undergoes electron transfer in inverted region. All the low frequency solvent modes are included in $\Delta G^0$ factor. In inverted region, the relationship of $\ln(K_{et})$ and $-\Delta G^0$ is less than quadratic and $K_{et}$ can be expressed as

$$k_{\mathrm{et}} \propto \exp\left( -S - \gamma \frac{\left| \Delta G^0 - \lambda_{out} \right|}{h\nu_{phonon}} \right), \qquad \text{where } \gamma = \ln\left( \frac{-\Delta G^0}{\lambda_{out}} \right) - 1 \tag{1.7}$$

It formulates "energy gap law" in which the probability of ET decreases linearly with increasing energy gap.[1.58,1.68,1.70] The prominent examples of such systems are intramolecular electron transfer in metal-polypyridyl complexes which occurs through non-radiative decay. This is one of the reasons that the emission quantum yield is low for ligand localized charge transfer states of transition metal complexes.

The above formulation is true for strongly coupled system. In weakly coupled system, the quantum mechanical formulation of non-adiabatic ET reaction is expressed as

$$k_{\mathrm{ET}} = \frac{4\pi^2}{h} H_{AB}^2 (\mathrm{FCWD}) \tag{1.8}$$

where, FCWD is Franck-Condon weighted density of states. Equation (1.8) states about "Fermi's Golden rule",[1.58,1.68] according to which the radiationless transition is function of density of excited vibrational levels of final states that matches to energy of initial states and vibronic coupling between initial and final states.

### 1.2.3 Electron transfer (ET) at semiconductor/dye interface: Gerischer Model

The interfacial electron transfer reaction in Marcus model is extension of problem from homogenous medium to heterogamous medium. The participation of multitude of delocalized energy level and restricted reaction coordinates due to phase difference at interface, bring constrain on simplified Marcus version of ET reaction. The elaborate expression for forwards and back electron reactions is given in Gerischer electron transfer model. In Gerischer approach, bath fluctuations of solvated states (reduced or oxidized) are described by Gaussian function *viz.* $W_{ox}$ and $W_{Red}$. Figure-1.5 shows simplified Gerischer model for semiconductor/electrolyte interface.

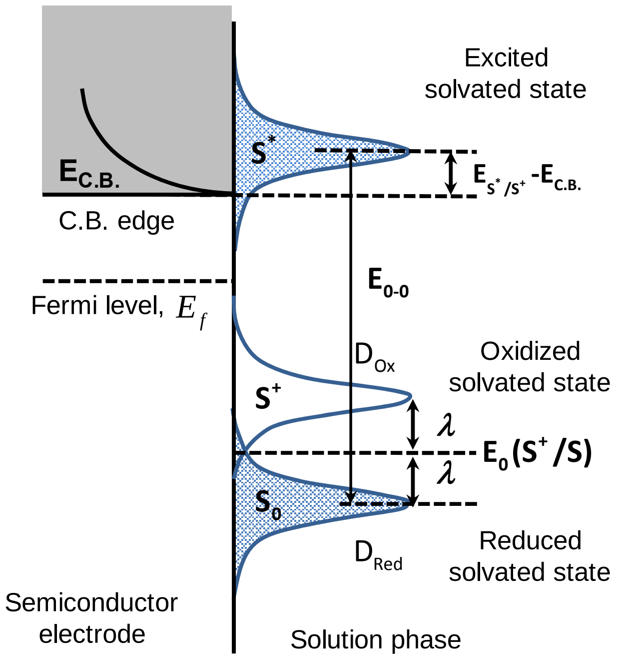

**Figure 1.5:** Gerischer diagram of semiconductor electrode/redox couple interface.

The Gaussian distribution of empty (oxidized) and occupied (reduced) states are given as

$$W_{\mathrm{Ox}} = W_{Ox}^{0} \exp\left( \frac{-(E - eE_{F,redox}^{o} + \lambda)^2}{4K_B T\lambda} \right) \tag{1.9}$$

$$W_{\mathrm{Red}} = W_{\mathrm{Re}d}^{0} \exp\left( \frac{-(E - eE_{F,redox}^{o} - \lambda)^2}{4K_B T\lambda} \right) \tag{1.10}$$

Where, $W_{\mathrm{Ox}}$ and $W_{\mathrm{Red}}$ represents probability of finding solvated state at energy E level.[1.38,1.53,1.71] The density of states of oxidized and reduced species is given by:

$$D_{\mathrm{Ox}} = C_{Ox}W_{ox} \text{ and } D_{\mathrm{Red}} = C_{\mathrm{Re}d}W_{red} \tag{1.11}$$

In figure-1.5, the identical Gaussian distribution curves represent equal concentration of redox couple ($C_{Ox} = C_{\mathrm{Re}d}$) and equal reorganization energy of oxidized and reduced solvated states. A decrease or an increase in $C_{Ox}/C_{\mathrm{Re}d}$ concentration ratio from unity, shift the Fermi level $eE_{redox}^{o}$ (intersection point of two distribution curve) up or down depending upon the relative magnitude of distribution curves. The result is same as predicted from Nernst equation, [1.72]

$$E_{F,\mathrm{Re}dox} = E_{F,\mathrm{Re}dox}^{0} - K_B T \ln\left( \frac{C_{Ox}}{C_{\mathrm{Re}d}} \right) \tag{1.12}$$

The same is true for excited state Fermi level ($eE_{redox}^{*}$), which can be obtained by adding energy of 0-0 transition between 0th vibrational level in the ground and excited state. Thus,

$$E_{F,refox}^{*}(S^{*}/S^{+}) = E_{F,refox}^{0}(S^{0}/S^{+}) + E_{0-0}(S/S^{*}) \tag{1.13}$$

The rate of back electron transfer can be expressed as

$$k_{\mathrm{et}} = \kappa_{\mathrm{t}} Z_{el} \int_{E_c}^{\infty} f(E)\rho(E)W_{Ox}(E)dE \tag{1.14}$$

Where, $Z_{el}$ is the frequency along reaction coordinates and $\kappa_{\mathrm{t}}$ is the transmission factor. $f(E)$ and $\rho(E)$ represent Fermi function and density of states (DOS) respectively, given by:

$$f(E)=\left(1+\exp\left(\frac{E-E_f}{K_BT}\right)\right)^{-1} \quad \& \quad \rho(E)=\frac{8\sqrt{2}\pi m^{3/2}}{h^3}\sqrt{E} \qquad (1.15)\ \&\ (1.16)$$

The term $\int_{E_c}^{\infty} f(E)\rho(E)dE$ defines total density of electron near surface ($n_S$).[1.43,1.53,1.73] Assuming that electron transfer occurs near conduction band edge $E_c$, then rate of backward ET is given by:

$$k_{ET}^{Backward} = \kappa_{\mathrm{t}} Z_{el} n_S \exp\left(-\frac{\left(E_c - E_{F,refox}^{0} + \lambda\right)^2}{4K_B\lambda T}\right) \qquad (1.17)$$

Likewise, forward ET can be expressed as

$$k_{ET}^{Forward} = \kappa_{\mathrm{t}} Z_{el} N_c \exp\left(-\frac{\left(E_c - E_{F,refox}^{*} - \lambda\right)^2}{4K_B\lambda T}\right) \qquad (1.18)$$

where, $N_c$ represents effective density of unoccupied states at lower edge of conduction band. The exponential term used in equation (1.18), is essentially same as obtained from Marcus-Hush theory provided that $-\Delta G^0$ is expressed in terms of electrochemical potential of electrode (conduction band edge- $E_C$) and redox couple (standard redox potential; $U_{redox}^{o} = E_{F,refox}^{0}/e$).

$$\Delta G^0 = eU_{redox}^{*} - E_C \qquad (1.19)$$

Hence,

$$k_{\mathrm{et}} = \kappa_{\mathrm{t}} Z_{el} \exp\left(\frac{-(E_C - eU_{redox}^{*} - \lambda)^2}{K_BT}\right) \qquad (1.20)$$

In term of Marcus-Hush theory, forward ET reaction is sum of all ET steps over dense fold acceptor states (conduction band) which are represented by DOS ($N_c$) in Gerischer model. So, forward ET reaction can be pictorially presented as figure-1.6.

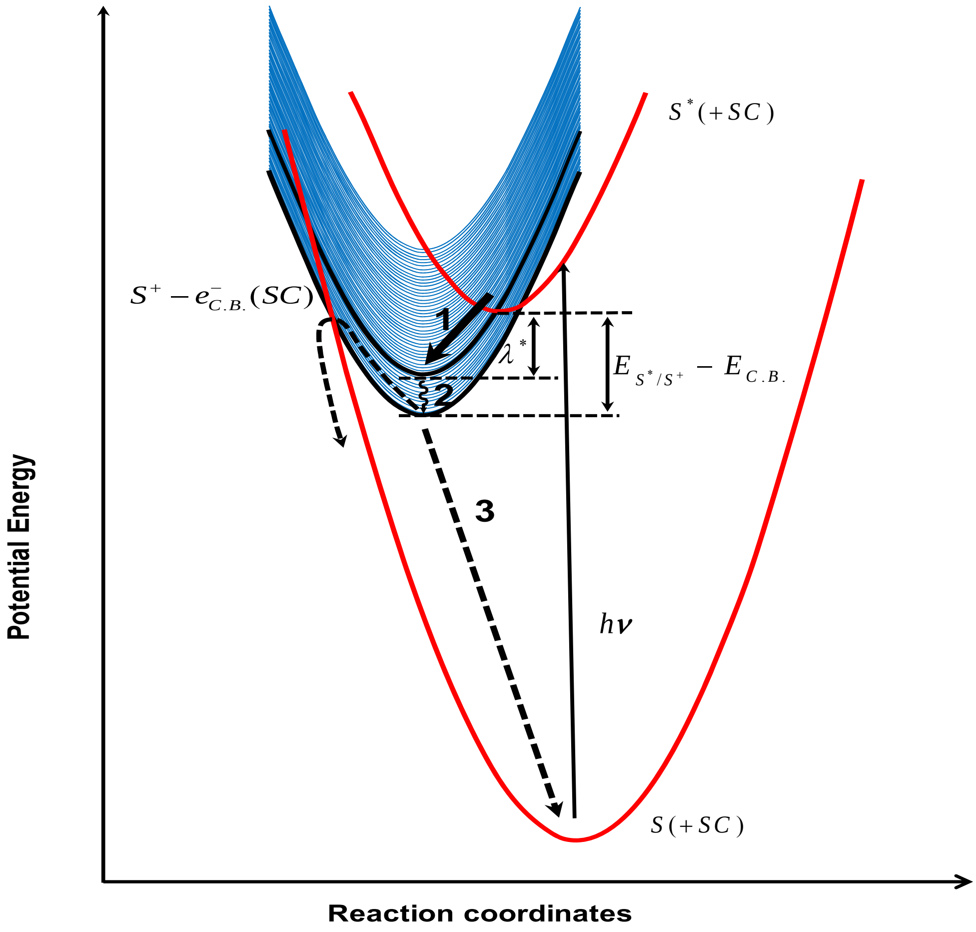

**Figure 1.6:** Marcus model of IET reaction. Electron injection occurs from an excited state to a continuum of conduction band. Bold arrow -1: barrier less forward ET from S* to matching acceptor states. Curved arrow -2: electron thermalization in C.B. of $TiO_2$ semiconductor. Dashed arrow -3: back electron transfer in Marcus inverted region.

In Marcus model, the driving force for forwards electron injection and back electron transfer reactions is different due to dissimilar Fermi level energy in ground and excited state (see eq$^n$ (1.13) and (1.19)). In a known example of $Ru^{II}(SCN)_2(dcbpy)_2$ complex (N3 dye), the $U^0_{redox}$ and $U^*_{redox}$ values are observed to be 1.1 V (*vs.* NHE) and -0.65 V ($E_{0-0} = 1.75eV$), respectively and the reorganization energy ($\lambda$) is reported as ~0.35eV in ground state.[1.17] The conduction band edge ($E_C$) energy of $TiO_2$ electrode is ~ -0.45 eV (*vs.* NHE).[1.74] Thus, forward electron transfer reaction occurs in Marcus normal region whereas back electron transfer occurs in inverted region. Therefore, the forward electron transfer reactions are much faster than back electron transfer (BET) reactions. The electron injection rates are maximum when excited state (S*) is above conduction band edge to the extent of its reorganization energy ($\lambda$).

*i.e.*
$$E_{S^*/S^+} - E_{C.B.} = \lambda \tag{1.21}$$

Following a resonant phonon coupling ($E_{S^*/S^+} - E_{C.B.} = \lambda$), barrier-less electron injection take place in ~100fs time scale in non-adiabatic limit. Considering the large DOS in $TiO_2$, the condition is more or less realized for most of organic and inorganic sensitizer molecules. For $TiO_2$ electrode material, the DOS ($N_C$>$10^{21}$) is much higher than minority charge carrier injected in $TiO_2$ electrode ($N_S$ ~$10^{19}$).[1.75] Thus, apart from qualitative results from Marcus ET model, Gerischer model numerically validate the slow BET reactions in comparison to electron injection reactions. From thermodynamic aspect, forward ET reactions are more favorable due to increase in entropy and so are less favorable in back electron transfer reactions. Thus, either of ET model shows an extremely fast electron injection reaction over back electron transfer reaction. This forms the basis of primary photoconversion process in DSSC. Evidently, in real DSSC, other factor such as sensitizer binding mode as well as strength, surface heterogeneity and trap states, redox electrolyte concentration *etc.* also affect the interfacial electron transfer kinetics.

In electronically coupled dye/$TiO_2$ system, the electron transfer rate equations (1.17 and 1.18) are modified by $|\bar{H}(E)|^2$ parameter which represent average coupling between sensitizer excited state (S*) and dense fold acceptor states. For electron injection process, the rate of electron transfer is given by “Fermi’s Golden Rule” (eq$^n$ 1.8).

$$k_{\text{inj}} = \frac{4\pi^2}{h}|H|^2 \,(\text{FCWD}) = \frac{4\pi^2}{h}|H|^2\left(\frac{n_a}{\hbar\omega}\right) \tag{1.22}$$

where, $n_a$ is effective density of empty electronic states in $\hbar\omega$ energy spacing of cation oscillator. For a semiconductor material having large DOS, $n_a = 1$. The average oscillating frequency of dye cation is $\varpi = 1500cm^{-1}$ and the electronic coupling matrix is given by $|H| > 200cm^{-1}(\sim K_B T)$ .[1.76] This gives a first order rate constant for electron injection reaction ~ $10^{13}$s$^{-1}$. However, care should be taken in accessing electron injection from higher vibrational level of excited states because the $|H|$ parameter becomes time dependent. Nonetheless, it still gives a fair estimation of electron injection process from hot singlet excited states into high DOS of $TiO_2$ material. A further higher order of “electron injection” reaction rates can arise from existence of excited state manifolds such as single and triplet states of transition metal complexes, or surface heterogeneity giving a distribution of acceptor states. For these reasons, the multiexponential electron injection kinetics are reported in >100fs to <100ps time scale.[1.39,1.77]

The electron injected into hot states, thermalizes and then reaches to bottom of conduction band. Since, the back electron transfer reaction are slow (Marcus inverted region), the wait time allow thermalized electron to fall into surface states below conduction band edge. The density of states in bottom of conduction band is fairly low (equation (1.16)), so the electron trapping becomes part of surface electron transfer reactions.[1.47] The trap states arising from surface dangling bond, are exponentially distributed in mid band gap of semiconductor material and given by exponential Boltzmann distribution function,

$$g_{\exp}(\mathrm{E}) = \frac{N_{\exp}}{K_B T_0}\exp\left(-\frac{E_{C.B.}-E}{K_B T_0}\right) \tag{1.23}$$

where, $N_{\exp}$ is total density of exponentially distributed trap states ~$10^{19}$ $\mathrm{cm}^{-3}$ for mesoporous $TiO_2$ films. $T_0$ is temperature related parameter which describe depth of trap states. Typically, $K_B T_0$ parameter is ~60-100meV for $TiO_2$ crystal.[1.78]

The injected electrons are trapped in surface localized states below C.B. down to Fermi level of solution phase ($E_{f,0}$- which depends of electrolyte concentration, see eq$^{n}$ 1.12). The trapped electron transfer to possible acceptor states is hindered by thermal activation barrier till thermal detrapping releases electron.[1.79] The thermal detrapping time is given by

$$\tau = \frac{\exp\left(E_T - E_{C.B.}/K_B T\right)}{\nu_{th}} \tag{1.24}$$

where, $\nu_{th}$ frequency is ~$10^{12}$-$10^{13}$ $\mathrm{s}^{-1}$. This gives a lifetime of ~100ps to ~μs time scale which is of the order of charge recombination reactions.[1.34,1.43,1.80] Thus, back electron transfer rate equation (1.17) is extended for trap state contribution,

$$k_{BET}^{total} = k_{BET}^{C.B.} + k_{BET}^{S} \tag{1.25}$$

$$k_{BET}^{S} = \kappa_t^{'} Z_{el}^{'} \int_{E_{f,0}}^{E_{C.B.}} f(E-E_f) g^s(E) \exp\left(-\frac{\left(E - E_{\mathrm{Re}dox} + \lambda\right)^2}{4K_B \lambda T}\right) dE \tag{1.26}$$

The term $\int_{Ef}^{E_{C.B.}} f(E-E_f) g^s(E) dE$ is Fermi function weighted occupancy of trap states in $E_{f,0} < E < E_{C.B.}$ range. The $g^s(E)$ function is extendable for different kind of trapping mechanism such as dangling bond in surface region, columbic trapping due to electrolyte, cation adsorption on surface *etc*.

The trap states due to surface dangling bonds are results of incomplete coordination of surface metal ions. So, surface adsorption of sensitizer molecules partially completes the coordination sphere. This is a passive way through which surface binding mode affects back electron transfer dynamics. The active role of surface binding mode is to resolve electronic coupling strength which decides electron reactions in non-adiabatic or adiabatic limits. For weak binding mode, the interfacial electron transfer reactions are described in previous formulation in non-adiabatic limits. In strong coupling system, charge transfer (CT) transition occurs through adiabatic route. In adiabatic limit, both electron injection and BET reactions rate are increased due to direct CT processes. The interesting part of CT interaction is direct measurement of ET parameters through spectroscopic observables. In CT donor-acceptor system, the activation energy ( $\Delta G^{\#}$ ) and electronic coupling parameter ( $\left|H\right|^2$ ) are given as,

$$E_{op} = h\nu_{CT} = \lambda + \Delta G^0 \tag{1.27}$$

From eq$^n$ (1.2)

$$\Delta G^* = \frac{E_{op}^2}{4\left(E_{op} - \Delta G^0\right)} \tag{1.28}$$

This gives "Hush's Law" for mixed valence complexes,[1.81] that in limit of $\Delta G^0 = 0$

$$\Delta G^* = \frac{E_{op}}{4} \tag{1.29}$$

From Marcus model, (assuming $\lambda^*_{(\text{E. S.})} = \lambda_{(\text{G. S.})}$ )

$$h\nu_{abs} = \Delta G^0 + \lambda \tag{1.30}$$

$$h\nu_{em} = \Delta G^0 - \lambda \qquad (1.31)$$

$$\lambda = \frac{h\nu_{abs} - h\nu_{em}}{2} = \frac{h\nu_{st}}{2} \qquad (1.32)$$

$$\Delta G^0 = \frac{(h\nu_{abs} + h\nu_{em})}{2} \qquad (1.33)$$

The electronic coupling parameter is given by Mullikan-Hush relation,[1.82]

$$H_{AB} = 2.05\times10^{-2}\left[\frac{\varepsilon_{\max}\Delta\bar{\nu}_{1/2}}{\bar{\nu}_{\max}}\right]^{1/2}\frac{\bar{\nu}_{\max}}{r} \qquad (1.34)$$

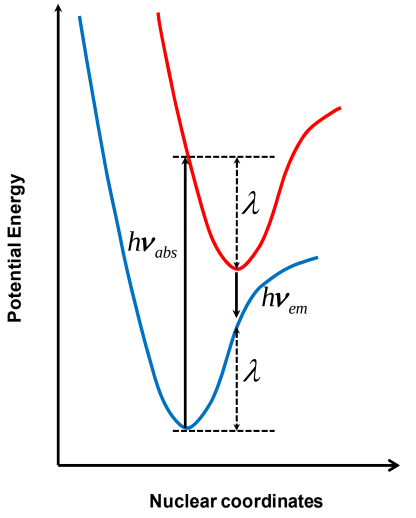

**Figure1.7:** PES of GS and ES.

where $\varepsilon_{\max}$ ($dm^3\ mol^{-1}\ cm^{-1}$) is the molar extinction coefficient of CT absorption band maximum, $\Delta\bar{\nu}_{1/2}$ ($cm^{-1}$) is the full width at half maximum of the CT band, $\bar{\nu}_{\max}$ ($cm^{-1}$) is energy at the band maximum, and r (Å) is the inter nuclear distance between the redox sites. The $\varepsilon_{\max}$, $\Delta\bar{\nu}_{1/2}$ and $\bar{\nu}_{\max}$ can be obtained by the optical absorption measurements and r can be calculated using the Edward’s volume increment method [1.83]. Thus, interfacial electron transfer reaction in adiabatic limit can be predicted from spectroscopic observables.

## 1.3 Semiconductor material:

Semiconductors comprise the class of materials in which conduction and valance band are separated out by mid band gap energy. In bulk semiconductor, conduction band (C.B.) and valence band (V.B.) consist of continuum of delocalized electronic states which originate from tight binding approximation of constituting atomic orbitals. At 0K, the electronic states are fully occupied in valence band whereas that of conduction band remains empty. In principle, no electronic state exists in forbidden energy gap ($E_g$). Typical value of mid band gap energy is 0.5

to 3.5 eV which depends on energetics and tight binding of atomic orbitals. At room temperature, some of the electrons are thermally lifted to conduction band by breaking chemical bonds and the empty locations in valence band are treated as positively charged holes ($h^+$). It is because of such low density of minority charge carriers ($n^0 \to e^-$ and $p^0 \to h^+$), the conductivity of semiconductor is measured between metal (overlapped C.B. and V.B.) and insulator ($E_g > 5eV$) class of materials. The density of electron and hole charge carrier is given by Fermi function weighted occupancy of electronic states. From equation (1.15) and (1.16),

$$n^0 = \int_{E_C}^{\infty} f(E)\rho(E)dE = \int_{E_C}^{\infty} \left(1 + \exp\left(\frac{E - E_F}{K_B T}\right)\right)^{-1} \times \frac{8\sqrt{2}\pi m^{3/2}}{h^3}\sqrt{E}dE$$

$$n^0 = N_C \exp\left(-\frac{E_C - E_F}{K_B T}\right), \text{ where } N_C = \frac{2\left(2\pi m_e^* K_B T\right)^{3/2}}{h^3} \qquad (1.35)$$

likewise,

$$p^0 = N_V \exp\left(-\frac{E_F - E_V}{K_B T}\right), \text{ where } N_V = \frac{2\left(2\pi m_h^* K_B T\right)^{3/2}}{h^3} \qquad (1.36)$$

Thus, intrinsic charge carrier density is expressed by Boltzmann distribution function.[1.13,1.43,1.53,1.73,1.84] $N_C$ is effective density of states within few K<sub>B</sub>T above conduction band and $m^*_{e/h}$ represents effective mass of electron/ hole given by curvature of respective bands. *i.e.*

$$m^* = \hbar^2 \Big/ \left(\frac{d^2E}{dk^2}\right) \qquad (1.37)$$

For intrinsic semiconductor, $n^0 = p^0$, using equation (1.35) and (1.36)

$$E_F = \frac{E_C + E_V}{2} + \frac{K_B T}{2} \ln\left(\frac{m_h^*}{m_e^*}\right)^{3/2} \qquad (1.38)$$

Assuming $m_e^* = m_h^*$, Fermi level is positioned in mid of $E_g$ band gap as shown in figure-1.8.

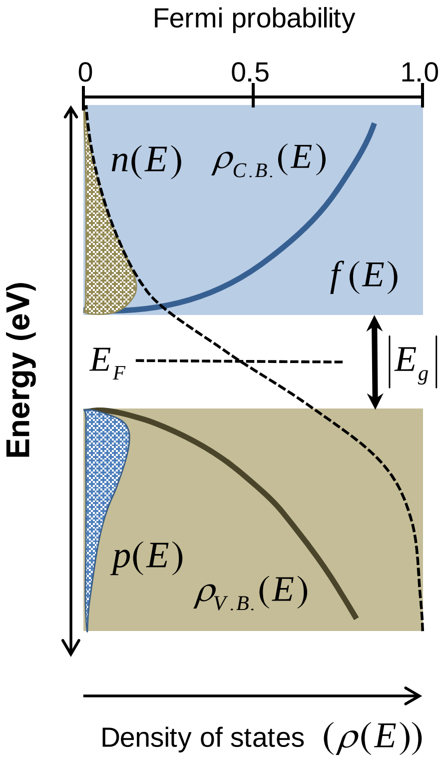

**Figure 1.8:** Schematic presentation of DOS ($\rho(E)$), charge carrier densities ($n(E)$ & $p(E)$) as a function of energy (conduction and valence band). Total density of charge carrier ($n^0$ & $p^0$) is integral area of Fermi function weighted DOS (shown here as shaded area).

Effective mass defines the charge carrier movement under periodic crystal potential of semiconductor material which is different for conduction and valence band because of different shape and energy of involved atomic orbitals. For example, the valence and conduction band of ionic $TiO_2$ crystal is composed of 2p orbital of $O^{2-}$ ions and 3d orbitals of $Ti^{4+}$ ions, respectively. So, electron and hole effective mass may not be same in C.B. and V.B. and vary for different semiconductor material. For example, $m^*_{e(TiO_2)} \sim 6m_0$ ($5m_0$ to 15 $m_0$ reported), $m^*_{h(TiO_2)} \sim 2m_0$, $m^*_{e(ZnO)} \sim 0.19m_0$, $m^*_{h(ZnO)} \sim 0.45m_0$ etc.[1.85-1.89] Since, the effective density of states is function of effective mass (equation 1.35 and 1.36), the DOS also vary for different semiconductor. For example, $DOS_{(TiO_2)}^{(C.B.)} \sim 10^{20} cm^{-1}$ and $DOS_{(ZnO)}^{(C.B.)} \sim 10^{18} cm^{-1}$.[1.90,1.91] These values represent density of electronic continuum states in bulk semiconductors. The electronic states are discretized when the crystal dimensions become sizable to lattice units.[1.92,1.93] In such size quantization region, the band gap energy increases with decreasing size in a proportion of reduced effective mass which is expressed by Brus equation, [1.94]

$$\Delta E_g = \frac{h^2}{8\mu R^2} - \frac{1.8e^2}{\varepsilon_S R} \qquad (1.39)$$

where, $\mu$ is reduced effective mass given by $\mu^{-1} = (m_e^*)^{-1} + (m_h^*)^{-1}$. The critical radius below which size quantization is realized, is expressed as exciton Bohr radius,[ 1.92,1.93] given by

$$R_b = \frac{\varepsilon_S a_0 m_0}{\mu}, \qquad \text{where } a_0 \sim 3\text{Å} \text{ Bohr radius for H-atom} \qquad (1.40)$$

According to this equation, the band gap energy increases as particle size decreases and the effect is comprehended in proportion to reduced effective mass. For example the reduced effective mass of $TiO_2$ is ~1.63-2.72$m_0$ and that of ZnO is 0.16 $m_0$. Thus, the effect of size quantization is more in ZnO ($R_b \sim 3-10nm$) than $TiO_2$ ($R_b < 1.8nm$) material. Figure-1.9 shows mid band gap energy ($E_g$) changing from bulk to size quantization region. The mid band gap energy $E_g$ is spectroscopic observable and it corresponds to light absorption threshold. For example, wide band gap material such as $TiO_2$, ZnO etc. absorbs light in short wavelength region <390nm whereas small band gap material such as Si, GaAs exhibit optical response in entire visible and near IR region. The optical response is given by Beer's law,

$$A = \ln\left(\frac{I_0}{I}\right) = \alpha l, \qquad (1.41)$$

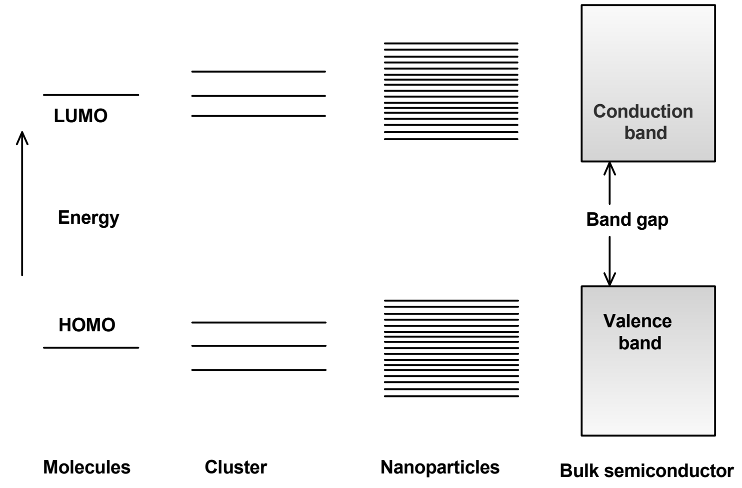

**Figure 1.9:** Size quantization effect: Discrete molecular energy levels gradually converging into energy bands with increasing particle size.

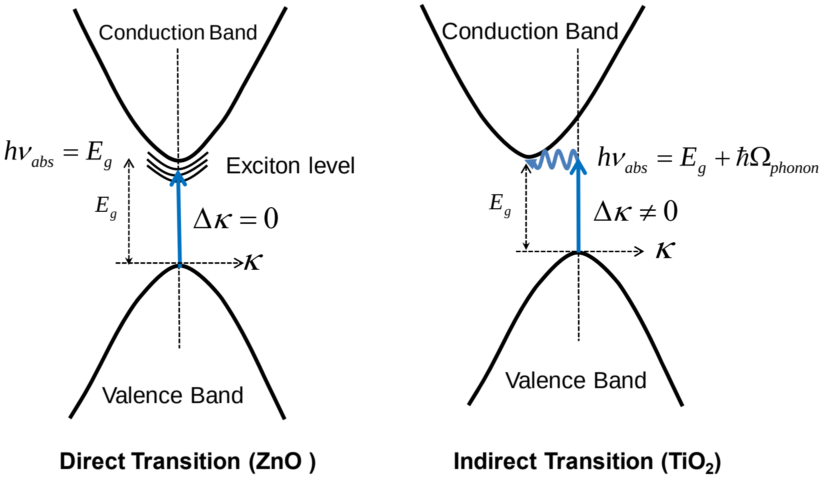

**Figure 1.10:** Direct bandgap and indirect bandgap transitions in ZnO and $TiO_2$ semiconductors.

where, absorption coefficient ($\alpha$) is function of wavelength. In direct band gap semiconductor material such as ZnO (Figure-1.10), the optical transition from V.B. to C.B. occurs at same $\kappa$(kappa) value (crystal momentum). Therefore, absorption coefficient ($\alpha$) is strong function of photon energy, [1.13,1.53,1.73,1.95]

$$\alpha \sim \left(E_{ph} - E_g\right)^{1/2} \quad (1.42)$$

For optically allowed transition, $\alpha$ values are typically in the range of $10^4$-$10^5$ cm$^{-1}$ near threshold energy ($E_g$). However, in indirect band gap materials such as $TiO_2$, the lowest energy optical transitions are forbidden due to different $\kappa$(kappa) of conduction and valence bands. Therefore, $\alpha$ values are much smaller ~$10^2$ cm$^{-1}$ near threshold energy ($E_g$) and given by

$$\alpha \sim \left(E_{ph} - E_g\right)^{2} \quad (1.43)$$

On light absorption, the electron is lifted to conduction band and the intrinsic charge carrier density ($n$ and $p$) increases above their equilibrium values ($n^0$ and $p^0$). In this situation the quasi Fermi level of electron and hole are separated out,

$$E_{F,n} = E_{C.B.} - \ln\left(\frac{N_C}{n}\right) \quad (1.44)$$

$$E_{F,p} = E_{V.B.} + \ln\left(\frac{N_V}{n}\right) \quad (1.45)$$

The Fermi level of electron is lifted up towards conduction band in interface region whereas that of bulk level remains same as in dark condition. So, minority charge carrier diffuses out of the excitation region and drift toward bulk region. This produces photovoltaic effect in narrow band gap semiconductor material. In wide-band gap semiconductor materials such as $TiO_2$ and ZnO, light absorption in visible region is very poor. For such semiconductors, surface derivatization with light absorbing sensitizer molecules produces analogous photoaction. DSSC is excellent example of employing wide band gap semiconductor material into photo induced electrochemical reactions.

### 1.4 Spectral sensitization using molecular system:

Spectral sensitization of wideband gap semiconductor material such as $TiO_2$ and ZnO is achieved by attaching light absorbing dye molecules on surface.[1.96,1.97] The chemical binding on semiconductor surface sets up electronic coupling which opens interfacial electron transfer pathways.[1.98] The electronic coupling strength varies for different surface binding groups *viz.* catecholate > phosphate > carboxylate *etc.* A strong coupling favors electron injection kinetics over excited state relaxation processes in sensitizer dye molecules.

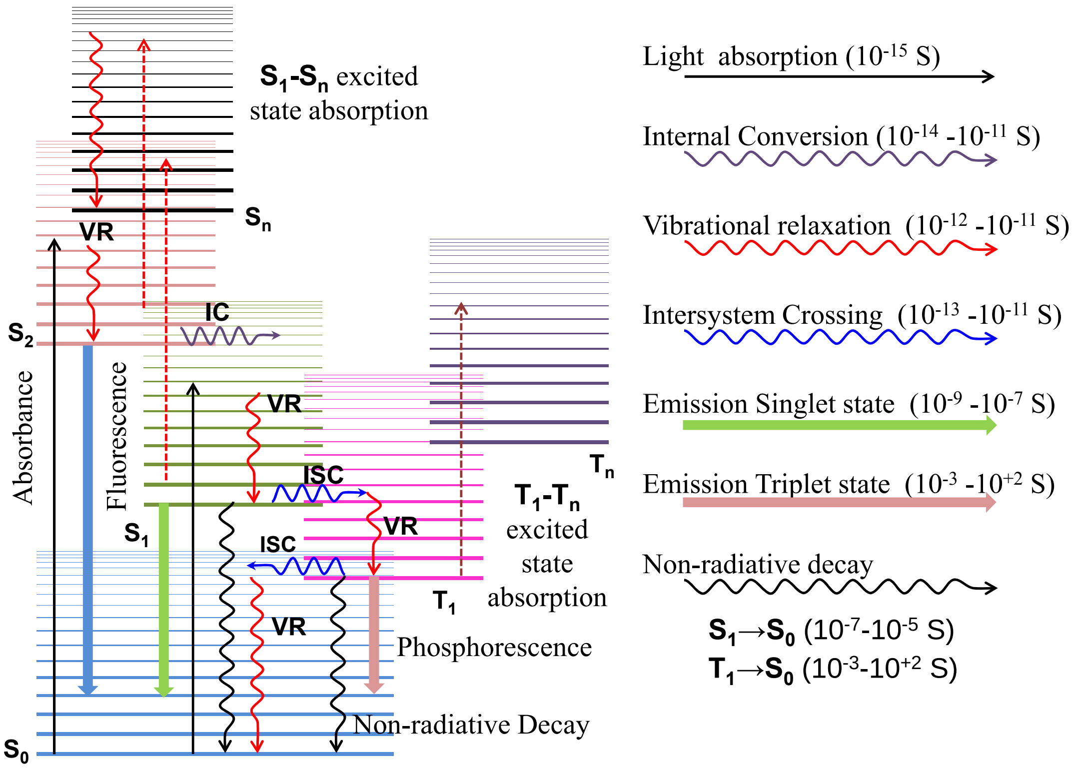

**Figure 1.11:** Jablonski diagram depicting various excited state relaxation process. Radiative processes are shown by solid straight arrow (absorption and emission), non-radiative processes are shown by curved arrow (internal conversion (IC), Vibrational relaxation (VR), Intersystem crossing (ISC) and non-radiative decay). Typical time scales are shown in seconds (S).

The intramolecular relaxation processes in molecular sensitizer are shown in Jablonski diagram (figure-1.11),[1.99]. The electronic excited states are populated by optical transition in sensitizer molecules, as shown in Jablonski diagram. The nature of electronic transition depends on sensitizer molecules *viz.* π→π* and n→π* transitions are more prevalent in organic sensitizer molecules whereas metal to ligand (dπ→ π*) charge transfer transitions (MLCT) are characteristics to organometallic complexes. In all cases, the optical response is solely determined by $S_0$-$S_1$ (in some cases $S_0$-$S_2$ also) energy gap. The essential condition of spectral sensitization is surface adsorption of dye molecules which have their excited state energy higher than $TiO_2$ conduction band edge and absorbs light in visible region. On satisfying these thermodynamic requirement, effectiveness of sensitizer molecules depends on kinetic parameters as described before. Various strategies adopted in modifications of sensitizer molecules which exhibit broad spectral coverage, strong electronic coupling, ultrafast electron injection but slow back electron reaction on semiconductor surface.

## 1.5 Thesis overview:

In present thesis, kinetics study of half-cell reaction in dye sensitized wideband gap semiconductor nanoparticle in solution- and film- phase are carried out using transient detection techniques such as femtosecond time-resolved transient absorption spectroscopy and picosecond time-resolved emission spectroscopy. The main aim of these studies is to understand the interfacial electron transfer (IET) dynamics by using new dye molecules in sensitization of wideband gap semiconductor nanomaterials. Different molecular level modifications are used to improve optical response and/or kinetics control over interfacial charge separation in dye/$TiO_2$ NPs. The molecular level modifications have been assessed in electron injection and back electron transfer reactions on $TiO_2$, $ZrO_2$, ZnO nanomaterials. The molecular modifications are sought for improvement in established sensitizer such as Ru(II)-polypyridyl complexes and also to address shortcomings of known sensitizer such as porphyrin dyes. In addition, the inspiration from natural photosynthetic antenna system is drawn in efficient spectral sensitization of ZnO QDs. Most of surface electron transfer reactions are studied on $TiO_2$ nanoparticles. In this thesis work, catechol moiety is used as linkage to metal oxide semiconductor surface except in photosynthetic antenna complex where naturally occurring carboxylate functionality is used.

The spectroscopic observables are used in detection of various transient species produced during interfacial charge transfer reactions. For examples, excited states of dye, conduction band electrons, cation formed after electron injection *etc.* all have differentiated by their unique spectral absorbance in visible and near IR region. The assignments of the transient species are further validated by cross correlated electron transfer kinetics. For instance, back electron transfer dynamics are correlated in decay of cation absorbance, ground state bleach recovery and decay of conduction band electron absorbance. All such kinetic studies show the feasibility of newer sensitizer molecules in primary photoconversion processes (Section-1.2).

## 1.6 Scope of the thesis: DSSC and biomimetic systems

In this thesis work, Os(II)-polypyridyl complexes, porphyrin aggregates are employed in study of surface electron transfer reactions on $TiO_2$ nanomaterials. A new class of electronic transition- “ligand-to-ligand charge transfer (LLCT)” has been explored in heteroleptic Ru(II)-polypyridyl complexes and the “intramolecular charge separation” property has been utilized in interfacial electron transfer on $TiO_2$ nanoparticle film. Large functional array- “phycocyanin-allophycocyanin pigments” and “trinuclear Ru(II)/Os(II)-polypyridyl complexes” have been employed in interfacial electron transfer studies where “sequential energy/electron transfer” antenna function have been confirmed. All the experimental findings have been depicted in various schemes. These experimental findings are applicable in DSSC and also help in exploration of new biomimetic systems.

## 1.7 References:

[1.1] Plant energetics, Author: O. S. Ksenzhek, A. G. Volkov, Academic Press, 1st edition, 1998.

[1.2] Energy for the 21st century: A Comprehensive Guide to Conventional and Alternative Sources, 2nd edition, Author: R. L. Nersesian, Publisher: M. E. Sharpe, New York, 2010.

[1.3] N. Armaroli, V. Balzani, Angew. Chem. Int. Ed. 2006, 45, 2.

[1.4] J. Chow, R. J. Kopp, P. R. Portney, Science, 2003, 302, 1528.

[1.5] Solar Cells and Their Applications, Edited: Larry D. Partain, Lewis M. Fraas, 2nd edition, John Wiley & Sons, 2010.

[1.6] N. S. Lewis, Science, 2007, 315, 798.

[1.7] R. Eisenberg, D. G. Nocera, Inorg. Chem., 2005, 44, 6799.

[1.8] Chemistry for a Sustainable Future (view point), Environmental Science and Technology (ACS), 2007, 4840.

[1.9] G. M. Whitesides, G. W. Crabtree , Science, 2007, 315, 796.

[1.10] E. Becquerel, C.R. Acad. Sci. Paris,1839, 9 , 561.

[1.11] M. D. Archer, J. Appl. Electrochemistry, 1975, 5, 17.

[1.12] A. Goetzberger, C. Hebling, H. –W. Schock, Materials Science and Engineering: R: Reports, 2003, 40, 1.

[1.13] Handbook of Photovoltaic Science and Engineering, Edited: A Luque, S. Hegedus, John Wiley and Sons Ltd (England), 2nd edition, 2011.

[1.14] M. A. Green, Prog. Photovolt.: Res. Appl., 2005, 13, 447.

[1.15] A. Goetzberger, J. Luther, G. Willeke, Solar Energy Materials and Solar Cells, 2002, 74, 1.

[1.16] Next Generation Photovoltaics: high efficiency through full spectrum utilization, Edited: Antonio Martí, Antonio Luque, Institute of Physics Publishing (London), 2003.

[1.17] A. Hagfeldt, G. Boschloo, L. Sun, L. Kloo, H. Pettersson, Chem. Rev. 2010, 110, 6595.

[1.18] Third Generation Photovoltaic: Advanced Solar Energy Conversion, Edited: M.A. Green, Springer series in photonics, 2003.

[1.19] W. Shockley, H. J. Queisser, J. Appl. Phys. 1961, 32, 510.

[1.20] B. O'Regan, M. Grätzel, Nature, 1991, 353, 737.

[1.21] M. Grätzel, Inorg. Chem. 2005, 44, 6841.

[1.22] M. A. Green, K. Emery, Y. Hishikawa, W. Warta, Prog. Photovolt.: Res. Appl., 2011, 19, 84.

[1.23] M. Grätzel, Pure Appl. Chem., 2001, 73, 459.

[1.24] solar cells that mimic plants, (technology focus by N. Anscombe), Nature Photonics, 2011, 5, 266.

[1.25] M. Grätzel, Prog. Photovolt: Res. Appl., 2006, 14, 429.

[1.26] A. Hagfeldt, Michael Grätzel, Acc. Chem. Res. 2000, 33, 269.

[1.27] A. Mishra, M. K. R. Fischer, P. Bäuerle, Angew. Chem. Int. Ed., 2009, 48, 2474.

[1.28] C. Klein, Md. K. Nazeeruddin, P. Liska, D. Di Censo, N. Hirata, E. Palomares, J. R. Durrant, M. Grätzel, Inorg. Chem., 2005, 44, 178.

[1.29] T. Bessho, E. Yoneda, J. –H. Yum, M. Guglielmi, I. Tavernelli, H. Imai, U. Rothlisberger, Md. K. Nazeeruddin, M. Grätzel, J. Am. Chem. Soc., 2009, 131, 5930.

[1.30] T. W. Hamann, R. A. Jensen, A. B. F. Martinson, H. Van Ryswykac, J. T. Hupp, Energy Environ. Sci., 2008, 1, 66.

[1.31] H. J. Snaith, Adv. Funct. Mater., 2010, 20, 13.

[1.32] A. B. F. Martinson, T. W. Hamann, M. J. Pellin, J. T. Hupp, Chem. Eur. J. 2008, 14, 4458.

[1.33] A. Hagfeldtt, M. Grätzel, Chem. Rev., 1995, 95, 49.

[1.34] A. Listorti, B. O'Regan, J. R Durrant, Chem. Mater., 2011, 23, 3381.

[1.35] B. C. O'regan, J. R. Durrant, Acc. Chem. Res., 2009, 42, 1799.

[1.36] S. Ardo, G. J. Meyer, Chem. Soc. Rev., 2009, 38, 115.

[1.37] J. N. Clifford, E. Palomares, Md. K. Nazeeruddin, M. Grätzel, J. Nelson, X. Li, N. J. Long, J. R. Durrant, J. Am. Chem. Soc., 2004, 126, 5225.

[1.38] D. F.Watson, G. J. Meyer, Annu. Rev. Phys. Chem. 2005, 56, 119.

[1.39] N. A. Anderson, T. Lian, Annu. Rev. Phys. Chem., 2005, 56, 491.

[1.40] S. E. Koops, B. C. O'Regan, P. R. F. Barnes, J. R. Durrant, J. Am. Chem. Soc. 2009, 131, 4808.

[1.41] H. J. Snaith, Adv. Funct. Mat., 2010, 20, 13.

[1.42] A. Hagfeldt, M. Grätzel, Acc. Chem. Res. 2000, 33, 269.

[1.43] Encyclopedia of Electrochemistry, Edited: A. J. Bard, M. Stratmann, S. Licht, 2007.

[1.44] J. Bisquert, D. Cahen, G. Hodes, S. Rühle, A. Zaban, J. Phys. Chem. B, 2004, 108, 8106.

[1.45] J. R. Durrant, S. A. Haque, E. Palomares, Coord. Chem. Rev., 2004, 248, 1247.

[1.46] T. Hannappel, B. Burfeindt, W. Storck, F. Willig, J. Phys. Chem. B, 1997, 101, 6799.

[1.47] J. Bisquert, A. Zaban, P. Salvador, J. Phys. Chem. B, 2002, 106, 8774.

[1.48] G. Ramakrishna, D. A. Jose, D. K. Kumar, A. Das, D. K. Palit, H. N. Ghosh, J. Phys. Chem. B, 2005, 109, 15445.

[1.49] G. Ramakrishna, S. Verma, D. A. Jose, D. K. Kumar, A. Das, D. K. Palit, H. N. Ghosh, J. Phys. Chem. B, 2006, 110, 9012.

[1.50] S. A. Haque, E. Palomares, B. M. Cho, A. N. M. Green, N. Hirata, D. R. Klug, J. R. Durrant, J. Am. Chem. Soc., 2005, 127, 3456.

[1.51] D. Kuciauskas, J. E. Monat, R. Villahermosa, H. B. Gray, N. S. Lewis, J. K. McCusker, J. Phys. Chem. B, 2002, 106, 9347.

[1.52] R. A. Marcus, Annu. Rev. Phys. Chem. 1964, 15, 155.

[1.53] Surface electron transfer processes, Author: R. J. D. Miller, G. L. McLendon, A. J. Nozik, W. Schmickler, F. Willig, Publisher: John Wiley & Sons, 1995.

[1.54] M. D. Newton, N. Sutin, Ann. Rev. Phys. Chern., 1984, 35, 437.

[1.55] R. A. Marcus, N. Sutin, Biochim. Biophys. Acta, 1985, 811, 265.

[1.56] E. J. Heller, Acc. Chem. Res., 1981, 14, 368.

[1.57] I. M.M. de Carvalho, M. H. Gehlen, J. Photochem. Photobiol. A: Chem., 1999, 122, 109.

[1.58] P. Chen, T. J. Meyer, Chem. Rev. 1998, 98, 1439.

[1.59] X. Dang, J. T. Hupp, J. Am. Chem. Soc., 2000, 122, 10956.

[1.60] S. G. Yan, J. S. Prieskorn, Y. Kim, J. T. Hupp, J. Phys. Chem. B, 2000, 104, 10871.

[1.61] D. A. Gaal, J. T. Hupp, J. Am. Chem. Soc. 2000, 122, 10956.

[1.62] M. Hilgendorff, V. Sundström, J. Phys. Chem. B, 1998, 102, 10505.

[1.63] Electron Transfer in Chemistry, Edited: V. Balzani, Wiley-VCH, Weinheim, 2001.

[1.64] C. A. Koval, J. N. Howard, Chem. Rev., 1992, 92 , 411.

[1.65] N. S. Lewis, J. Phys. Chem. B, 1998, 102, 4843.

[1.66] J. Mohr, W. Schmickler, J.P. Badiali, Chem. Phys., 2006, 324, 140.

[1.67] M. Tachiya, J. Phys. Chem. 1993, 97, 5911.

[1.68] P. F. Barbara, T. J. Meyer, M. A. Ratner, J. Phys. Chem., 1996, 100, 13148.

[1.69] P. F. Barbara, G. C. Walker, T. P. Smith, Science, 1992, 256, 975.

[1.70] G. J. Kavarnos, N. J. Turro, Chem. Rev., 1986, 86, 401.

[1.71] H. Gerischer, Surf. Sci., 1969, 18, 97.

[1.72] W. Nernst, Z. Phys. Chem., 1889, 4, 129.

[1.73] Semiconductor electrochemistry, Author: R. Memming, Wiley-VCH, 2002.

[1.74] M. Grätzel, Nature, 2001, 414, 338.

[1.75] A. J. Nozik, R. Memming, J. Phys. Chem. 1996, 100, 13061.

[1.76] Dye-sensitized solar cells, Edited: K. Kalyanasundaram, EPFL Press, Lausanne, 2010.

[1.77] G. Benkö, J. Kallioinen, J. E. I. Korppi-Tommola, A. P. Yartsev, V. Sundström, J. Am. Chem. Soc., 2002, 124, 489.

[1.78] J. van de Lagemaat, A. J. Frank, J. Phys. Chem. B, 2001, 105, 11194.

[1.79] G. Boschloo, A. Hagfeldt, J. Phys. Chem. B, 2005, 109, 12093.

[1.80] J. Nelson, Phys. Rev. B, 1999, 59, 15374.

[1.81] N . S. Hush, Electrochim. Acta, 1968, 13, 1005.

[1.82] Inorganic Electronic Spectroscopy, A. B. P. Lever, 2nd ed., Elsevier, Amsterdam, 1984.

[1.83] J.T. Edward, J. Chem. Edu., 1970, 47, 261.

[1.84] Fundamentals of Semiconductors: Physics and Materials Properties, Edited: P. Y. Yu, M. Cardona, Springer, 4th ed., 2010.

[1.85] X. Chen, S. S. Mao, Chem. Rev. 2007, 107, 2891.

[1.86] S. Monticone, R. Tufeu, A.V. Kanaev, E. Scolan, C. Sanchez, Appl. Surf. Sci. 2000, 162-163, 565.

[1.87] N. Serpone, D. Lawless, R. Khairutdinov, J. Phys. Chem. 1995,99, 16646.

[1.88] Handbook of Nanophysics: Nanoparticles and Quantum Dots, Edited: K. D. Sattler, CRC Press, Taylor & Francis Group, 2010.

[1.89] Zinc Oxide: Fundamentals, Materials and Device Technology, Edited: H. Morkoç, Ü. Özgür, Wiley-VCH, 2009.

[1.90] I. Abayev, A. Zaban, V. G. Kytin, A. A. Danilin, G. Garcia-Belmonte, J. Bisquert, J. Solid State Electrochem., 2007, 11, 647. (and references therein)

[1.91] A. R. Hutson, Phys. Rev.,1957, 108, 222.

[1.92] Semiconductor nanocrystals: from basic principles to applications, Edited: D. J. Lockwood, L. Tsybeskov, Kluwer Academic, Plenum Publishers, New York, 2003.

[1.93] Semiconductor Nanocrystal Quantum Dots: Synthesis, Assembly, Spectroscopy and Applications, Edited: A. L. Rogach, Springer-Verleg, 2008.

[1.94] M. G. Bawendi, M. L. Steigerwald, L. E. Brus, Annu. Rev. Phys. Chem., 1990, 41, 477.

[1.95] Physics of Semiconductor Devices, Edited: S. M. Sze, K. K. Ng, John Wiley & Sons, Hoboken, New Jersey, 2007.

[1.96] K. Vinodgopal, X. Hua, R. L. Dahlgren, A. G. Lappin, L. K. Patterson, P. V. Kamat, J. Phys. Chem., 1995, 99 , 10883.

[1.97] G. J. Meyer, Inorg. Chem., 2005, 44, 6852.

[1.98] J. Moser, S. Punchihewa, P. P. Infelta, M. Gratzel, Langmuir, 1991, 7, 3012.

[1.99] Principles of Molecular Photochemistry: An Introduction, Edited: N. J. Turro, V. Ramamurthy, J. C. Scaiano, C. A. Sausalito, University Science Books, 2009.

# CHAPTER 2

# EXPERIMENTAL TECHNIQUES

## 2.1 Introduction:

The interfacial electron transfer reactions in dye sensitized metal oxide nanoparticles viz. $TiO_2$ and ZnO semiconductor material are aimed in present thesis work. Transmission electron microscopy (TEM) is used for nanomaterial characterization. Steady state absorption and emission spectroscopy are used in spectral sensitization studies of wide band gap semiconductor nanoparticles. The excited state relaxation of sensitizer molecules and interfacial electron transfer reactions on sensitized surfaces are performed using transient detection techniques. The transient emission is detected in time correlated single photon counting (TCSPC) and streak camera measurements. The transient absorption measurements are carried out using femtosecond time resolved "visible pump/ visible-near IR probe" absorption spectrometer. A pulse radiolysis technique is used in ascertaining the cation spectra of sensitizer molecules. The principle of detections and basic instrumental layouts are described in this chapter.

## 2.2 Transmission Electron Microscopy (TEM):

### 2.2.1 Introduction:

Semiconductor nanoparticles and quantum dots are characterized by transmission electron microscopy technique. A TEM offers real "atomic scale" space imaging of nanoparticles. It furnishes information about the atomic column's distribution with spatial resolution of ~1nm or even better and also about chemical identity of crystalline material.[2.1,2.2] In TEM, the incident electron beam is diffracted by lattice planes of specimen crystal in different directions.[2.3] The electron diffraction is wave property and the resolution should be diffraction limited. The microscopic resolution is given by classic Rayleigh criteria,[2.4]

$$\delta \sim \frac{1.22\lambda}{\beta} \tag{2.1}$$

where, $\delta$ is resolvable distance for a given $\beta$ collection angle. The de Broglie wavelength ($\lambda$) of an electron with 100keV accelerating potential is ~4pm which should gives microscopic resolution on atomic scale (Ångström). However, the wavelength limited resolution could not be experienced due to non-accessibility of "perfect" electron lens.[2.5]

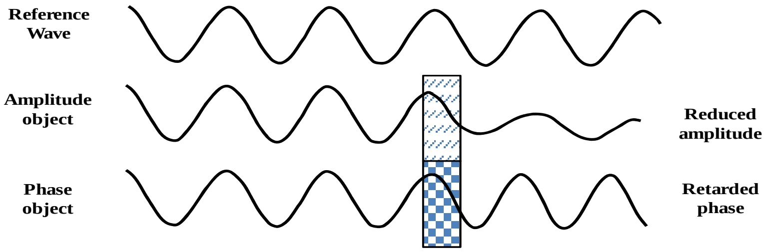

**Figure 2.1**: amplitude and phase modulation in light passing through specimen.

The high resolution TEM images are obtained in phase contrast mode.[2.1,2.4] The electron wave-specimen interaction changes the phase and amplitude of diffracted electron beam with respect to incident or non-interacting beam. The phase difference between interacting and non-interacting electron wave produces interference image to which the amplitude difference renders the image contrast. For thin sample, the electron wave absorption is negligible and the two dimensional (2D) projection of the crystal structure is valid approximation for Fourier transform of projected potential (specimen's) in amplitude contrast.[2.1,2.6] In such a "weak phase object approximation (WPOA)", the transmitted wave function (exit of specimen) is linearly related with projected potential. Thus, crystal acts as phase grating and the incident plane wave produces different “plane spatial frequency” after Bragg’s diffraction. The superposition of diffracted beam with non-interacting beam produces an image contrast. The image contrast does not resembles to real image of crystal structure as the exit wave (from specimen) smeared (point spread) before reaching to image plane. It causes further phase change and higher order interferences. The exit wave front can be retracted from image plane by simulating the electron scattering events and subsequent image formation. For this purpose, advance simulation methods are incorporated in “contrast transfer function (CTF)” which transform “contrast image” to final “image wave".[2.1,2.4,2.7] The Fourier transform of CTF give smearing (point spread) function which reciprocate source image in TEM measurements.

### 2.2.2 TEM layout:

Typical layout of transmission electron microscope is shown in figure-2.2. It comprises an illumination system, a specimen grid, an objective lens, magnifications system, a data recording system and the chemical analysis attachments (if any). The main components of illumination system are electron gun and condenser lens. The electron gun is typically a thermionic emission source or a field emission source (FEG). Thermionic sources are either tungsten filaments or lanthanum hexaboride ($LaB_6$) crystals (more common). The field emitters are fine tungsten needles which are operated at large electric potential pertaining to anode. The beam coherence is higher in field emission source as compared to thermionic emission source and used specifically in high coherence lattice imaging or high spatial resolution microanalysis.[2.8] In thermionic source, a fine electron probe is generated by condenser lens which is placed before the specimen stage. The specimen stage and objective lens are vital components of TEM machine. The electron beam interaction with thin specimen produces diffraction pattern at rear focal plane of

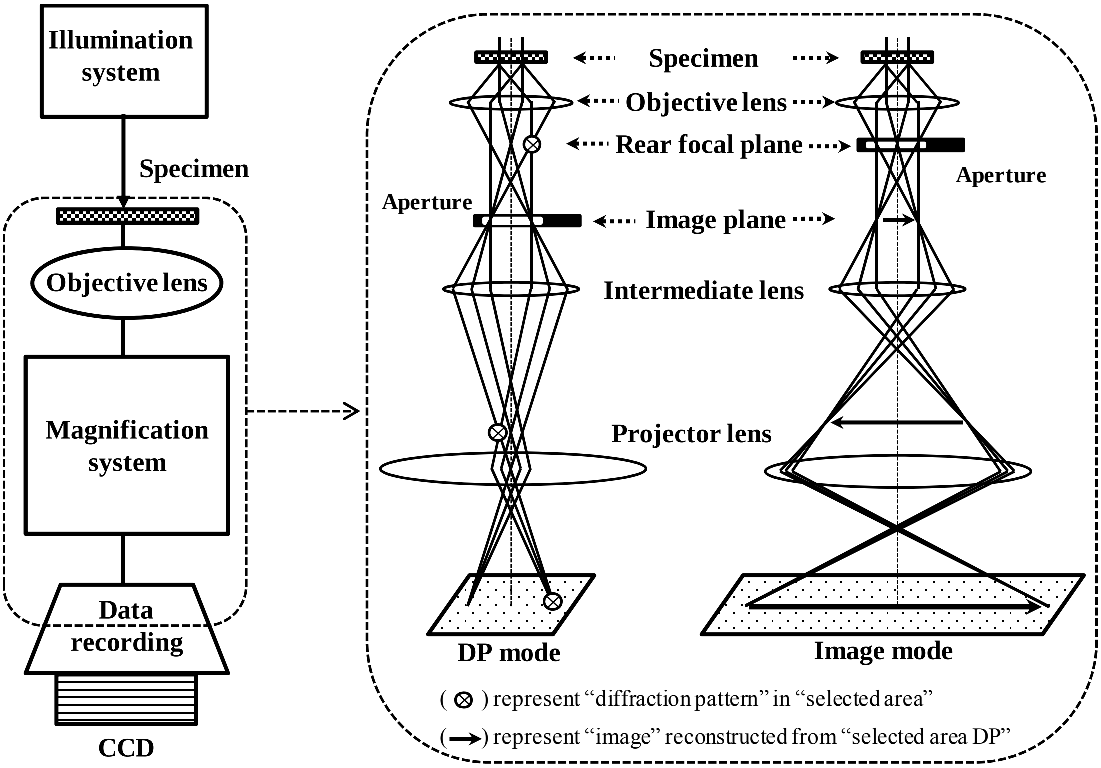

**Figure-2.2**: Schematic layout of transmission electron microscope. Ray diagram of (i) DP and (ii) Image mode TEM operation.

objective lens which carry forward and reconstruct the image on image plane. Depending on specimen investigations, rear focal plane or image plane is taken as virtual objective plane for its projection on detection window. Accordingly, the detection is regarded as diffraction pattern (DP) mode and image mode TEM measurements. The DP or image modes are subsequently magnified for viewing and recording. The magnification component comprises intermediate lens and projector lens which typically give ~$10^6$ order of image magnification. The data recording is done through charge coupled device (CCD). The three components- "illumination, specimen and imaging system" constitutes "column" of TEM. The electron-optical column is kept under high vacuum to minimize electron gun oxidation in thermionic electron gun or to get pristine surface in FEG. The lenses are adjusted by computer operated functions. The fine information about specimen is obtained by different kind of electron beam interaction with specimen. For example, ionizing interaction with inner shell electron of specimen atoms is used in analytical electron microscopy including energy dispersive X-ray spectroscopy (EDS) and electron energy-loss spectroscopy (EELS). In DP mode, selected area electron diffraction (SAED) pattern is used to identify crystals and their relative orientation. TEM image mode is used to get real image contrast of nano-materials.

### 2.2.3 Image formation:

The image formation is consequence of Bragg's diffraction contrast of electron wave with respect to unperturbed wave front. The angular distribution of elastically scattered electrons produces diffraction pattern whereas the spatial distribution leads to "image contrast". The diffracted beam from specimen propagates in non-near axis manner which introduces aberration in non-linear transformation of exit wave into image wave. The aberration corrections of magnetic lenses in column are very critical to TEM image quality and addressed in details.

The first operation using TEM is to project the diffraction pattern of rear focal plane or the image reconstructed at first image plane on to viewing screen (typically CCD). For this purpose, a direct illumination of whole specimen is inappropriate as high intensity electron gun can cause damage to CCD and selected area diffraction is used in TEM operation. In DP mode, an aperture is inserted on image plane which produces virtual aperture on specimen plane. Only the beam impinging within this virtual aperture is sampled in imaging system. In this "selected area electron diffraction (SAED)" mode, the direct beam (elastically scattered) is blocked and the diffracted beam is projected on screen. This is known as dark field (DF) imaging operation. In

DF imaging, a tilt beam "off the optic axis" is more appropriate to get better SAED information whereas parallel illumination is better in classical imaging mode. For this purpose, there is provision of tilt beam illumination. Side entry holders of specimen in vertical column are now standards for tilt/rotation operation. In image mode, the aperture (objective aperture) is inserted on rear focal plane for which the conjugate plane is positioned at front focal plane. In this mode, direct transmitted/scattered beam is processed in image reconstruction. This is known as bright field (BF) imaging.

The resolution of TEM is restricted by lens aberration rather than wavelength criteria. The quality of electromagnetic magnification deteriorates by astigmatism, chromatic and spherical aberrations.[2.2,2.5,2.8] Astigmatism is related with non-uniformity of magnetic field or circular aperture which produces different focal planes for the beam propagating in different optical planes. The magnetic astigmatism is rectified using quadrupole, sextupole or octupole field whereas aperture astigmatism is subject to its fabrication design.[2.9] Even in symmetrical field, a fundamental defect always exists- a spherical aberration which imposes different focal plane for off-axis propagating rays.[2.10] The more "off-axis" diffracted electron rays are focused before numerical focal plane (Gaussian image plane). This put fundamental limit on TEM resolution as the unresolved error may carry forward to other magnification stages and mistaken in resolution optimization. Since, the interference pattern is discerned as disc images, different focal plane vary in disc projection. The confidence on disc projection is given by dimension of disc with least confusion which lies in between hypothetical planes. The disc diameter is given for paraxial rays by following term:

$$\delta = C_S \theta^3 \tag{2.2}$$

The term $\delta$ is radius of disc which is analogous to Rayleigh criteria for resolution given in equation (2.1). $C_S$ is spherical aberration coefficient and $\theta$ is small angle from optic axis.[ 2.2, 2.5,2.8,2.10] From eq$^n$ (2.1) and (2.2), optimum resolution seeks trade-off in collection angle ( $\beta$ ) to meet Rayleigh criteria and spherical aberration. Thus, optimum resolution (in term of radius) is given by:

$$r_{\min} \approx 0.91\ (C_S \lambda^3)^{1/4} \tag{2.3}$$

The chromatic aberration is related with deviation from electron wave coherence properties (frequency, wavelength, or energy). However, the energy variation is very low (~0.1eV) in relative to ~100 keV electron beam and considered only after spherical aberration ( $C_S$ ) correction. Thus, TEM resolution is largely governed by spherical aberration corrections. In HR-TEM, typical value of $r_{\min}$ is 0.2-0.3nm range which is function of high accelerating voltage and spherical aberration coefficient.

The lens aberrations are rectified using small dimension apertures before and after the specimen stage. The size of objective aperture defines angle of exposure ( $\alpha$ ) and collection ( $\beta$ ) which are related with "depth of field" (measure of extent the object is in focus) and "depth of focus" (range in which image remains in focus). It also improves the image contrast (relative intensity between area of interest and adjacent non-interacting region). Typically, HR-TEM can perceive magnification up to 500,000x (500Kx) with 0.2nm and 2nm discernable object plane remains focused in 20nm and 200nm specimen thickens range. It allows CCD detection of DP and image mode which remains focused in this resolution.

## 2.3 Steady-state absorption, Circular dichroism and Fluorescence measurements

The optical transitions of dye molecules and semiconductor nanomaterials are monitored in UV-visible-near IR region (200-1000nm) using “Biomate” make steady state absorption spectrophotometer. Steady state absorption spectroscopy gives information about electronic transitions from ground state to excited state of organic and inorganic materials. The absorbance ($A$) of sample is given by “Beer-Lambert’s law”

$$A = \log\left(\frac{I_0}{I}\right) = \varepsilon_\lambda Cl \tag{2.4}$$

where, C and $l$ corresponds to chromophore concentration (mol $L^{-1}$) and optical path length (typically 1cm, quartz cell), respectively. The molecular extinction coefficient ($\varepsilon_\lambda$) is wavelength dependent property and vary for different “type of electronic transitions”. It allows quantitative and qualitative measurements such as solvent polarity effects on electronic transition of chromophore, charge-transfer interaction in donor-acceptor systems, sizing curve of semiconductor colloidal particles, and Benesi-Hilderbandt plot in evaluation of chromophores binding property *etc*.

The molar extinction coefficient of optically active chiral molecules is different for left (L) and right (R) circularly polarized light. So, one of two polarization components is absorbed more in identical illumination condition. The information about absorbance change ($\Delta A$) as a function of wavelength is ascertained in a circular dichroism (CD) spectrum

$$\Delta A = \left(\varepsilon_\lambda^L - \varepsilon_\lambda^R\right)Cl = \Delta\varepsilon_\lambda Cl \tag{2.5}$$

where, $\Delta\varepsilon_\lambda$ is molar circular dichroism. In a CD spectrophotometer, the absorbance change is recorded by alternative illumination of sample by left and right circularly polarized light. The CD spectrum is commonly used in monitoring configurational changes of different protein structure (folding and unfolding) and aggregation phenomena of biomimetic molecules. In this thesis work, JASCO-815 CD spectrophotometer is used in recording CD spectrum of porphyrin J-aggregates and phycocyanin proteins. The CD spectrums are recorded at 4° C under continuous $N_2$ purging in sample chamber.

The photon absorption event in molecular system follows “Franck Condon principle” of electronic transition in which higher vibrational levels of electronic excited states are directly populated. The photoexcited system undergoes vibration cooling to settle in $0^{th}$ vibrational state of corresponding excited states and finally returns to ground state by emitting light photon or through non-radiative decay. The photoluminescence (PL) is random process and the average time spent in singlet and triplet excited states are typically ~1ns-100ns and 1μs-100 seconds, respectively. Under continuous illumination condition, the time averaged (~μs) PL is measured by spectrofluorimeter. In this thesis work, the fluorescence of different dye molecules is measured by Hitachi spectrofluorimeter (model F-4010) having a 150 W continuous powered high-pressure xenon lamp as the excitation source. Photoluminescence in 200-850nm region is recorded by using suitable photomultiplier tube (PMT) *viz.* IP-28 (Hamamatsu, wavelength range 280-650nm) and R-928F (Hamamatsu, wavelength range 400-850nm) photo-detector. The interference from the excitation and scattered radiation is eliminated by placing appropriate filters before the emission monochromator. Right angle geometry for excitation beam line and PL collection optics is used for measurements. The emission quantum yield of fluorophores sample ($\phi_{sample}$) is calculated with respect to known reference value ($\phi_{reference}$),

$$\phi_{sample} = \frac{A_{reference}}{A_{Sample}} \times \frac{F_{sample}}{F_{refernce}} \times \phi_{reference} \qquad (2.6)$$

where, $A_{sample}$ and $A_{reference}$ are optical excitation densities and $F_{sample}$ and $F_{reference}$ are integrated area of PL spectrum of sample and reference, respectively under identical external conditions.[2.11] The PL spectrum and quantum yield is frequently used in spectral sensitization studies, solvatochromic effects, size quantization of semiconductor colloidal particles *etc*. The emission quantum yield is relative measure of radiative and non-radiative events, given by:

$$\phi = \frac{k_r}{k_r + k_{nr}} = \frac{\tau}{\tau_{0(natural)}} \qquad (2.7)$$

where, $\tau_0$ is intrinsic lifetime which is related with oscillator strength and $\tau$ is average life time a molecule spent in excited state before emitting a photon. Unperturbed excited state follows 1st order decay kinetics and a time dependent emission intensity is given by:

$$\mathrm{I} = I_0 \exp\left(-{}^{t}\!/_{\tau}\right) \qquad (2.8)$$

The order of emission kinetics changes in excited state energy and electron transfer reactions. Therefore, time resolved emission studies are widely used to monitor photoinduced reactions.

## 2.4 Time resolved emission measurements:

In time resolved emission studies, the PL intensity and polarization are measured as function of time. For this purpose, short pulse excitation sources such as mode locked laser (~80fs), diode laser (~66ps), LED laser (~750ps), or hydrogen flash lamp (~1.2 ns) are used in transient emission measurements. The delta pulse excitation allows observation of different excited state's evolution and its decay process in deconvolution algorithm. The transient emission signal comprises spectral and temporal profile in two dimensional (2D) set of data which can be recorded either in 1D-detection system by using monochromator and photo detector (*viz.* PMT or microchannel plate (MCP)) or in 2D detection system by using advanced streak camera, CCD *etc.* devices. The spectral resolution of transient emission depends on monochromator/spectrograph in use whereas temporal resolution depends on excitation source and photo-detector response. Besides this, the electronic signal processing also contributes a finite time resolution. Highest possible time resolution ~250fs is available in indirect nonlinear optical detection technique- “fluorescence up-conversion”.[2.12] In all the transient emission measurements, emitting photon’s counts are very low and detection at quantum limit makes time-resolved study a powerful tool to probe various photophysical processes. In particular, inter- and intra- molecular energy and electron transfer reactions in homo- and heterogeneous media including charge transfer interaction, solvatochromic effects, photo-sensitization *etc*. can be well resolved through transient emission studies.

The time resolved fluorescence can be measured in time-domain (photon counting) or frequency domain (phase shift) experimental set up. In present thesis work, time domain transient emission measurements are carried out by using “time-correlated-single-photon-counting (TCSPC)” and “steak camera” instruments. The operating principle of two techniques is different and described in details.

### 2.4.1 TCSPC measurements:

The working principle of TCSPC measurement,[2.12,2.13] is shown by block-diagram in figure-2.3. It comprises a diode laser for sample excitation (pulsed), monochromator for wavelength (emission) selection, PMT for recording the emission events, “constant fraction discriminator (CFD)” and “time-to-amplitude converter (TAC)” for gated photon counting, MCA for event histogram generation and finally, a computer for display and data analysis. TCSPC measurement starts with an electronic clock which trigger diode laser to generate a delta pulse (Gaussian pulse, ~66ps FWHM, repetition rate ~1 MHz). The excitation pulse splits and illuminates sample and photodiode (PD), simultaneously. The PD generates a “START” electronic signal whereas photoexcited sample excitation gives "photon emission events". The PD electronic signal is routed through "constant fraction discriminator (CFD)" which generates "START" trigger for "time-to-amplitude converter (TAC)". It initiates voltage ramps as a linear function of time (ns). The precision and accuracy of generating "START" trigger is maintained by "CFD" electronics which discriminate "ON signal" from time and amplitude electronic jitter.

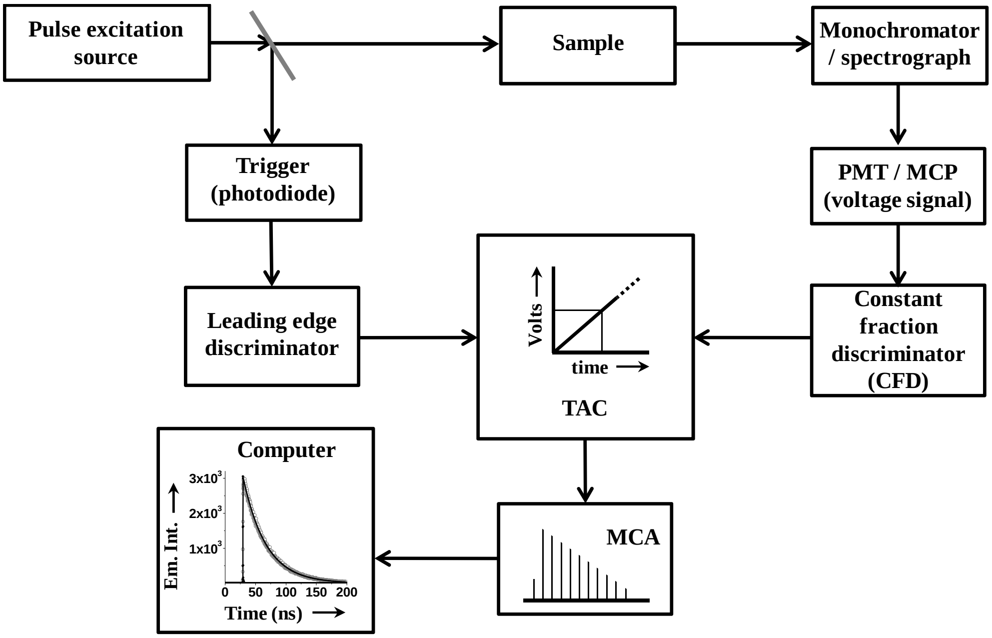

**Figure 2.3**: Block diagram of TCSPC set up

Meanwhile, the emitted photon which reaches first on PMT detector, is recorded and give "STOP" pulse feed to "CFD" (second) signal processor. The "CFD" generate a "STOP" trigger for "TAC" ramp. Thus, "TAC" runtime ($\Delta t$) correlates with "single photon" detection provided that the electronic delay is lower for "START" signal than "STOP" signal. It is ensured by adjusting electronic delay for scattering sample which has fastest instrument-photo response function (IRF) and hence, give fastest "STOP" trigger. Besides this, a false reading is discarded by a “window discriminator” which nullifies the “TAC” readout if it crosses “set” voltage limit. The “TAC” readout signal is processed by “analogue to digital (ADC)” converter and feed to “multichannel analyzer (MCA)”. The MCA register the “count” in different channels which are ordered in 1 to 1024 numbers. The channel width is electronic resolution of the TCSPC set-up and its sum over all channel numbers give TCSPC measuring “time range”. The “TAC” runtime differs for emitted photons and a histogram is generated with repetitive pulse excitation (~$10^4$ counts from 1MHz repetition pulses). The histogram represents true fluorescence decay profile if photon count rate is low because in this situation the statistics (uncertainties in data) is given by Poissonian distribution.[2.13,2.14] For this purpose, solid angle of photon collection is kept at minimum and right angle geometry is used. In this situation, the histogram corresponds to IRF convolute emission decay profile. The IRF has finite width for particular excitation source and is measured by scattering events. The intrinsic emission decay kinetics is than deconvoluted from recorded trace using IRF profile and instrument’s provided data analysis software.

In present thesis work, IBH make TCSPC instrumental set-up is used. Various diode lasers (*viz.* 406nm, 463nm, 589nm) with vertical polarization of excitation pulse (~66ps) are used as excitation source. An emission polarizer is used before collection optics and PL is recorded at magic angle (54.7°) polarization with respect to excitation beam.[2.13] Thus, all emission traces are anisotropy free and represents true emission intensity and time profile. The time resolved kinetics is fitted with non-linear least square analysis supported by instrument fitting program of IBH make. Typically, the decay profiles simulated in exponential decay function given by,

$$I(t)=\sum_{i=1}^{n}\alpha_i e^{-t/\tau_i} \tag{2.9}$$

Since, $\tau$ life is intrinsic function of particular emission events, the order "i" represents as many photophysical processes happening in the system.

In TCSPC measurements, the low photon counting (one in 100 emission events) makes the emission kinetics invariant to excitation source intensity which may vary due to manual adjustment of various laser heads. The robustness of sensitive detection gives reliable emission traces. In addition, the rising portion of photoelectron pulse of PMT, give IRF (<ns) better than PMT readouts (~ns). The use of MCP-PMT detector further improves IRF in sub ns regime. So, robustness, sensitivity, noise, choice of excitation source, high repetition rate *etc.* all together makes TCSPC a widely used time resolved techniques despite of it limitation in spectral profile determination and low resolution for ultrafast processes (sub ps to 100ps ).

### 2.4.2 Streak camera measurements:

The time profiles offered in TCSPC measurements are not always adequate to capture ultrafast processes. The ultrafast processes usually undergo a rapid spectral profile change in reaching to final emitting state. For such physico-chemical processes in which the spectral and temporal profiles are needed in ultrafast time scale, the streak camera detection is very reliable technique. The "state of art" instrumentation of streak camera delivers "photon flux intensity *vs.* time *vs.* position" 2D plot.[2.15] In streak camera, light emitting events are recorded as streak projections of illuminated points (coordinates/pixel). The emitting photons are wavelength dispersed on horizontal axis and photo-chronicle order is recorded as "photoelectron streaks" on vertical axis. The concept of "streak camera" detection is shown in figure-2.4. The photon flux reaching at different time on horizontal pixels varies in their group velocity. The streak camera transduces the group velocity information into phase velocity.

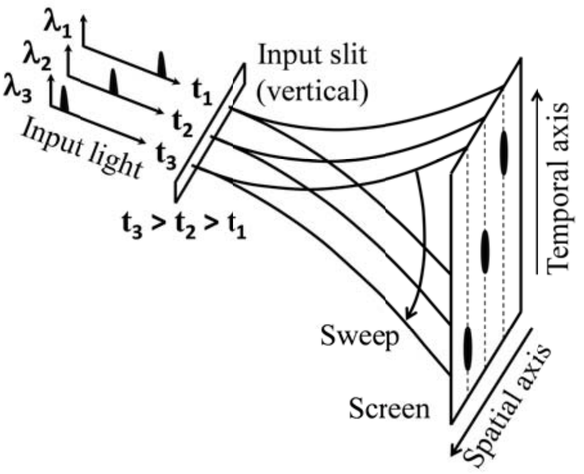

**Figure 2.4**: streak projection of incident photons as function of time and position

The fastest transduction is obtained by directly applying sweep voltage on photoelectrons and dispersing them on imaging screen. Thus, a streak camera imaging involves 2D mapping of photoelectrons which are spread in time and position. The operating principle of streak camera is shown in figure-2.5.

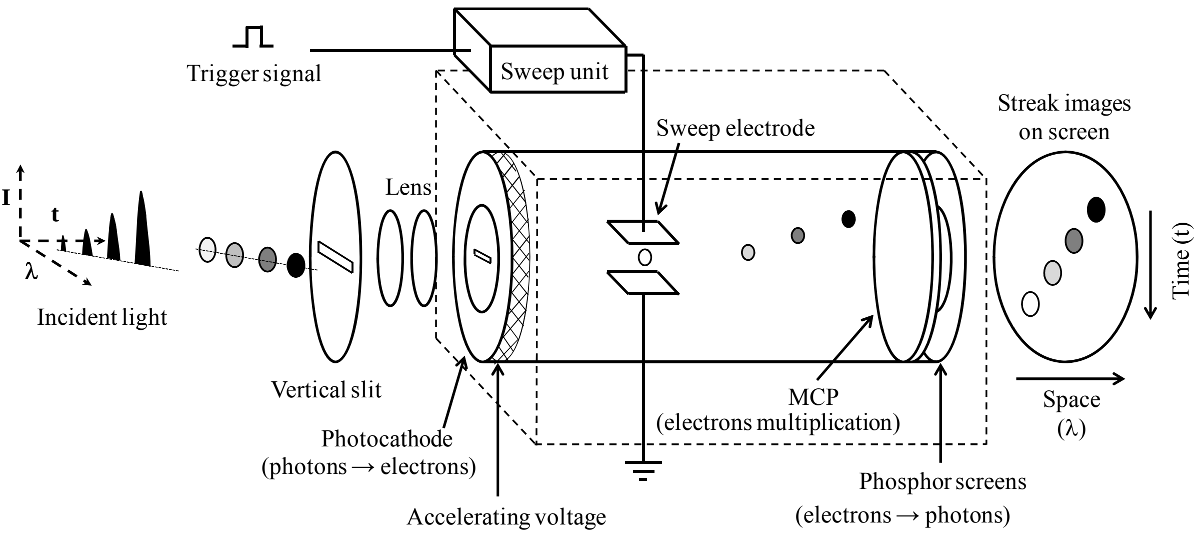

**Figure 2.5**: Schematic presentation of streak camera imaging technique.

The sample is excited using ultra short pulses (typically ~100fs) obtained from mode locked and amplified laser system. The PL of sample is wavelength dispersed by grating spectrograph and the 3D image $(t, \lambda, I)$ is projected on to vertical slits to get a fine stripe (horizontal) of spectrum (in X-direction). The wavelength dispersed light is focused onto photocathode which is connected to mesh plate where photoelectrons are generated in proportion to light intensity and then accelerated towards phosphor screen. As the electrons pass through sweep electrode pair, a high speed sweep voltage– synchronized with incident light- is applied. The high speed sweep deflects the electrons from top to bottom onto the multichannel plate (MCP) depending on the moment of their emission, thereby introducing the time resolution. Hence the photons which are emitted directly after photoexcitation experience a higher deflecting voltage then the photons emitted at a later time.

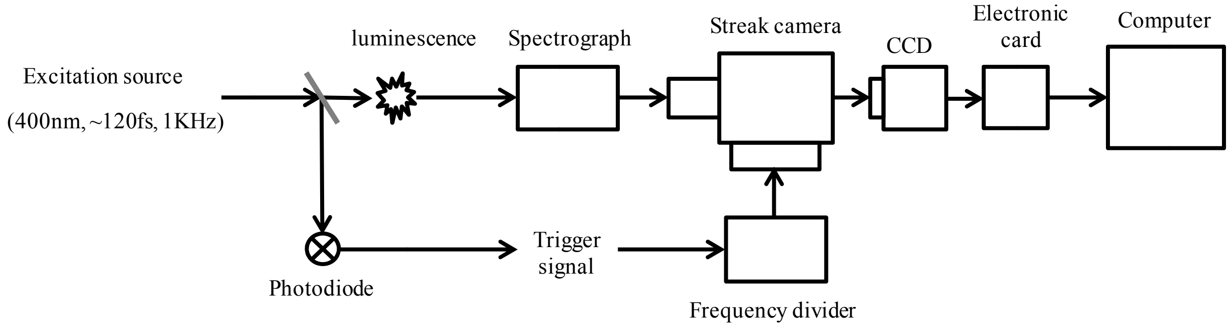

**Figure 2.6:** block diagram of streak camera imaging of photoluminescence: (1) optical pulse splits, one part excite sample and other used in PD trigger signal. (2) Trigger signal fed t frequency divider which synchronizes sweep frequency rate. (3) The luminescence is collected at magic angle and the spectrograph project a stripe of wavelength dispersed PL spectrum on streak tube. (4) Synchronized sweep of "Photoelectron" stripe produces 2D image on CCD. (5) CCD readout displayed in computer and analyzed by "OptoAnalyse" software.

In the MCP plates, incident electron flux multiplied ~$10^3$ times and then bombarded onto phosphor screen. The optical image on phosphor screen is known as "streak" image and recorded by CCD detection system. The streak image comprises intensity distribution as a function of time on vertical axis and as function of wavelength on horizontal axis. The uppermost position corresponds to earliest photon arriving at vertical slit. The transverse profile is sequential order of photon flux passing through vertical slit. Thus, in a streak camera, the photoelectrons stripe (horizontal; X-axis) is vertically (Y-axis; time axis) swept on phosphor screen and the 2D image is recorded in CCD. The functional diagram of time resolved emission measurement using streak camera is shown in figure-2.6.

In a single sweep streak camera, a 20ps sweep time for 18mm phosphor screen is possible (commercially available, [2.16]) which allows electron deflection at higher speed ($9x10^8$ $ms^{-1}$) than that of light ($3x10^8$ $ms^{-1}$). Therefore, pulse width limited time resolution (~100fs) is achievable in "single shot" streak camera measurements. However, the emission quantum yield is not always very high and requires signal averaging over certain period of time. It adds optical and electronic jitter (excitation source and sweep voltage synchronization unit) to time resolution. Even in single shot measurements, the time resolution can hardly better than ~1ps due to normal electronic signal processing in "sweep circuit". Besides this, femtosecond optical pulse is stretched up to 5ps in a grating spectrograph due to "group velocity distribution (GVD)",[2.17,2.22]. So, typical time resolution of streak camera is 5-20ps in averaging mode operation.

The image recorded in streak camera can have static and dynamics distortions due to uneven -accelerating and -deflecting electrical field in ~ns "time of flight" of photoelectrons. The "space-charge" effect introduces "longitudinal chromatic aberration" in planar accelerating field.[2.18,2.19,2.20] The "space charge" effects are minimized by not using photoelectron multiplication just after the photocathode tube and then using it after sweep electrode pair. This limits the photosensitivity of streak tube (*vs.* PMT). Also, non-uniformity of sensitive detection is added at every stage of streak projection *viz.* photocathode, MCP, phosphor screen, and then CCD detector. Thus, a careful calibration is required before use. In practice, the entire detection system including photodiode, electronics trigger circuitry, input optics, streak tube, CCD detector and its analysis software is delivered as single unit at the time of instrument installation.

In present thesis work, Optronis make streak camera- OPTOSCOPE-SC 10, GmbH, Germany with 2ps temporal system resolution is used. It comprises an electro-mechanical shutter operating at 10Hz. Its multi-alkali photocathode S25 (8 X 2 mm active area) offers 200-850nm spectral range for transient detection. The trigger sweep unit "TSU11-10" (bottom-to-top sweep) is operated between 10ps/mm to 1ns/mm. Single stage MCP -II125 (gating time 10ms, 350-850nm range) with 25mm active area and 1-1000 adjustable gain is used in gated or continuous mode. The IRF is measured to be 6ps using Coumarin-343 (exciton C519) as standard.

### 2.4.3 Streak camera vs. TCSPC measurements

The main advantage of streak camera imaging techniques is its ability to record wavelength dependent emission kinetics in single shot measurement. The signal averaging allows streaks pile up which enhances the counts very large in short time period (few minutes) as compared to TCSPC measurements (cumbersome for transient emission spectrum). Also, it offers a superior temporal resolution ~5-20ps as compared to TCSPC measurements (~70ps). The streak projection allows many photons counting in single shot and hence there is no dead time as experienced in TCSPC measurements. However, sensitivity and sweep distortion are main issues in preferring the streak camera technique over TCSPC measurements.

## 2.5 Time resolved absorption measurements: Pump-probe technique

### 2.5.1 Introduction:

The nature of transient species generated in photoinduced reaction is very diverse towards optical photo-response and changes under different chemical conditions such as pH, temperature, inert ambience, concentration, solvent polarity and viscosity *etc*. Time resolved emission studies are very specific to luminescent samples and non-radiative pathways cannot be identified. Therefore, kinetic study of various non-emitting processes such as electron transfer, cation formation, intermediacy of free radical, regeneration of ground state *etc*. requires a more versatile technique. Two colour, pump-probe absorption spectroscopy is universal tool for dynamic measurements of photo-induced processes.[2.21]

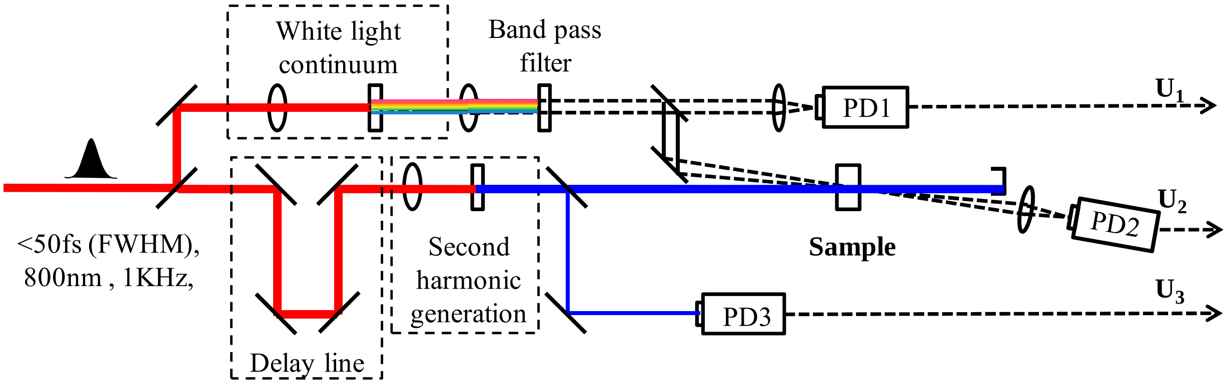

**Figure 2.7:** Optical layout of two colour pump-probe set-up.

In pump-probe study, an optical pulse (pump) is used to photo excites the sample (t=0 time) and the perturbation effect are observed by another colour probe-pulses ("t" delay time). For this purpose, the pump and probe optical beam lines are spatially overlapped in sample. The delay time between pump and probe pulses is generated either by increasing optical path length of probe pulses or by decreasing path length of pump pulses. Typical pump-probe measurement set-up is shown in figure-2.7. The photoaction (on sample) is examined by comparing the probe pulse intensities before and after pump pulse excitation. From Beer-Lambert law, the probe pulse intensity before ($I_0(\lambda_i)$) and after ($I(\lambda_i,\Delta t)$) pump pulse excitation can be given by,

$$I(\lambda_i,\Delta t) = I_0(\lambda_i)\times 10^{-\varepsilon_{(\lambda_i)}N_{(\Delta t)}l} \tag{2.10}$$

The optical density (OD) or absorbance (A) is experimental observable and defined as

$$A(\Delta t) = O.D.(\Delta t) = \log\frac{I_o(\lambda_i)}{I(\lambda_i,\Delta t)} = \varepsilon_{\lambda_i}N_{(\Delta t)}l \tag{2.11}$$

Assuming an exponentially decay of transient species

$$\ln\left(A(\Delta t)\right) = \ln\left(O.D.(\Delta t)\right) = \ln\left(\varepsilon_{\lambda_i}N_{(0)}l\right) - \frac{\Delta t}{\tau} \tag{2.12}$$

Thus, in a pump-probe transient absorption spectroscopy, population dynamics ($N_{(\Delta t)}$) are monitored by change in optical density as a function of delay time ($\Delta t$) at given $\lambda_i$ wavelength (probe). The absorbance change is calculated from photodiode readouts (voltage- U)

$$A(\Delta t) = \log\left(\frac{U_0}{U(\Delta t)}\right) \tag{2.13}$$

where, delay time is given by optical path length; $\Delta t = 2\,\Delta L/c$. In pump-probe spectroscopy, the optical path length can be varied with 0.1μm precision which corresponds to 0.66 fs delay time.

Thus, the temporal resolution is free from detection system and determined from optical pulse width (pump and probe pulses).

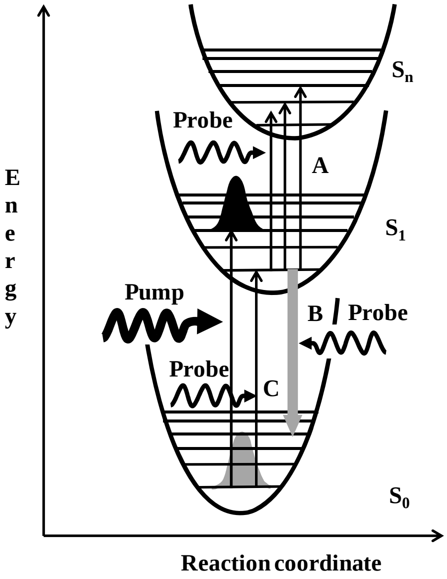

**Figure 2.8:** Scheme of the states involved in a pump probe experiment in a dye solution. (A) Excited state absorption, (B) Bleaching, and (C) Stimulated emission.

The transient absorption technique is illustrated for three levels molecular system in figure-2.8. With all molecules in ground state at thermal equilibrium, the sample acts as saturable absorber. A strong optical pump pulse depletes the ground state by exciting all the molecules into vibrationally hot states of first electronic excited state (${}^{n}S_1$). The ground state depletion causes a higher transmission of probe pulses if the probe wavelength coincides in absorption spectrum. It gives a negative absorbance ($I(\lambda_i, \Delta t) > I_0(\lambda_i)$) and known as "bleach". A higher transmission of probe pulses also possible if the probe wavelength coincides in PL spectrum and the negative absorbance is known as stimulated emission. The excited state transitions "$S_1 \rightarrow S_n$" causes attenuation of probe pulse intensity and it corresponds to "excited state absorption (ESA)".Thus for a simple system as depicted in figure-2.8, the population dynamics of excited state can be analyzed by bleach recovery, ESA decay, or SE decay kinetics at different probe wavelengths.

### 2.5.2 Requirement of amplifier laser system in pump-probe experiments:

A complex system, can involve many transition states and the related lifetime can vary from few femtoseconds to nanoseconds. So, femtosecond optical pulses are indispensable in time resolved studies. Since, the width of electronic transitions (absorption or emission) are more than spectral resolution of probe pulses; it makes easy to use different colour probe for intermediate transient steps. Thus, a continuum of probe wavelength is essential in pump-probe measurements. The excitation wavelength of pump pulse should coincide in absorption spectrum of sample. Ideally, excitation densities are kept below saturation where induced absorption ($\Delta A$) increases with excitation pulse energy. The pulse energy density,[2.22] in saturation limit of absorption, is given by

$$E_{sat} = \frac{h\nu_{ex}}{\sigma_{abs}} \tag{2.14}$$

For most of the organic dyes, inorganic complexes and semiconductor colloids (near band edge), the molar extinction coefficient is ~$10^4$-$10^5$ $M^{-1}cm^{-1}$ at 400 nm excitation wavelength. It gives ~ $10^{-16}$ -$10^{-17}$ $cm^2$ absorption cross section ($\sigma_{abs}$). Thus, ~ 1-10mJ$cm^{-2}$ saturation energy density is required for $\sim 63\%\ (=1-e^{-1})$ excitation of ground state population. This is very important parameter when considered in pump-probe spatial overlapping. In pump-probe experiments, pump-probe spatial overlapping (figure-2.9) is determined from pump probe beam cross section in relative to spatial width of optical pulses (pump-probe).

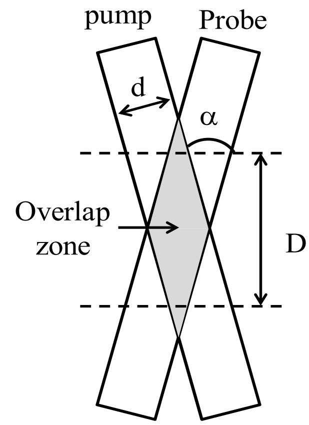

**Figure 2.9:** spatial overlapping of pump-probe pulse.

The spatial width (d) is function of pulse duration, given as $d = c\tau_{(FWHM)}$. The dimension of probe beam should be such that a probe pulse always reaches after pump pulse in the overlap zone (beam cross section area). For a large probe beam (spot size on sample), the probe pulse may reaches before pump pulse and hence not adequate for pump-probe experiments. Thus, ideal condition of spatial overlap would require

$$D \le \frac{d}{\sin\alpha} \tag{2.15}$$

For a ~100fs optical pulse and intersecting angle of ~5-8°, the probe beam dimension should be ~300 μm -200μm in overlap zone. Likewise, the sample thickness should be smaller than interaction zone in propagation direction $D/\sin\alpha$ ~ 3mm - 1.5mm. Accordingly, the pump spot dimension accordingly should be ~500μm. For such a spot size (~$10^{-7}$ cm$^2$), ~ 1-10mJ x $10^{-7}$ = 0.1-1 nJ per pulse excitation energy is required in pump-probe experiments. This gives lower limit of excitation density because the molar extinction coefficient may not be that high (~$10^4$-$10^5$ M$^{-1}$cm$^{-1}$) at excitation wavelength (400nm). Typically, ~10-100 nJ/pulse excitation density is required, [2.23] and femtosecond amplified system is core part of pump-probe instrumentation.

**2.5.3 Amplifier laser system:** Femtosecond amplifier laser system involves generation of ultra-short (fs) pulses, stretching of fs-pulse before amplification, multipass/regen amplification ($10^5$-$10^6$ times) of stretched pulses and then compression of amplified pulse.

### 2.5.3a Ultra short pulse generation: Ti:sapphire oscillator

In present pump-probe set-up, fs seed pulses are obtained from Ti:sapphire oscillator. In the oscillator, continuous wave (CW) laser light from diode pumped solid state (DPSS) laser is focused on Ti:sapphire crystal (TiS) which is placed at focus of spherical mirrors. The $Ti^{+3}$ ions in sapphire ($Al_2O_3$) matrix exhibits broad PL band in 660-1050nm region.[2.24] A high thermal conductivity (46 W/mK at 300 K) and optical damage threshold (8-10 J/cm$^2$) of Ti:sapphire crystal allows high power pumping by DPSS laser (532nm, ~3.8 W, CW).[2.25] The Ti:sapphire crystal is excited slightly off-axis through the back of one of the spherical mirror (astigmatism is minimum). The lasing cavity is operated in $TEM_{00}$ mode (800nm) at low lasing power. [2.26, 2.27] At high lasing power, the refractive index of gain medium changes with intensity of lasing beam,

$$\eta(\omega, I) = \eta_0(\omega) + \eta_2(\omega) I \tag{2.16}$$

The $\eta_2(\omega)$ represents nonlinear refractive index which is positive for Ti:sapphire crystal. The radial intensity distribution of a Gaussian beam ($TEM_{00}$) results a higher refractive index at the central axis (beam) than that at the wings.[2.28] So, the Ti:sapphire crystal acts as converging lens and the high lasing power is self-focused in gain medium which is known as "optical Kerr effect".[2.28,2.29] At high lasing power, the additional "Kerr lens" focal length ( $\delta$) is accommodated by adjusting cavity length more than the sum of focal length ($f_1$+$f_2$) of cavity mirrors. The Kerr lens forms a passive "intracavity" aperture and introduces power dependent loss which makes resonator unstable in CW mode.[2.30, 2.31] On slight cavity disturbance, a pulsed transmission of laser beam is energetically preferable over CW mode as the crystal acts saturable absorber.[2.32] Thus, Kerr lens self-focusing enforces a mode-locked lasing operation which is known as "Kerr lens mode (KLM)" locking.[2.33] Since, the bandwidth of gain medium (Ti:sapphire) is very large (>350nm), the passive mode locking (Kerr lens is passive object) can give pulse width as short as ~6fs ($\Delta t \sim \lambda^2 / c\Delta\lambda$; where $\lambda$ is central wavelength).[2.34] The pulse repetition rate is determined from round trip time in a resonator cavity ($t = 2L/c$). The high power pumping (3.8W; DPSS) of Ti:sapphire crystal (PL life time ~3.2μs) allows a typical ~80-100 MHz pulse repetition rate in oscillator. In a cavity round trip, the fs pulse is subject to GVD dispersion as it passes through Ti:sapphire crystal.[2.35] In GVD, the blue and red edge of optical pulse propagates with a relative delay of

$$\Delta t = \frac{(\eta_{blue} - \eta_{red})l}{c} = \frac{l(\Delta\lambda)}{c} D \tag{2.17}$$

For a Ti:sapphire crystal, $D = \dfrac{d\eta}{d\lambda} \cong 10^{-4} nm^{-1}$ which can give a ~200fs time spread.

Thus, the pulse compression components such as "two prism compressor",[2.36] or "chirped mirrors" are used in laser resonator cavity. Accordingly, the real pulse width depends on crystal thickness and "negative group delay dispersion" components. Typically, Ti:sapphire oscillator generates 20fs-120fs optical pulses. The non-linear Kerr lens also affects the "bi-refringent" properties of Ti:sapphire crystal which causes change in polarization. This is compensated by accurate alignment of "Brewster's angle surfaces" such as Ti:sapphire crystal and prism (if presents) surfaces.[2.37] In addition, the cavity losses are minimized at "Brewster's angle". The dispersion control, selection of fundamental wavelength, Ti$^{+3}$ doping in sapphire crystal and its thickens vary in design of commercially available Ti:sapphire oscillators.

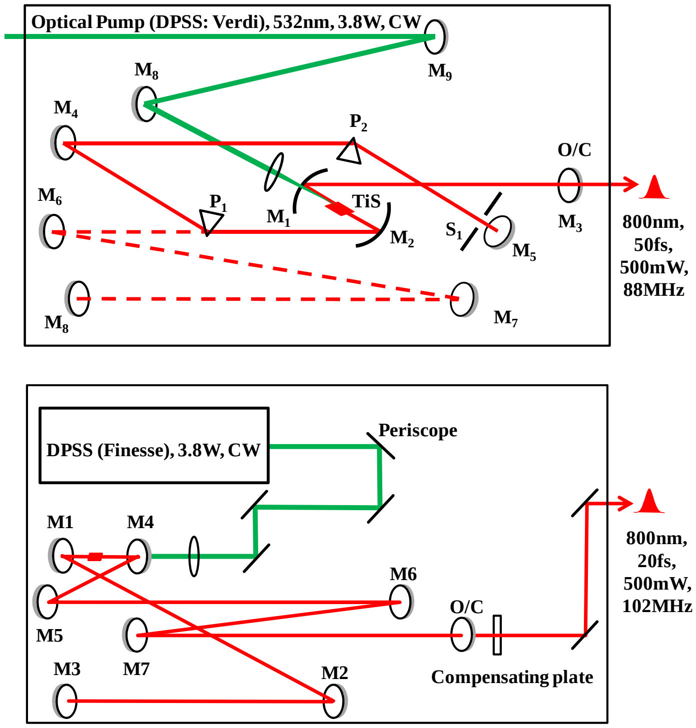

**Figure 2.10**: Optical layout of Ti:sapphire oscillator used in present pump-probe set-up: Top panel: two prism pair for negative GVD; Bottom panel: chirped mirrors for negative GVD.

In present thesis work - (1) CDP, Avesta (Russia) and (2) Femtosource$^{TM}$ synergy-20$^{TM}$ (supplied by Thales, France) oscillators are used. The optical layouts are shown in figure-2.10. In CDP, Avesta Ti:sapphire oscillator, two prism assembly with HR mirror is used for negative GVD dispersion. The 800nm fundamental optical pulse is selected by appropriate slit width between prism P2 and HR mirror M5 as the wavelengths are spatially spread in this region. The slit location and width are adjusted for 800nm wavelength and 50fs pulse width, respectively. The oscillator characteristics are ~50fs (FWHM), 500mW (4W DPSS pump power), 88MHz.In Femtosource$^{TM}$ synergy-20$^{TM}$ oscillators, chirped mirrors are used for GVD dispersion control. The chirped mirrors (M6 and M7) are designed for 800nm resonator cavity. Thus, oscillator parameters are fixed and give one output ~ 20fs(FWHM), 500mW (3.8 W DPSS pump power), 102MHz. In both the oscillators, the output power is not sufficient for pump-probe experiments which typically require >100nJ energy per pulse. So, oscillator's output pulses are used as seed pulses for regen/multipass amplification.

### 2.5.3b Amplification of ultra short pulses: Chirped pulse amplification

The ultra-short pulses of very high energy (~1μJ/pulse) are obtained from chirped pulse amplification (CPA) techniques.[2.17,2.38,2.39] In CPA, the short pulse is stretched in time by frequency chirping, amplified in optically pumped Ti:sapphire gain medium and then compressed to get back original ≤ 50fs pulses with amplified power (≥ 100 nJ/pulse energy). The chirped pulse amplification permits $>10^5$ amplification gain even using low repetitive pump laser such as 1 KHz Nd:YAG or Nd:YLF pump lasers. The schematic presentation of CPA technique is shown in figure-2.11.

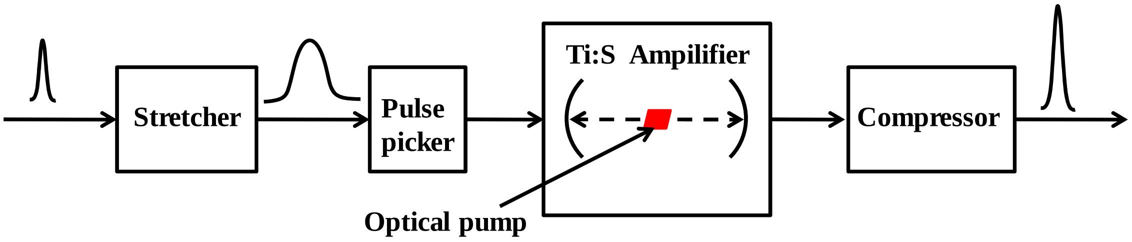

**Figure 2.11**: Box diagram showing chirped pulse amplification (CPA)

The pulse stretching by a large factor ($\sim 10^4$) is essential to avoid peak power damage (<5 GW/cm$^2$) of optics in amplification process.[2.40] In addition, the pulse duration before and after amplification is same for stretched pulse and the amplification gain is no more affected by GVD as is the case with femtosecond pulse. The basic principle of pulse stretching is illustrated in figure-2.12. It uses two gratings pair which are tilted against each other (not parallel). The pulse stretching is obtained from dispersion property of grating.[2.28,2.29] The ultra-short pulse (800nm) has inherent ~40-60nm band width. The longest wavelength (red) component is diffracted at bigger angle than shorter wavelength (blue) components. The wavelength dependent divergence introduces a path difference between red and blue components and stretches the pulse. After diffraction on second grating, all wavelength components propagate in same direction with “red part” at front and “blue part” at the tail end of pulses. After the stretcher, the pulse is wider in time and coloured in space. It is this “colour property” (red part ahead of blue part) which allow reversible pulse compression after amplification.

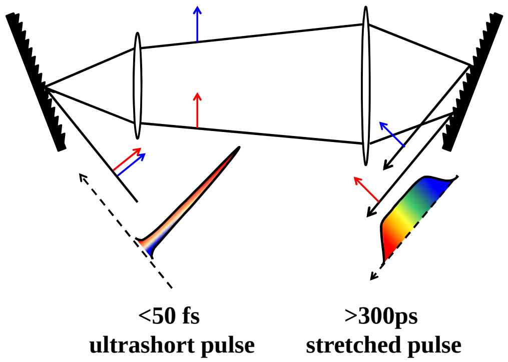

**Figure 2.12**: pulse stretching principles

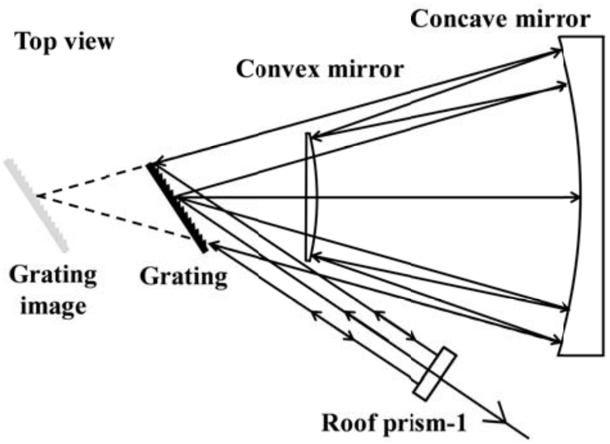

**Figure 2.13**: “Öffner stretcher” ray diagram

Figure-2.13 shows a typical ray diagram of aberration free “Öffner stretcher” which comprises two curved mirror (silver coated concave and convex mirrors) and a grating.[2.41] In this afocal system, the convex focal length is half of concave focal length and two mirrors are separated (~30cm) by concave focal length. This configuration permits spatial reconstruction of beam shape back to its original form after pulse stretching. After passing through stretcher, the pulse duration increases up to 300ps which than feed to amplification stage.

### 2.5.3c Regen amplification and Multipass amplification

The pulse amplification is achieved through repetitive passes of stretched pulse in optically pumped Ti:sapphire crystal. The Ti:sapphire crystal (highly doped) acts as gain medium which is pumped by 5-25W high power laser such as Nd:YAG, ND:YLF laser. The seed pulse amplifies after each pass in Ti:sapphire crystal by depleting the inversion. A strong optical pump regenerates the gain before next round trip of seed pulse. Thus, amplification by stimulated emission generates more intense light pulses after each transit through Ti:sapphire crystal. The amplification gain saturates after certain round trips and then the pulse is extracted from amplifier cavity and proceeds for compression. The commonly used multiple pass schemes are “confocal resonator” and “regenerative cavity” which differs in lasing power circulating in cavity.

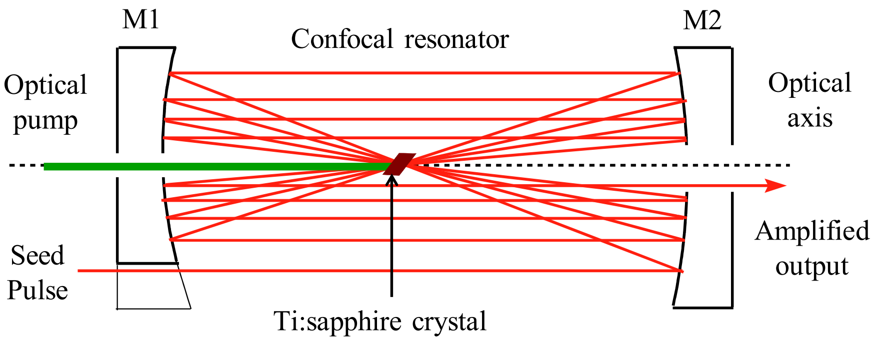

**Figure 2.14**: Optical scheme of confocal multi-pass Ti: Sapphire amplifier. M1 and M2 are two confocal mirrors with two difference focal lengths.

The “confocal resonator” is a bow-tie type amplifier in which multiple passes are made at slightly different location through amplifying medium.[2.42] The optical scheme of multipass Ti:sapphire amplifier is shown in figure-2.14. In this amplifier, the Ti:sapphire gain medium is confocal placed between two concave mirrors (slightly different radii of curvature) so that the beam walks slowly from side to the center of the mirror and than extracted. The number of multiple pass depends on geometrical configuration of confocal mirrors and the maximum number is limited by duration of pump pulse. Typical number of passes are 8-10 due to increasing difficulty of focusing all the passes on a single spot of Ti:sapphire crystal. Typical amplification is ~$10^5$ -$10^6$ order. This technique is simple in design but difficult in adjustments. Since, amplification is required in 8 multipass, the optical pumping of Ti:sapphire crystal is kept close to damage threshold (~10 $Jcm^{-2}$). It results very high pump fluence which is close to saturation fluence of Ti:sapphire crystal (1 $Jcm^{-2}$ at 800nm). As a result, the spontaneously emitted photons are picked in first amplification stage and give amplified spontaneous emission (ASE) pedestal (~nano second) with amplifying seed pulses on top of it.[2.17] The ASE can be minimized by using spatial aperture which allows only the seed pulse pass in confocal resonator. Nevertheless, 5-10% ASE remains in amplified output energy even after spatial filtering.

In present thesis work, MPA 50 set up from CDP, Avesta (Russia) is used in multipass pulse amplification. The Ti:sapphire crystal is optically pumped by second harmonic (532nm pulse with ~90ns duration) of Q-switched Nd:YAG laser operating at 5W and 1KHz repletion rate. The Q-switching is synchronized at 1KHz with oscillator clock signal. The high pump power (5W) allows complete recovery of gain in Ti:sapphire crystal (~3.2μs lifetime). The seed pulse is passed 8 time to match pump pulse duration (leading edge < 60ns) and amplified pulse is geometrically extracted.

In regenerative amplifier, the seed pulse is amplified in true resonant cavity. Unlike multipass amplifier in which pulse passes (entry and exit) are geometry defined, the regen amplifier uses pulse polarization for trapping and dumping the seed pulses (Figure-2.15).[2.43] For this purpose, it comprises high voltage, 2-step Pockels-cell and a broadband polarizer. The

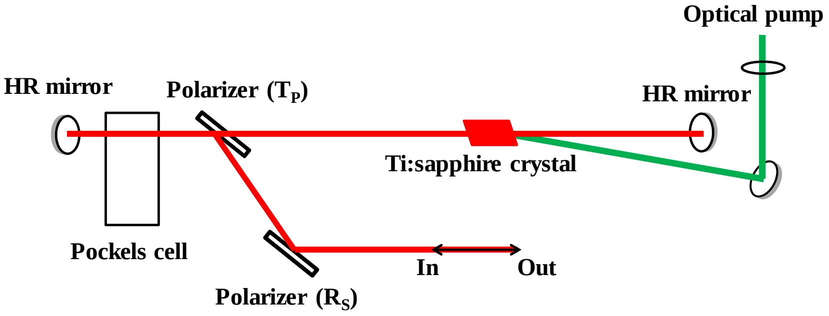

**Figure 2.15**: Optical scheme of regen Ti: Sapphire amplifier. M1 and M2 are HR-mirrors.

gain medium is placed in a resonator cavity which comprises HR mirrors (800nm). Initially when no high voltage is applied, the Pockels cell set as quarter wave plate. It acts as half wave plate in a round-trip of vertically polarized pulse (seed). As a result, the round-trip pulses are horizontally polarized and the polarizer ($T_P$ polarizer reflect vertical polarized pulses) allows seed pulse entry into regen cavity. When pulse is in regen cavity, high voltage (quarter wave volatge) is switched on the Pockels-cell crystal so that it become equivalent to half-wave plate. Thus, polarization of seed pulse remain unchanged in a cavity round trip and the trapped seed pulse amplifies each time it passes through optically pumped Ti:sapphire crystal. Regardless of gain per pass, the seed pulse is kept in regen cavity until it extracts the stored energy (TiS). The Pockels cell acts as “pulse picker” which block other seed pulses during regen amplification of first seed pulse. At the maximum of amplification, second voltage step (quarter wave voltage) is applied on the Pockels cell which changes the polarization of amplified pulse back to vertical. The vertical polarized pulse is then reflected from polarizer and extracted from the cavity.

Typically, regen amplification require 15-20 round trip of trapped pulse for ~$10^5$ optical gain. Since, regen cavity is true laser cavity, it operates in $TEM_{00}$ mode which acts as a spatial filter. Unlike multipass amplifier in which spatial mode quality deteriorate after each transit through Ti:sapphire crystal, the regen cavity preserve the Gaussian pulse profile. However, in a regen cavity, the amplification factor is limited by lasing power which depends on optical pumping power. At very high power, the effective gain band width of amplifier is narrower than PL spectrum (Ti:sapphire). Thus, pass after pass, the amplification at leading and trailing edge of the pulse is removed which causes “gain narrowing” of the pulse width (typically ~30nm for 20fs seed pulse (before stretch)). Therefore, the regen cavity is optically pumped at moderate ~5W power and broadband polarizer are used. This configuration gives ~$10^5$-$10^6$ amplification factors for ~nJ seed pulses. For further high energy pulse requirements, a second stage multipass amplifier can be used.

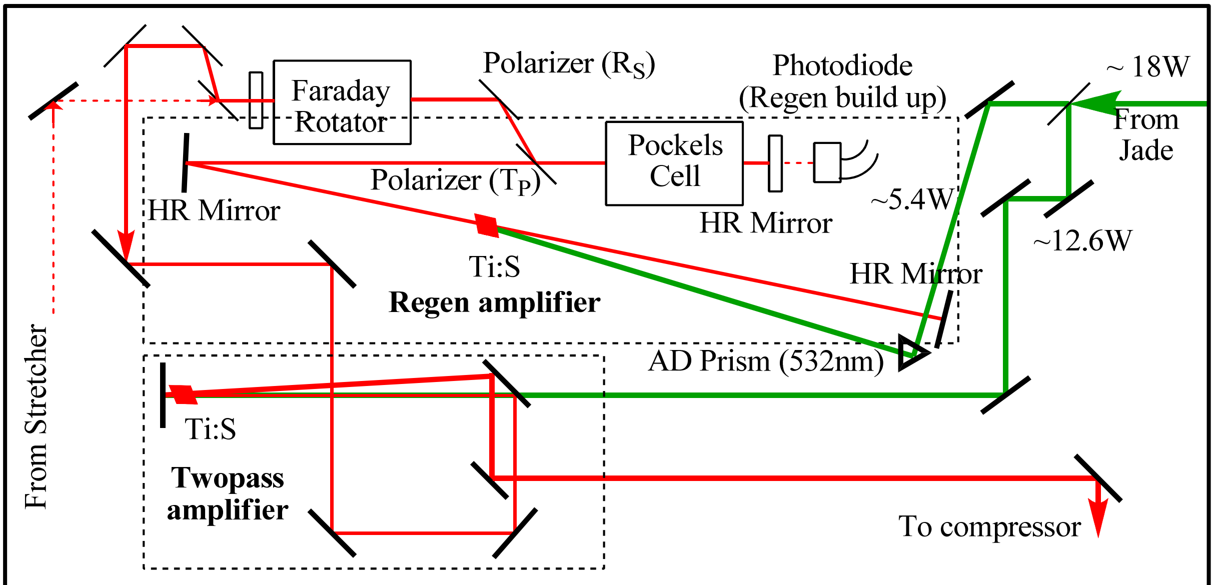

**Figure 2.16**: Optical layout of combined regen/twopass Ti: Sapphire amplifier

In present thesis work, a combined regen/twopass amplifier Alpha 1000, Thales laser system (France) is used in some of the pump-probe experiments. The optical layout of combined regen-twopass amplifier is shown in figure-2.16. It comprises a two-step high voltage Pockels cell-Medox for regen seeding and extraction of pulse, Faraday rotator and half-wave plate assembly for polarization change of input beam and output beam (back to original). The Ti:sapphire crystal in regen and twopass amplifier is optically pumped by second harmonic (527nm, 300ns pulse duration) of Q-switched ND:YLF laser ( JADE laser) operating at 1KHz repetition rate and ~18W output power. In present configuration, ~5.4W of JADE output is used in regen cavity and remaining ~12.6W is used in twopass amplifier. The Q-switching and Pockels-cell voltage steps are synchronized by Master Clock which gets trigger signal (photodiode) form master oscillator. The regen cavity build up times are ~ 122ns and ~92ns in absence and presence of seed pulse, respectively. The combined regen/twopass configuration offers ~3.5W amplified power output which then feed into compressor to generate very high energy ultra short pulses.

### 2.5.3d Pulse compressor:

The amplified pulse is compressed by two grating pair as shown in figure-2.17.[2.17,2.22,2.28, 2.29, 2.44] Unlike pulse stretcher in which pulse is stretched in afocal grating configuration, the pulse compressor have parallel grating configuration for negative dispersion so that the “red” part travels more than “blue” part of amplified pulse (stretched).

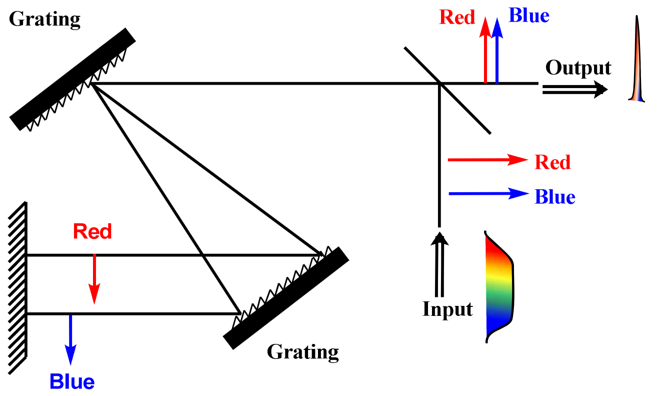

**Figure 2.17**: pulse compressor principles

For complete recovery of ultra-short-pulses, one need as many variable as the order of phase distortion introduced at different stages of CPA *i.e.* spectral phase of stretcher (2nd order), amplifier (3rd order) and compressor itself (4th order). Therefore, the grating angles (compensate 2nd order dispersion), groove density, spatial separation of grating pair (compensate 3rd order dispersion) are very critically adjusted in any laser amplifier system. In general, the groove density of first grating and distance between two grating pair is kept very large which compress the pulse to its original value <50fs. The typical total amplification factor in chirped pulse amplification method is $10^5$-$10^6$ which provides <50fs optical pulse (800nm) with very high energy >1mJ/pulse at 1KHz repetition rate (pump frequency 1KHz). The high energy pulses with ultra-short duration offer very high peak power which allow other non-linear interactions useful in pump probe experiments such as white light generation and second harmonic generation.

### 2.5.4 Pump pulse: Second harmonic generation

The 800nm fundamental output of Ti:sapphire amplifier laser system is frequency doubled in BBO ( β-babrium borate) crystal to get 400nm optical pump pulses which is adequate in photoexcitation of most of dye, semiconductor colloids, proteins *etc.* samples. The second harmonic generation is based on non-linear polarization of crystal due to very high pulse energy (peak power). The dielectric polarization,[2.29] of the crystal can be given by,

$$P(r,t) = \varepsilon_0 E_{(r,t)} + \varepsilon_0 \chi^{(2)} E^2_{(r,t)} + \varepsilon_0 \chi^{(3)} E^3_{(r,t)} + ... \qquad (2.18)$$

At very high pulse energy (MW-GW $\text{cm}^{-2}$), the contribution of second order susceptibility $\chi^{(2)}$ (~$10^{-10}$V$\text{cm}^{-1}$) is significant, which can be represented as

$$P^{(2)} = \varepsilon_0 \chi^{(2)} E^2_{(r,t)} = \varepsilon_0 \chi^{(2)} \left\{ E_0(\varphi) \cos(\omega_{inc} t - k_{(\omega)}.r) \right\}^2$$
$$P^{(2)} = \frac{1}{2} \varepsilon_0 \chi^{(2)} E_0^2(\varphi) + \frac{1}{2} \varepsilon_0 \chi^{(2)} E_0^2(\varphi) \cos(2\omega_{inc} t - k_{(2\omega)}.r) \tag{2.19}$$

This equation represents that on satisfying phase matching condition, *i.e.* $k_{(\omega_1+\omega_2)} = k_{(\omega_2)} + k_{(\omega_2)}$, the second order nonlinearity generates light photon ($2\omega$) with energy twice to that of incident light photon ($\omega$). This condition is satisfied in bi-refringent crystal such as BBO (type-I; $\eta_e(2\omega, \theta) = \eta_o(\omega)$ ).[2.29] In present pump-probe set-up, 100µJ/pulse energy of 800nm fundamental pulse is focused on 0.5mm BBO crystal to generate 10µJ/pulse energy of 400nm SHG pump pulse (figure-2.7). The BBO crystal is preferably selected for its very high damage threshold (5GWcm$^{-2}$) and suitable phase matching for 400nm SHG.

### 2.5.5 Probe pulse: Third order non-linear interaction

In pump-probe spectroscopy, white light continuums of probe pulses are needed for detection of transient species. The white light can be generated in third order non-linear interaction of high energy pulses with matter. A <100fs pulse with ~10µJ energy can start the self-phase modulation due to very high peak power (~0.1 GW). For a Gaussian pulse,[2.22] the intensity distribution can be given as,

$$I = I_o \exp\left( -\frac{t^2}{\tau^2} \right) \tag{2.20}$$

The intensity dependent non-linear refractive index (equation-2.14), changes the phase of the electric field of impinging light photon. For an instantly changing total refractive index, the phase is given by,

$$\phi(t) = -k(t)L = -\frac{\omega L \eta(t)}{c} \tag{2.21}$$

The time dependent phase change leads to frequency change given as,

$$\delta\omega = \frac{\partial\phi(t)}{\partial t} \tag{2.22}$$

The sign of “frequency difference” changes as pulse pass on leading edge to tail portion and the pulse spectrum is broadened after transit through transparent medium. Being third-order non-linear phenomena (instantaneous electric field change), all frequencies are well ordered in time with same pulse duration. In the experimental setup presented here, white light is generated by focusing a small part of 800 nm fundamental (~2 μJ) on to a sapphire window of 1.5 mm thickness (Figure 2.7). The spectrum of white light pulses is centered at 800 nm and bandwidth extends from 400nm to 1000 nm. A non-divergent, low energy white light continuum is generated by keeping the energy of the fundamental pulses just above the threshold for continuum generation. This is accomplished with the help of neutral a density filter and suitable apertures.

### 2.5.6 Pump-probe transient absorption spectrometer: Measurement set-up

In present thesis work two different amplifiers laser system are used in pump-probe study:

(1) CDP, Avesta (Russia) multipass amplifier:

(i) Ti:Sapphire oscillator: 800nm fundamental with ~50fs FWHM , ~5nJ/pulse energy at 88MHz repetition rate.

(ii) Nd:YAG pump laser: 532nm fundamental pump pulse with ~90ns FWHM, ~5mJ/pulse energy at 1KHz repetition rate.

(iii) Ti: Sapphire Multipass amplifier: 800nm fundamental pulse with ~50fs (FWHM), ~0.3-1mJ energy/pulse at 1KHz repetition rate.

(2) Thales, Alpha 1000 (France) regen amplifier:

(i) Femtosource Synergy-20 Ti:Sapphire Oscillator: 800nm fundamental with ~20fs FWHM , ~5nJ/pulse energy at 102MHz repetition rate.

(ii) Jade-1 Nd:YLF pump laser: 527nm fundamental pump pulse with ~160ns FWHM, ~18mJ/pulse energy at 1KHz repetition rate.

(iii) Combined regen/twopass Ti: Sapphire amplifier: 800nm fundamental pulse with ~40fs (FWHM), ~1-3mJ energy/pulse at 1KHz repetition rate

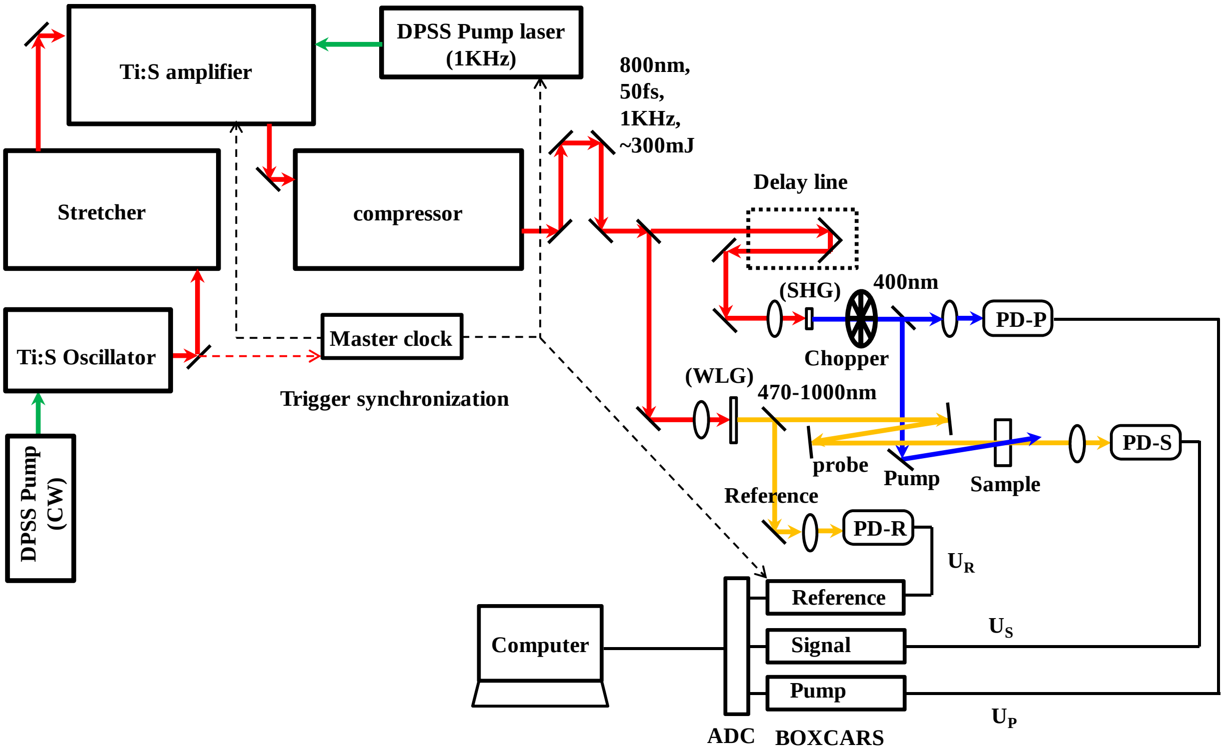

**Figure 2.18:** A schematic complete diagram showing the transient absorption spectrometer for detection in the visible region and near IR region.

The block diagram of amplifier laser system and pump-probe set-up are shown in figure-2.18. In present configuration, 250-300mW (1KHz) power of amplifier laser system is used in pump probe set-up. The "neutral density filter" are used to adjust beam intensity for white light continuum (470-1000nm probe) and second harmonic (400nm pump) generation. The white light continuum is splits into two parts- reference and signal (probe) beam line. The signal beam is focused into 1mm or 2mm quartz flow cell and transmitted lights is filtered through 20nm bandpass "interference filters" in a range of 470-1000nm. The sample solution is circulated using peristaltic pump (mechanical). The polarization of pump beam line is adjusted at 54.7° magic angle to eliminate any reorientation dynamics of sample molecules. The pump and probe beams are collinearly (6-8°) overlapped on flow cell and spot dimensions are adjusted according to pulse spatial overlap (pump~500μm, probe~300μm). The transmitted intensities of signal, reference and pump beams are recorded by "integrating" photodiode (voltage readout- $U_S$, $U_R$ and $U_P$ respectively). A chopper operating at 500Hz, is used to block every alternate pump pulses so that ratio of transmitted intensities of consecutive probe pulses corresponds to transient absorbance. For accuracy of measurements, the signal at $\Delta t$ delay time is defined as,

$$S(\Delta t) = \frac{U_S}{U_R} \tag{2.23}$$

So that,

$$\Delta A(\Delta t, \lambda) = -\log_{10}\left(\frac{S(\Delta t)}{S(0)}\right) \tag{2.24}$$

where, $S(0)$ is signal pulse without pump pulse (blocked by chopper after every). Since, probe and reference pulses are generated from single "white light continuum" pulse, the transient absorption artifacts due to "shot-to-shot" laser fluctuation are eliminated. The signal-to-noise ratio is further improved by averaging the calculated signal over more than 1000 shots for each delay time and this is done two times in "back and forth" motion of optical delay stage. The signal calculation, signal averaging, optical delay stage movements, data recording *etc.* actions are automated using "data acquisition program (DAQt1.vi)" which run through LABVIEW interface. It links the motion controller of optical delay line with electronic inputs from photodiodes (signal, reference, and pump). The photodiode readout feeds into respective "BOXCAR" averagers (in normal averaging mode). After getting "trigger" from master clock, "BOXCAR" readouts are fed to analogue-to-digital convertor (ADC) which than transfer the signal to LABVIW interface via GPIB port. So, whole data processing is computer controlled and the dynamics are recorded in ASCI format which later used in kinetics fitting and in making transient spectrum. A motion master MM3000 is used for optical delay line which can move optical stage with accuracy of 0.1μm and up to 36cm maximum length. It precisely generates pump-probe delay between 0.66fs to 1.2 ns. Typical temporal resolution of this pump-probe set up is measured by bleach signal of meso-tetrakis-(4-sulphanatophenyl) porphyrin dianion (TPPS) at 710 nm ($\lambda_{pump}$ 400 nm, aqueous solution at pH 1) and observed to be ~120fs. The kinetics are recorded in -100ps to +1ns delay time in 470-1000nm region at 20nm intervals. After a series of measurements, 2D data array $\Delta A(\Delta t, \lambda)$ is obtained and the time resolved spectrum is generated by taking $\Delta A(\lambda)$ data at fixed delay time.

### 2.6 Pulse Radiolysis

Pulse radiolysis technique is used for *in situ* generation of dye cation in solution phase and then recording transient the absorption at μs-ms time scale. The technique is based on initial physicochemical effects of ionizing radiation on matter [2.45-2.47]. This technique has been used as a complementary tool to the transient absorption measurements. In brief, 50 ns pulses from a 7 MeV linear accelerator (Ray technology, UK) were used to irradiate the solutions in the cuvettes (path length, 1 cm). The typical radiation dose was about 7 Gy, as measured by an air-saturated 0.05 mol dm$^{-3}$ KCNS dosimeter, taking Gε for $(SCN)_2^{\bullet-}$ as 21522 dm$^3$ mol$^{-1}$ cm$^{-1}$ per 100 eV at 500 nm. The transient optical absorption was monitored by a kinetic spectrophotometric arrangement using a 450 W pulse xenon lamp (Kratos) as the analyzing light source in conjunction with a monochromator (Kratos GM-252), photomultiplier (Hamamatsu R955) and digital storage oscilloscope (Tektronix, TDS 220). Suitable light filters were used to prevent UV photolysis of the solutions and to minimize the noise from the stray light.

## 2.7 Materials:

Titanium(IV) tetraisopropoxide $\{Ti[OCH(CH_3)]_4\}$ (97%), Zinc(II) acetate $\{Zn(CH_3COO)_2\}$ (99.99% anhydrous), HEPES, EDTA, 3-Mercaptopropionic acid (MPA) , NaOH, Urea, methanol (spectrophotometric grade), acetonitrile (spectrophotometric grade), were procured from Sigma-Aldrich and were used as received. Nanopure water (Barnsted System, USA) was used for making aqueous solutions. All other reagents were of AR grade and procured from S.D. Fine Chemicals (India). Solvents were degassed thoroughly with IOLAR grade dinitrogen gas before use in the preparation of all standard solutions.

## 2.8 Reference:

[2.1] J. M. Cowley, D. J. Smith, Actra. Cryst. 1987, A43, 737.

[2.2] Transmission Electron Microscopy: A Textbook for Materials Science, Authors: D. B. Williams, C. B. Carter, Springer Science + Business Media, 2nd ed. 2009.

[2.3] A. Howie, M. J. Whelan, Proc. R. Soc. Lond. A, 1961, 263, 217.

[2.4] R. H. Web, Rep. Prog. Phys., 1996, 59, 427.

[2.5] Transmission electron microscopy: Physics of Image Formation; Authors: L. Reimer, H. Kohl, Springer Science + Business Media, 4th edition, 2008.

[2.6] Electron diffraction techniques, Volume 1-2, Edited: J. M. Cowley, Oxford university press, 2002.

[2.7] Transmission electron microscopy: physics of image formation and microanalysis, Author: L. Reimer, Springer, 1997.

[2.8] M. T. Otten, W. M. J. Coene, Ultramicroscopy, 1993, 48, 77.

[2.9] M. Varela, A.R. Lupini, K. van Benthem, A.Y. Borisevich, M.F. Chisholm, N. Shibata, E. Abe, S.J. Pennycoo, Annu. Rev. Mater. Res., 2005, 35, 539.

[2.10] Aberration-Corrected Imaging in Transmission Electron Microscopy: An Introduction, author: R. Erni, Imperial College Press, London, 2010.

[2.11] J. N. Demasa, G. A. Crosby, J. Phys. Chem., 1971, 75, 991.

[2.12] Principles of Fluorescence Spectroscopy, Author: J. R. Lakowicz, 3rd edition, Springer, 2006.

[2.13] Advanced Time-Correlated Single Photon Counting Techniques, Author: W. Becker, Springer, 2005.

[2.14] Y. Chen, J. D. Müller, P. T. C. So, E. Gratton, Biophysical Journal, 1999, 77, 553.

[2.15] Streak camera for time-domain fluorescence (In Topics in fluorescence spectroscopy Vol. 1: Techniques), T. M. Nordlund 1991, pp. 183. Edited: J. R. Lakowicz. Plenum Press, New York.

[2.16] Femtosecond streak camera, FESCA-200, Hamamtsu Photonics, Japan.

[2.17] Femtosecond Laser Pulses: Principles and Experiments, Edited: C. Rullière, Springer Science + Business Media, 2nd edition, 2005.

[2.18] B. –L. Qian, H. E. Elsayed-Ali, J. Appl. Phys., 2002, 97, 462.

[2.19] W. E. King, G. H. Campbell, A. Frank, B. Ree, J. F. Schmerge, B. J. Siwick, B. C. Stuart, P. M. Weber, J. Appl. Phys., 2005, 97, 111101.

[2.20] H. Niu, W. Sibbett, Rev. Sci. Instrum., 1981, 52, 1830.

[2.21] P. Foggi, L. Bussotti, F. V. R. Neuwahl, Int. J. Photoenergy, 201, 3, 103.

[2.22] Ultrashort Laser Pulse Phenomena: Fundamentals, Techniques, and Applications on a Femtosecond Time Scale, Edited: J.-C. Diels, W. Rudolph, 2nd edition, Academic Press, Elsevier, 2006.

[2.23] Femtochemistry and Femtobiology: Ultrafast Events in Molecular Science, Edited: M. M. Martin, J. T. Hynes, Elsevier, 1st edition, 2004.

[2.24] P. F. Moulton, J. Opt. Soc. Am. B, 1986, 3, 125.

[2.25] J. M. Eggleston, L. G. Deshazer, K. W. Kangas, IEE J. Quantum Electronics, 1988, 24, 1009.

[2.26] A. Sanchez, R. E. Fahey, A. J. Strauss, R. L. Aggarwal, Opt. Lett., 1986, 11, 363.

[2.27] J. Harrison, A. Finch, D. M. Rines, G. A. Rines, P. F. Moulton, Opt. Lett., 1991, 16, 581.

[2.28] Laser Spectroscopy: Basic concept and instrumentation, Author: W. Demtröder, 3rd edition, Springer (India) Private Limited, 2004 (First Indian Reprint).

[2.29] Photonics: Linear and Nonlinear Interactions of Laser Light and Matter, Edited: R. Menzel, Springer (India) Private Limited, 2004 (First Indian Reprint).

[2.30] J. Herrmann, J. Opt. Soc. Am. B, 1994, 11,498.

[2.31] M. Piché, Opt. Commun., 1991, 86, 156.

[2.32] G. Steinmeyer, D. H. Sutter, L. Gallmann, N. Matuschek, U. Keller, Science, 1999, 286, 1507.

[2.33] T. Brabec, Ch. Spielmann, P. F. Curley, F. Krausz, Optics Letters, 1992, 17, 1292.

[2.34] M. T. Asaki, C. –P. Huang, D. Garvey, J. Zhou, H. C. Kapteyn, M. M. Murnane, Opt. Lett., 1993, 18, 977.

[2.35] N. Sarukura, Y. Ishida, H. Nakano, Opt. Lett., 1991, 16, 153.

[2.36] R. L. Fork, O. E. Martinez, J. P. Gordon, Opt. Lett., 1984, 9, 150.

[2.37] X. Zhu, M. Piché, G. D. Goodnob, R. J. D. Miller, Opt. Commun., 1998, 145, 123.

[2.38] D. Strickland, G. Mourou: Opt. Commun., 1985, 62, 419.

[2.39] M. D. Perry, G. Mourou, Science, 1994, 264, 917.

[2.40] G. Mourou, Appl. Phys. B, 1997, 65, 205.

[2.41] G. Cheriaux, P. Rousseau, F. Salin, and J. P. Chambaret, Barry Walker, L. F. Dimauro, Opt. Lett.,1996, 21, 414.

[2.42] P. Georges, F. Estable, F. Salin, J.P. Poizat, P. Grangier, A. Brun, Opt. Lett., 1991, 16, 144.

[2.43] J.E. Murray, W.H. Lowdermilk, J. Appl. Phys, 1980, 51, 3548.

[2.44] E. B. Treacy, IEEE Journal of Quantum Electronics, QE, 1969, 5, 454.

[2.45] G. E. Adams, J. W. Boag, J. Currant, B. D. Michael, in Pulse Radiolysis Edited: M. Ebert, J. P. Keene, A. J. Swallow, J. H. Baxendale, Academic Press, London, 1965, 117.

[2.46] E. M. Fielden, in The Study of Fast Processes and Transient Species by Electron Pulse Radiolysis Edited: J. H. Baxendale, F. Busi, Springer, 1982, 59,

[2.47] R. V. Benasson, E, J. Land, T. G. Trusscott, Flash Photolysis and Pulse Radiolysis, Pergamon, Oxford University Press, Oxford, 1983.

# CHAPTER 3

# INTERFACIAL ELECTRON TRANSFER DYNAMICS ON TiO$_2$ AND ZrO$_2$ NP SURFACE SENSITIZED BY CATECHOL FUNCTIONALIZED Os(II)-POLYPYRIDYL COMPLEXES: A CHARGE TRANSFER EMISSION STUDY.

## 3.1 Introduction:

Spectral sensitization of mesoporous TiO$_2$ electrodes with molecular chromophores is the basis of efficient solar energy conversion in dye sensitized solar cell (DSSC).[3.1] The mechanism involves interfacial electron-transfer (IET) reactions which are studied using various dye molecules and semiconductor materials.[3.2-3.9] In sensitization studies, Ru(II)-polypyridyl complexes are used extensively because of strong optical response in visible region and long lived metal-to-ligand charge transfer (MLCT) excited states[3.1-3.10]. Ru$^{II}$(dcbp)$_2$(NCS)$_2$ complex (dcbp is 4,4′- dicarboxylic-2,2′-bipyridine) has shown an impressive 10.4% light to electricity conversion efficiency.[3.1,3.2] However, most of the Ru(II)-polypyridyl complexes do not absorb solar photon below 1.77 eV energy which restrict the maximum photocurrent that could be drawn from such devices. [3.10] At shorter wavelength, photon energy excess to conduction band (CB) energy (offset) of TiO$_2$ material is lost in electron thermalization process. Thus, light harnessing in red region of solar spectrum is also very important and has inspired design and synthesis of new metal(II)-polypyridyl complexes. The osmium(II)-polypyridyl complexes absorb light in visible and near IR region [3.11-3.17] and hence suitable for spectral sensitization of TiO$_2$ semiconductor material. The large spin-orbit coupling in Os(II)-polypyridyl complex results $^3$MLCT absorption and emission in near IR region.[3.18]

An efficient sensitization process requires strong electronic coupling in dye/TiO$_2$ system which depends on the nature of chemically adsorbed binding groups. The catechol moiety offers stronger binding on TiO$_2$ surface as compared to other surface binding functionality such as carboxylate, phosphate etc.[3.19,3.20] The strong catecholate-TiO$_2$ linkage is attributed to formation of a five-member chelate ring on TiO$_2$ surface.[3.20,3.21] Thus, catechol functionalized Os(II)-polypyridyl complexes are suitable for both efficient and broad spectral sensitization.[3.22] In this chapter, newly designed and synthesized Os(II)-polypyridyl complexes, having pendant catechol functionality with varying degree of conjugation is used in IET study on TiO$_2$ nanoparticle (NP) surface. The variation in conjugation length is supposed to tune the energy of excited triplet states appropriately for IET process. The photophysical properties of Os(II)- polypyridyl complexes and the electron-transfer kinetics from photoexcited $^1$MLCT or $^3$MLCT to the TiO$_2$ NP and ZrO$_2$ NPS are addressed in this chapter. ZrO$_2$ NPs are used as an inert material towards IET reactions due to its higher energy CB than MLCT states of Os(II)-complexes.[3.9]

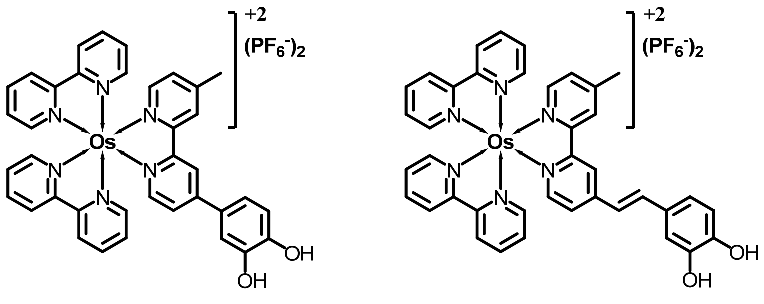

**Complex-1** **Complex-2**

Scheme-3.1: Structure of complex-**1** and complex-**2**

The structure of catechol functionalized Os(II)-polypyridyl complexes comprising 4-[2,2’]bipyridinyl-4-yl-benzene-1,2-diol (**L1**) and 4-[2- (4’-methyl-[2,2’]bipyridinyl-4-yl)-vinyl]-benzene-1,2-diol (**L2**) ligands are shown in Scheme-3.1. The sensitization processes are observed in steady state absorption and photoluminescence (PL) studies. These studies have revealed the charge-transfer (CT) interaction between complex-**1** (or -**2**) and $TiO_2$ NPs. The electron transfer path ways are investigated by transient emission measurements on sensitized semiconductor surface. In time resolved emission studies, the CT emission are monitored which furnish information about back electron-transfer kinetics in strongly coupled dye/$TiO_2$ system.

### 3.2 Materials:

$Os(bpy)_2Cl_2$, $Os(bpy)_3[PF_6]_2$,[3.23] 3-(3,4-Dimethoxy-phenyl)-propanal (**A**)[3.24] (Scheme 3.2) pyridasyl pyridinium iodide salt (**B**)[3.24] (Scheme 3.2) and $L_2$[3.25] were synthesized following reported procedure. $[^tBu_4N]PF_6$ was used as background electrolyte for electrochemical studies and was recrystallized from ethanol solvent before use. Diisopropylamine, pyridine and acetonitrile were dried and distilled over $CaH_2$ prior to use. All reactions were performed under argon atmosphere, unless stated otherwise. Water used was doubly distilled. All other chemicals and solvents were obtained locally and were used as such without further purification.

### 3.3 Synthesis of Complex-1 and complex-2:

#### 3.3a. Synthesis of 4-(3, 4-Dimethoxy-phenyl)-(2, 2’bipyridinyl) ($Me_2L_1$):

Pyridasyl pyridinium iodide salt (**A**) 5.2 g (0.015 mol) was dissolved in 50 ml glacial acetic acid in a 250 mL R.B flask. To this solution ammonium acetate 12.0 g (0.13 mol) was added and it was stirred at 100°C. Further, 3.0 g (0.015mol) of 3-(3, 4-Dimethoxy-phenyl)-

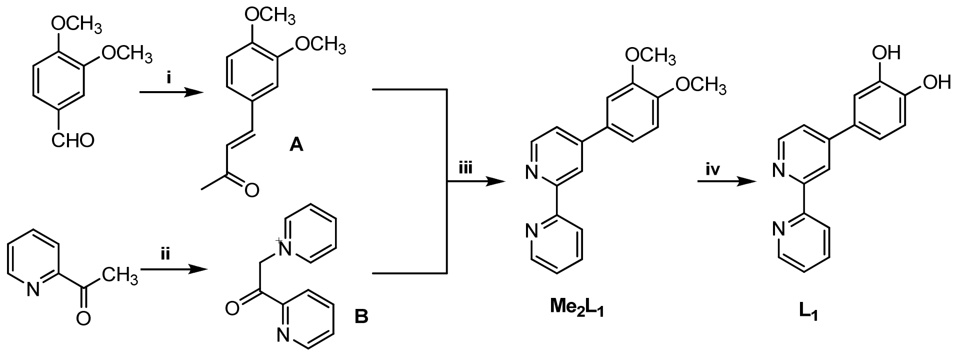

i: $CH3CHO$, EtOH, 28% NaOH, 0°C, 30 min; ii:Pyridine, Reflux, 90 min, $N_2$ atmosphere;
iii: $CH3COOH$, $CH3COO^{-}NH_4^{+}$; iv: pyridine-HCl, 190°C, 180 min.

**Scheme 3.2:** Reaction Scheme for the synthesis of the ligand $\mathbf{L_1}$.

propanal (**B**) was added to this in three interval of 1.5 hrs at 100°C and was kept at that temperature with stirring for 16 hrs. Then the reaction mixture was allowed to cool at room temperature and acetic acid was evaporated completely under vacuum. To this about 50 ml of water was added. pH of this solution was adjusted to ~ 8.0 and then the desired compound was extracted with chloroform. Chloroform layer was dried over anhydrous $MgSO_4$ and evaporated to get the $Me_2L_1$ in crude form. This was purified by gravity chromatography using silica as stationary phase and methanol-chloroform (5:95; v/v) as eluent. Yield: 0.80 g (18%). ES-MS; ($M^+$): 293 (100% ); $^1H$ NMR ( $CD_3OD$, ppm ): $\delta$ 8.72-8.62 (m, 3H, $H_{pyridyl}$), 8.44 (d, J= 8.0 Hz, 1H, $H_{pyridyl}$), 7.84 (t, J = 8 Hz, 1H, $H_{pyridyl}$) 7.50(d, J= 8Hz, 1H, $H_{pyridyl}$), 7.29-7.190 ( m, 3H, $1H_{pyridyl}$, $2H_{\ phenyl}$), 6.91( d, J = 8Hz, 1H, $H_{phenyl}$ ), 3.99(S, $3H_{4\text{-methoxy}}$), 3.946(S, $3H_{3\text{-methoxy}}$) IR ( KBr pellet, $cm^{-1}$): 1604 (C=C, C=N ).

**3.3b. Synthesis of 4-[2,2']Bipyridinyl-4-yl-benzene-1,2-diol ($\mathbf{L_1}$):** 4-(3,4-Dimethoxy-phenyl)-[2,2']bipyridinyl (0.6 g, 2.05 mmol) was added to molten pyridinum chloride (made from 16 ml of dry pyridine and 17.5 ml of conc. HCl at 190°C) at 160°C and then the temperature was raised and maintained at 190°C for 3 hrs under nitrogen atmosphere. After cooling it to room temp, the resultant solid mass was dissolved in water and the pH of the solution was adjusted to approximately 2.0. Undesired organic impurities were removed by extraction with chloroform, and then the pH of this aqueous solution was adjusted between 6 to7 with aqueous KOH. Then the desired product was extracted into the chloroform layer by solvent extraction and was dried over anhydrous $MgSO_4$. Chloroform was removed under vacuum to isolate the crude product and was further purified by recrystallization from hot ethanol. Yield: 0.3 g ( 58%). ES-MS; ($M^+$) 265 (100%). $^1H$ NMR ( $CD_3OD$, ppm ): δ 8.65-8.46 (m, 3H, $H_{pyridyl}$), 8.30 (d, J= 8Hz, 1H, $H_{pyridyl}$), 7.95(t, 1H, $H_{pyridyl}$), 7.60 (d, J= 8Hz, 1H, $H_{pyridyl}$), 7.46-7.19 (m, 3H, $H_{pyridyl}$, $H_{phenyl}$), 6.91(d, 1H, J= 8.2, $H_{phenyl}$). IR (KBr pellet,$cm^{-1}$): 1604 (C=C, C=N).

**3.3c Complex -1:** $[Os(bpy)_2Cl_2].2H_2O$ (0.070 g, 0.114 mmol) and $\mathbf{L_1}$ (0.030 g, 0.114mmol) dissolved in 50 ml of ethanol-water mixture (1:1, v/v) was allowed to reflux for 16 hours with constant stirring under inert atmosphere. Then ethanol was removed under vacuum and the desired crude complex was precipitated as red-orange solid by adding excess of aqueous $KPF_6$ solution. This was filtered off, washed with cold water and air-dried. This crude product was further purified by gravity chromatography using silica as stationary phase and $CH_3CN$–saturated aqueous $KPF_6$ solution (98:2, v/v) as eluent. Then acetonitrile was removed under vacuum and the desired pure complex was extracted in dichloromethane layer by solvent extraction. Dichloromethane was removed under reduced pressure to isolate the pure compound. Yield: 0.062 g (52%); Elemental analysis: Calculated C 40.90, H 2.67, N 7.95, Experimental C 40.72, H 2.58, N 7.65; ES-MS; ($M^+$-$PF_6$) 911(85%), ($M^+$-$2PF_6$) 766 (60%). $^1H$ NMR ($CD_3CN$, ppm): δ 8.63 (2H, d, J= 8.4Hz $H_{6,6'}$ ($L_1$)); 8.48 (4H, d, J= 8.2Hz, $2H_{6,6'}$ (bpy)); 7.86 (4H, t, J= 7.8Hz, $2H_{4,4'}$(bpy)); 7.72-7.48 (7H, m, $2H_{5,5'}$ (bpy), $H_{3,3',4'}$ ($L_1$); 7.37-7.27 (8H, m, $2H_{3,3'}$(bpy), $2H_{5,5'}$($L_1$), $H_{5,6}$(phenyl)); 6.99 (1H, d, J= 8.2Hz, $H_3$(phenyl). IR (KBr pellet, $cm^{-1}$): 3450 (-OH), 1603 (C=C, C=N), 847 ($PF_6$). $E_{1/2}$ (V vs. Fc/Fc$^+$, ΔE (mV)): Os$^{II/III}$ 1.17 V, (105 mV); $L_1/L_1^{\bullet-}$ -1.24 (80 mV), bpy/bpy$^{\bullet-}$ -1.48 (100 mV), -1.73V(110 mV).

**3.3d Complex -2:** This was synthesized following procedure mentioned above, except **$L_2$** was used instead of **$L_1$** for the reaction with $[Os(bpy)_2Cl_2].2H_2O$. $Os(bpy)_2Cl_2.2H_2O$ (0.156 g, 0.30 mmol) and 4-[2-(4'-Methyl-[2,2']-bipyridinyl-4-yl)-vinyl]benzene-1,2-diol (**$L_2$**) (0.110 g, 0.36 mmol) were used for the reaction. Similar workup procedure was adopted for achieving the complex **II** in pure form. Yield: 0.19g (63%); Elemental analysis: Calculated C 42.70, H 2.91, N 7.66, Experimental C 42.98, H 2.78, N 7.82; ES-MS; ($M^+$-$PF_6$) 951 (15%), ($M^+$-$2PF_6$) 806 (5%). $^1H$ NMR ($CD_3CN$, ppm): δ 8.5 (6H, m, $4H_{6,6'}$(bpy), $2H_{6,6'}$ ($L_2$)); 8.07 (4H, t, J= 7.6 Hz, $4H_{4,4'}$ (bpy)); 8.01 (1H, s, $H_3$ ($L_2$)); 7.82 (1H, d, J= 5.8 Hz, $H_{3'}$ ($L_2$)); 7.76-7.56 (5H, m, $4H_{5,5'}$(bpy), 1H (ethenyl)); 7.43-7.35 (6H, m, $4H_{3,3'}$(bpy), $2H_{5,5'}$($L_2$)), 7.23 (1H, d, 8.2 Hz, $H_5$ (phenyl)); 7.03 (1H, d, J= 8.2 Hz, $H_6$ (phenyl)); 7.13 (1H, d, J= 16.6Hz, (ethenyl)); 6.86 (1H, d, J= 8.2Hz, $H_3$ (phenyl)); 2.56 (3H, s, $-CH_3$). IR (KBr pellet, cm$^{-1}$): 3450 (-OH), 1603 (C=C, C=N), 847 ($PF_6$). IR (KBr pellet, Cm$^{-1}$) 3450(-OH), 1603 (C=C, C=N), 847 ($PF_6$). ); $E_{1/2}$ (V vs. Fc/Fc$^+$, ΔE (mV)): Os$^{II/III}$ 1.14 V, (100 mV); $L_2/L_2^{\bullet-}$ -1.21 (85 mV), bpy/bpy$^{\bullet-}$ -1.46 (100 mV), -1.71V(120 mV).

**3.4 Synthesis of $TiO_2$ nanoparticles:** Nanometer-size $TiO_2$ was prepared by controlled hydrolysis of titanium (IV) tetraisopropoxide.[3.26] A solution of 5 ml $Ti[OCH(CH_3)_2]_4$ (Aldrich, 97%) dissolved with 95 ml isopropyl alcohol (Aldrich) was added drop-wise (1ml/min) to 900 mL of nanopure water (2 $^0$C) at pH 1.5 (adjusted with $HNO_3$). The solution was continuously stirred for 10-12 hours until a transparent colloid was formed. The colloidal solution was concentrated at 35-40 $^0$C with a rotary evaporator and then dried with nitrogen stream to yield a white powder. $ZrO_2$ NPs were also prepared from $Zr[OCH(CH_3)_2]_4$ precursor by suing same procedure. In the present work, ~15gm/lit TiO$_2$ NPs is used in sensitization process if not mentioned otherwise.

## 3.5 Results and discussion:

### 3.5.1 TEM of TiO$_2$ NPs:

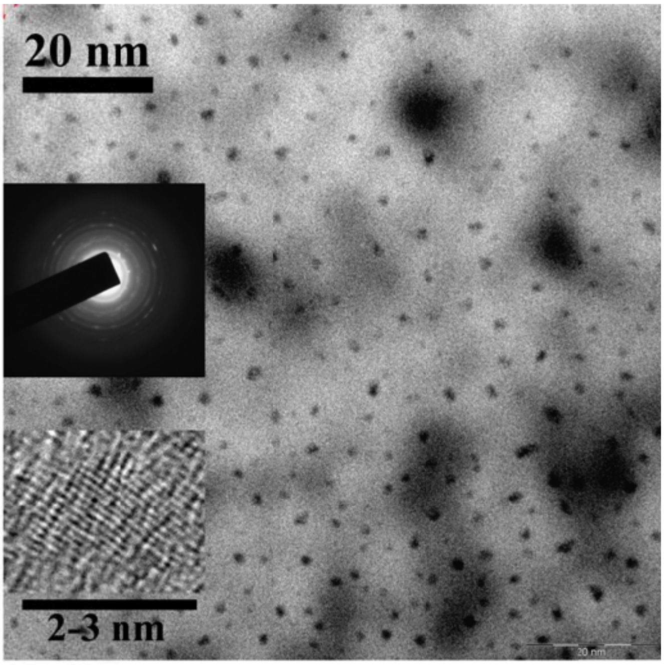

**Figure 3.1**. TEM image of TiO$_2$ NPs. Insides window shows HRTEM and SAED pattern of prepared TiO$_2$ NPs.

Figure-3.1 shows TEM image of as prepared TiO$_2$ NPs. The particle size is observed to be 2-3 nm. Figure-3.1 inset shows HRTEM and SAED pattern of TiO$_2$ NP. The HRTEM and SAED pattern confirms crystallinity of as prepared TiO$_2$ NPs.

**3.5.2 Cyclic voltammetry**: Electrochemical experiments with Os(II)-complexes (**I** and **II**) were carried out with a CH-660A (USA) electrochemical instrument; a conventional three-electrode cell assembly was used. Acetonitrile, dried and distilled prior to the experiment, was used as solvent for electrochemical studies. A saturated Ag/AgCl electrode was used as reference and platinum was used as working electrode for all measurements. Ferrocene was added at the end of each experiment as internal standard and all potentials are quoted versus the ferrocene/ferrocenium (Fc/Fc$^+$) couple. Oxidation redox potential of Os-cat1 (**I**) and Os-cat2 (**II**) molecule has been determined to be 1.17 V and 1.14 V respectively against Ag/AgCl electrode.

### 3.5.3 Photophysical properties of Os-complexes:

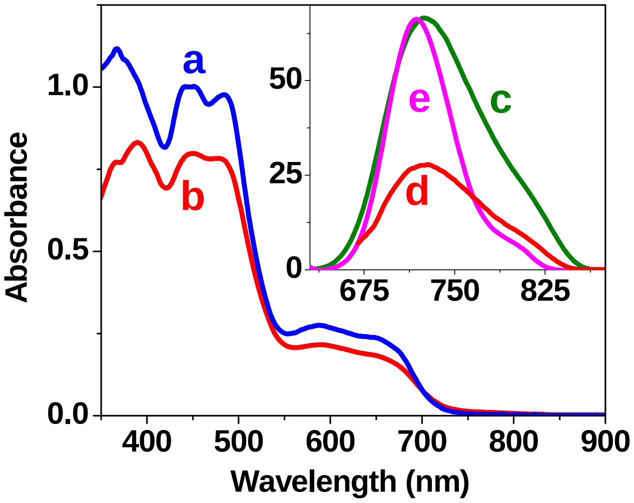

**Figure 3.2**. Optical absorption spectra of a) complex-**1** and b) compelx-**2**) in acetonitrile at 298 K. [Inset: Steady state emission spectra of complex-**1** at 298 K exciting at c) 450 nm, d) 650 nm and e) at 78K exciting at 450 nm]

Figure 3.2 shows the optical absorption of Os(II)-complexes (-**1** and -**2**). The absorption bands in 200-350nm are predominantly diimine ligand based π-π* transitions or metal ion centered d-d transitions.[3.27] considering the absorption cut off edge of TiO$_2$ NP edge (>370nm), only the intense absorption in 380-750nm region is discussed in further photophysical study. The broad absorption bands in 400-550nm is assigned to spin-allowed $d\pi_{Os(II)} \rightarrow {}^1\pi^*_{L/bpy}$ based $^1$MLCT transitions whereas the longer wavelength absorption in 550-750nm region is attributed to spin-forbidden $^3$MLCT transitions, which gain intensity in the Os(II)complexes because of enhanced spin-orbit coupling—a common feature for heavy metal centers.[3.28,3.29] The inset in figure 3.2 shows the PL spectra of complex-**1** in ethanol solution. It comprises a broad PL band in 650-850 nm region (peak at 725 nm). The PL spectra are observed to be same for photoexcitation in $^1$MLCT (450nm) and $^3$MLCT (650nm) absorption bands. In Os(II)-polypyridyl complexes, spin-orbit coupling matrix is very large and ISC occurs very efficiently in ultrafast time scale (<100fs).[3.28-3.31] Therefore, the broad PL band of complex-**1** is assigned to $d\pi_{Os(II)} \leftarrow {}^3\pi^*_{bpy}$ and $d\pi_{Os(II)} \leftarrow {}^3\pi^*_{\mathbf{L1}}$ based mixed $^3$MLCT transitions.

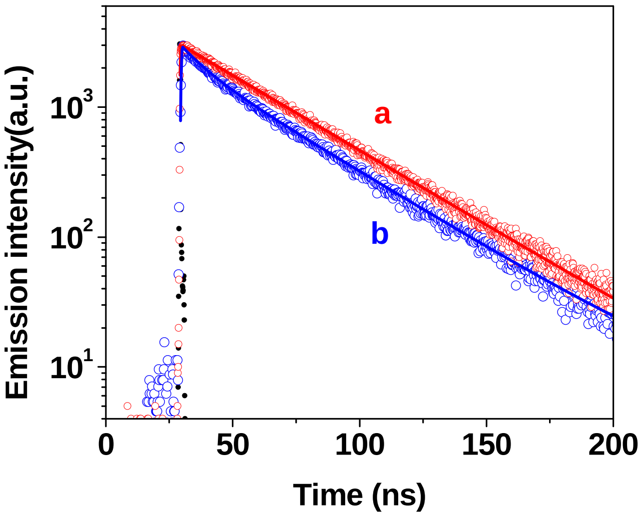

**Figure 3.3:** Transient emission decay kinetics monitored at 670nm probing a) complex-**1** in acetonitrile, b) $[Os^{II}(bpy)_3]^{+2}$ in acetonitrile after 453 nm excitation.

The presence of two different $^3$MLCT states in compelx-**1** is confirmed in transient emission measurements. Figure 3.3 shows transient emission decay profiles of complex-**1** and a standard reference complex- $[Os^{II}(bpy)_3]^{+2}$. Compelx-**1** exhibits a biexponential PL kinetics which is fitted with ~9 ns and ~35 ns time constants (table-3.1). However, $[Os(bpy)_3]^{+2}$ complex exhibits a single exponential emission decay kinetics with ~37 ns decay time constant. The longer lifetime is close to earlier reported values of Os$^{II}$-diminine complexes (~50ns).[3.32] The biexponential nature of PL kinetics of compelx-**1** reveals mixed $^3$MLCT states character. The longer component ~35ns and shorter components ~9ns are assigned to $d\pi_{Os(II)} \leftarrow {}^3\pi^*_{bpy}$ and $d\pi_{Os(II)} \leftarrow {}^3\pi^*_{\mathbf{L1}}$ transitions, respectively. In compelx-**1**, the non-radiative channels are active in catecholate ligand **L1** due to H-bonding network of catecholate functionality. It results a shorter excited state lifetime of **L1** ligand associated $^3$MLCT as compared to that of bpy ligand.[3.27] This is supported by PL kinetics of complex-**2** which also exhibits a biexponential decay (~7ns and ~35ns; table-3.1). On comparison of complex-**1** and -**2**, the variation in shorter decay time constants reflects slightly different chemical nature **L1** and **L2** ligands.

### 3.5.4 Dye binding with nanoparticles:

The binding strength of sensitizer dye molecule on semiconductor NP's surface controls interfacial electronic coupling which influences the excited-state properties as well as IET kinetics.[3.33] A strong electronic coupling ensures efficient spectral sensitization by facilitating electron injection process against the loss of photoexcitation energy in radiative or non-radiative decay channels.[3.34] In present study, the binding strength is evaluated by relative change in optical absorption spectra of complex-**1** in presence of $TiO_2$ colloidal solutions.

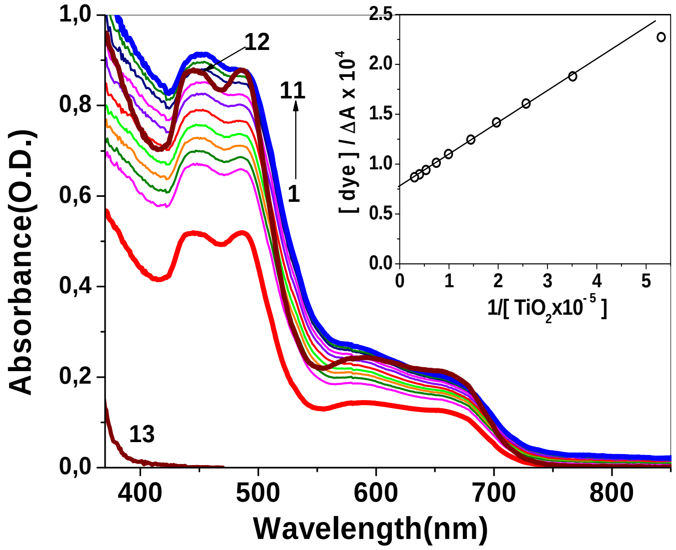

**Figure 3.4**: Optical absorption spectra of complex-**1** (25 μM) in presence of various $TiO_2$ concentrations- 1) 0.0, 2) 0.29, 3) 0.43, 4) 0.59, 5) 0.79, 6) 1.04, 7) 1.5, 8) 2.0, 9) 2.8, 10) 3.7; 11) 5.0 $gL^{-1}$. 12) Normalized spectra of complex-**1**. 13) optical spectra of $TiO_2$ NPs (5 gm/L). (Inset: Benesi-Hildebrandt plot of the complex-**1** /$TiO_2$ complex monitored at 530 nm).

Figure 3.4 shows the optical absorption spectrum of complex-**1** in absence and in presence of $TiO_2$ NPs at different concentrations (aqueous solution, pH 2.5). On addition of $TiO_2$ NPs, the absorbance increases and the spectrum become broad as well as red shifted. Red shift and broadening of spectrum are attributed to strong electronic interaction between complex-**1** and $TiO_2$ NP. The strong interaction is reported earlier in catechol linked systems such alizarin[3.35], tri-phenyl methane (pyrogallol red and bromo-pyrogallol red) dye[3.19] and porphyrin-catechol[3.36]. In such system, the catechol binding enables strong electronic coupling which facilitates CT complex formation. The CT interaction has been proposed in molecular modeling studies of dye/$TiO_2$ system by Batista and coworkers.[3.37] Moser *et. al.*[3.38] and Rajh *et.*

*al.*[3.39] reported experimental evidence of CT complex in dye-catechol/TiO$_2$ NPs. In compelx-**1**/TiO$_2$ system, the strong electronic interaction introduces lower energetics CT states to $^3$MLCT manifolds which results red shift of optical absorption spectra on addition of TiO$_2$ NPs (Figure 3.4). The CT complex formation can be expressed as:

$$\mathbf{TiO_2 + I \longrightarrow [TiO_2^{\delta-\cdots\cdots}I^{\delta+}]_{Complex}} \qquad (3.1)$$

The molar extinction co-efficient ~1.27 x 10 $^4$ cm$^{-1}$ M$^{-1}$ of the TiO$_2$-**1** complex is determined from Benesi-Hilderbandt,[3.19] plot shown in the inset of Figure 3.4. Further, the binding constant (equilibrium constants) for complex-**1**/TiO$_2$ system is observed to be 2.5X10$^5$ M$^{-1}$.

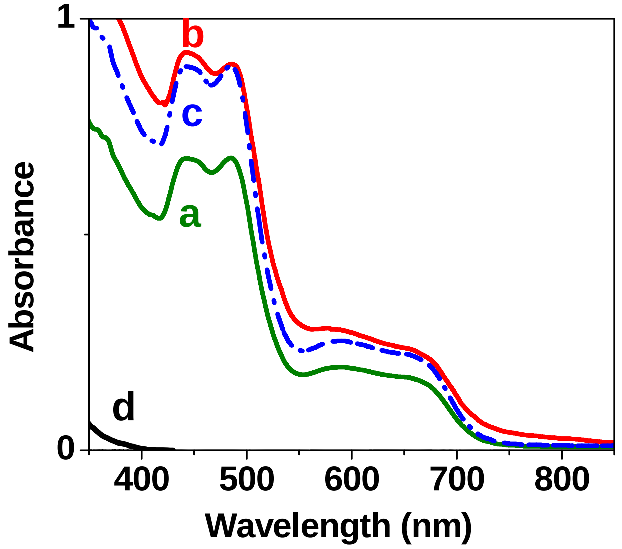

**Figure 3.5**: Optical absorption spectra of complex-**1** a) in water, b) on ZrO$_2$ NPs (20gm/L). c) normalized spectra of compelx-**1** and d) ZrO$_2$ NPs [complex-**1** concentration ~ 50 μM]

The relative increase in absorbance and subsequent red shift shows CT interaction between complex-**1** and ZrO$_2$ NP. The CB energy (offset) of ZrO$_2$ (band gap ~5.2eV) is higher than that of MLCT excited states and hence it does not favour electron injection from complex-**1** to ZrO$_2$ NP.[3.9] The observed CT spectral features can be associated with surface states which are energetically below CB of $ZrO_2$ NP.[3.40] The surface state mediated CT states are reported earlier in quinizarin/$ZrO_2$, enediol/$ZrO_2$ and alizarin/$ZrO_2$ systems.[3.40-3.42] A comparison of complex-**1**/$TiO_2$ and complex-**1**/$ZrO_2$ systems reveal a larger CT interaction in former system. It is attributed to higher density of states (DOS) in $TiO_2$ (CB) NP as compared that of $ZrO_2$ (surface state) NP.[3.40, 3.43]

### 3.5.5 Steady state emission of complex-1 on $TiO_2$ and $ZrO_2$ NPs surface:

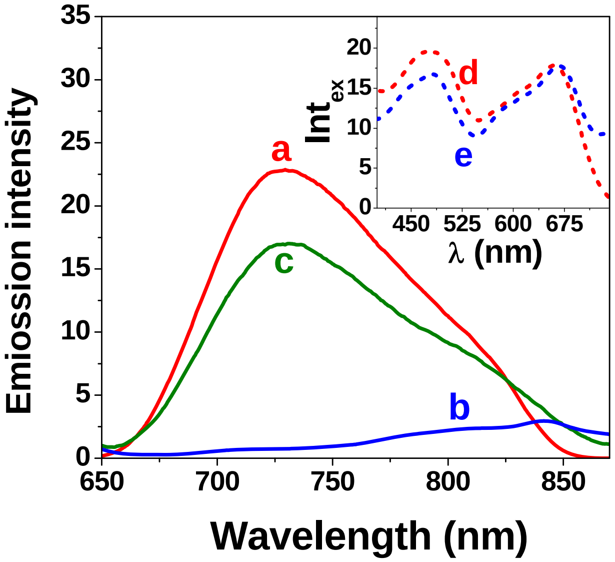

**Figure 3.6:** PL spectra of complex-**1** a) in water, b) on $TiO_2$ NPs (20gm/L) and (c) on $ZrO_2$ nanoparticle (20gm/L) surface. $\lambda_{ex}$ is 450 nm and optical density at excitation wavelength kept 0.3 for all the samples. Inset: Excitation spectra complex-**1** d) in water ( $\lambda_{em}$ = 730nm) and e) on $TiO_2$ NPs surface ( $\lambda_{em}$ = 844nm).

The electron transfer emission quenching measurements are used to understand the effectiveness of spectral sensitization in dye/$TiO_2$ system. Figure 3.6 shows emission spectrum of complex-**1** in absence and in presnec $TiO_2$ and $ZrO_2$ NPs ($\lambda_{ex}$ 450 nm). The emission intensity of complex-**1** decreases significantly on addition of $TiO_2$ NPs. The energy levels of the photoexcited $^1$MLCT and $^3$MLCT states of complex-**1** are above the CB edge of $TiO_2$ NP as shown in Scheme-3.3. Therefore, electron transfer from photoexcited MLCT states to CB ($TiO_2$ NP) is energetically favourable. It causes a significant emission quenching in complex-**1**/$TiO_2$ system (figure 3.6). In addition to PL quenching, a new PL band appears in red region of PL spectrum (Figure 3.6b). Similar red shift in quenched PL band been reported earlier in coumarin 343/$TiO_2$, xanthene/$TiO_2$ and quinizarin/$ZrO_2$ *etc.* systems and attributed to CT emission.[3.41-3.42,3.44-3.45] In strongly coupled catechol-$TiO_2$ system, the excited states of dye molecule mixes with many acceptor states (CB) of $TiO_2$ NPs and result a new low energetic CT states. So, the red shifted emission of complex-**1**/$TiO_2$ system is assigned to CT emission which represents charge recombination luminescence through CT states. The overall process is presented in equation given below.

$$\boxed{[\mathbf{TiO_2}\ \mathbf{-Dye}]_{\mathbf{complex}} \xrightarrow[\textbf{(1)Electron injection } (\mathbf{k'_{inj}})]{h\nu} [\mathbf{e^-_{CB}(TiO_2)}\ \mathbf{+\ Dye^+}] \xrightarrow[\textbf{(2) Recombination}]{h\nu_{CT}\ \textit{(CT emission)}} [\mathbf{TiO_2}\ \mathbf{-Dye}]_{\mathbf{complex}} \qquad (3.2)}$$

The quenching effects and red shifted PL band are also observed in complex-**1**/$ZrO_2$ NP as shown in figure 3.6c. However, the effects are relatively small as compared to complex-**1**/$TiO_2$ system. In complex-**1**/$ZrO_2$ system, the PL quenching is not expected because the CB energy of $ZrO_2$ NP is higher than MLCT states and an upward electron transfer is energetically unfavorable. So, the emission quenching is attributed to surface state which are exponentially distributed below conduction band edge ($ZrO_2$).[3.46] The strong electronic coupling through catechol (complex-1) chelation on $ZrO_2$ surface compensates the lesser density of surface-states ($ZrO_2$) as compared to high continuum of DOS in $TiO_2$ CB and creates significant CT interaction. The surface state mediated CT states have been reported in quinizarin sensitized $ZrO_2$ NPs where 4,5 diol group of quinizarin dye form strong chelate binding on $ZrO_2$ surface.[3.40-3.42] In this PL study, the surface state mediated CT states are revealed in complex-**1** sensitized $ZrO_2$ NPs.

### 3.5.6 Time-resolved emission studies in dye/semiconductor system:

The CT emission corresponds to recombination luminescence which can be monitored by transient emission studies. However, not many system exhibit recombination luminescence due to lack of strong electronic interaction between dye and $TiO_2$ NPs. The CT luminescence is reported earlier only in few strongly coupled composite systems such as coumarin (C343), xanthene, quinizarin sensitized metal-oxide semiconductor NPs.[3.40-3.42,3.44-3.45] The CT interaction in strongly coupled C343-$TiO_2$ system is later reconfirmed by Hupp and co-workers using stark emission spectroscopy.[3.47] In present study, the CT emission is observed in steady state PL studies of complex-**1**/$TiO_2$ and complex-**1**/$ZrO_2$ NPs system. Therefore, time-resolved emission technique is employed to study BET dynamics in strongly coupled complex-**1** and compelx-**2** sensitized $TiO_2$ and $ZrO_2$ system.

Figure 3.7 shows the time-resolved emission measurements of complex-**1** in acetonitrile, in aqueous solution, on $TiO_2$ and $ZrO_2$ nanoparticle surface ($\lambda_{ex}$ 453 nm). In aqueous solution, the transient emission of complex-**1** decays biexponentially with 2.2 ns (58 %) 20.5 ns (42 %) time constants (table-3.1) which is attributed to mixed $^3$MLCT states comprising $^3\pi*$ states of bpy and **L1** ligands. The decay time constants decrease in aqueous solution as compared to that

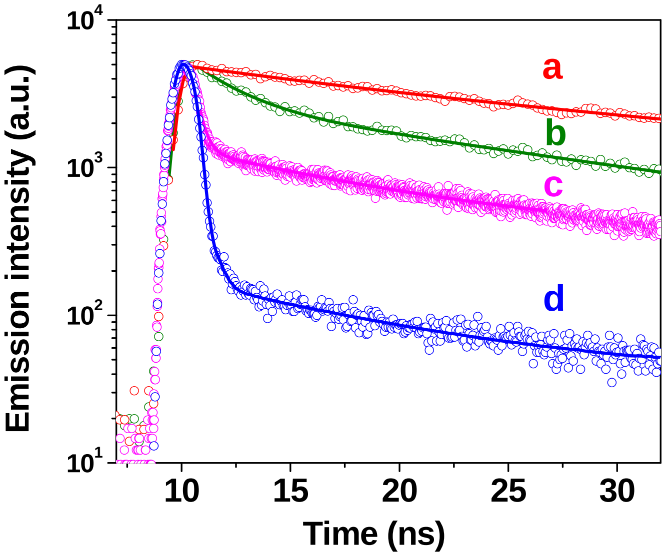

**Figure 3.7**: Single-photon-counting studies of complex-1 in different media, a) in acetonitrile, b) in water, c) in ZrO$_2$ colloid (20.0 gm/L), d) in TiO$_2$ colloid (20gmm/L) after 453 nm excitation. Emission wavelength was kept for all the measurements at 670 nm.

in acetonitrile solution (table-3.1). This could be explained by active H-bonding network of complex-**1** through catechol moiety which is sufficiently higher in aqueous solution as compared to that in acetonitrile. Figure 3.7d and 3.7c shows the emission decay trace of compelx-**1** on TiO$_2$ NP and ZrO$_2$ NP surface. The emission kinetics are best fitted biexponentially with time constants of 0.16 ns (99.7 %) & 9.8 ns (0.3 %) in complex-**1**/TiO$_2$ NP and 0.33 ns (78 %) & 9.8 ns (22 %) on complex-**1**/ZrO$_2$ NP (table-3.1).

The ultrashort sub ns time component (~160ps-660ps) can arise due to pH change or IET reactions on addition of TiO$_2$ or ZrO$_2$ NPs. Earlier, Wrighton and co-workers have reported change in photophysical property of Ru(II)-polypyridyl complexes as a function of pH.[3.48] However, steady state absorption and transient emission decay kinetics of complex-**1** are observed to be same in pH 1.5 to 8.5 range. Thus, the remote possibility that the shorter decay

**Table 3.1:** Emission life times of complex-**1** (Os-cat1) and -**2** (Os-cat2) in different media

| **Sample** | **Acetonitrile** | **Water** | **$ZrO_2$** | **$TiO_2$** |
|---|---|---|---|---|
| **$\lambda_{excitation}$ = 453 nm, $\lambda_{emission}$ = 670 nm** | | | | |
| Os-Cat1<br>(10 μM) | 9.63 ns (27 %)<br>36.5 ns (73 %) | 2.2 ns (58 %)<br>20.5 ns (42 %) | 0.33 ns (78 %)<br>9.8 ns (22 %) | 0.16 ns (99.7 %)<br>9.8 ns (0.3 %) |
| Os-Cat2<br>(10 μM) | 7.45 ns (65 %)<br>35.8 ns (35 %) | 2.1 ns (81 %)<br>18.7 ns (19 %) | 0.36 ns (84 %)<br>7.43 ns (16 %) | 0.18 ns (99.6 %)<br>7.42 ns (0.4 %) |
| **$\lambda_{excitation}$ = 589 nm , $\lambda_{emission}$ = 750 nm** | | | | |
| Os-Cat1<br>(10 μM) | 9.2 ns (4 %)<br>33 ns (96 %) | 2 ns (7%)<br>21 ns (93 %) | 0.66 ns (72 %)<br>19 ns (28 %) | 0.16 (65%)<br>0.59 ns (34%)<br>>10 ns (1 %) |
| Os-Cat2<br>(10 μM) | 7.2 ns (13 %)<br>33 ns (87 %) | 1.5 ns (37 %)<br>21 ns (63 %) | 0.62 ns (87 %)<br>16 ns (13 %) | 0.18 (63%)<br>0.6 ns (35.5%)<br>>10 ns (1.5 %) |

components ~160-330 ps is originated from change in pH on $TiO_2$ and $ZrO_2$ surface is excluded. Recent ultrafast transient absorption studies of catechol functionalized $Ru^{II}(bpy)_2$(bp-CH=CH-catechol) or porphyrin-catechol sensitized $TiO_2$ have confirmed that electron injection in strongly coupled dye/$TiO_2$ system is single exponential and pulse-width limited (< 50 fs).[3.25, 3.36] Therefore, the ultrashort component (~160-330 ps) observed in transient emission study of complex-**1**/$TiO_2$ can not be assigned to electron injection processes. So, the ultrafast process is attributed to CT emission on both nanoparticle surfaces. The longer ~9.8 ns time component is assigned to $^3$MLCT state of complex-**1** on nanoparticle surface. It represents that a small fraction of surface adsorbed complexes do not participate in IET process on $TiO_2$ or $ZrO_2$ NPs and decay through its inherent relaxation channels. However, the $^3$MLCT lifetime of complex-**1** on $TiO_2$ NPs (or $ZrO_2$ NPs) surface is observed to be longer than that of unbound complex-**1** in aqueous solution (~2.2ns). This is attributed to non-accessibility of H-bonding network to surface bound complex on $TiO_2$ or $ZrO_2$ NP which increases $^3$MLCT excited state lifetime. The transient emission kinetics have also been measured by exciting all the samples at 589nm. The 589nm excitation source is used for direct photoexcitation of $^3$MLCT absorption band of complex-**1** and complex-**2,** and to understand involvement of $^3$MLCT excited state in interfacial electron transfer process. Kinetic decay traces are fitted exponentially and presented in table 3.1.

### 3.5.7 Electron transfer dynamics from CT emission:

Transient emission studies of complex-**1** and complx-**2** (table-3.1) revealed an ultrafast decay process on sensitized $TiO_2$ and $ZrO_2$ surface which has been attributed to CT emission. The CT emission appears due to radiative recombination of electron and dye cation. It is only applicable to strong electronically coupled dye/$TiO_2$ system. On photoexcitation, CT states are directly populated on nanoparticle surface. Thus, CT state decay corresponds to back electron transfer process. A transient emission study elucidate following process:

$$[e^-(MO_2) + Dye^+] \xrightarrow{\qquad\qquad} [MO_2 - Dye]_{Adsorb} + h\nu_{CT}\ (\text{emission}) \qquad (3.3)$$

Scheme-3.3 shows interfacial electron transfer mechanism determined from time resolved emission study. In Scheme-3.3, the ground state energy level of sensitizer molecule is the oxidation potential of complex-**1** and **-2** which are determined from cyclic voltammetry study and found to be 1.17 V and 1.14 V, respectively. The energy levels of $^1$MLCT and $^3$MLCT excited states are determined from the intersection of the optical absorption spectrum of singlet

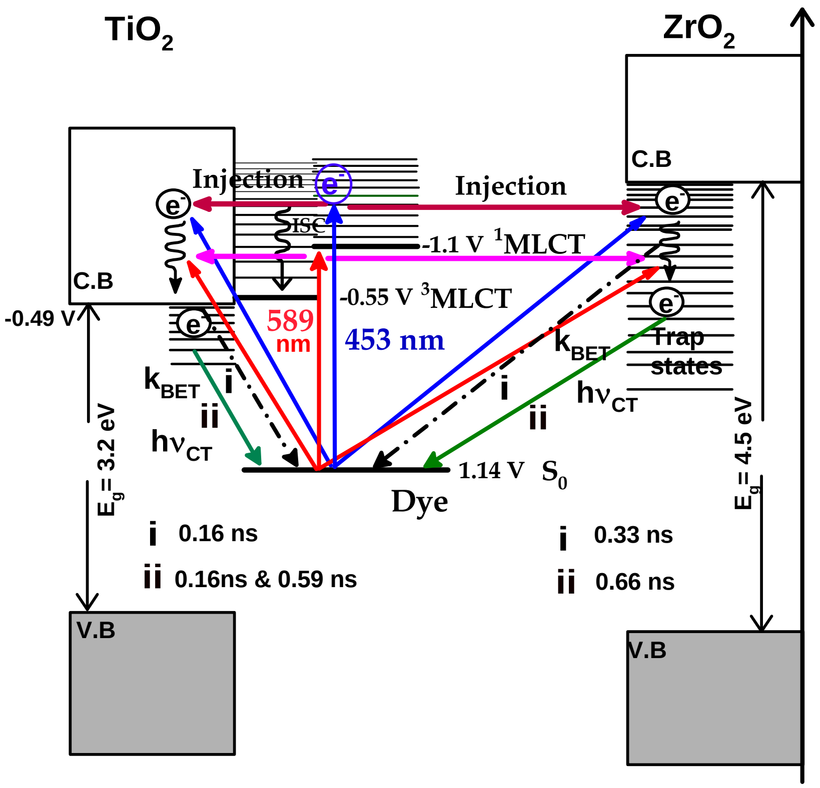

**Scheme 3.3:** Mechanistic Scheme showing 3 level model which consists of the ground state (S$_o$) state, the excited singlet ($^1$MLCT) and triplet ($^3$MLCT) states of Os-cat1 (**I**) adsorbed on TiO$_2$ and ZrO$_2$ NPs. Excitation of 453 nm inject electrons into the conduction band of TiO$_2$ NPs and shallow surface states of ZrO$_2$ NPs. Excitation of 589 nm excitation inject electron into the conduction band of TiO$_2$ NPs and deeper surface states of ZrO$_2$ NPs.

and triplet MLCT bands. The calculated energy levels for the triplet ($^3$MLCT) and singlet ($^1$MLCT) states are presented in Scheme-3.3 as –0.55 V and –1.1 V, respectively. Thus, electron transfer from photoexcited complex-**1** (or -**2**) to TiO$_2$ NPs is energetically allowed. On 453nm photoexcitation, the charge separated species (e- in TiO$_2$ and dye+) are produced either directly through CT transition or via electron injection from unthermalized MLCT manifolds. Presence of CT states makes charge recombination process a radiative process which is observed in transient emission decay with 0.16ns time constants (table-3.1). In case of $ZrO_2$ NPs, the electron transfer to conduction band is energetically forbidden. However, the strong catechol binding facilitates CT interaction with surface states lying below CB edge of $ZrO_2$ NPs. The surface states mediated CT monitored in transient emission studies. It reveals a slow CT recombination in complex-**1**/$ZrO_2$ system (0.33ns) as compared to that of complex-**1**/$TiO_2$ system (0.16ns). According to Gerischer model of surface electron transfer, the rate of BET process is function of DOS (semiconductor material).[Chapter-1, 3.49] So, the slow CT recombination is attributed to lower DOS in $ZrO_2$ material as compared to that of $TiO_2$ material.[Chapter-1]

The CT recombination dynamics are also studied by following 589nm photoexcitation in $^3$MLCT absorption band. It reveals a multiexponentially CT recombination (0.16ns, 0.59ns and >10ns, table-3.1) in complex-**1**/$TiO_2$ system. The $^3$MLCT states of compelx-**1** are energetically close to conduction band edge of $TiO_2$ NPs where density of exponentially distributed surface states is significant. Thus, electron injection occurs both in surface states and conduction band of $TiO_2$ NP. This leads to biexponential CT recombination. The DOS at surface is much lower than DOS in conduction band. So, the slower ~0.59ps decay components is attributed to surface mediated CT relaxation (~0.59ns) whereas faster ~0.19ns decay components is assigned to electron recombination from $TiO_2$conduction band to dye cation. The surface state mediated CT recombination is further confirmed in 589nm photoexcitation studies of complex-**1**/$ZrO_2$ system. It reveals a slow 0.66ns CT recombination as compared to that in 453nm photoexcitation study (0.33ns, table-1). In complex-**1**/$ZrO_2$ system, deep trap and shallow trap states are populated by 589nm and 453nm photoexcitation, respectively. As a result, CT recombination is observed to be different in two different photoexcitation studies.

## 3.6. Conclusion:

Spectral sensitization of $TiO_2$ and $ZrO_2$ nanoparticles by using newly synthesized Os(II)-polypyridyl complexes **-1** and **-2** have been studied. The optical studies show that unlike Ru(II)-polypyridyl complexes, a direct photoexcitation of $^3$MLCT states in Os(II)-polypyridyl complexes extends the optical response from visible to near IR region. The efficient sensitization process is confirmed in steady state absorption and emission studies. These studies reveal that catechol functionalized Os(II)-polypyridyl complexes form CT complex with $TiO_2$ and $ZrO_2$ NPs. On photoexcitation, the electron injections take place from the Os(II)-complexes to the conduction band of $TiO_2$ NP and surface states of $ZrO_2$ NP. The charge recombination process is monitored by CT emission kinetics in TCSPC measurements. The charge recombination dynamics have been observed to be different on photoexcitation in $^1$MLCT and $^3$MLCT absorption bands. Detailed comparative studies of CT dynamics in sensitized $TiO_2$ and $ZrO_2$ NPs have revealed the participation of intermediate surface states in charge recombination process.

## 3.7 References:

[3.1] B. O’Regan, M. Grätzel, Nature, 1991, 353, 737.

[3.2] M. K. Nazeeruddin, P. Pechy, T. Renouard, S. M. Zakeeruddin, R. Humphry-Baker, P. Comte, P. liska, L. Cevey, E. Costa, V. Shklover, L. Spiccia, G. B. Deacon, C. A. Bignozzi, M. Gratzel, J. Am. Chem. Soc. 2001, 123, 1613.

[3.3] M. K. Nazeeruddin, S. M. Zakeeruddin, R. Humphry-Baker, M. Jirousek, P. Liska, N. Vlachopoulus, V. Skhlover, C. H. Fischer, M. Gratzel, Inorg. Chem. 1999, 38, 6298.

[3.4] C.R. Rice, M.D. Ward, M.K. Nazeeruddin, M. Gratzel, New J. Chem., 2000, 24, 651.

[3.5] T. Hannapel, B. Burfeindt, W. Storck, F. Willig, J. Phys. Chem. B 1997, 101, 6799.

[3.6] J.B. Asbury, E. Hao, Y.Q. Wang, H. N. Ghosh T. Lian, J. Phys. Chem. B 2001, 105, 4545

[3.7] G. Sauve, M. E. Cass, S. J. Doig, I. Lauermann, K. Pomykal, N. S. Lewis, J. Phys. Chem. B. 2000, 104, 3488.

[3.8] S. Atobello, R. Argazzi, S. Caramori, C. Contado, S. Da Fre, P. Rubino, C. Chone, G. Larramona, C.A. Bignozzi, J. Am. Chem. Soc. 2005, 127, 15342.

[3.9] Y. Tachibana, J. E. Moser, M. Gratzel, D. R. Klug, J. R. Durrant, J. Phys. Chem. 1996, 100, 20056.

[3.10] A. Hagfeldt, G. Boschloo, L. Sun, L. Kloo, H. Pettersson, Chem. Rev. 2010, 110, 6595.

[3.11] C. Chiorboli, M. A. J. Rodgers, F. Scandola, J. Am. Chem. Soc. 2003, 125, 483.

[3.12] T. A. Heimer, E. J. Heilweil, C. A. Bignozzi, G. J. Meyer, J. Phys. Chem. A 2000, 104, 4256.

[3.13] D. Xu, J. Z. Zhang, B. Hong, J. Phys. Chem. A 2001, 105, 7979.

[3.14] D. Kuciauskas, J.E. Monat, R. Villahermosa, H. B. Gray, N. S. Lewis, J. K. McCusker, J. Phys. Chem. B 2002, 106, 9347.

[3.15] P. G. Hoertz, D.W. Thompson, L. A. Friedman, G.J. Meyer, J. Am. Chem. Soc. 2002, 124, 9690.

[3.16] H. B. Baudin, J. Davidsson, S. Serroni, A. Juris, V. Balzani, S. Campagna, L. Hammarstrom, J. Phys. Chem. A 2002, 106, 4312.

[3.17] F. Barigelletti, L. D. Cola, V. Balzani, R. Hage, J.G. Haasnoot, J. G. Vos, Reedijk, Inorg. Chem. 1991, 30, 641.

[3.18] E. M. Kober, B. P. Sullivan, W. J. Dressick, J. V. Caspar, T. J. Meyer, J. Am. Chem. Soc., 1980, 102, 7383

[3.19] G. Ramakrishna, H. N. Ghosh, A. K. Singh, D. K. Palit, J. P. Mittal, J. Phys. Chem. B 2001, 105, 12786.

[3.20] W. R. Duncan, O. V. Prezhdo, Annu. Rev. Phys. Chem. 2007, 58, 143.

[3.21] C. Creutz, M. H. Chou, Inorg. Chem. 2008, 47, 3509.

[3.22] C. R. Rice, M. D. Ward, M. K. Nazeeruddin, M. Grätzel, New J. Chem., 2000, 24, 651.

[3.23] M. M. Richter, K. J. Brewer, Inorg. Chim. Acta 1991, 180 (1), 125.

[3.24] Kelly-Basetti, M. Bernadette, Darren J.; Cundy, Suzanne M. Pereira, Wolfgang H. F. Sasse, G. Paul Savage, Gregory W. Simpson, Bioorg. Med. Chem. Letters 1995, 5 (24), 2989.

[3.25] G. Ramakrishna, D. A. Jose, D. KrishnaKumar, A. Das, D. K. Palit, H. N. Ghosh, J. Phys. Chem. B 2005, 109, 15445.

[3.26] H. N. Ghosh, J. Phys. Chem. B 1999, 103, 10382.

[3.27] D. A. Jose, P. Kar, D. Koley, B. Ganguly, W. Thiel, H. N. Ghosh, A. Das, Inorg. Chem. 2007, 46, 5576.

[3.28] E. M. Kober, J. V. Caspar, B. P. Sullivan, T. J. Meyer, Inorg. Chem. 1988, 27, 4587.

[3.29] Photochemistry and Photophysics of Coordination Compounds II, Editors: V. Balzani, S. Campagna, Springer, Topics in Current Chemistry Series, Volume 281, 2007, 101.

[3.30] N. H. Damrauer, G. Cerullo, A. Yeh, T. R. Boussie, C. V. Shank, J. K. McCusker, Science, 1997, 275, 54.

[3.31] A. C. Bhasikuttan, M. Suzuki, S. Nakashima, T. Okada, J. Am. Chem. Soc. 2002, 124, 8398.

[3.32] M. L. Fetterolf, H. W. Offen, J. Phys. Chem. 1985, 89, 3320.

[3.33] A. Hagfeldt, M. Gratzel, Chem. ReV. 1995, 95, 49.

[3.34] A. Listorti, B. O'Regan, J. R Durrant, Chem. Mater. 2011, 10.1021/cm200651e

[3.35] G. Ramakrishna, A. K. Singh, D. K. Palit, H. N. Ghosh, J. Phys. Chem. B 2004, 108, 1701.

[3.36] G. Ramakrishna, S.Verma, D. A. Jose, D. Krishna Kumar, A. Das, D. K. Palit, H. N. Ghosh, J. Phys. Chem. B 2006, 110, 9012.

[3.37] L. G. C. Rego, V. S. Batista, J. Am. Chem. Soc. 2003, 125, 7989.

[3.38] J. Moser, S. Punchihewa, P. P. Infelta, M. Gratzel, Langmuir 1991, 7, 3012.

[3.39] T. Rajh, L. X. Chen, K. Lukas, T. Liu, M. C. Thurnauer, D. M. Teide, J. Phys. Chem. B 2002, 106, 10543.

[3.40] G. Ramakrishna, A. K; Singh, D. K; Palit, H. N. Ghosh, J. Phys. Chem. B 2004, 108, 4775.

[3.41] G. Ramakrishna, H. N. Ghosh, Langmuir 2004, 20, 7342

[3.42] T. Rajh, L. X. Chen, K. Lukas, T. Liu, M. C. Thurnauer, D. M. Tiede, J. Phys. Chem. B 2002, 106, 10543.

[3.43] N. A. Anderson, T. Lian, Annu. Rev. Phys. Chem. 2005, 56, 491.

[3.44] H. N. Ghosh, J. Phys. Chem. B 1999, 103, 10382.

[3.45] G. Ramakrishna, H. N. Ghosh, J. Phys. Chem. B 2001, 105, 7000.

[3.46] L. M. Peter, J. Phys. Chem. C 2007, 111, 6601

[3.47] K. A. Walters, D. A. Gaal, J. T. Hupp, J. Phys. Chem B 2002, 106, 5139.

[3.48] P. J. Giordano, C. R. Bock, M. S. Wrighton, J. Am. Chem. Soc. 1978, 100, 6960.

[3.49] Semiconductor electrochemistry, Edited by Rüdiger Memming, Wiley-VCH, 1st edition, 2001.

# CHAPTER 4:

# HEAVY ATOM EFFECTS ON INTERFACIAL ELECTRON TRANSFER REACTION IN M(II)–POLYPYRIDYL (M=Ru/Os) COMPLEX SENSITIZED $TiO_2$ NP: AN ULTRAFAST TIME-RESOLVED ABSORPTION STUDY.

## 4.1 Introduction:

Interfacial electron transfer (IET) dynamics play a crucial role in determining the efficiency of dye sensitized solar cell (DSSC).[4.1-4.3] In DSSC, the primary charge separation is result of preferential electron injection (in conduction band of $TiO_2$) over excited state decay of sensitizer dye molecules followed by regeneration of dye due to electron transfer from $I^-/I_3^-$ redox couple to oxidized dye.[4.4,4.5] In the interim, the injected electron can be recaptured by oxidized sensitizer molecules and incur loss to primary energy conversion process.[4.6] Thus, the light conversion process depends on kinetic competition between various electron transfer steps at dye sensitized $TiO_2$ interface.[4.7] The strength of electronic coupling determines the yield of long lived and energetically charge separated states. The optimization of coupling strength is highlighted earlier by Durrant and co-workers.[4.8] The strong electronic coupling facilitates higher electron injection yields but renders a fast back electron transfer process which shortens the life of charge separated species.[4.9] Therefore, a slow back electron transfer (BET) process in strongly coupled system is desirable for improved device function and aimed in design of prospective sensitizer molecules.[4.10,4.11] The seminal work by O’Regan and Grätzel has projected ruthenium(II)-diimine complexes as prospective sensitizer molecules for DSSC.[4.1,4.12] Ru(II)-polypyridyl complexes manifest an efficient electron injection yield on account of long lived (>100ns lifetime) and energetically suitable $^3$MLCT states.[4.11,4.13] In past two decades, vast number of Ru(II)-diimine complexes have been designed, synthesized and used in sensitization study which led to an empirical electron transfer model in DSSC.[4.3,4.4] The electron transfer from excited state (ES) of sensitizer dye molecules to conduction band (CB) of $TiO_2$ NP (-0.45V *vs*. NHE) and then cation transfer from oxidized dye to $I^-/I_3^-$ redox electrolyte (~0.6V *vs*. NHE) imposes certain energy requirements on MLCT ground- (> +1.2 V *vs*. NHE) and excited- states (> |-0.5| V *vs*. NHE).[4.14] This inhibits the optical response of Ru(II)-diimine complexes in near IR region ( > 700nm). However, the calculated accumulated photocurrent suggests higher light conversion efficiency in longer wavelength region (700nm - 900nm).[4.3] In this regard, OsII)-polypyridyl complexes draw certain advantage over analogous Ru(II)-complexes as the large spin-orbit coupling in Os(II) metal ion produces direct $^3$MLCT state absorption in longer wavelength region.[4.15] The broad spectral response throughout visible and NIR region and comparable ground and excited state energetic makes Os(II)-polypyridyl complexes a potential sensitizer for photo-electrochemical energy conversion devices.

Large spin-orbit coupling matrix of Os(II)-polypyridyl complexes ($\zeta_{Os}$ = 3381cm$^{-1}$) as compared to that of Ru(II)-polypyridyl complexes ($\zeta_{Ru}$ = 1042cm$^{-1}$) facilitates intersystem crossing (ISC) which redistributes the photoexcitation energy among $^1$MLCT and $^3$MLCT states. It also causes a shorter excited state lifetime of Os(II)-complexes than its analogous Ru(II)-complexes.[4.15] Thus, the electron transfer mechanism in above two M(II)-polypyridyl complexes are supposed to be different and a comparative study can reveal fundamental aspect of IET processes in DSSC.

In literature, the electron injection from excited state of Ru(II)-polypyridyl complexes to $TiO_2$ nanoparticles (NPs) has been reported as fast as < 100fs.[4.16] It suggests that electron injection initiates from directly photoexcited vibronically hot $^1$MLCT states.[4.17] Sandstorm and co-workers, Durrant and co-workers have also shown that electron injection from vibronically hot $^1$MLCT states competes with rapid $^1$MLCT→$^3$MLCT ISC process.[4.18,4.19] The electron injection from $^3$MLCT states have been reported in longer 1-100 ps time scale.[4.18-4.20] Interestingly, such multiexponential electron injection processes are largely observed in carboxylate functionalized Ru(II)- polypyridyl complexes which bind moderately on mesoporous $TiO_2$ film in presence of solvent environment.[4.7,4.21] However, Willing and co-workers have reported single exponential ultrafast (<25fs) electron injection under ultra-high vacuum by using carboxylate dye- $Ru^{II}(dcbpy)_2(SCN)_2$.[4.21] Further, the single exponential ultrafast electron injection in solution phase is also observed using catechol-functionalized Ru(II)- polypyridyl complexes *viz.* $Ru^{II}(bpy)_2$(bp-CH=CH-catechol), $Ru^{II}(bpy)(SCN)_2$(bp-CH=CH-catechol) dyes.[4.22,4.23] So, the debate is whether strong electronic coupling always ensures a single exponential electron injection or the inter system crossing redistribute the ES population in MLCT manifolds (singlet and triplet) and then the electron transfer occurs.

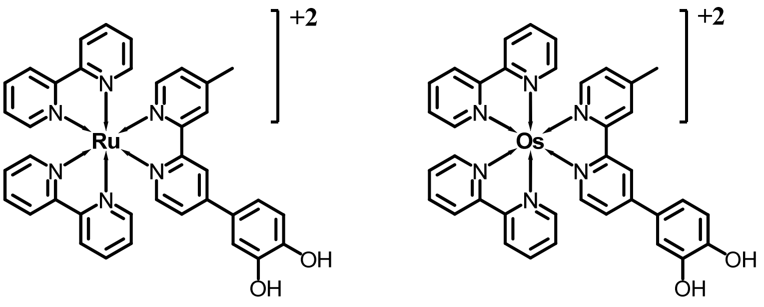

**Complex-1** **Complex-2**

Scheme 4.1: Structure of complex-**1** and complex-**2**

In this work, newly synthesized Ru(II)- and Os(II)-polypyridyl complexes ($[M(bpy)_2L_1]^{2+}$ where M = Os(II) or Ru(II); bpy is 2,2'-bipyridyl and **L1** is 4-[2,2']-bipyridinyl-4-yl-benzene-1,2-diol) have been used to understand the heavy atom effects on IET reactions. A well dispersed $TiO_2$ NPs suspension is prepared in aqueous solution at pH < 2.5 (zeta potential < +30mV above pH4).[4.24] At low pH (<2.5), surface binding group such as carboxylate (pKa~3.5 for $H^+$ + $COO^{2-}$) and phosphate (pKa ~7 for $H^+$ + $HPO^{2-}$),[4.26] tend to desorb from $TiO_2$ NPs surface whereas catechol chelation [4.9,4.25] supports dye immobilization on $TiO_2$ surface. So, catechol functionalized Ru(II)- and Os(II)-polypyridyl complexes are used in fundamental study of electron transfer on $TiO_2$ NP's surface in aqueous solution. The transient species produced in interfacial electron transfer reactions have characteristic absorption in visible and near IR region.[4.21,4.22,4.27-4.29] So, femtosecond transient absorption spectroscopy detecting in visible and near IR region is used to study the IET process.

## 4.2 Materials:

$TiO_2$ NPs, 4-(2,2'Bipyridinyl-4-yl)-benzene-1,2-diol (**L1**) ligand and complex-**2** used were same as reported in chapter 3. $Ru^{II}(bpy)_2Cl_2$ was synthesized following the reported method.[4.30]

### 4.2.1 Synthesis of complex-1

$[Ru(bpy)_2Cl_2].2H_2O$ (0.07 g, 0.072 mmol) and **L1** (0.02 g, 0.07 mmol) dissolved in 50 ml of ethanol-water mixture (1:1, v/v) was refluxed for 8 h with constant stirring under inert atmosphere. Then ethanol was removed under vacuum and the desired crude complex was precipitated as red-orange solid by adding excess of aqueous $KPF_6$ solution. This was filtered off, washed with cold water and air-dried. This crude product was further purified by gravity chromatography using silica as stationary phase and $CH_3CN$–saturated aqueous $KPF_6$ solution

(98:2, v/v) as eluent. Then acetonitrile was removed under vacuum and the desired pure complex was extracted in dichloromethane layer by solvent extraction. Dichloromethane was removed under reduced pressure to isolate the pure compound. Yield: 0.070 g (52%); Elemental analysis: Calculated C 44.68, H 2.92, N 8.69, Experimental C 44.7, H 2.8, N 8.5; ES-MS; ($M^+$-$PF_6$) 823 (29%). $^1$H NMR ($CD_3CN$, ppm): δ 8.70 (2H, d, J = 9.0Hz $H_{6,6'}$ ($L_1$)); 8.51 (4H, d, J = 8.2Hz, $2H_{6,6'}$ (bpy)); 8.06 (4H, t, J = 7.6Hz, $2H_{4,4'}$(bpy)); 7.82-7.58 (7H, m, $2H_{5,5'}$ (bpy), $H_{3,3',4'}$ ($L_1$); 7.42-7.29 (8H, m, $2H_{3,,3'}$(bpy), $2H_{5,5'}$($L_1$), $H_{5,6}$(phenyl)); 6.99 (1H, d, J = 8.2Hz, $H_3$(phenyl). IR (KBr pellet, $cm^{-1}$): 3450 (-OH), 1604 (C=C, C=N), 842 ($PF_6$). $E_{1/2}$ (V vs. Ag/AgCl, ΔE (mV)): $Ru^{II/III}$ 1.32 V, (102 mV); $L_1/L_1^{\bullet -}$ -1.38 (80 mV), bpy/$bpy^{\bullet -}$ -1.62 (100 mV), -1.9 V (85 mV).

### 4.3 Results and discussion:

**4.3.1 Cyclic voltammetry**: Electrochemical studies revealed that $M^{II/III}$ redox potential (with respect to NHE) for complexes **1** and **2** are +1.32 V ($Ru^{II/III}$) and +1.14 V ($Os^{II/III}$), respectively and this difference in $M^{II/III}$ (M=Ru/Os)-redox potential is reflected in the observed red shift of the MLCT band for Os-complex as compared to the Ru-complex.

### 4.3.2 Spectroscopic properties: UV-vis absorption spectra

The spectral sensitization of $TiO_2$ NPs system using structurally similar $Os^{II}(bpy)_2$(bp-CH=CH-catechol complex, has been discussed in chapter-3 where the strong electronic interaction is confirmed by steady state absorption, emisison and time resolved emission studies.[4.31] In this chapter, steady state absorption is presented to show sensitizing ability of complex-**1** and complex-**2**. Figure 4.1 shows the optical absorption spectra of complexes -**1** and -**2** in absence and in presence of $TiO_2$ NPs. Since $TiO_2$ NPs strongly absorb light below 380nm and also, 400nm excitation source is used in femtosecond time resolved absorption studies, than the intense absorption band in 380-750nm region is explained in discussion. Ru(II)-complex (-**1** ) exhibits strong absorption band in 400-550nm region which is assigned to $d_{Ru(II)} \rightarrow \pi^*_{(bpy)}$ and $d_{Ru(II)} \rightarrow \pi^*_{L1}$ $^1$MLCT transitions.[4.22,4.31] Complex-**2** shows a new absorption band in 550-750nm region in addition to $^1$MLCT absorption band in 400-550nm region. The large spin-orbit coupling of Os(II)-complex (-**2**), allows spin forbidden ground state to $^3$MLCT absorption in 600-750nm region.[4.16,4.31,4.32]

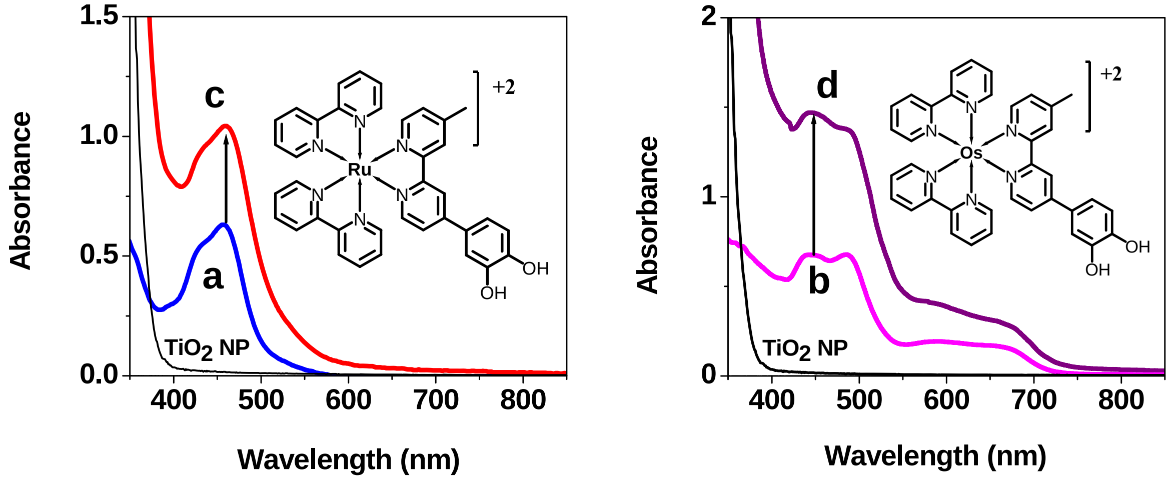

**Figure 4.1**: Optical absorption spectra of complex a) -**1** in water, b) -**2** in water; c) -**1** on $TiO_2$ nanoparticle surface and d) -**2** on $TiO_2$ NP dispersed in water (concentration of -**1** was kept ~38 μM and concentration of -**2** was kept ~30 μM ).

On addition of $TiO_2$ NPs, the absorbance of complex-**1** and -**2** increase significantly and the absorption spectrum is red shifted. The remarkable increase in absorbance and spectral broadening are attributed to strong electronic coupling between complex -**1** (or -**2**) and $TiO_2$ NP. It resembles to an efficient spectral sensitization process.[4.31]

### 4.3.3 Excited state dynamics of free complex -1 and -2 in acetonitrile:

The IET dynamics is aimed in transient absorption studies. In IET process, electron injection initiates from photoexcited MLCT manifolds.[4.1-4.14] A prior knowledge about transient absorption of photoexcited MLCT states helps in differentiation of transient species produced in IET process.[4.18,4.22] Therefore, transient absorption studies of complex **-1** and **-2** are carried out in inert media such as acetonitrile solvent.

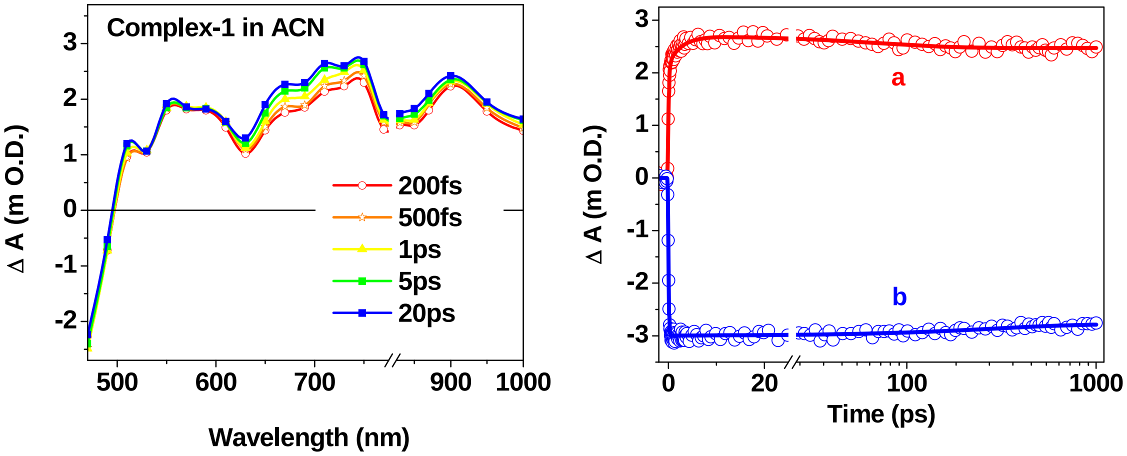

**Figure 4.2**: Left Panel: Transient absorption spectra of complex-**1** in acetonitrile solution following excitation at 400nm laser pulse at 200 fs, 500 fs, 1 ps, 5 ps, and 10 ps time delays. Right Panel: a) ESA decay at 710 nm, b) bleach recovery at 470nm.

Figure-4.2 shows transient absorption spectrum and few selected kinetics of complex-**1** in acetonitrile solvent after 400nm photoexcitation. It comprises bleach in 480-500nm region, broad positive and structured absorption band in 510-1000nm region. Earlier, McCusker and co-workers, have reported broad excited state absorption (ESA) of Ru(II)-complex in 500-800nm region and assigned it to $^3$MLCT states.[4.33] The rapid ISC promotes $^1$MLCT into low energy $^3$MLCT states in ultrafast <50fs time scale.[4.34] Bhasikuttan *et al* have reported $^1$MLCT→

$^3$MLCT conversion in ~50fs time scale.[4.35] So, the positive absorption in longer than 200fs time scale is assigned to ESA mainly due to $^3$MLCT states. This is supported by ESA and bleach recovery kinetics presented in right panel of figure-4.2. The ESA kinetics at 710nm shows a long lived (>1ns) transient species (in this case MLCT state) which can be related with slow bleach recovery kinetics (>1ns) at 480nm. The emissive $^3$MLCT state lifetime of Ru(II)-complex (-**1**) is in the range of >300ns (time resolved emission studies; chapter 5). So, the long lived transient species observed at 710nm is assigned to $^3$MLCT states. The rise of transient signal at 710nm is best fitted biexponentially with < 100 fs (94.3%) and 7 ps (6.7%) time constants. Earlier, McCusker and co-workers have rationalized TA kinetics of Ru(II)-complexes by $^1$MLCT→$^3$MLCT ISC and then vibrational cooling of $^3$MLCT state in 5ps time scale.[4.34] Likewise in Ru(II)-complex (-**1**), the pulse width limited growth component is attributed to formation of vibronic hot $^3$MLCT state. The slow ESA growth (~7ps in 710nm TA kinetics) is observed to be wavelength dependent but remained absent in bleach recovery kinetics at 480nm. Therefore, it is assigned to vibrational relaxation in $^3$MLCT manifold of Ru(II)-complex (-**1**). The 400nm photoexcitation of Ru(II)-complex populates higher Frank-Condon (FC) states of $^1$MLCT state which rapidly converge to hot $^3$MLCT state through an ultrafast ISC process. Non-thermalized $^3$MLCT undergo vibrational cooling in 5-15ps time scale and results long lived $^3$MLCT states (>300ns).

Figure 4.3 shows TA spectrum and kinetics of complex-**2** in acetonitrile solvent after 400nm photoexcitation. It comprises a negative absorption in 480-700nm region and a positive absorption band in 700-1000nm region. The $^3$MLCT state photoluminescence (PL) of Os(II)-complex is observed in 675-850nm region (PL peak at 730nm; Chapter-3).[4.31] So, the negative absorption band in 550-700nm region cannot be assigned to stimulated emission. The negative absorption band (550-700nm) matches well with steady state $^3$MLCT absorption band in 550-700nm region and hence assigned to bleach due to $S_0 \rightarrow {}^3$MLCT transitions. The increased bleach in 480-550nm region resembles to $^1$MLCT absorption band. The positive absorption band in 700-1000nm region is assigned to ESA of $^3$MLCT state as described in TA spectrum of Ru(II)-complex (-**1**) in acetonitrile. In Os(II)-complex (-**2**), the spin-orbit coupling matrix element is much larger than that of Ru(II)-complex. Therefore, a crossover from vibronic hot $^1$MLCT state (directly populated by 400nm photoexcitation) to $^3$MLCT manifold takes place very efficiently. The vibrational cooling in $^3$MLCT manifolds of Ru(II)-complex (-**1**) is observed in 500-1000nm region and the same is expected in Os(II)-complex (-**2**). So, the bleach growth in 550-700nm region is assigned to overlapping ground state bleach and ESA decay due to vibrational cooling in $^3$MLCT state. In thermalization process, the FC states relaxes to ν = 0 states along $^3$MLCT energy surface. So, the TA kinetics in blue region (<700nm) corresponds to decay of higher FC

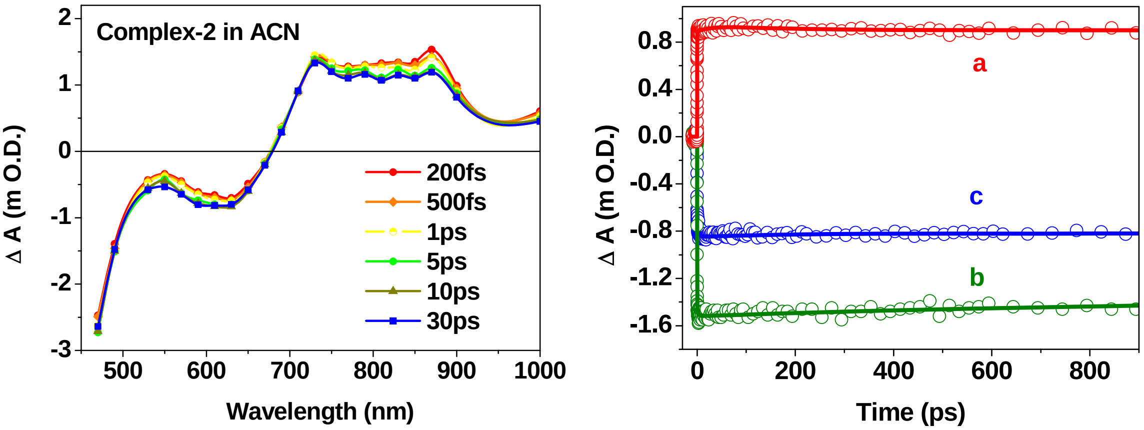

**Figure 4.3**: Left panel: The transient absorption spectra of complex-**2** in acetonitrile solution after 400nm photoexcitation at 200 fs, 500 fs, 1 ps, 5 ps, 10 ps, and 30 ps time delays. Right Panel: a) ESA deacy at 710 nm, b) bleach recovery at 490nm and c) 610nm.

state whereas TA kinetics in red region (>700nm), probe the filling of lower energy FC states. So, the growth in 550-700nm region corresponds to decay of higher FC states which can be simultaneously probed by growth of TA signal at 710nm. The vibrational cooling in $^3$MLCT manifold is observed to be ~4 ps at 610nm bleach growth signal. The ESA decay at 710nm is best fitted with 150ps (5.3%) and >1ns (94.7%). In time-resolved emission study (chapter-3, table-3.1), $^3$MCLT state emission lifetime of Os(II)-complex (-**2)** is found to be 7.45 ns (65 %) and 35.8 ns (35 %). So, >1ns time component (710nm TA kinetics) is assigned to long lived $^3$MLCT state of Os(II)-complex (-**2**).

### 4.3.4 Transient absorption measurements of complex -1/TiO$_2$ and complex-2/TiO$_2$ NPs:

The IET dynamics in complex- **1** and -**2** sensitized TiO$_2$ NPs are carried out using femtosecond time resolved absorption spectroscopy. The transient species involved in such studies are photoexcited MLCT states, conduction band electron of TiO$_2$ NPs and oxidized complexes -**1** and -**2**. The information about excited MLCT states are elucidated in TA study in acetonitrile solvent (in absence of TiO$_2$ NPs). The absorption spectrum of oxidized complex-**1** and -**2** are monitored separately using pulse radiolysis technique.[4.22] In pulse radiolysis study, a selective one electron oxidation of complex-**1** and complex-**2** are carried out in presence of azide radical which is produced insitu by 7 MeV electron pulse interaction with N$_2$O saturated NaN$_3$ aqueous solution. The radiolysis reactions are given below

$$H_2O \quad \backslash/\backslash/\backslash/\backslash/\backslash/\backslash/\backslash \longrightarrow H^{\bullet}, OH^{\bullet}, e_{aq}^{-} \text{ and other related products}$$

$$e_{aq}^{-} + N_2O \longrightarrow N_2 + O^{\bullet -}$$

$$O^{\bullet -} + H_2O \longrightarrow OH^{\bullet} + OH^{-}$$

$$N_3^{-} + OH^{\bullet} \text{ (or } O^{\bullet -}\text{)} \longrightarrow N_3^{\bullet} + OH^{-} \text{ (or } O^{2-}\text{)}$$

$$N_3^{\bullet} + \text{complex} \longrightarrow N_3^{-} + \text{complex}^{\bullet+}$$

Figure-4.4 shows absorption spectrum of cation complex **-1, -2** and cation ligand **L1** after 2µs time delay with respect to electron pulse interaction. Oxidized complex-**1** and **-2**, exhibit a broad and red shifted transient absorption peak in 590-600nm region as compared to that of free ligand cation **L1**$^{\bullet+}$ (absorption peak at 380nm). This clearly shows that the peak in 525-650nm region corresponds to oxidized $M^{+3}(bpy)_2$(bp-CH=CH-catechol) complex (M = Ru and Os). The prior assignment of cation absorption peaks and excited MLCT states help in identifying the transient species observed later in transient absorption studies of complex **-1** and **-2** sensitized $TiO_2$ NPs.

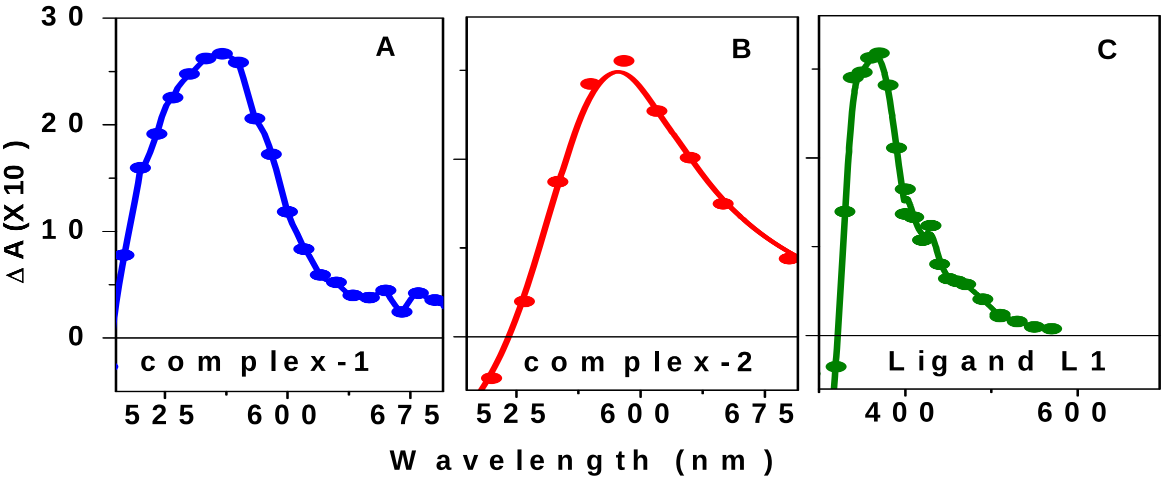

**Figure 4.4**: The transient absorption spectra of oxidized a) complex-**1,** b) complex-**2, c)** Ligand **L1** in aqueous solution. (Y-axis is scaled a.u. for comparison purpose)

Figure 4.5 shows the transient absorption spectrum of complex **-1** and **-2** sensitized $TiO_2$ NPs. Both the TA spectrum comprises a positive absorption band in 525-650 nm region, a broad absorption band in 650-1000nm region, a negative absorption band in <500nm region at 200fs delay time. The TA band in 525-650nm matches well with cation spectrum of respective complexes (Figure-4.4) and hence attributed to complex$^{\bullet+}$ cation. The negative absorption band is assigned to bleach recovery in respective Ru(II)- and Os(II)-complex sensitized TiO$_2$ NPs. Bleach recoveries of complex-**1** and -**2** are observed to be faster in presence of TiO$_2$ NPs than that in absence of TiO$_2$ NPs. A relatively fast bleach recovery corresponds to BET process in which oxidized dye recaptures the injected electron from TiO$_2$ NPs. The broad positive band in 650-1000nm region is observed to be different from ESA (650-950nm) of $^3$MLCT state measured in TA study of complex-**1** and -**2** in acetonitrile (in absence of TiO$_2$ NP, figure-4.2 and -4.3). Earlier, Grätzel and co-workers have reported a broad absorption of TiO$_2$ film in this region ( 700-1000nm) by applying a negative bias (voltage).[4.36] The band gap energy of bulk TiO$_2$ semiconductor material is 3.2eV which results in absorbance cut off above 390 nm. So, the positive absorption band in 700-1000nm region is assigned to a characteristic absorption due to

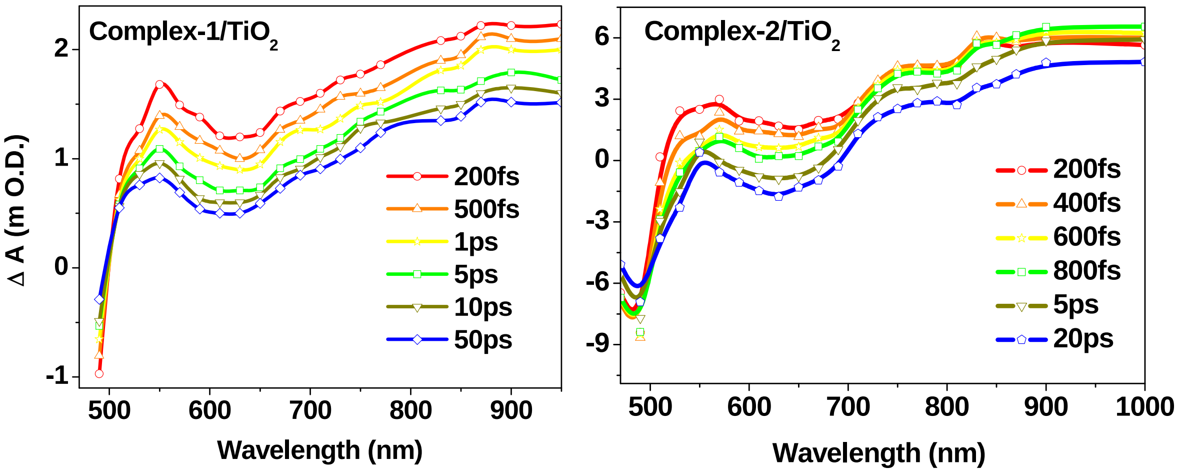

**Figure 4.5:** Left panel : Transient absorption spectra of complex-**1** sensitized TiO$_2$ NPs, Right panel: Transient absorption spectra of complex-**2** sensitized TiO$_2$ NPs at 200 fs, 500 fs, 1 ps, 5 ps, 10 ps, and 50 ps time delays after photoexcitation at 400 nm.

CB electron of $TiO_2$ semiconductor material. Similar, TA band of CB electron ($TiO_2$) has also been reported in other dye/$TiO_2$ systems.[4.16-4.22,4.27-4.29]. In present study, the electron injection dynamics are explored by rise of TA signal in 700-1000nm region whereas BET dynamics are monitored by decay of 1000nm TA kinetics or bleach recovery kinetics at 490nm.

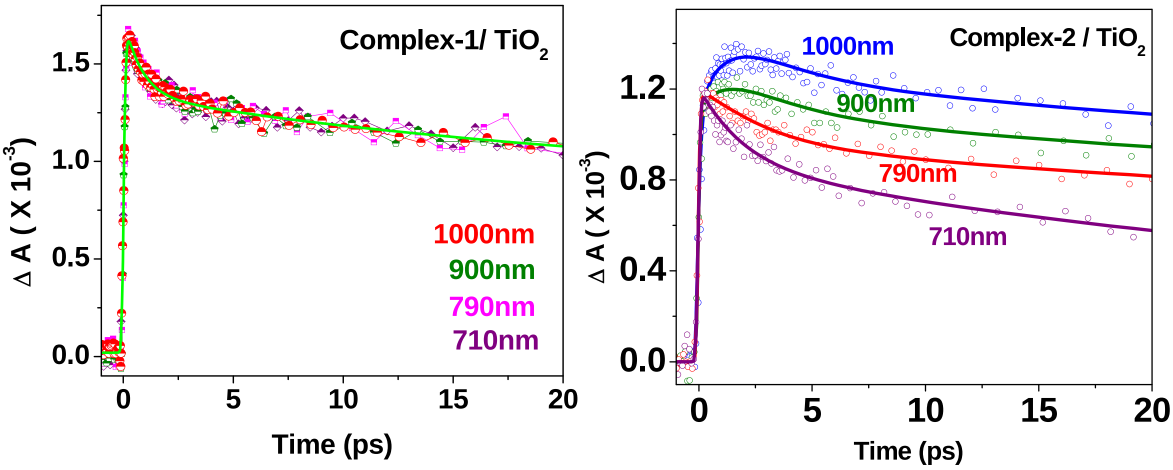

**Figure 4.6**: Left panel: TA kinetics of complex-**1** sensitized $TiO_2$ NP, Right panel: TA kinetics of complex-**2** sensitized $TiO_2$ NP, at 710nm, 790nm, 900nm and 1000nm probe wavelengths.

Figure-4.6 shows the normalized TA kinetics up to 20ps time scale at different monitoring wavelength in 700-1000nm region. In complex-**1**/$TiO_2$ system (figure-4.6; left panel), the electron injection kinetics are observed to be pulse width limited (<100fs) at all the monitoring wavelengths. However, wavelength dependent TA kinetics are observed in complex-**2**/$TiO_2$ system (figure-4.6 (right panel)). The TA kinetics deviates from single exponential growth in blue region (710nm) to bi-exponential growth in red region (1000nm). The Os(II)-complex (-**2**) comprises significant ESA ($^3$MLCT states) in 700-850nm region (figure-4.3) which overlap with

TA band of CB electron ($TiO_2$) in 700-1000nm region. The ESA contribution is minimum at 1000nm. Therefore, the electron injection kinetics is monitored by growth of TA signal at 1000nm which is best fitted bi-exponentially with $\tau_1 < 100$ fs (42%) and $\tau_2 = 1.7$ ps (58%) time constants.

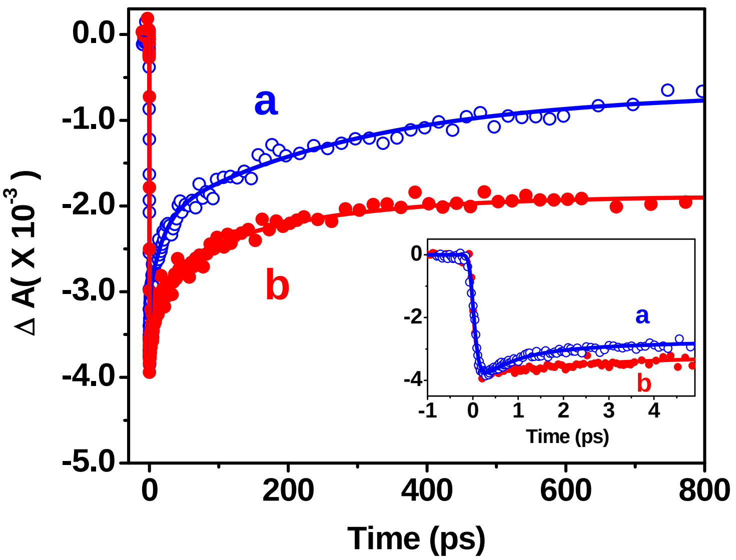

**Figure 4.7:** Bleach recovery kinetics at 490 nm in a) complex-**1**/$TiO_2$ system and b) complex-**2**/$TiO_2$ system. (Inset: bleach recovery in short time scale)

The decay of TA kinetics at 1000nm corresponds to BET process in which CB electron ($TiO_2$) is recaptured by oxidized complex cation radical and regenerates the ground state of dye. However, the wavelength dependent TA kinetics in 700-1000nm restrict unambiguous assignment of BET process. So, the back electron transfer dynamics in two systems are monitored by bleach recovery kinetics at 490nm. Figure 4.7 shows a comparison of bleach recovery dynamics (490nm) in long and short (inset) time scale. The BET kinetics are multi-exponentially fitted with $\tau_1$ = 0.8 ps (29%), $\tau_2$ = 20 ps (21%), $\tau_3$ > 300 ps (50%) in complex-**1**/$TiO_2$ system and $\tau_1$ = 2.0 ps (12%), $\tau_2$ = 35 ps (17%), $\tau_3$ > 300 ps (71%) in complex-**2**/$TiO_2$ NPs.

### 4.3.5 Interfacial electron transfer dynamics:

The interfacial charge separation at dye sensitized $TiO_2$ interface constitutes an important electron transfer step in operating mechanism of DSSC. In DSSC, Ru(II)-bipyridyl dyes have shown record 8-11% light conversion efficiency.[4.3,4.4] For this reason, the IET processes are investigated extensively for Ru(II)-polypyridyl complexes sensitized $TiO_2$ NP's film by using femtosecond transient absorption study in visible and IR region.[ 4.16-4.22,4.27-4.29] Majority of such transient studies have shown that the electron injection initiates from higher FC states (vibrationally "hot") of directly photoexcited $^1$MLCT state in <100fs time scale. However, these studies differ in occurrence of slow electron injection components. For example, Durrant and co-workers have observed bi-exponential <150 fs (50%) and 1.2 ps (50%) electron injection and then in later study, also observed a multiexponential <100 fs (29%), 1.0 ps (25%), and 13 ps (46%) electron injection behavior in carboxylate functionalized RuN3 {$Ru(II)(dcbpy)_2(SCN)_2$} sensitized $TiO_2$ film.[4.19,4.37] Furthermore, Benko *et al* have reported multi-exponential < 100fs (70 %), 1.8ps (0.2 (15%), 10ps ( 1 (3%), and 50ps ( 5 ps (12%) electron injection in RuN3/$TiO_2$ film.[4.18] The multiexponential electron injection is also observed in $Ru(bpy)_2(dcbpy)/TiO_2$ film by Piotrowiak and co-workers.[4.38] McCusker and co-workers have compared the electron injection kinetics in structurally identical Ru(II) and Os(II)-complexes and found multiexponential electron injection in both the systems.[4.33] In these studies, the slower electron injection (1-100ps) was attributed to electron injection from thermalized $^3$MLCT states or to surface heterogeneity arising from $TiO_2$ film preparation. All these studies were conducted with carboxylate functionalized Ru(II)-complexes on mesoporous $TiO_2$ film where surface binding strengths are moderate due to presence of solvent environment. Since, the electron transfer kinetics are function of electronic coupling strength, than the slow electron injection from $^3$MLCT states (1-100ps) could be arising from moderate electronic coupling which allows $^1$MLCT→$^3$MLCT ISC parallel to electron injection processes. In strongly coupled dye/$TiO_2$ system, the electron injection kinetics may outcompetes $^1$MLCT→$^3$MLCT ISC process. Earlier, Willig and co-workers have indicated role of strong electronic coupling in single exponential electron injection in RuN3/$TiO_2$ film under ultra-high vacuum.[21] This is confirmed by IET studies using catechol functionalized Ru-complexes such as $Ru(bpy)_2$(bp-CH=CH-catechol) and $Ru(bpy)(SCN)_2$(bp-CH=CH-catechol) on $TiO_2$ NPs which have shown ultrafast (<100fs) and single exponential (100%) electron injection process in solution and film phase.[4.22,4.23] In these studies, catecholate assisted strong electronic coupling facilitates the electron injection entirely from $^1$MLCT state or unthermalized MLCT states of Ru(II)-complexes. However, in Os(II)-complexes, the large spin orbit coupling results a more efficient ISC process than Ru(II)-complexes which may competes with ultrafast electron injection process. The heavy atom effects on IET reactions are explored by comparison of electron injection and BET kinetics in Ru(II)- and Os(II)- complex sensitized $TiO_2$ systems.

Figure 4.8 shows a comparison of electron injection kinetics in Ru(II)- and Os(II)-complexes (-**1** and -**2**) sensitized $TiO_2$ NPs by monitored TA at 1000nm. The electron injection accomplishes in pulse width limited time (<100fs) in Ru(II)-complex (-**1)** /$TiO_2$ system whereas it proceeds bi-exponentially in Os(II)-complex (-**2**)/$TiO_2$ system. In Ru(II)-complex (-1)/$TiO_2$ system, the catechol assisted strong electronic coupling facilitates electron transfer much before $^1$MLCT → $^3$MLCT crossover can occur. So, the single exponential ultrafast electron injection

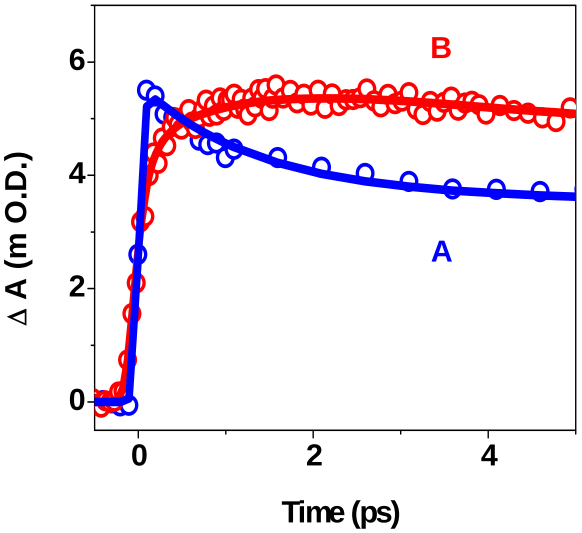

**Figure 4.8**. TA kinetic traces of conduction band electron monitored at 1000 nm in A) -**1**/TiO$_2$ and B) -**2**/TiO$_2$ systems after excitation at 400 nm.

corresponds to unthermalized $^1$MLCT states. However, large spin-orbit coupling matrix of Os(II)-complexes, conduces the ISC in ultrafast time scale. Therefore, the electron injection from unthermalized $^1$MLCT competes with rapid ISC to $^3$MLCT states in Os(II)-complex (-**2**)/TiO$_2$ system. As a result, the bi-exponential <100fs (42%) and 1.7ps (58%) electron injection kinetics is observed and attributed to unthermalized $^1$MLCT and thermalized $^3$MLCT states.

The electron injection pathways in two systems are shown in scheme-4.2. In scheme-4.2, the ground state energy level resembles to oxidation potential of Ru(II)- and Os(II)- complex (-**1** and -**2**) determined in cyclic voltammetry. The excited state $^1$MLCT and $^3$MLCT energetics are calculated from corresponding MLCT absorption band edges. The ES energetics (MLCT) and surface binding strength (catechol) are very similar, still electron injection kinetics are apparently different in two systems. In heavier metal Os(II)-complex, an efficient ISC redistribute ES populations in $^1$MLCT and $^3$MLCT states before the electron injection accomplishes in ultrafast

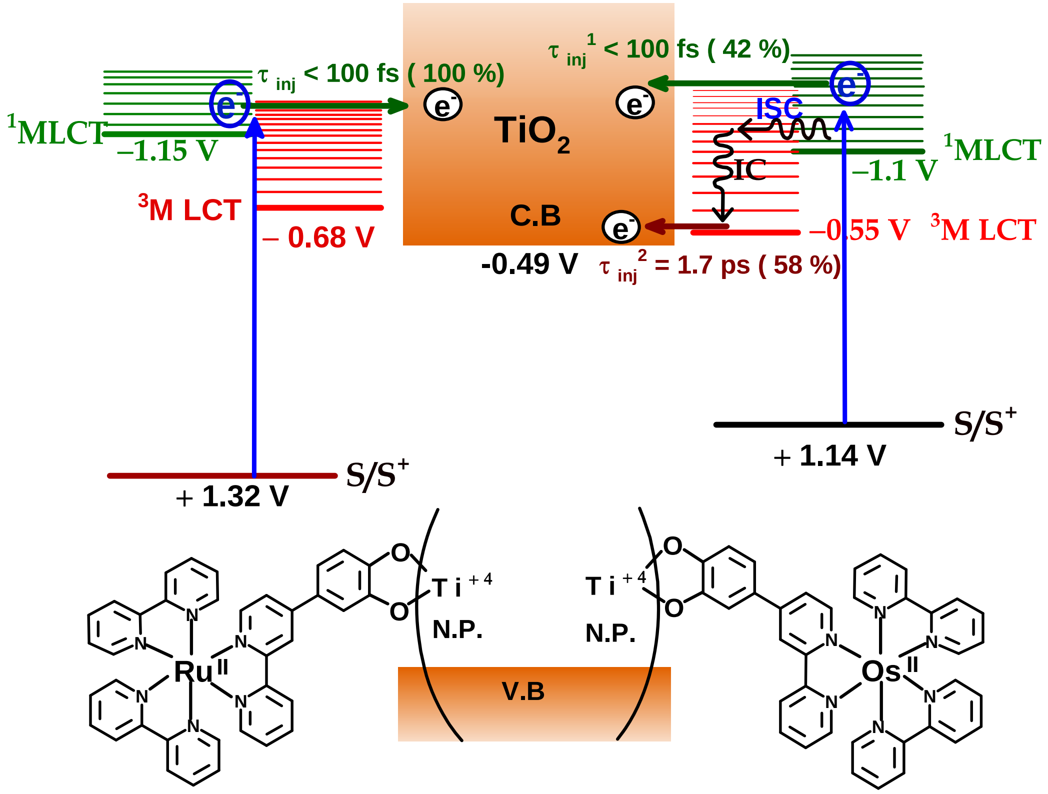

**Scheme 4.2**: Mechanistic scheme showing three-level model which consists of the ground state ($S_o$), excited triplet state ($^3$MLCT) and excited singlet ($^1$MLCT) state of complexes -**1** and -**2** adsorbed on TiO$_2$ NP.

time. The electron injection from unthermalized $^1$MLCT and thermalized $^3$MLCT states occur in <100fs and ~1.7ps time scale (scheme-4.2). Furthermore, the BET dynamics also observed to be slower in Os(II)-complex (-**2**)/TiO$_2$ system as compared to Ru(II)-complex (-**1**)/TiO$_2$ system (see figure 4.7). Os(II) is strong π-donor than Os(III) and Ru(III) is strong π-acceptor than Ru(II).[4.39,4.40] Therefore, long lived charge separation in complex-**2**/TiO$_2$ NPs system is attributed to intrinsic stability of Os(III) ion than Ru(III) ion in presence of π-acceptor bpy ligand.

## 4.4. Conclusion:

The interfacial electron transfer mechanism is established in Ru(II)- and Os(II)-complex sensitized $TiO_2$ NPs by using femtosecond transient absorption spectrometer. The catechol functionality is used for its strong binding on $TiO_2$ surface. The spectral sensitization is confirmed by steady state absorption studies. The optical absorption studies show that the $^1$MLCT absorption band of Ru(II)-complex (-**1**) and $^1$MLCT-$^3$MLCT absorption bands of Os(II)-complex (-**2**) efficiently sensitize the $TiO_2$ NPs in 400-550nm and 400-750nm regions, respectively. The IET is studied by exciting the sensitized $TiO_2$ NPs samples at 400nm which selectively populates $^1$MLCT energy surface at higher Frank-Condon states of both the complexes. The transient produced in IET reactions are identified through their characteristic absorption *viz.* conduction band electron in 850-1000nm region, complex cation radical in 550-650nm region and ground state bleach in 470-500nm region. The transient absorption kinetics at 1000nm reveal an ultrafast (<100fs, pulse width limited) single exponential electron injection in $Ru^{II}(bpy)_2$(bp-catechol)/$TiO_2$ system. The ultrafast electron injection is attributed to strong electronic coupling on $TiO_2$ interface which facilitates electron transfer from unthermalized $^1$MLCT states. The TA kinetics of $Os^{II}(bpy)_2$(bp-catehol)/$TiO_2$ system has revealed a bi-exponential <100fs (42%), 1.7ps (58%) electron injection process. In Os(II)-complexes, the large spin-orbit coupling conduces an efficient intersystem crossing which populates $^3$MLCT state simultaneous to electron transfer from unthermalized $^1$MLCT states. Thus, electron transfers from unthermalized $^1$MLCT states and thermalized $^3$MLCT state results bi-exponential electron injection kinetics. Back electron transfer dynamics are monitored by bleach recovery dynamics at 490nm. Bleach recovery kinetics revealed a slower back electron dynamics in $Os^{II}(bpy)_2$(bp-catehol)/$TiO_2$ system as compared to $Ru^{II}(bpy)_2$(bp-catehol)/$TiO_2$ system. This study suggest that

Os(II)-complexes can be better sensitizer due to their broad optical absorption band and slow back electron dynamics in comparison to analogous Ru(II)-complexes.

## 4.5 References:

[4.1] B. O'Regan, M. Grätzel, Nature, 1991, 353, 737.

[4.2] S. Ardo, G. J. Meyer. Chem. Soc. Rev., 2009, 38, 115.

[4.3] A. Hagfeldt, G. Boschloo, L. Sun, L. Kloo, H. Pettersson, Chem. Rev. 2010, 110, 6595.

[4.4] A. Hagfeldt, M. Gratzel, Chem. ReV. 1995, 95, 49.

[4.5] B. A. Gregg, Coord. Chem. Rev., 2004, 248, 1215.

[4.6] A. Listorti, B.O'Regan, J. R Durrant, Chem. Mater, 2011, .

[4.7] S. A. Haque, E. Palomares, B. M. Cho, A. N. M. Green, N. Hirata, D. R. Klug, J. R. Durrant, J. Am. Chem. Soc. 2005, 127, 3456.

[4.8] J. R. Durrant, S. A. Haque, E. Palomares, Coord. Chem. Rev., 2004, 248, 1247.

[4.9] G. Ramakrishna, H. N. Ghosh, A. K. Singh, D. K. Palit, J. P. Mittal, J. Phys. Chem. B 2001, 105, 12786.

[4.10] B. C. O'Regan, J. R. Durrant, Acc. Chem. Res. 2009, 42, 1799.

[4.11] G. J. Meyer, Inorg. Chem. 2005, 44, 6852.

[4.12] M. K. Nazeeruddin, A. Kay, I. Rodicio, R. Humphry-Baker, E. Mueller, P. Liska, N. Vlachopoulos, M. Graetzel, J. Am. Chem. Soc., 1993, *115* , pp 6382.

[4.13] K. Kalyansundaram, Coord. Chem. Rev., 1982, 46, 159.

[4.14] M. Grätzel, Inorg. Chem. 2005, 44, 6841.

[4.15] Photochemistry and Photophysics of Coordination Compounds II, Editors: V. Balzani, S. Campagna, Springer, Topics in Current Chemistry Series, Volume 281, 2007, 101.

[4.16] N. A. Anderson, T. Lian, Annu. Rev. Phys. Chem. 2005. 56, 491.

[4.17] N. A. Anderson, T. Lian, Coord. Chem. Rev. 2004, 248, 1231.

[4.18] G. Benkö, J. Kallioinen, J. E. I. Korppi-Tommola, A. P. Yartsev, V. Sundström, J. AM. Chem. Soc. 2002, 124, 489.

[4.19] Y. Tachibana, J. E. Moser, M. Gra1tzel, D. R. Klug, J. R. Durrant, J. Phys. Chem. 1996, 100, 20056.

[4.20] J. Kallioinen, V. Lehtovuori, P. Myllyperkiö, J. E. Korppi-Tommola, Chem. Phys. Lett. 2001, *340*, 217.

[4.21] T. Hannappel, B. Burfeindt, W. Storck, F.Willig, J. Phys. Chem.B 1997, *101*, 6799.

[4.22] G. Ramakrishna, D. A. Jose, D. KrishnaKumar, A. Das, D. K. Palit, H. N. Ghosh, J. Phys. Chem. B 2005, 109, 15445.

[4.23] P. Kar, S. Verma, A. Das, H. N. Ghosh, J. Phys. Chem. C, 2009, 113, 7970.

[4.24] D. Lee, D. Omolade, R. E. Cohen, M. F. Rubner, Chem. Mater. 2007, 19, 1427.

[4.25] C. Creutz, M. H. Chou, Inorg. Chem. 2008, 47, 3509.

[4.26] David R. Lide, ed., CRC Handbook of Chemistry and Physics, 89th Edition (Internet Version 2009), CRC Press/Taylor and Francis, Boca Raton, FL.

[4.27] H. N. Ghosh, J. Phys. Chem. B 1999, 103, 10382.

[4.28] J. Z Zhang, Acc. Chem. Res. 1997, 30, 423.

[4.29] D. P. Colombo, Jr., R. M. Bowman, J. Phys. Chem. 1996, 100, 18445.

[4.30] B.P. Sullivan, D.J. Salmon, T.J. Meyer, Inorg. Chem. 1978, 17, 3334.

[4.31] S. Verma, P. Kar, A. Das, D. K. Palit, H. N. Ghosh, J. Phys. Chem. C 2008, 112, 2918.

[4.32] E. M. Kober, J. V. Caspar, B. P. Sullivan, T. J Meyer, Inorg. Chem. 1988, 27, 4587.

[4.33] D. Kuciauskas, J. E. Monat, R. Villahermosa, H. B. Gray, N. S. Lewis, J. K. McCusker, J. Phys. Chem. B 2002, 106, 9347.

[4.34] N. H. Damrauer, G. Cerullo, A. Yeh, T. R. Boussie, C. V. Shank, J. K. McCusker, Science, 1997, 275, 54.

[4.35] A. C. Bhasikuttan, M. Suzuki, S. Nakashima, T. Okada, J. Am. Chem. Soc. 2002, 124, 8398.

[4.36] G. Rothenberger, D. Fitzmaurice, M. Grätzel, J. Phys. Chem., 1992, 96, 5983.

[4.37] Y. Tachibana, S. A. Haque, I. P. Mercer, J. R. Durrant, D. R. Klug, J. Phys. Chem. B 2000, 104, 1198.

[4.38] T. D. M. Bell, C. Pagba, M. Myahkostupov, J. Hofkens, P. Piotrowiak, J. Phys. Chem. B 2006, 110, 25314.

[4.39] W. Kaim, V. Kasack, Inorg. Chem. 1990, 29, 4696.

[4.40] B. Sarkar, W. Kaim, A. Klein, B. Schwederski, J. Fiedler, C. Duboc-Toia, G. K. Lahiri, Inorg. Chem. 2003, 42, 6172.

# CHAPTER 5:

# HOLE STABILIZATION BY LIGAND LOCALIZED CHARGE TRANSFER STATES IN Ru(II)–POLYPYRIDYL COMPLEX SENSITIZED TiO$_2$ NP FILM: AN ELECTRON DONOR ANTENNA EFFECT.

## 5.1 Introduction:

Ruthenium(II)-polypyridine complexes have been used extensively in dye sensitized solar cell (DSSC) for their rich optoelectronic and redox properties.[5.1] The quest of higher conversion efficiency than Grätzel's DSSC (10.4%) [5.2], has led to design of numerous Ru(II)-complexes with attractive spectral and redox properties. The photophyiscal studies of these complexes have drwan an appropriate structure-function correlation in fine tuning of "metal-to-ligand charge-transfer (MLCT) state" energy levels. [5.3-5.5] The electron donor and electron acceptor groups substituted diimine ligands have shown a new class of excited states- "ligand localized charge transfer (LCT)" states.[5.6,5.7] Thus, the optical response is significantly modified by new "intra-ligand charge-transfer (ILCT)" or "ligand-to-ligand charge-transfer (LLCT)" transitions in addition to aboriginal MLCT transitions.[5.8,5.9] By varying the chemical nature of ancillary ligands, it has become possible to decrease the energy of LCT states than MLCT states. The photophysical internal conversion (IC) from MLCT to LCT states lead to higher degree of intramolecular charge separation in which positive and negative charge localize on electron -donor and -acceptor groups. A direct photo-excitation in LCT band offers a diffusionless intramolecular charge separation which can be very useful in DSSC[5.10-5.15] photocatalysis, electrochemiluminescence etc.[5.16]

In DSSC, the interfacial charge separation is result of an ultrafast electron injection from photoexcited dye to $TiO_2$ conduction band and a slow back electron transfer (BET) process.[5.17] The presence of electron donor groups can stabilize the oxidized dye cation which increase long lived charge separation at dye/$TiO_2$ interface. Earlier, Durrant, Nazeerudin and co-workers[5.18] have observed an improved interfacial charge separation by using aromatic amine substituted Ru(II)-complexes. Chen *et al*[5.19, 5.20] have shown higher light-to-electricity conversion efficiency than Grätzel's DSSC by using carbazole substituted thiophene-moieties in bipyridine ligand. In such systems, the electron donor group has helped in cation (hole) transfer away from $TiO_2$ surface. The desired action can be established in diffusionless process by LCT states. So, it is important to understand the interfacial electron transfer (IET) pathways in such systems where charge separation/recombination can be controlled by changing the electron donor ability of ancillary bipyridyl ligands.

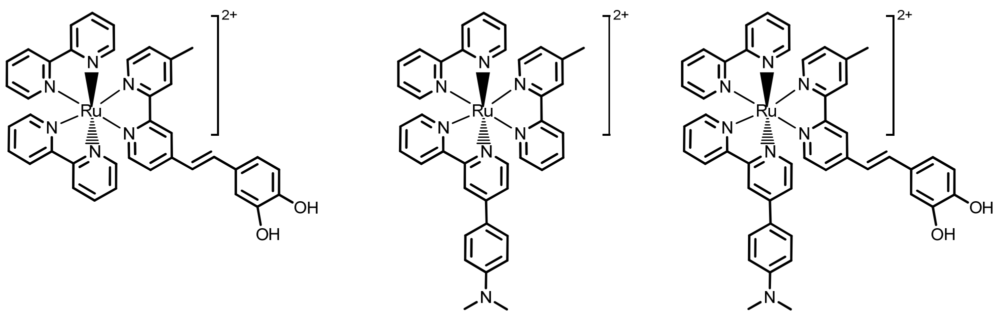

**Complex-1** **Complex-2** **Complex-3**

**Scheme 5.1a**: Structure of complex-**1,** complex-**2** and complex-**3**

Scheme-5.1a shows newly synthesized Ru(II)-complexes -**1**, -**2** and -**3** which vary in chemical nature of the ancillary ligands. The N,N'-dimethylamniophenyl moiety of **L2** ligand and the catechol moiety (also its extended π-conjugation) of **L1** ligand act as electron donor and electron acceptor groups. Earlier, Zhang and co-workers [5.21] have reported ILCT states in dimethylamino-α-styryl substituted $Ru^{II}$- diimine complex which is structurally related to complex-**2**. Further, Chou, Chi and co-workers [5.22] have reported LLCT states in $Ru^{II}$ complex which comprises a tridentate 5-(2,2'-bipirydin-6-yl)-3-(trifluoromethyl)-1H-pyrazole ligand. So, the presence of electron donor (**L2**) and acceptor ligands (**L1**) can enable the LLCT states in complex-**3**.[5.23, 5.24] In present chapter, the LCT states are explored by comparing the photophysical properties *viz.* steady state absorption, photoluminescence (PL) and transient emisison of complexes -**1** , -**2** and -**3**. The photophysical properties of LCT state are described in part-5A of this chapter.

Complexes -**1** and -**3** comprises catechol moieties that can bind strongly on $TiO_2$ surface. The catechol assisted strong electronic coupling facilitates an efficient electron injection from unthermalized $^1$MLCT states but renders a fast back electron transfer dynamics in Ru(II)-complex/$TiO_2$ system, as described in chapter-4. In this chapter, the effects of LLCT states on IET are explored by femtosceond transient absorption studies of complexes -**1** and -**3** sensitized $TiO_2$ film which are presented in part-5B of this chapter-5.

## 5.2 Materials:

4-(N,N'-Dimethylamino-phenyl)-propanal (A) and Pyridacyl pyridinium iodide salt (B) and 4-(2,2'Bipyridinyl-4-yl)vinyl-benzene-1,2-diol (**L1**), Complexes -**1** and -**1**.$Me_2$ were synthesized by following previously reported procedure.[5.25, 5.26]

### 5.2.1 Synthesis of Complexes -2 and -3:

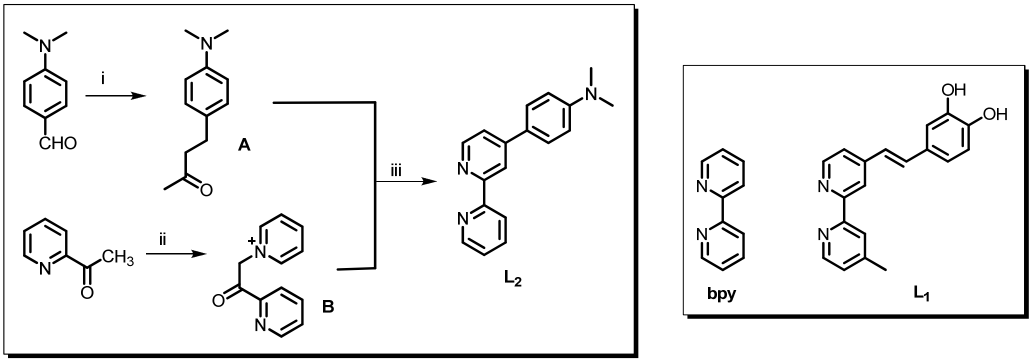

**Scheme 5.2:** Synthetic methodology adopted for the synthesis of **L2** and molecular structures of the different ligands.

**(i) 4-(N,N-Dimethylamino-phenyl)-propanal (A**) : 4-N,N-dimethylamino benzaldehyde(16.6 g) and acetaldehyde (5.6 ml) was dissolved in 40 ml of ethanol (95 %). The mixture was cooled to 0 ºC and to this 36 ml of 28 % NaOH solution was added slowly; while the solution was stirred vigorously and temperature of the reaction mixture was maintained under 10 ºC (15 minutes). After stirring further for 30 minutes at room temperature, 200 ml of water was added and the desired compound was extracted thrice with 50 ml of ether. Then ether layers were collected and washed twice with 50 ml of brine solution before drying and then dried over anhydrous $MgSO_4$. Evaporation of ether followed by distillation at reduced pressure gave the product as highly viscous yellow oil. This compound was further used for the next step without any purification. **(ii)** Pyridacyl pyridinium iodide salt (**B**) was synthesized following the literature procedure.[5.27]

**(iii) Synthesis of 4-(N,N-Dimethylamino-phenyl)-(2,2'-bipyridine)**: Pyridacyl pyridinium iodide salt (**B**) (5.2 g, 0.015 mol) was dissolved in 50 ml glacial acetic acid in a 250 ml R.B flask. To this solution ammonium acetate (12.0 g, 0.13 mol) was added and stirred at 100 ºC. Further, 3.0 g (0.015 mol) of 4-(N,N-dimethylamino-phenyl)-propanal (**A**) was added to this in three interval of 1.5 h at 100 ºC and was kept at that temperature with stirring for 16 h. Then the reaction mixture was allowed to cool to room temperature and acetic acid was evaporated completely under vacuum. To this about 50 ml of water was added. pH of this solution was adjusted to ~ 8.0 and then the desired compound was extracted with chloroform. Chloroform layer was dried over anhydrous $MgSO_4$ and evaporated to get the **L2** in crude form. This was purified by gravity chromatography using silica as stationary phase and methanol-chloroform (5:95; v/v) as eluent. Yield: 0.80 g (18%). ES-MS; ($M^+$): 275 (100% ); $^1$H NMR ( $CD_3OD$; ppm ): δ 8.71-8.63 (m, 1H, $H_{pyridyl}$), 8.42 (d, *J = 8.0 Hz*, 1H, $H_{pyridyl}$), 7.72 (d, *J = 8 Hz*, 4H, $H_{pyridyl}$), 7.27 (d, *J = 8 Hz*, 1H, $H_{pyridyl}$), 7.33-7.26 (m, 1H, 1$H_{pyridyl,}$), 6.91 (d, *J = 8 Hz*, 1H, $H_{phenyl}$), 6.85 (d, *J = 8 Hz*, 2H, $H_{phenyl}$), 3.06 (s, 6$H_{methyl}$). IR (KBr pellet, cm-1): 1604 (C=C, C=N).

**(iii) Synthesis of Complex-2**. To 50 ml Ethanol, 80 mg (0.154 m mol) of Ru(bpy)$_2$C**L2**. 2$H_2O$ and 42 mg (0.154 m mol) of 4-(N,N-dimethylamino)-2,2'-bipy was added. This reaction mixture was heated to reflux for 8 h. To this aqueous solution of excess $KPF_6$ was added and stirred for few minutes. Then ethanol was removed under reduced pressure and the orange solid suspended in water was obtained. This resulting orange solid was then filtered and washed with cold water and ether. Purification on alumina as stationary phase and acetonitrile as eluent afforded the desired complex as a dark orange solid. Yield: 30 %; MS (ESI-MS) m/z: 834 ($M^+$ - $PF_6$); $^1$H NMR ($CD_3CN$, ppm): δ 8.66 (2H, d, *J = 7 Hz*, 2$H_{\mathbf{L2}}$ 5,6 ); 8.51 (5H, d, *J = 8.2*, $H_{bpy\ 3,3',}$ $H_{L3'}$); 8.09-8.01 (6H, m, $H_{bpy\ 6,6',}$ $H_{\mathbf{L2}\ 6,6'}$); 7.79-7.72 (7H, m, $H_{bpy\ 4,4'}$, $H_{phenyl}$, $H_{\mathbf{L2}}$); 7.42-7.36 (5H, m, $H_{bpy\ 5,5'}$,$H_{\mathbf{L2}\ 5'}$); 6.85 (2H, d, *J = 9 Hz*, , $H_{Phenyl}$); 3.04 (6H, s, $H_{\mathbf{L2}CH3}$); IR(KBr pellete, cm$^{-1}$): 847 (-$PF_6$). Calculated for $RuC_{38}H_{33}N_7P_2F_{12}$: C 46.63, H 3.40, N 10.02; Found: C 46.5; H 3.38; N 9.98. C, 46.8; H, 3.44; N, 9.93.

**(iv) Synthesis of Complex-3**. To 30 ml DMF, 75 mg (0.282 m mol) of $RuCl_3.3H_2O$ and 45 mg(0.282 m mol) of 2,2'-bipy was added. After stirring in the dark for 2 h at 90 ºC and maintaining an Ar atmosphere, 85 mg (0.282 mmol) of 4-[2-(4'-methyl-2,2'-bipyridinyl-4-yl)vinyl]benzene-1,2-diol (**L1**) was added at 120 ºC and stirred for 4 h. 77.5 mg (0.282 mmol) of 4-(2,2'-bipyridin-4-yl)-N,N-dimethylaniline (**L2**) was added to this reaction mixture and was heated to 145 ºC for 4 h more. After evaporation of DMF under reduced pressure, aqueous solution of excess $KPF_6$ was added and sonicated for 5 minutes. An orange solid was precipitated and collected by filtration after repeated washing with cold with water and ether. Purification on alumina as stationary phase and acetonitrile as eluent afforded the desired complex as a dark orange solid. Yield: 30 %; Calculated for $RuC_{47}H_{41}N_7O_2P_2F_{12}$: C 50.6, H 3.67, N 8.7; Found: C 51.0, H 3.7, N 8.51; MS (ESI-MS) m/z: 837 (M-2$PF_6$); $^1$H NMR ($CD_3CN$, ppm): δ 9.68 (H, s, $H_{3L3}$); 8.65 (2H, d, J = 7 Hz, $2H_{bpy\ 6,6'}$); 8.49 (3H, d, J = 8.2, $H_{\mathbf{L2}\ 3',6'}$, $H_{\mathbf{L2}\ 3'}$); 8.05 (4H, t, J = 7.4 Hz, $H_{\mathbf{L2}\ 4'5}$, $H_{bpy\ 4,4'}$); 7.81-7.66 (9H, m, $H_{bpy\ 5,5'}$, $H_{ethenyl}$, $H_{\mathbf{L1}\ 5'}$, $H_{\mathbf{L2}6}$), $H_{phenyl\ 5,6}$, $H_{\mathbf{L2}\ 3,5}$); 7.55 (2H, s, $H_{\mathbf{L1}\ 3}$), 7.29-7.23 (4H, m, $H_{bpy\ 3,3'}$), $H_{\mathbf{L2}\ 5',6'}$); 6.85 (2H, d, J = 9 Hz, $H_{\mathbf{L2}\ 2,6}$); 6.76 (3H, d, J = 9 Hz, , $H_{ethenyl}$, $H_{\mathbf{L1}\ 5}$, $H_{\mathbf{L2}\ 6}$); 3.04 (6H, s, $H_{\mathbf{L2}\ CH3}$); 3.03 ( 3H, s, $H_{\mathbf{L1}\ CH3}$); IR(KBr pellete, cm-1): 3435 (-OH), 847 (-$PF_6$). $E_{1/2}$ (in $CH_3CN$): 1.24 ($Ru^{2+}/Ru^{3+}$); -0.82 (**L1**/**L1**$^{-}$) *vs* Ag/AgCl.

### 5.3 Results & Discussion:

**5.3.1 Cyclic voltammetry**: Electrochemical studies revealed that $Ru^{II/III}$ redox potential (with respect to Ag/AgCl) for complexes **-1, -2** and **-3** are +1.32 V, +1.25 V and +1.24 V, respectively and this difference in $Ru^{II/III}$ redox potential is reflected in the observed red shift of the MLCT band for complex **-3** as compared to the its hoteroleptic complex **-1**.

## Part 5A: Photophysical Study of Ligand Localized Excited State in Ru(II)-Polypyridyl Complexes: A Combined Effect of Electron Donor-Acceptor Ligand

### 5.3.2 Steady state absorption and emission spectra of L1 and L2 ligands (unbound):

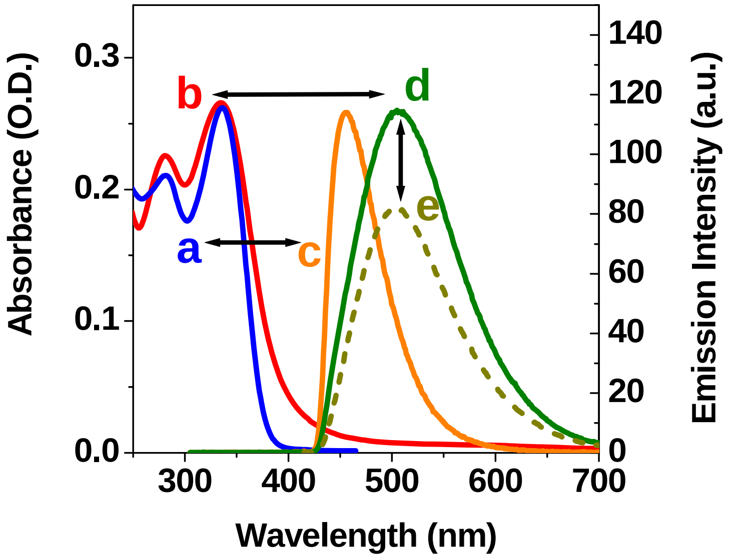

**Figure 5.1**: Steady state absorbance spectra of (a) **L1** ligand and (b) **L2** ligand. Emission spectra of (c) **L1** ligand, (d) **L2** ligand with 300nm excitation (bold lines) and (e) **L2** ligand with 400nm excitation (short dash line) in neutral condition in acetonitrile solvent.

Figure-5.1 show steady state absorption and PL spectra of unbound (free) **L1** and **L2** ligands in acetonitrile solvent. Electronic spectra of **L1** (Figure 5.1a) shows a prominent π-π* transition at 336nm, along with some n-π* transition at even shorter wavelength. The absorption spectra of **L2** (Figure 5.1b) reveals that the tail of the absorption band (maxima at 336nm) extends beyond 500nm. The weaker absorption that extends beyond 500nm can be assigned to intra-ligand charge transfer (ILCT) transitions. This is further supported by red shift (~50nm) in emission maxima ($\lambda_{em}$ 455nm) of **L2** ligand ($\lambda_{ex}$ 300 and 400nm) than **L1** ligand ($\lambda_{em}^{max}$ 505nm). The absorption and PL spectra of **L2** ligand reveal low energy intramolecular CT state as compared to π-π* locally excited (LE) state.

### 5.3.3 Steady state absorption spectra of complexes -1, -2 and -3.

Figure 5.2 shows the optical absorption spectra of complexes -**1**, -**2** and -**3** in acetonitrile solvent. Complex-**1** exhibits two broad absorption bands in 325-375nm and 375-550nm regions which are assigned to π-π* LE and $d\pi_{Ru(II)} \rightarrow \pi^*_{L1/bpy}$-based MLCT transitions, respectively.[5.29, 5.30] No appreciable change is observed in electronic spectra for complex-**1** after addition of $HNO_3$ acid into acetonitrile solvent.

The broader absorption band of complex-**2** (Figure 5.2b) as compared to that of complex-**1** in longer wavelength region ($\lambda$ >350nm) represents an overlapped MLCT and ILCT electronic transitions. Earlier, Zhang and co-workers [5.21] have reported similar ILCT electronic transitions in -$NMe_2$ group substituted Ru(II)-polypyridyl complex. The presence of ILCT state in complex-**2** is supported by decrease in optical density (Figure 5.1b') after addition of $HNO_3$ acid in acetonitrile solvent. In presence of $HNO_3$, the ILCT transitions are expected to be eliminated with the protonation of the $–N_{NMe2}$-centre ($–NH^+_{NMe2}$ formation) and is perhaps reflected in decrease in the absorbance in 350-410nm region. On the contrary, the protonation of the $–N_{NMe2}$-centre ($–NH^+_{NMe2}$ formation) is also expected to lower the **L2**-based LUMO energy level and thus with the narrower HOMO-LUMO gap, the $d\pi_{Ru(II)} \rightarrow \pi^*_{L2/bpy}$-based MLCT transition is expected to shift to the longer wavelengths. Thus, the observed absorption spectra (Figure 5.1b') in 410-600nm region (protonated complex-**2**) is result of two opposing influences

The spectral change in 350-400nm region and slight decrease in overall optical density (350-550nm region) after protonation shows the presence of ILCT electronic transitions in complex-**2**.

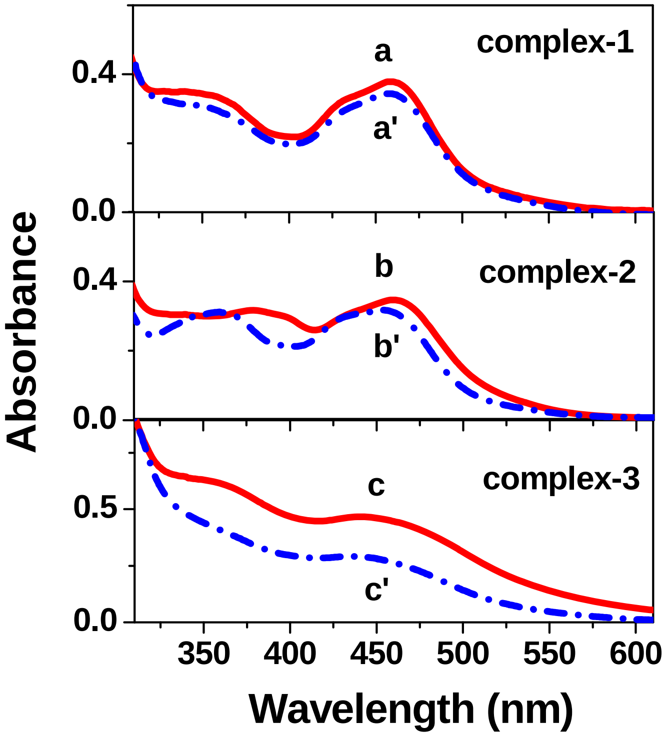

]**Figure 5.2**: Optical absorbance spectra of (a) complex-**1**, (b) complex-**2** and (c) complex-**3** in neutral (bold lines) and (a') complex-**1**, (b') complex-**2** and (c') complex-**3** in acidic (dash-dot lines) condition in acetonitrile solvent (concentration of all complexes were kept same).

Complex-**3** exhibits a broad absorption spectrum (figure 5.1c) in 350-50nm region. NMe$_2$ functionality in **L2** ligand and the extended π-conjugation of catechol functionality in **L1** ligand are expected to favour LLCT transitions in complex-**3**. The presence of MLCT and LLCT transitions broaden the absorption spectrum in longer wavelength region. Earlier, Chi and Chou and their co-workers [5.23, 5.24] have also reported LLCT transitions in Os(II)-polypyridyl complexes comprising electron donor and acceptor ligands. In complex-**3**, HOMO-LUMO energy gap for this $\pi_{\mathbf{L2}}$(HOMO) → $\pi^*_{\mathbf{L1}}$-based transition is expected to be narrower than that one would expect for $\pi_{\mathbf{L2}}$ (HOMO) → $\pi^*_{\mathrm{bpy}}$-based transition in complex-**2** and accounts for the longer wavelength absorbance with tail extending to ~ 575 nm (Figure 5.1c). The absorption spectrum decreases and blue shifted after addition of $HNO_3$ acid in acetonitrile solvent (figure 5.1c'). The protonation of -$NMe_2$ group suppress the electron donor character of **L2** ligand which inhibits interligand electron transfer processes, a condition essential for LLCT excited state.[5.31] Thus, the significant decrease in the absorption band on protonation of complex-**3** indicates strong contribution of LLCT electronic transition in neutral complex-**3**.

### 5.3.4 Steady state PL spectroscopy of complexes -1, -2 and -3:

The PL of Ru(II)-polypyridyl complexes originates from $^3$MLCT states which are populated by an ultrafast $^1$MLCT →$^3$MLCT intersystem crossing (ISC). [5.32-5.35] Figure 5.3 shows the PL spectrum of complex -**1**, -**2** and -**3** in acetonitrile solvent. Complex -**1** shows PL peak at 621nm which is assigned to the $^3$MLCT → $S_0$ transition. The PL quantum yield (QY) of the complex-**1** is observed to be 0.023 ($\phi_1$) by using $Ru^{II}(bpy)_3(PF_6)_2$ as reference ($\phi$ = 0.062 at $\lambda_{max}^{emission}$ = 611 nm).[5.1, 5.36] The PL-QY increases increases two times in complex -**1Me$_2$** ($Ru^{II}(bpy)_2$(bp-CH=CH-ph(OMe)$_2$)) where –OH group is replaced with –OMe group in **Me$_2$L1** ligand. Thus, the low PL-QY of complex-**1** is attributed to non-radiative decay through H-bonding network of catechol moiety.[2.29]

Complex-**2** exhibits PL maxima at 623nm and the PL-QY is measured to be 0.016 ($\phi_2$). The lower PL-QY of complex-**2** than complex-**1** can be due to internal conversion of $^3$MLCT states to low emissive $^3$LLCT states. The $^3$LLCT states are less emissive due to absence of heavy atom spin density. [5.37, 5.38] The PL-QY of complex-**2** further reduces ~2.9 times after addition of HNO$_3$ acid in to acetonitrile solvent (figure 5.3b'). However, the PL-QY of complex-**1** remains same under acidic solvent environment (figure 5.3a'). Thus, the drastic reduction of PL-QY is possibly due to increase in non-radiative decay on protonation of NMe$_2$ group of **L2** ligand. This suggests a weak ILCT character in complex-**2**.

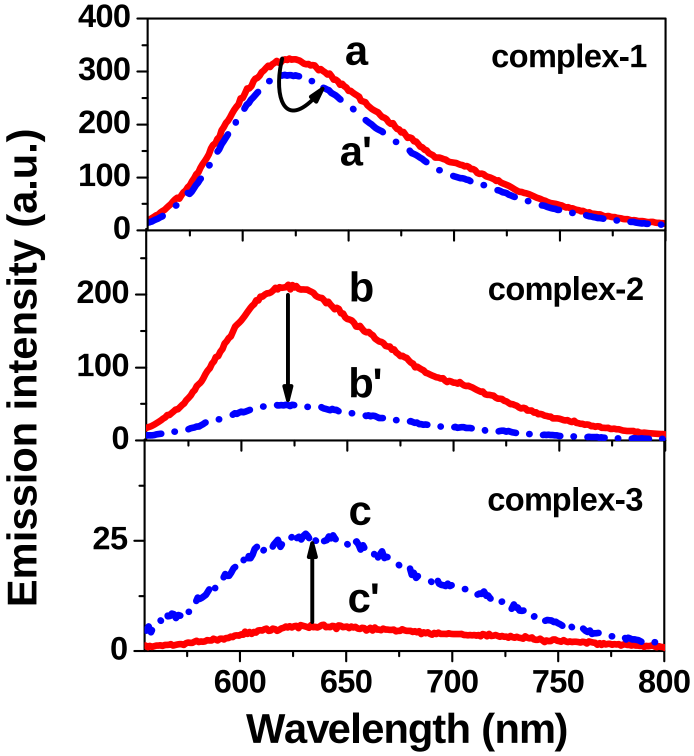

**Figure 5.3:** PL spectra of (a) complex-**1**, (b) complex-**2** and (c) complex-**3** in neutral (bold lines) and (a') complex-**1**, (b') complex-**2** and (c') complex-**3** in acidic (dash-dot lines) condition in acetonitrile solvent (All PL spectrum are recorded in aerated acetonitrile solvent and normalized with respect to same optical density at excitation wavelength).

Figure 5.3c show red shifted PL maxima at 640 nm of complex-**3** than that of complex -**1** and -**2** (figure- 5.3a and -5.3b). The PL-QY of complex-**3** is observed to be extremely low ~ 0.0006 ($\phi_3$) as compared to that of complex-**1** ($\phi_1$ = 0.023) and complex-**2** ($\phi_2$ = 0.016). The extremely low PL-QY cannot be explained alone by non-radiative decay channel caused by H-bonding network of catechol moiety as observed in complex-**1** or $^3$ILCT state as observed in complex-**2**. This can be attributed to $^3$LLCT states which are observed in absorption study of complex -**3** (Figure-5.2c). The $^3$LLCT states are very low energy ES than $^3$MLCT states which causes an increased non-radiative decay to GS as per energy gap law. [5.39] Under extreme condition of surface crossing between shallow potential energy surface of $^3$LLCT states and $S_0$ GS (scheme-5.3), thermally activated vibronic states may cause extremely low PL-QY of complex-**3**. [5.21,5.22,5.40,5.41] Interestingly, the PL-QY of complex-**3** increases ~4 times after addition of $HNO_3$ acid in acetonitrile solvent (figure 5.3c'). In acidic condition (acetolintrile-$HNO_3$), the protonation of $NMe_2$ moiety of **L2** ligand suppress the electron donor character of **L2** ligand which in turn suppress the strong LLCT character of complex-**3**. As a result, the emission intensity increases in protonated acetonitrile solvent. This indicates strong LLCT character in complex-**3**. Furthermore, the PL-QY of protonated complex-**2** and complex-**3** are observed to be of same which suggests that the room temperature PL is due to $^3$MLCT state.

### 5.3.5 Effect of pH on 1:1:1 physical mixture of Ru$^{II}$(bpy)$_3$, L1, L2 molecular species:

Figure 5.4 (left panel) shows the protonation effect on excitation and PL spectra of 1:1:1 physical mixture of Ru(bpy)$_3$ complex, **L1** and **L2** ligands in acetonitrile solvent. The photoexcitation at 400nm exhibits two PL peaks at 505nm and 615nm with a small shoulder at 455nm in neutral condition. The 455nm PL is not observed in 1:1 physical mixture of Ru(bpy)$_3$ complex and **L2** ligands as shown in right panel. Thus, the observed PL spectra corresponds to sum of individual PL spectrum of **L1** ligand (455nm), **L2** ligand (505nm) and Ru(bpy)$_3$ complex (615nm). On protonation (top panel *vs.* bottom panel), the PL due to **L2** ligand (505 nm) reduces (~14 times) significantly whereas the PL due to Ru(bpy)$_3$ complex (615nm) remain unchanged.

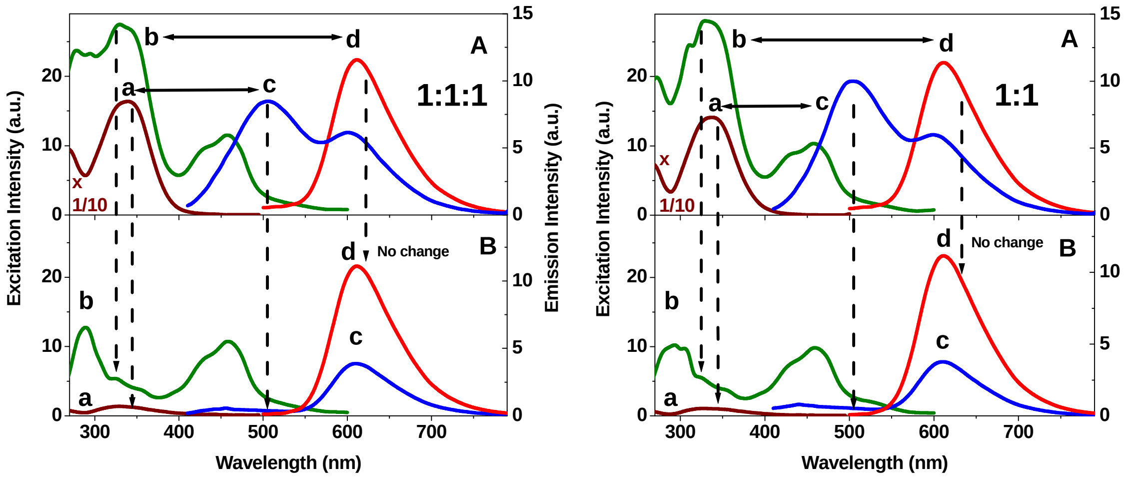

**Figure 5.4**: Left Panels - 1:1:1 physical mixture of Ru(bpy)$_3$ complex, **L1**, **L2** ligands ; Right Panels - 1:1 physical mixture of Ru(bpy)$_3$ complex, **L2** ligand; Top Panels – acetonitrile solvent; bottom panels- HNO$_3$-acetonitrile solvent. (a) Excitation spectra of 505nm PL (actual intensity divided by 10 in panel-A), (b) excitation spectra of 615 PL, (c) PL spectra at 400 nm photoexcitation and (d) PL spectra at 460nm photoexcitation.

In presence of HNO$_3$, intraligand CT transition are suppressed by protonation of -NMe$_2$ moiety (electron donor) of **L2** ligand whereas $d\pi_{Ru(II)} \leftarrow \pi^*_{bpy}$ MLCT transition (absorption peak at 460nm) in Ru(bpy)$_3$ complex remains unchanged (figure-5.4). Thus, 460nm photoexcitation results identical emission spectra. This is further evidenced in excitation spectra recorded in neutral and acidic conditions. The excitation spectrum for 615nm emission wavelength shows no significant changes in 400-600nm region on protonation. However, the excitation spectra in 300-400nm region are adversely affected with addition of HNO$_3$ in acetonitrile solution. The excitation spectra in 300-400nm region is dominated by intraligand CT transition of **L2** and π-π* of **L1** ligands. So, protonation of -NMe$_2$ moiety (**L2** ligand) produces a hypochromic blue shift in excitation spectrum. It is evident that 1:1:1 physical property is entirely different from that of complex-3 (figure-5.3). Thus, the observed difference in a photophysical property of complex-**1**, -**2** and -**3** are due to LCT states.

### 5.3.6 Steady state PL studies at low temperature (77K):

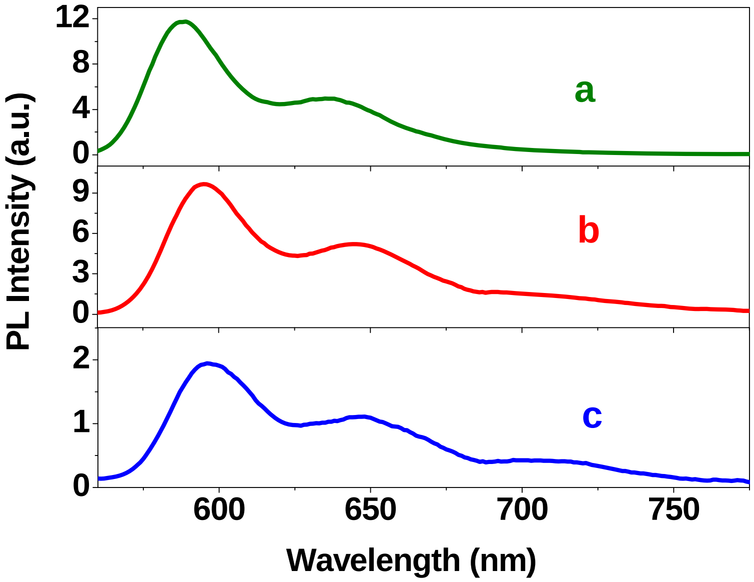

**Figure 5.5:** Uncorrected PL spectra of (a) complex-**1**, (b) complex-**2** and (c) complex-**3** at 77K in ethanol methanol mixture (v/v 4:1).

The LCT states are very less emissive due to thermally activated non-radiative decay processes at room temperature. Therefore, the PL is recorded at 77K in ethanol-methanol mixture (4:1 v/v). Figure 5.5 shows the uncorrected PL spectra of complex-**1**, -**2** and -**3** at 77K. The PL spectral feature in 570-670nm region are observed to be same as that of Ru(bpy)$_3$ complex reported by Balzani and co-workers,[5.42]. So, the spectral features in this region (570-670nm) can be assigned to vibronic progression in $^3$MLCT states. At 77K, complex-**2** and complex -**3** exhibit new PL bands in 670-760nm region and its PL intensities are observed to be comparable as that of complex-**1**. The new red shifted emission band in 670-750nm region is attributed to the ILCT excited states of complex-**2** and LLCT excited states of complex-**3**. The emission decay kinetics are measured at 77K and observed to be ~9μs and ~22μs, respectively.

### 5.3.7 Time resolved emission (TCSPC) studies of complexes -1, -2 and -3:

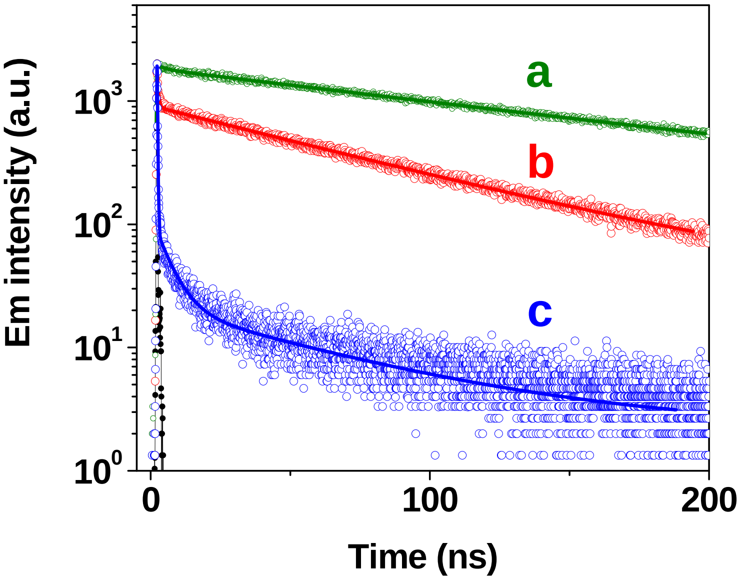

**Figure 5.6:** PL-kinetics of (a) complex-**1**, (b) complex-**2**, (c) complex-**3** in aerated acetonitrile. ($\lambda_{\text{excitation}}$ = 406nm; laser source ~ 66ps FWHM).

Figure 5.6 shows PL-kinetics of complex-**1**, -**2** and -**3** in acetonitrile solvent (aerated). The PL-kinetics of complex-**1** ($\lambda_{\text{monitor}}$ ~621 nm ) is best fitted bi-exponentially with 3.6 ns (7%) and 150

**Table-5.1 :** Time resolved emission kinetics data of complex-**1**, -**2** and -**3.**

| λ $_{ex}$ = 406nm | Complex-**1**<br>(λ $_{em}$ = 621nm) | Complex-**2**<br>(λ $_{em}$ = 623nm) | Complex-**3**<br>(λ $_{em}$ = 640nm) |
|---|---|---|---|
| Aetonitrile<br>Air (O$_2$) | 3.6 ns (7%)<br>150 ns (93%) | 700 ps (47%)<br>80 ns (53%) | 200 ps (97%)<br>3.5 ns (2%)<br>74ns (1%) |
| Aetonitrile<br>Inert (N$_2$) | 6 ns (6 %)<br>315 ns (94%) | 700 ps (45%)<br>> 300 ns (55%) | 200 ps (96%)<br>3.2 ns (3.2%)<br>>500 ns (1.8%) |
| HNO$_3$ +<br>Aetonitrile<br>Air (O$_2$) | 4.2 ns (14%)<br>150 ns (86%) | 380 ps (85%)<br>6 ns (7.4%)<br>140 ns(7.6%) | 340 ps (87%)<br>3.7 ns (8%)<br>140 ns (5%) |

ns (93%) time constants (table-5.1). The bi-exponential decay is reconfirmed in deaerated conditions (6ns (6%), > 315ns (94%); table 5.1) Similar, bi-exponential PL-kinetics are observed for analogous Os$^{II}$(bpy)$_2$(**L1**) complex in chapter-3 and are ascribed by mixed $^3$MLCT states involving bpy and **L1** ligands. [5.43] Likewise, the shorter and longer time constants (~3.6ns and ~150ns) are assigned to $\pi^*_{(\mathbf{L1})} \rightarrow d_{Ru(II)}$ and $\pi^*_{(bpy)} \rightarrow d_{Ru(II)}$ $^3$MLCT transitions. This is supported by single exponential PL-kinetics of Ru$^{II}$(bpy)$_3$ complex which is fitted with ~150ns time constant.

Figure 5.6b shows PL-kinetics of complex-**2** ($\lambda_{monitor}$ 623nm) which is bi-exponentially fitted with 700ps (47%) and 80 ns (53%) time constants (table-5.1). The bi-exponential PL-kinetics is reconfirmed in deaerated acetonitrile solvent and found to be 700ps (45%) and >

**Table-5.2 :** Transient emission kinetics data of 1:1:1 physical mixture of Ru$^{II}$(bpy)$_3$, **L1** and **L2.**

| $\lambda_{ex}$ = 406nm | Ru$^{II}$(bpy)$_3$ | **L2** ligand | Ru$^{II}$(bpy)$_3$ + **L2** (1:1) | Ru$^{II}$(bpy)$_3$ + **L1** + **L2** (1:1:1) |
|---|---|---|---|---|
| Aetonitrile<br>Air (O$_2$) | ~150 ns (100%) | 0.9 ns (77.6%)<br>3.6 ns (22.6%) | 0.9 ns (72.9%)<br>3.6 ns (24.9%)<br>153ns (2.2%) | 0.9 ns (72.6%)<br>3.6 ns (24.7%)<br>153ns (2.7%) |

***L1** ligand has no absorption at 406nm. **$\lambda_{\text{monitor wavelength}}$ = 615 nm

300ns (55%), (table-5.1). It rule out the possibility of PL-quenching by dissolved O$_2$ in acetonitrile as reported in literature.[5.44] Interestingly, such fast decay kinetics (700ps) is not observed in 1:1 physical mixture of Ru(bpy)$_3$ and **L2** molecular entity (table-5.2). Therefore, the fast (~700ps) PL decay resembles to intramolecular energy/electron process (scheme-5.3). In complex-**2**, the presence of strong electron donating N,N'-dimethylaminophenyl moiety (**L2** ligand) introduces low energy $^3$ILCT states (PL at 77K) to $^3$MLCT states (manifold). The $^3$MLCT→$^3$ILCT IC is evidenced in low PL-QY of complex-**2** at room temperature.[5.45] Earlier, the $^3$MLCT→ $^3$ILCT IC is reported to be as fast as ~100 ps. [5.37-5.38] In present study, 700 ps component can be assigned to $^3$MLCT→ $^3$ILCT IC process. The longer time component (80 ns in aerated condition or > 300 ns in deaerated condition) is assigned to remaining $^3$MLCT excited states. Herein, the lifetime of populated $^3$ILCT states may not be observed in TCSPC measurement either due to their longer lifetime (> μs time domain [5.46, 5.47]) or due to radiationless decay nature of $^3$ILCT states.

Figure 5.6c shows the PL-kinetics of complex-**3** (($\lambda_{\text{monitor}}$ 640nm) which is best fitted with 200ps (97%), 3.5ns (2%) and 74ns (1%) time constants (Table-5.1). The PL-kinetics is

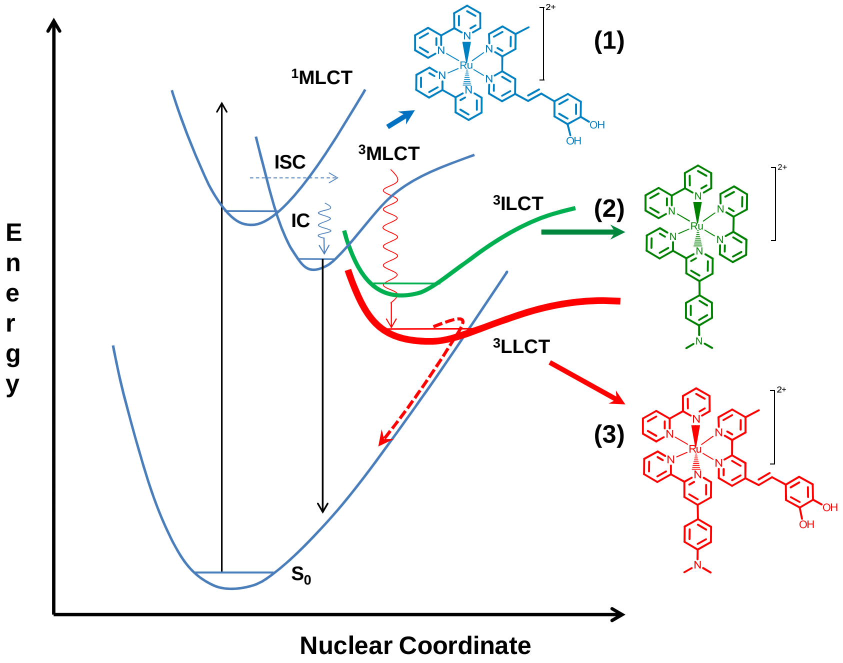

**Scheme 5.3:** A simplified pictorial representation of different photophysical processes in complexes -**1** (blue), -**2** (green) and -**3** (red) (A common ground state (S$_0$), $^1$MLCT and $^3$MLCT states are shown for the sake of convenience only).

reconfirmed in deaerated condition and best fitted with 200ps (95%), 3.2ns (3.2%) and >500ns (1.8%) time constants (table-5.1). Interestingly, the short (200ps) component (~97%) is not observed in complex-**1**, complex-**2** and 1:1:1 physical mixture of Ru$^{II}$(bpy)$_3$, **L1** and **L2** molecular entities (table-5.1 and -5.2). In complex-**3**, the presence of electron -donor and -acceptor ligands (**L2** and **L1**) introduces low energy $^3$LLCT states (PL at 77K) to $^3$MLCT manifolds. The $^3$MLCT$\rightarrow$$^3$LLCT IC is evidenced in extremely low PL-QY of complex-**3** at room temperature. Earlier, $^3$MLCT$\rightarrow$$^3$LLCT IC is reported as fast as < 30ps.[5.48] So, the shortest component (200ps) of complex-**3** can reasonably be attributed to $^3$MLCT$\rightarrow$$^3$LLCT IC. Other time components (3.5ns and 74ns in aerated condition) are too low (total 3%) to assign properly.

Earlier, Yeh et al [5.49] have shown $^3$ILCT→$^3$LLCT conversion time as 4.9ns. So, 3.5ns time constant can either be associated with $^3$ILCT→$^3$LLCT conversion or related with $^3$MLCT states of **L1** ligand ($\pi^*_{(bp\text{-}CH=CH\text{-}catechol)} \rightarrow d_{Ru(II)}$ process). The longer component (74ns in aerated condition or >500ns in deaerated condition) can be assigned to $^3$MLCT excited states.

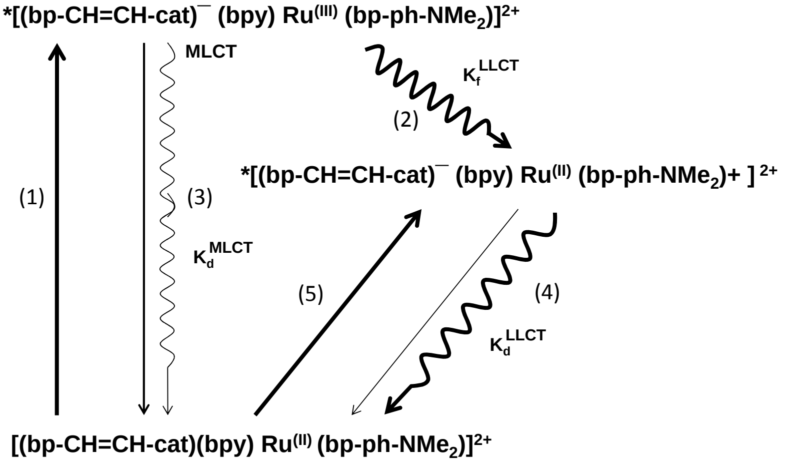

**Scheme 5.4:** Straight arrow (1) and (5) represent direct $S_0$ → MLCT and $S_0$ → LLCT transitions; curved arrow (2), (3) and (4) indicate radiationless transitions; bold arrow indicates dominant photo processes.

The physical interpretation of $^3$MLCT→$^3$LLCT internal conversion process is depicted in scheme-5.4. In photoexcited $^3$MLCT state of complex-**3**, the presence of strong oxidant Ru$^{(III)}$ ion helps in removing an electron from NMe$_2$ moiety of **L2** ligand and produces interligand charge separated (between **L1** and **L2** ligand) excited states (LLCT states). This is supported by earlier study [5.1,5.50] of reductive quenching of $^3$MLCT state (*[(bpy)$^{-\bullet}$Ru$^{(III)}$(bpy)$_2$]$^{+2}$ complex) in presence of triethylamine or N,N'-dimethylaniline. So, $^3$MLCT→ $^3$LLCT IC can be interpreted as intramolecular electron transfer reaction.[5.8-5.9,5.51] The photoexcitation in LLCT absorption band can directly populate the interligand charge separated excited states as depicted in scheme-5.4.

### 5.3.8 Time resolved emission studies (TCSPC) of complexes -1, -2 and -3 at low pH:

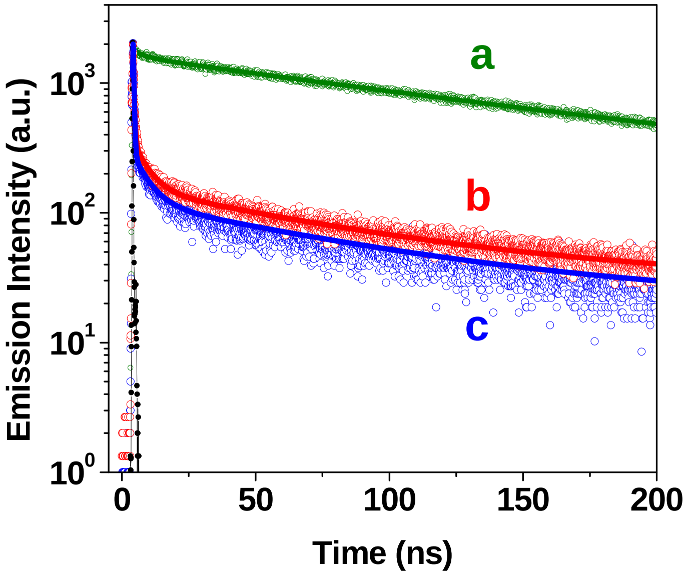

**Figure 5.7**: PL-kinetics of protonated (a) complex-**1**, (b) complex-**2** and (c) complex-**3** at respective emission peak wavelengths in aerated acetonitrile with HNO$_3$ solvent. ($\lambda_{\text{excitation}}$ = 406nm; laser source ~ 66ps FWHM)

Steady state PL studies of complexes -**1**, -**2** and -**3** have shown that LCT states are suppressed by protonation of N,N'-dimethylaminophenyl moiety of **L2** ligand. The protonation effects are further studied in PL-kinetics to reconfirm the $^3$MLCT→ $^3$LCT IC process. Figure 5.7a shows PL-kinetics of complex-**1** in presence of excess of H+ ions (acetonitrile) which is best fitted with 4.2 ns (14%) & 150ns (86%) time constants. Thus, the PL-kinetics are observed to be same in acidic and in neutral condition (table-5.1). The slight increase of shorter component (5.2ns, 14%)

can be due to decrease of $\pi^*_{\mathbf{L1}}$ ($^3$MLCT) energy than $\pi^*_{\mathbf{bpy}}$ ($^3$MLCT) energy which leads to higher excited state population in former $^3$MLCT ($\pi^*_{\mathbf{L1}}$) state.[energy gap law; 5.52] Figure 5.7b shows the emission decay profile of protonated complex-**2** and best fitted with multi-exponential time constants of 380 ps (85%), 6ns (7.4%) and 140ns (7.6%) (table-5.1). Similar PL-kinetics is observed for complex-**3** (Figure 5.7c) which is multi-exponentially fitted with time constants of 340 ps (87%), 3.7 ns (8%) and 140 ns (5%) (table-5.1). The PL-kinetics of complexes -**2** and -**3** are almost similar in acidic solvents but change drastically in no-proton donor solvents. The LCT excited state of complex-**2** and cmplex-**3** differs in degree of intramolecular charge separation nature (ILCT *vs.* LLCT) thus also varies in excited state energies. As a result, the $^3$MLCT→ $^3$LCT internal conversion process occurs with different time constants (700ps *vs.* 200ps) and with different amplitudes (45% *vs.* 96%) in complexes -**2** and -**3**. However, the LCT states are suppressed in acidic condition and hence both the complexes exhibit similar PL-kinetics. Since, the non-radiative pathways are more active in acidic condition as suggested by reduction in PL-QY of complex-**2**, than the 360 ± 20ps time constant is assigned to quenching of $^3$MLCT sate due to non-radiative process in protonated complex -**2** and -**3**.

## 5.4A **Conclusion:**

The LLCT state has been explored in newly synthesized Ru$^{I}$I(bpy)(**L1**)(**L2**) complex, where bpy=2,2’-bipyridyl, **L1** = 4-[2-(4’-methyl-2,2’-bipyridinyl-4-yl) vinyl] benzene-1,2-diol and **L2** = 4-(N,N-Dimethylamino-phenyl)-(2,2’ bipyridine). For this purpose, steady state absorption spectra, PL spectra and PL-kinetics of complexes -(**1**) Ru$^{II}$(bpy)$_2$(**L1**), -(**2**) Ru$^{II}$(bpy)$_2$(**L2**), and **-(3)** Ru$^{II}$(bpy)(**L1**)(**L2**) are compared in different environment such as aerated *vs.* deaerated, protonated *vs.* de-protonated and ambient *vs.* low temperature. In addition, 1:1:1 physical mixture of $Ru^{II}(bpy)_3$, **L1** and **L2** ligands is also used to reaffirm LLCT states of complex-**3**. These studies reveal that presence of electron donor -**L2** and electron acceptor -**L1** ligands introduces low energy LLCT states to MLCT manifolds of complex-**3**. As a result, the optical response of complex-**3** improves but PL quantum yield decreases drastically due to quenching of $^3$MLCT states. The $^3$MLCT→ $^3$LLCT internal conversion is observed to occur in ~200 ps time scale. In addition, the photophysical studies also reveal that LLCT states can be directly populated by photoexcitation in 350-600nm region. In LLCT states, electron and cation (hole) are localized on ancillary ligands **L1** and **L2**, respectively. Thus, complex-**3** can be a potential sensitizer for $TiO_2$ material on account of increased electron density on catechol bound **L1** ligand and hole localization on remote $NMe_2$ bound **L2** ligand.

## Part 5B: Efficient Charge Separation in Ru(II)-Polypyridyl Complex Sensitized TiO$_2$ Film: Hole Stabilization by LLCT states

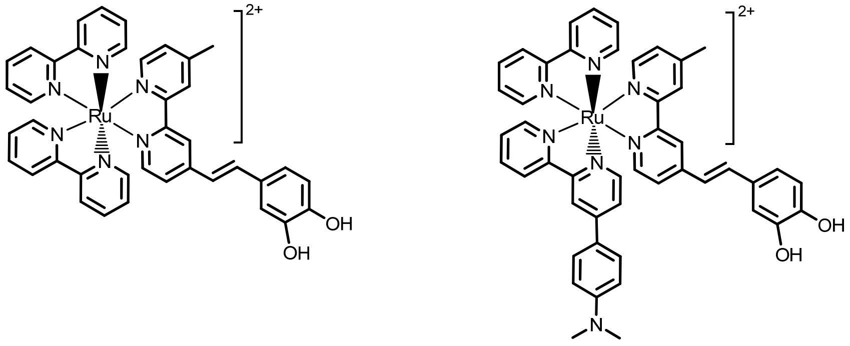

**Complex-1** **Complex-3**

**Scheme 5.1b**: *Structure of complex-**1** and complex-**3**

(* Structures are same as presented in Scheme-5.1a)

The ligand localized charge separated states are investigated in part-A of this chapter. The ligand-to-ligand charge transfer (LLCT) state of complex-**3** offer new electron transfer pathways on sensitized TiO$_2$ film. The effects of LLCT states on interfacial electron transfer (IET) dynamics are explored by femtosecond time resolved absorption studies and presented in part-B of this chapter.

## 5.3B Results and discussion

**5.3.9 $TiO_2$ film preparation and sensitization:** $TiO_2$ nanoparticle (NP) paste is purchased from Solaronix (Switzerland) and used for preparation of mesoporous $TiO_2$ film as described in literature.[5.53] In brief, $TiO_2$ paste is spread out on to a saphire plate of 25 mm diameter and 1.5mm thickness by using doctor blade technique. The $TiO_2$ layer is air dried and than sintered at 450 °C for 30 minutes. The $TiO_2$ film is cooled at 80 °C and dipped for 12 hr in 300 μM of complexes -**1** and -**3** in acetonitrile. While soaking, the complex -**1** and -**3** are loaded onto $TiO_2$ films via 5-membered ring of catecholate -$TiO_2$ linkage. The sensitized $TiO_2$ films are rinsed 5 times with spectroscopy grade acetonitrile. For transient absorption studies, an optical cell is assembled by inserting a teflon spacer (50 micron thickness) between dye-sensitized-$TiO_2$-film covered saphire plate and a blank quartz plate. The cell is filled with acetonitrile solvent in order to perform transient absorption (TA) studies in neutral condition. Also, the same cell assembly is used further for TA studies in protonated condition by using acetonitrile-$HNO_3$ medium.

### 5.3.10 Spectral sensitization of $TiO_2$ NPs: UV-vis absorption spectra:

The MLCT and LLCT electronic transitions have already been described in photophysical study of complex -**3** in part-B of this chapter. Figure-5.8 shows the steady state absorption spectra of complex-**1** and complex-**3** (equal concentration) in absence and in presence of $TiO_2$ NPs. Complex-**3** exhibits higher molar extinction coefficient than complex-**1** due to presence of additional LLCT transitions in 400-650nm region. The optical absorption spectrum of complex-**3** increases and becomes narrower in presence of $TiO_2$ NPs. The broad absorption spectrum of complex-**3** is result of various rotational conformers of $NMe_2$ groups (**L2** ligand) which lead to distribution of HOMO energy levels. The strong catecholate binding of complex-**3** on $TiO_2$

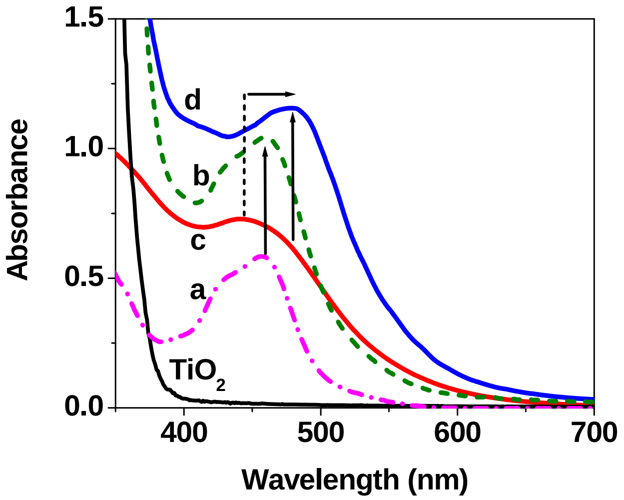

**Figure 5.8**: Optical absorption spectra of a) complex -**1** in water, b) complex -**3** in water; c) complex -**1** /TiO$_2$ and d) complex-**3**/TiO$_2$ NPs dispersed in water.

surface causes a partial charge separation (CT complex) in ground state (GS).[5.43] The electron donating nature of NMe$_2$ group stabilizes positive charge within complex-**3** in particular rotational conformation and enhances CT interaction. As a result, the absorption spectrum becomes narrower and highly red shifted after addition of TiO$_2$ NPs. The relative increase of absorbance shows significant sensitization of TiO$_2$ NPs by using complexes -**1** and -**3**.

### 5.3.11 Excited state dynamics of free complex-3 in acetonitrile:

The excited state absorption (ESA) due to $^3$MLCT states of Ru$^{II}$(bpy)$_2$(bpy-catechol) has been described in chapter-4. The effect of low energy LLCT states on excited state (ES) kinetics are explored by transient absorption (TA) study of complex-**3**. Figure-5.9 shows TA spectrum of complex-**3** and comparison of ESA kinetics of complex-**1** and -**3** at 610nm. The TA spectrum of complex-**3** exhibits a broad positive absorption bands in 540-1000nm region and a bleach band

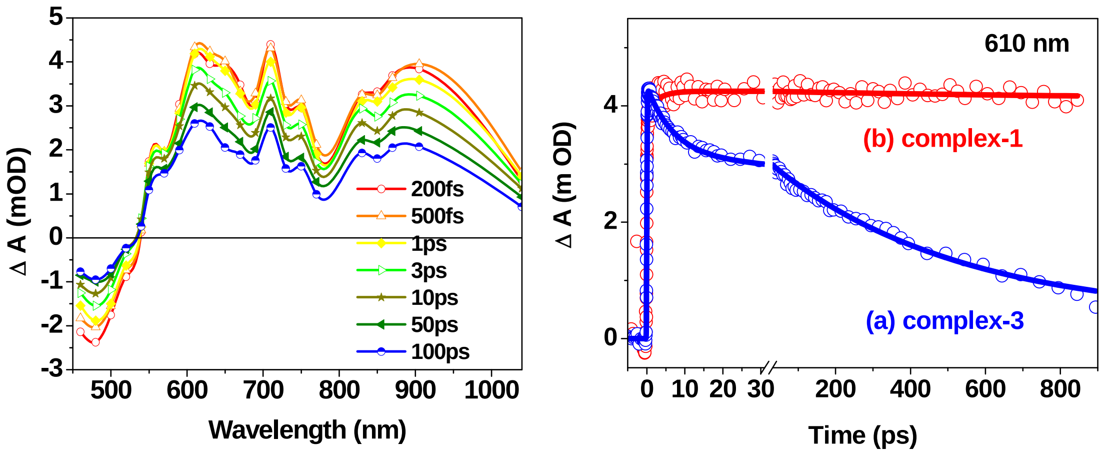

**Figure 5.9**: Left Panel: TA spectra of complex-**3** in acetonitrile solution following excitation at 400nm laser pulse at 200fs, 500fs, 1ps, 3ps, 10ps, 20ps, 50ps, and 100 ps time delays. Right Panel: TA kinetics of a) complex-**3**, b) complex-**1** at 610nm.

in 470-530nm region. The positive absorption band is assigned to ESA of $^3$MLCT states because $^1$MLCT→$^3$MLCT intersystem crossing (ISC) occur in pulse width limited time (<100 fs).[5.32,5.33, chapter-4] This is supported by earlier TA study of complex-**1** in which ESA due to $^3$MLCT state is observed in 500-1000 nm region.[5.28,5.54] The negative absorption band in 470-530nm region corresponds to the ground state bleach of complex -**3**.

The ESA kinetics of complex-**3** is monitored at 610nm (figure 5.9, right panel) which is best fitted multiexponentially with 7 ps (27.7 %), 500ps (64.4%) & > ns (8%) time constants. Similar, TA kinetics is also observed at 1000nm which is best fitted with 5ps (30%), 500ps (64%) and > ns (6%) time constants. The TA kinetics reveal an extensive decay of $^3$MLCT states in <1ns time scale which is very uncommon for Ru(II)-polypyridyl complexes.[5.54,5.55] No such decay is observed in ESA kinetics (610nm) of complex-**1** as shown in figure-5.9 (right panel). The ESA kinetics of complex-**1** is best fitted with a biexponential growth (<100fs

(+91.5%) and 3ps (+8.5%)) and a very long decay (>1ns, -00%) time constants. The shorter growth component (<100fs) is assigned to $^1$MLCT→$^3$MLCT ISC and then evolution of $^3$MLCT states. The slow growth component (3ps) is attributed vibrational cooling of hot $^3$MLCT states. The long decay component (>1ns) is assigned to thermalized $^3$MLCT state (~150ns, table 5.1, part-5A).

The extensive ESA decay kinetics of complex-**3** than that of complex-**1** can be attributed to $^3$MLCT→ $^3$LLCT internal conversion (IC). The $^3$MLCT→ $^3$LLCT IC is supported by bleach recovery kinetics measured at 460nm which is best fitted with 7 ps (48.2%), 500ps (11.7%) and > 1ns (40.1%) time constants. The bleach recovery kinetics is observed to be slower than ESA decay kinetics which suggests that MLCT excited state decays to LLCT states rather than to GS. It is observed in earlier TA study of $Os^{II}$(bpy)(bpy-catechol) (chapter-4) that ESA and bleach bands are overlapped in in 550-750nm region (overall negative absorption band). Likewise, , the ESA due to $^3$LLCT state and bleach due to $^1$MLCT state of complex-**3** can overlap at 460nm. Therefore, the bleach recovery kinetics (7ps and 500ps) can be assigned to growth of ESA due to $^3$ILCT. However, a clear growth is not observed in positive absorption band in 540-100nm which is probably due to strong TA of $^3$MLCT states appearing in this region. As shown in scheme -5.3, -5.4, part-A(chapter-5), the $^3$MLCT→ $^3$LLCT IC is related to intramolecular charge transfer which involve rotation of N,N'-dimethylaminophenyl group with respect to bpy ligand.[56-58] The rotational dynamics of N,N'-dimethylaniline group is reported in 3-10ps time scale.[5.59,5.60] Therefore, the shortest decay components (6 ± 1 ps) observed in TA decay profile (610nm) of complex-**3** can be assigned to the rotation of ph-$NMe_2$ moiety with respect to bpy ligand. The longer components (500ps) can be attributed to internal conversion from $^3$MLCT into $^3$LLCT states. The remaining lowest contribution (6-8%) with > ns time component components (> ns, 6-8%) can be attributed to $^3$LLCT of complex-**3**.

### 5.3.12 Transient absorption spectra of complex -1/$TiO_2$ film.

A prior knowledge of IET dynamics involving MLCT excited state of complex-**1**/$TiO_2$ system is necessary to understand the role of LLCT state in complex-**3**/$TiO_2$ system. Since, LLCT state require polar but no-proton donor solvents, $TiO_2$ NP film is used in IET study as it allows polar solvent environment with and without $HNO_3$ acid. Figure -5.10 shows TA spectrum of complex-**1**/$TiO_2$ film in acetonitrile solvent.

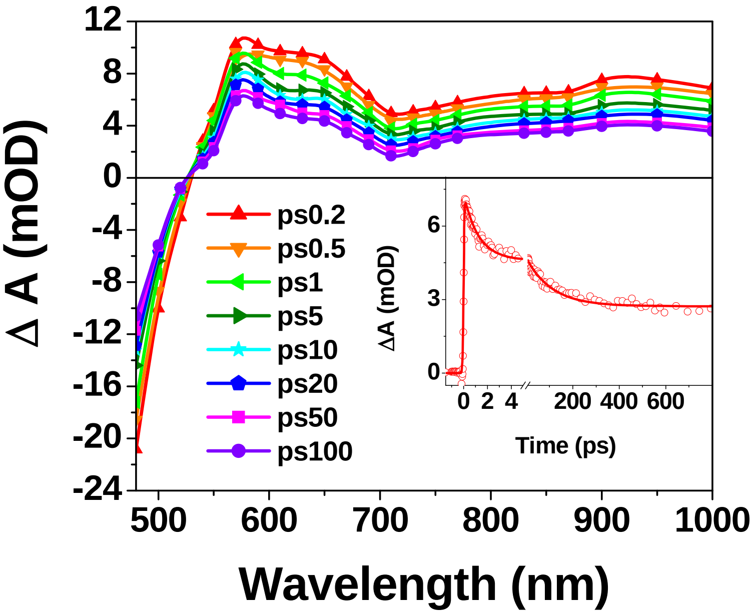

**Figure 5.10:** TA spectra of complex-**1**/$TiO_2$ film in presence of acetonitrile following excitation at 400nm laser pulse at 200 fs, 500 fs, 1 ps, 5ps, 10ps, 20ps, 50ps, and 100 ps time delays. [Inset shows the kinetic trace at 610 nm].

It comprises a broad positive absorption band in 540-1000nm and a negative absorption band in 480-530nm region. The positive absorption band in 540-670nm region is attributed to complex-**1**$^{\bullet+}$ cation absorption. The assignment is based on cation spectrum obtained in pulse radiolysis study.[5.28] The negative absorption band in 460-500nm region is assigned to ground state bleach and the broad positive absorption band in 730-100nm is assigned to transient absorption of conduction band electron.[Chapter-4] The electron injection process is monitored by rise of TA signal at 900 nm. The back electron transfer (BET) dynamics is studied by TA decay kinetics at 900nm (conduction band electron), 610nm (complex-**1**$^{\bullet+}$ cation) and 470nm (bleach recovery). A pulse width (< 80fs) limited electron injection and multi exponential 1.2 ps (35.9 %), 100ps (26.8 %) and > 1ns (37.3 %) BET dynamics is observed at 610nm (complex-**1**$^{\bullet+}$ cation) which is shown in figure-5.10(inset).

### 5.3.13 Transient absorption spectra of complex -3/TiO$_2$ film.

Figure 5.11 shows TA spectrum of complex -**3**/TiO$_2$ which comprises a broad positive absorption band in 540-1000nm and a negative absorption band in 480-520nm region. A comparison of TA spectra of complex-**3** and complex-**3**/TiO$_2$ film reveals that the positive absorption band increases in shorter wavelength region of 500-570nm. So, the TA band in 570-730nm region can be assigned to complex-**3**$^{\bullet+}$ cation spectrum. A comparison of TA spectra of complex -**1**/TiO$_2$ and complex -**3**/TiO$_2$ reveals that complex-**3**$^{\bullet+}$ cation spectrum (540-730nm) is broader than complex-**1**$^{\bullet+}$ cation spectrum (540-670nm) The significant broadening of cation spectrum is attributed to presence of electron donor property of dimethylaniline moiety attached to bpy ligand in complex-**3**. The negative absorption band in 460-520nm region corresponds to ground state bleach and the broad absorption band in 750–1000 nm region is attributed to conduction band electron in TiO$_2$ film. Like complex-**1**/TiO$_2$ system, the electron injection and BET dynamics are studied by monitoring the TA signal at 900nm, 610nm and bleach decay kinetics at 490nm. A single exponential, pulse width limited (< 80fs) electron injection is observed in 900nm TA rise signal. The BET is monitored at 610nm which is fitted multiexponentially with time constants of 2ps (15.4 %), 200ps (24 %) and > 1ns (60.6 %) (Figure-5.11, inset).

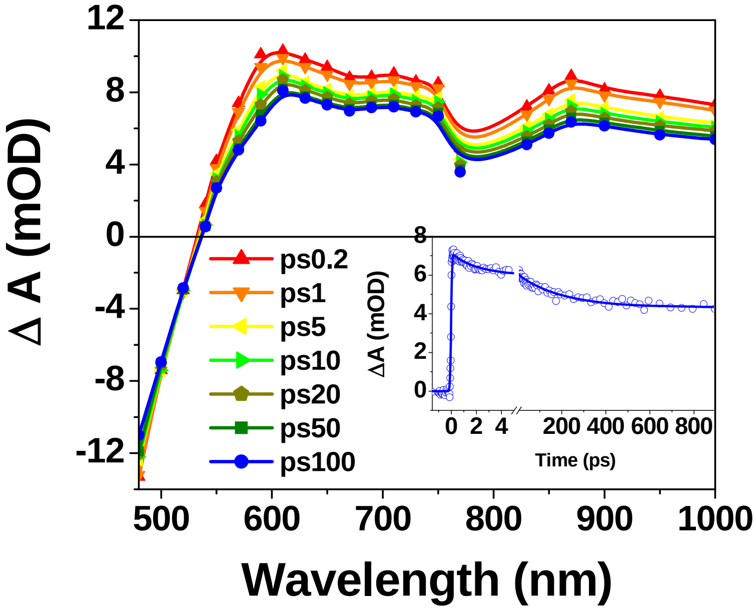

**Figure 5.11**: TA spectra of complex-**3** sensitized TiO$_2$ NPs film in presence of acetonitrile at 200 fs, 1 ps, 5 ps, 10 ps, 50 ps and 100ps time delays after excitation at 400 nm. [Inset shows the kinetic trace at 610 nm].

### 5.3.14 Interfacial electron transfer dynamics:

The electron injection from $Ru^{II}(bpy)_2(bpy\text{-}catechol)$ complex to $TiO_2$ NPs has been observed in pulse width limited time (<100fs) and ascribed by strong electronic coupling at catechol-dye/$TiO_2$ interface in chapter-4. Similar ultrafast electron injection kinetics is observed in complexes -**1** and -**3** sensitized $TiO_2$ film. This suggests both complexes are strongly coupled to $TiO_2$ NPs (in film). However, BET dynamics are observed to be different in complex -**1**/$TiO_2$ and complex -**3**/$TiO_2$ systems.

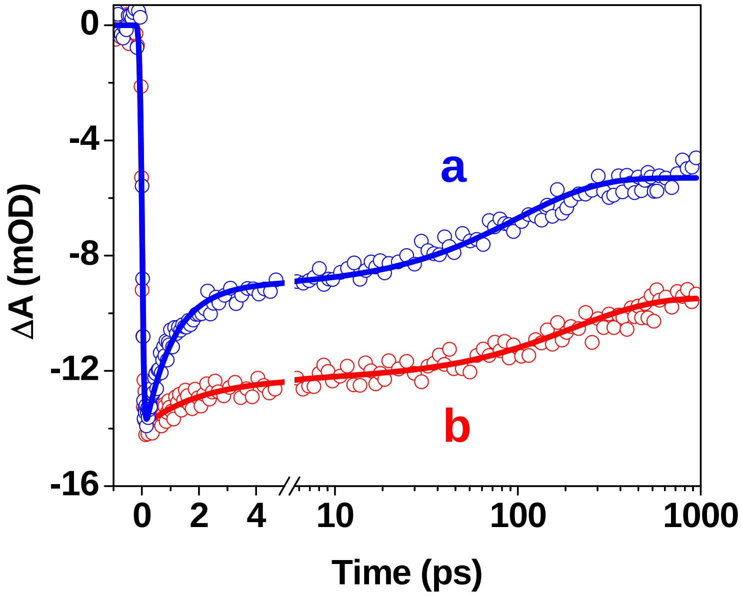

**Figure 5.12**: BET kinetics monitored by bleach recovery at 480nm in (a) complex-**1**/$TiO_2$ and (b) complex-**3/**$TiO_2$ film following excitation with 400 nm laser pulse.

Figure 5.12 shows a comparison of BET dynamics in two systems. The bleach recovery kinetics is fitted multiexponentially with 2ps (11.8%), 200ps (20.7%) and > 1ns (67.5%) time constants for complex-**3**/$TiO_2$ system and 1ps (37%), 100ps (26%) and > 1ns (37%) for complex -**1**/$TiO_2$ systems. The slow BET dynamics of complex-**3**/$TiO_2$ than that of complex-**1**/$TiO_2$ system is due to electron donor $NMe_2$ moiety which acts as secondary electron donor to oxidized

Ru(+3) ion. This is supported by earlier reports on secondary electron donating properties of N,N'-(di-p- anisylamino) moiety in Ru(II)-complex/TiO$_2$ system.[5.18] In complex-**3**/TiO$_2$ film, the cation transfer from Ru (+3) center to secondary electron donor center (NMe$_2$ of **L2** ligand) results an increase of spatial charge separation at dye/TiO$_2$ interface. It slows down the BET process in complex-**3**/TiO$_2$ film which is in accordance to electronic coupling matrix described in Marcus semiclassical theory of electron transfer.[5.61] The cation transfer corresponds to $^3$MLCT→$^3$LLCT internal conversion. However, photoexcitation in LLCT band (350-600nm region) results a direct electron injection in TiO$_2$ film and hole localization on NMe$_2$ moiety. The

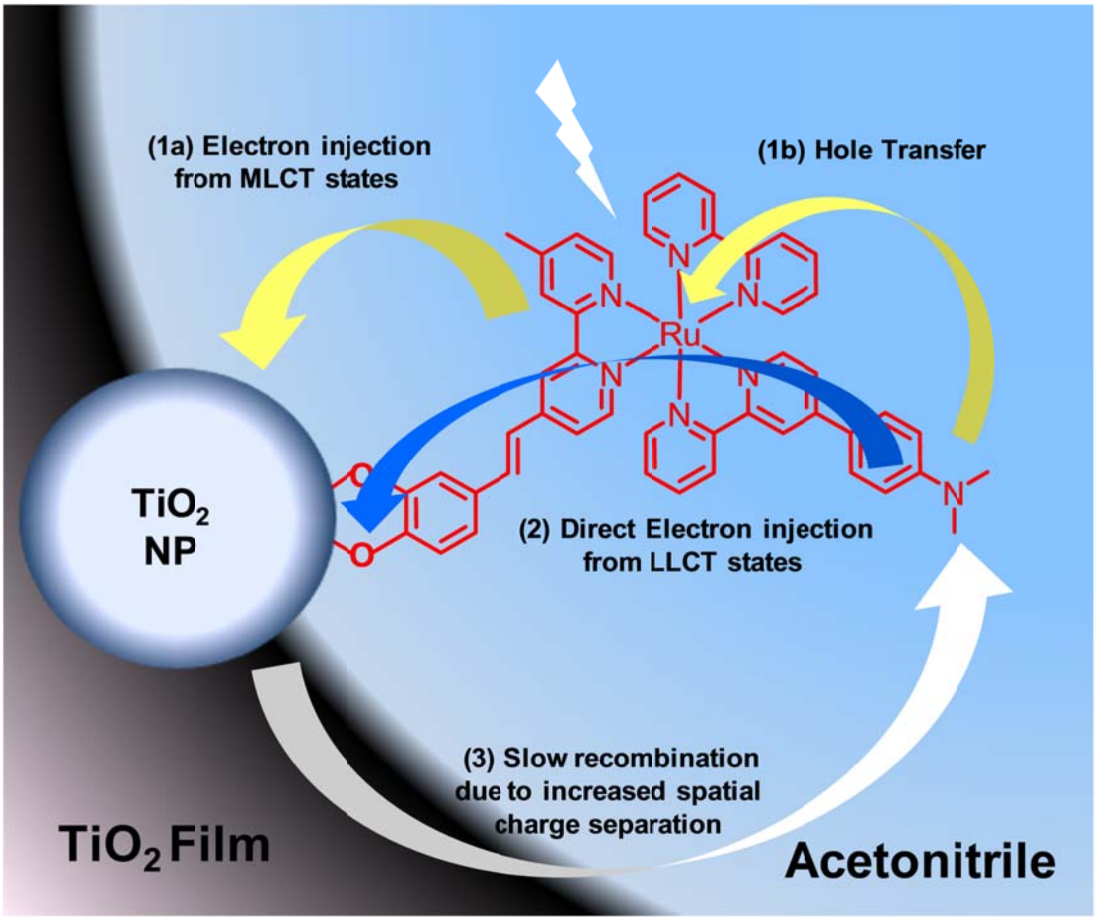

**Scheme 5.5**: Schematic representation of IET in complex -**3**/TiO$_2$ film.

LLCT states which are produced in either way causes increased spatial charge separation on complex-**3**/$TiO_2$ interface as compared to that on complex-**1**/$TiO_2$ interface. Scheme-5.5 shows a direct and stepwise electron transfer in complex-**3**/$TiO_2$ film.

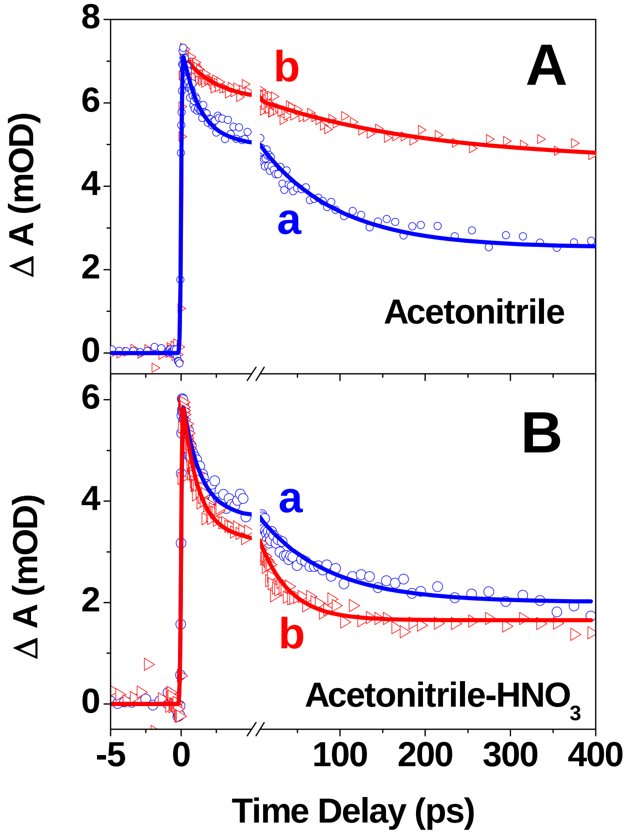

**Figure 5.13**: BET kinetics monitored by TA of $e^-$(C.B. $TiO_2$) at 900nm in (a) complex-**1**/$TiO_2$ and (b) complex-**3**/$TiO_2$ film; Panel-A: in neutral condition (acetonitrile ); Panel-B: in acidic condition ($HNO_3$ -acetonitrile).

The hole stabilization on electron donor moiety of complex-**3** is reconfirmed by carrying out IET study in acidic conditions. Figure-5.13 shows TA kinetics of two systems at 900nm in acetonitrile (Panel-A) and in acidic-acetonitrile ($HNO_3$) environment (Panel-B). In acid free acetonitrile solvent environment, TA kinetics of conduction band electron (figure-5.13, top panel) are observed to be same as bleach recovery kinetics (figure-5.12). However, in acidic acetonitrile ($HNO_3$ added) environment, the back electron transfer dynamics are observed to be faster in complex -**3**/$TiO_2$ film (1 ps (44.4 %), 35ps (29.4%) and > 1ns (26.2%)) as compared to complex -**1**/$TiO_2$ system (1.2 ps (38%), 80ps (28.8%) and > 1ns (33.2%) ). In acidic condition (low pH), protonation of $NMe_2$ group of complex -**3** inhibit LLCT state. As a result, the hole remain localized on Ru(III) ion in protonated complex -**3** and its proximity to $TiO_2$ surface is same as that in complex -**1**/$TiO_2$ system. The presence of protonated amino group increases the π-acceptor ability of Ru(III) centre and a fast BET dynamics is observed in protonated complex -**3**/$TiO_2$ system. A fast BET in complex -**3**/$TiO_2$ system is also supported by Marcus semiclassical theory of electron transfer.[5.61] The theory states that BET (in dye/$TiO_2$ system) occur in Marcus inverted region ($-\Delta G_0 > \sim 1$ eV). The $-\Delta G_0$ for BET reaction in aforementioned systems can be calculated by using $\Delta G_0 = EC - E_{S/S+}$ expression ($Ec = -0.49V$ and $E_{S/S+}$ = redox potential of dye) and is found to be 1.81 eV and 1.73 for complex -**1**/$TiO_2$ and -**3**/$TiO_2$ system. So, the fast BET of protonated-complex -**3**/$TiO_2$ system than that of complex -**1**/$TiO_2$ system can be due to lower $-\Delta G$ and/or increased π-accepting ability of Ru(III) ion.

### 5.4B Conclusion:

The presence of electron donor (**L2**) and electron acceptor (**L1**) ligands introduces low energy LLCT states to MLCT manifold of complex-**3**. It results an increased spectral sensitization of $TiO_2$ film. The effects of LLCT state on IET process are rationalized by carrying out femtosecond transient absorption (TA) studies of complex-**3**/$TiO_2$ film in neutral and acidic conditions. In presence of no-proton donor polar solvent (acetonitrile), a pulse width limited

(<100fs) electron injection from photoexcited MLCT and LLCT states are observed on account of strong catecholate binding on $TiO_2$ surface. The hole is directly or stepwise transferred to electron donor ligand (**L2**) after electron injection from LLCT and MLCT states, respectively. The direct photoexcitation to LLCT states helps in achieving an increased spatial charge separation in pulse width limited time (< 100fs). As a result, we have observed a slow back electron transfer process (BET) in complex -**3**/$TiO_2$ system in relative to complex -**1**/$TiO_2$ system. This study shows that Ru(II)-polypyridyl complexes comprising LLCT states can be a better photosensitizer for increased electron injection yield and slow BET processes in comparison to Ru(II)-polypyridyl complexes with MLCT states only.

## 5.5 References:

[5.1] A. Juris, V. Balzani, F. Barigelletti, S. Campagna, P. Belser, A. von Zelewsky, Coord. Chem. Rev. 1988, 84, 85.

[5.2] M.K. Nazeeruddin, P. Pechy, T. Renouard, S.M. Zakeeruddin, R. Humphry-Baker, P. Comte, P. Liska, L. Cevey, E. Costa, V. Shklover, L. Spiccia, G.B. Deacon, C.A. Bignozzi, M. Grätzel, J. Am. Chem. Soc. 2001, 123, 1613.

[5.3] M. Maestri, N. Armaroli, V. Balzani, E. C. Constable, A. M. W. C. Thompson, Inorg. Chem. 1995, 34, 2759.

[5.4] K. Kalyanasundaram, M. Grätzel, Coord. Chem. Rev. 1998, 77, 347.

[5.5] K. Kalyanasundaram, Coord. Chem. Rev. 1982, 46, 159.

[5.6] A. Vogler, H. Kunkely, Coments on Inorg. Chem.1990, 9, 201.

[5.7] S.I. Gorelsky, E.S. Dodsworth, A.B.P. Lever, A.A. Vlcek, Coord. Chem. Rev. 1998, 174, 469.

[5.8] T. A. Perkins, D. B. Pourreau, T. L. Netze, K. S. Schanze, J. Phys. Chem. 1989, 93, 4511.

[5.9] Y. Wang, B. T. Hauser, M. M. Rooney, R. D. Burton, K. S. Schanze, J. Am. Chem. Soc. 1993, 115, 5675.

[5.10] B. O'Regan, M. Grätzel, Nature 1991, 353, 737.

[5.11] M. K. Nazeeruddin, Q. Wang, L. Cevey, V. Aranyos, P. Liska, E. Figgemeier, C. Klein, N. Hirata, S. Koops, S. A. Haque, J. R. Durrant, A. Hagfeldt, A. B. P. Lever, M. Grätzel, Inorg. Chem. 2006, 45, 787.

[5.12] P. G. Bomben, K. C. D. Robson, P. A. Sedach, C. P. Berlinguette, Inorg. Chem. 2009, 48, 9631.

[5.13] C. A. Bignozzi, R. Argazzi, C. J. Kleverlaan, Chem. Soc. Rev., 2000, 29, 87.

[5.14] M. K. Nazeeruddin, F. D. Angelis, S. Fantacci, A. Selloni, G. Viscardi, P. Liska, S. Ito, B. Takeru, M. Grätzel, J. Am. Chem. Soc. 2005, 127, 16835.

[5.15] H. -J. Park, K. H. Kim, S. Y. Choi, H. –M. Kim, W. I. Lee, Y. K. Kang, Y. K. Chung, Inorg. Chem., 2010, 49, 7340.

[5.16] K.-S. Chen, W. -H. Liu, Y. -H. Wang, C. -H. Lai, P. -T. Chou, G. -H. Lee, K. Chen, H. -Y. Chen, Y. Chi, F. -C. Tung, Adv. Funct. Mater. 2007, 17, 2964.

[5.17] D. Kuang, S. Ito, B. Wenger, C. Klein, J.-E Moser, R. Humphry-Baker, S. M. Zakeeruddin, M. Grätzel, J. Am. Chem. Soc. 2006, 128, 4146.

[5.18] N. Hirata, J.-J.Lagref, E. J. Palomares, J. R. Durrant, M. K. Nazeeruddin, M. Grätzel, D. D. Censo, Chem. Eur. J. 2004, 10, 595.

[5.19] C.-Y. Chen, S.-J. Wu, J.-Y. Li, C.-G. Wu, J.-G. Chen, K.-C. Ho, Adv. Mater. 2007, 19, 3888.

[5.20] C.-Y. Chen, S.-J. Wu, C.-G. Wu, J.-G. Chen, K.-C. Ho, Angew. Chem. Int. Ed. 2006,. 45, 5822.

[5.21] L.-Q. Song, J. Feng, X.-S. Wang, J.-H. Yu, Y.-J. Hou, P.-H. Xie, B. -W. Zhang, J. -F. Xiang, X.-C. Ai, J.-P. Zhang, Inorg. Chem. 2003, 42, 3393.

[5.22] M. –X, Li, X. Zhou, B. –H. Xia, H. –K. Zhang, Q. –J. Pan, T. Liu, H. –G. Fu, C. –C. Sun, Inorg. Chem. 2008, 47, 2312.

[5.23] Y. Chi, P. -T. Chou, Chem. Soc. Rev. 2007, 36, 1421.

[5.24] S. -W. Li, Y. -M. Cheng, Y. -S. Yeh, C. -C. Hsu, P. -T. Chou, S. -M. Peng, G. -H. Lee, Y. -L. Tung, P. -C. Wu, Y. Chi, F. -I. Wu, C. -F. Shu, Chem. Eur. J. 2005, 11, 6347.

[5.25] A.D. Shukla, A.Das, Polyhedron, 2000, 19, 2605.

[5.26] A. D. Shukla, B. Whittle, H. C. Bajaj, A. Das, M. D. Ward, Inorg. Chim. Acta 1999, 285, 89.

[5.27] A. Das, J. A. Mccleverty, M. D. Ward, C. J. Jones, A. M. W. C. Thompson, Polyhedron, 1992, 11, 2119.

[5.28] G. Ramakrishna, D. A. Jose, D. K. Kumar, A. Das, D. K. Palit, H. N. Ghosh, J. Phys. Chem. B 2005, 109, 15445.

[5.29] D. A. Jose, P. Kar, D. Koley, B. Ganguly, W. Thiel, G. Ramakrishna, D. K. Palit, H. N. Ghosh and A. Das; Inorg. Chem. 2007, 46, 5576.

[5.30] V. Balzani, A. Juris, M. Venturi; Chem Rev. 1996, 96, 759.

[5.31] X. Han, L. -Z. Wu, G. Si, J. Pan, Q. -Z. Yang, L. -P. Zhang, C. -H. Tung, Chem. Eur. J. 2007, 13, 1231.

[5.32] N. H. Damrauer, G. Cerullo, A. Yeh, T. R. Boussie, C. V. Shank, J. K. McCusker, Science, 1997, 275, 54.

[5.33] A. C. Bhasikuttan, M. Suzuki, S. Nakashima, T. Okada, J. Am. Chem. Soc. 2002, 124, 8398.

[5.34] J. N. Demas, D. G. Taylor, Inorg. Chem. 1979, 18, 3177.

[5.35] J. N. Demas, A. W. J. Adamson, Am. Chem. Soc. 1971, 93, 1800 and references therein.

[5.36] B. Durham, J. V. Caspar, J. K. Nagle, T. J. Meyer, J. Am. Chem. Soc. 1982, 104, 4803.

[5.37] M. -F. Charlot, Y. Pellegrin, A. Quaranta, W. Leibl, A. Aukauloo, Chem. Eur. J. 2006, 12, 796.

[5.38] Y. Pellegrin, A. Quaranta, P. Dorlet, M. F. Charlot, W. Leibl, A. Aukauloo, Chem. Eur. J. 2005, 11, 3698.

[5.39] P. Chen, T. J. Meyer, Chem. Rev. 1998, 98, 1439.

[5.40] P. -T. Chou, Y. Chi, Eur. J. Inorg. Chem. 2006, 17, 3319.

[5.41] N. H. Damrauer, T. R. Boussie, M. Devenney, J. K. McCusker, J. Am. Chem. Soc. 1997, 119, 8253.

[5.42] A. Juris, V. Balzani, P. Belser, A. V. Zelewsky, Helvetica Chmica Acta, 1981, 64, 2175.

[5.43] S. Verma, P. Kar, A. Das, D. K. Palit, H. N. Ghosh, J. Phys. Chem. C 2008, 112, 2918.

[5.44] S. Ji, W. Wu, W. Wu, P. Song, K. Han, Z. Wang, S. Liu, H. Guod, J. J. Zhao, Mater. Chem. 2010, 20, 1953.

[5.45] A. C. Benniston, A. Harriman, D. J. Lawrie, A. Mayeux, Phys. Chem. Chem. Phys. 2004, 6, 51.

[5.46] J. V. Caspar, T. J. Meyer, J. Am. Chem. Soc. 1983, 105, 5583.

[5.47] K. F. Mongey, J. G. Vos, B. D. MacCraith, C. M. McDonagh, C. Coatesc, J. McGarvey, J. Mater. Chem. 1997, 7, 1473.

[5.48] T. A. Perkins, D. B. Pourreau, T. L. Netzel, K. S. Schanze, J. Phys. Chem. 1989, 93, 4511.

[5.49] Y. -S. Yeh, Y. -M. Cheng, P. -T. Chou, G. -H. Lee, C. -H. Yang, Y. Chi, C. -F. Shu, C. -H. Wang, ChemPhysChem 2006, 7, 2294.

[5.50] N. Kitamura, H. –B. Kim, S. Okano, S. Tazuke, J. Phys. Chem. 1989, 93, 5750.

[5.51] J. D. Lewis, L. Bussotti, P. Foggi, R. N. Perutz, J. N. Moore, J. Phys. Chem. A 2002, 106, 12202.

[5.52] S. R. L. Fernando, U. S. M. Maharoof, K. D. Deshayes, T. H. Kinstle, M. Y. Ogawa, J. Am. Chem. Soc. 1996, 118, 5783.

[5.53] H. Choi, C. Baik, S. O. Kang, J. Ko, M.-S. Kang, M. K. Nazeeruddin, M. Grätzel, Angew. Chem. Int. Ed. 2008, 47, 327.

[5.54] S. Verma, P. Kar, A. Das, D. K. Palit, H. N. Ghosh, Chem. Eur. J. 2010, 16, 610.

[5.55] J. B. Asbury, R. J. Ellingson, H. N. Ghosh, S. Ferrere, A. J. Nozik, T. Lian, J. Phys. Chem. B 1999, 103, 3110.

[5.56] L.-Q Song, J. Feng, X.-S. Wang, J.-H. Yu, Y.-J. Hou, P.-H. Xie, B. -W. Zhang, J. -F. Xiang, X.-C. Ai, J.-P. Zhang, Inorg. Chem. 2003, 42, 3393.

[5.57] Z. R. Grabowski, K. Rotkiewicz, W. Rettig, Chem. Rev., 2003, 103, 3899.

[5.58] W. Rettig, W. Majenz, R. Lapouyade, F. Haucke , J. Photochem. Photobio. A, 1992, 62, 415.

[5.59] M. M. Martin, P. Plaza, P. Changenet-Barret, A. Siemiarczuk, J. Phys. Chem. A 2002, 106, 2351.

[5.60] A. Onkelinx, G. Schweitzer, F. C. D. Schryver, H. Miyasaka, M. V. Auweraer, T. Asahi, H. Masuhara, H. Fukumura, A. Yashima, K. Iwai, J. Phys. Chem. A 1997, 101, 5054.

[5.61] Marcus, R. A.; Sutin, N. Biochim. Biophys. Acta 1985, 811, 265.

# CHAPTER 6

# EXCITON-COUPLED CHARGE-TRANSFER DYNAMICS IN PORPHYRIN J-AGGREGATE/ TIO$_2$ NP COMPLEX.

## 6.1 Introduction:

An ordered self-assembly of porphyrin molecules mimics antenna function of efficient energy transfer.[6.1, 6.2] The multilayer interfacing of porphyrin ring constitutes long range association of π-network. The strong intermolecular dipole-dipole interactions transform the localized π−π∗ transition of monomer into delocalized coherent excited [6.1-6.4] states of porphyrin aggregate. The exciton emerging from such coherent electronic states are energetically different from localized excited states and the energy gradient begins the migration of photosynthetic exciton. Thus, an ordered porphyrin aggregates can serve the function of wave guide where photoexcitation energy is funneled to reaction center via exciton migration. The scheme is inspired by natural light harvesting complexes [6.5,6.6] where protein scaffolds serve as template for strong excitonic interaction and long range dipole-dipole interaction which causes a gradual energetic shift of light absorbing chromophores from peripheral to core-reaction center. Thus an efficient downhill energy transfer is result of perfect chromophore stacking in antenna templates. However, porphyrin molecules are self-assembled by discrete or collective response of van der Waals, π−π∗, electrostatic and hydrogen bonding interactions.[6.7-6.9] Such self-assembly are susceptible to stacking disorders which lead to loss of photoexcitation energy in exciton trapping processes.[6.10,6.11] The exciton trapping imposes major difficulty in mimicking the energy transfer functionality of natural antenna complexes. In recent time, various porphyrin aggregates have been used to understand the exciton spectral and temporal properties

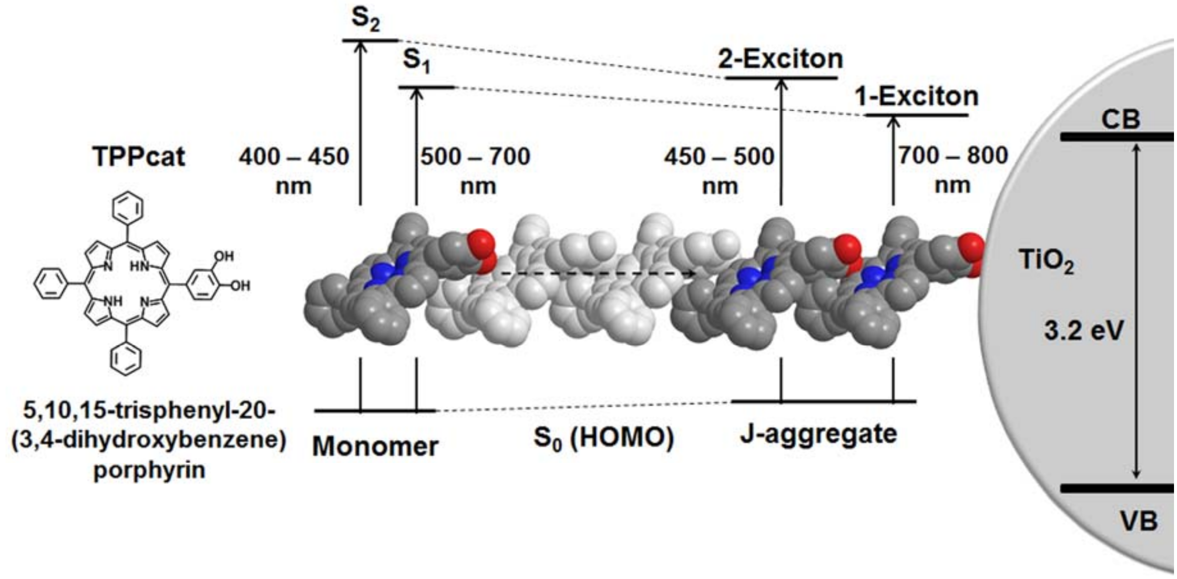

**Scheme 6.1:** Schematic diagram of porphyrin-J-aggregate/TiO$_2$ composite. The "head-to-tail" stacking pattern of porphyrin molecules in J-aggregate introduces exciton absorption band (450-500nm and 700-800nm) in spectral sensitization of TiO$_2$ NP.

in relevance to `light-harvesting-photovoltaic devices, photodynamic therapeutic use and advanced nonlinear optical materials.

The use of different functionality such as $SO_3^{-2}$, $PO_3^{-2}$, $COO^-$, OH on mesosubstituted phenyl ring have allowed different stacking pattern of porphyrins which has succeeded in controlling the intensity, width and relative energetic shift of exciton band.[6.16] In particular, the "edge-to-edge" stacking pattern of porphyrin J-aggregate has drawn significant attention due to their large optical response, ease of formation using zwitterionic-porphyrins and energy directing properties in comparison to cofacial H-aggregates.[6.12-6.15] In H-aggregates, smaller size domains act as exciton traps due to their lower exciton energy as compared to that of larger domains (Kasha's exciton theory [6.4]). So, J-aggregates are suitable for long range energy transfer processes in self-assembled molecular system. The large optical response of porphyrin J-aggregates is linked to low energetic Soret- and Q- exciton band in comparison to Soret- and Q-excited states of monomer.[6.12-6.16]

The excitonic interaction expands the optical response of porphyrin J-aggregates in visible region as compared to that of monomer porphyrin (scheme-6.1). The unique energy directional property and large optical response transform the porphyrin-J-aggregates into efficient photosensitizer for $TiO_2$ semiconductor material. The concept has been highlighted earlier in excitonic solar cell (XSC).[6.17] In such devices, the exciton is generated directly at hetero-interface or diffuses to it where it dissociates into free charge carriers. In particular, the electron is injected into conduction band (CB) of $TiO_2$ semiconductor substrate whereas hole resides on molecular adsorbate. Therefore, porphyrin-J-aggregate/$TiO_2$ system represents an electron-donor-antenna-bridge/acceptor material for DSSC.[6.20-6.21]

In porphyrin-J-aggregate/$TiO_2$ system, the exciton dissociation is conditional to charge-selective contacts where thermodynamic requirement is stated by barrier height between exciton-levels (donor) and substrate-Fermi level (acceptor). In this regard, $TiO_2$,[6.22] is proven semiconductor material for solar energy conversion due to its higher density of states (DOS), lower CB energetics and strong surface linkages. All these factors favor interfacial exciton dissociation. As counterpart, porphyrin-J-aggregate shows an ease of oxidation, large electrochemical activity and higher extinction coefficient which can formulates an efficient electron injection on $TiO_2$ substrate.[6.23-6.24] However, the kinetic factors which control the interfacial exciton dissociation are not very encouraging for photo-conversion process. The problems realized are exciton motion and its ultrafast decay which competes with interfacial charge carrier generation.[6.12, 6.25-6.26] Furthermore, the weak coupling offered by a near perpendicular meso-substituent phenyl bridge on porphyrin, refrains the exciton coherence from photo-conversion process.[6.27] A substantial criticality also arises from naturally fast decaying excited states ($S_2$ state ~ 50-300fs, $S_1$ state ~ 1-10 ns),[6.28, 6.29] of porphyrin monomer which coherence accounts for further ultrashort exciton life in J-aggregates. The reported exciton life time are as short as few 100 fs to 100 ps.[6.13, 6.30, 6.31] In addition, the aggregation defect (exciton trap) due to molecular displacement introduces non-radiative loss of photoexcitation energy.[6.32-6.34] These factors collectively restrict porphyrin antenna functioning towards interfacial charge separation which also occurs in ultrafast time domain.[6.35] As a result, porphyrin aggregates are less exemplified,[6.25-6.26,6.36] in sensitization studies. For practical realization, electron transfer from exciton states to the CB ($TiO_2$) should take place before onset of exciton decay (intrinsic) or exciton-exciton annihilation,[6.37,6.38] due to rising exciton concentration in the vicinity. So, in the present investigation, the major concern is to understand the generation of free charge carrier at semiconductor (substrate) interface by overruling the ultrafast exciton relaxation processes.

For this purpose, porphyrin catechol (TPPcat) is used in electron transfer study as it can aggregate and couple with $TiO_2$ nanoparticle surface through its meso-substituted catechol moiety (Scheme-6.1). The sensitizer molecule with catecholate moiety is known for its strong charge transfer (CT) complex formation with $TiO_2$ nanoparticle (NP).[6.39-6.43] The catehcol-$TiO_2$ linkage can favor interfacial exciton dissociation due to its higher binding energy ( ~1.15eV),[6.44,6.45] as compared to intrinsic exciton binding energy (usually large ~ 0.8-1.0 eV),[6.46] in porphyrin aggregates. So, catechol functionalized porphyrin-J-aggregates are used to study the interfacial exciton dissociation on sensitized $TiO_2$ NP's surface. Steady state absorption, emission, time-correlated-single-photon-counting (TCSPC) and femtosecond transient absorption spectroscopic studies are employed to understand the exciton spectral and temporal properties in generation of free charge carriers in porphyrin-J-aggregate/$TiO_2$ system.

## 6.2 Materials:

5,10,15-trisphenyl- 20-(3,4-dihydroxybenzene) porphyrin (TPPcat) synthesized following reported procedure.[6.47] $TiO_2$ NPs are prepared as mentioned in chapter-3.

### 6.2.1 J-aggregate preparation:

The aggregation process is optimized by varying the concentration in 1 – 125 μM range and then varying the pH in 1-10 range for each selected concentration. After detailed UV-visible studies, the optimum concentration of 20μM is selected for aggregate formation. The J-aggregate formation is optimized at pH 1.8. A stock solution of TPPcat (310 μM) is prepared in spectroscopy grade methanol. A known volume of stock solution is diluted to 20μM and $HNO_3$ acid is added immediately to adjust pH 1.8. The J-aggregation process start just after few minutes as monitored with UV-Vis spectroscopy. Finally, a stable J-aggregate is obtained and further no significant effects are seen even after many hours at room temperature. In another 20μM TPPcat aqueous solution, HCl acid is added to stabilize monomer TPPcat at pH 1.8. Mili-Q water is used for all sample preparation.

## 6.3 Results and discussion

### 6.3.1 J-aggregate formation: CD spectrum

Exciton coupled CD method is used to probe J-aggregate formation.[6.48] Figure-6.1 shows CD spectrum of monomer-TPPcat (1.8pH, HCl-aqueous solution) and J-aggregate (1.8pH, $HNO_3$-aqueous solution). The CD spectra of TPPcat-J-aggregates shows bisignate CD signature at

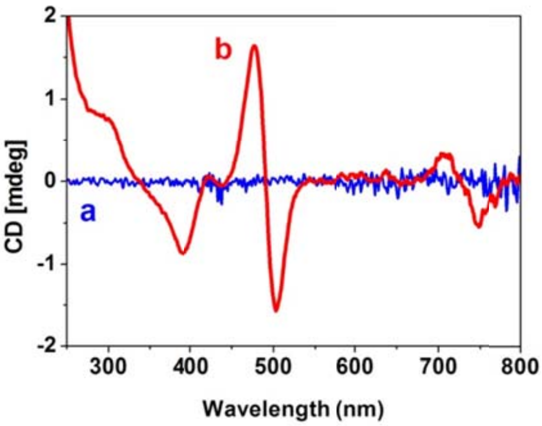

**Figure 6.1**: CD spectrum of 20μM TPPcat: (a) monomer, (b) J-aggregate.

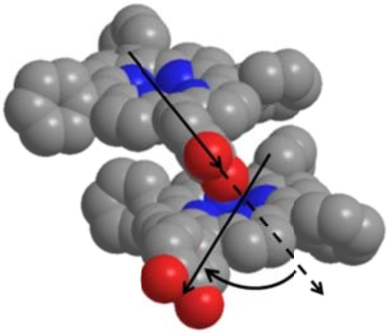

**Scheme-6.2**: J-aggregate-TPPcat.

490nm and 750nm which matches nicely with Soret and Q-exciton absorption peaks (addressed in next section). However, the monomer TPPcat shows no CD in this region. This suggest that nitrate ion might be facilitating the formation of J-aggregate through electrostatic interaction and H-bonding within the solvent network structure.[6.49-6.52] Presence of CD signature clearly show J-aggregate of TPPcat at pH 1.8 in HNO$_3$-aquous solution and monomer form of TPPcat at pH 1.8 in HCl-aqueous solution. The CD couplet pattern indicates the positive chiral twist (scheme-6.2) in J-aggregates which form the basis of exciton-coherence along aggregation axis.

### 6.3.2 Spectral sensitization of TiO$_2$ NPs: UV-Vis absorption spectrum

Figure 6.2a shows the absorption spectra of protonated monomer TPPcat at pH 1.8 in HCl-aqueous solution. It comprises a Soret band ($S_2 \leftarrow S_0$ transition) in 400-450 region and Q-band ($S_1 \leftarrow S_0$ transition) in 500-700 region (figure 6.1a). In non-protonated condition [6.47], monomer TPPcat exhibits one strong Soret band at 422nm and four minor Q-band's peaks at

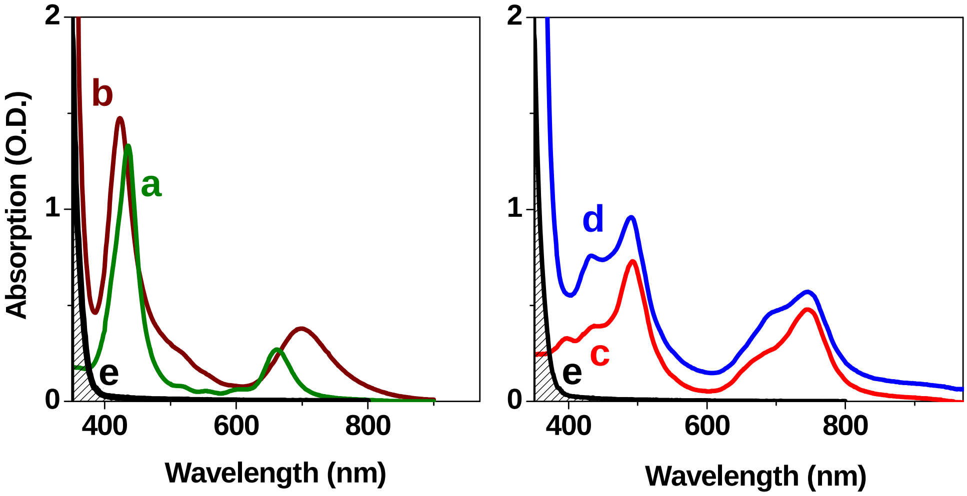

**Figure 6.2:** Optical absorption spectra of TPPcat (20 μM): (a) Monomer, (b) Monomer/$TiO_2$, (c) J-aggregate, (d) J-aggregate / $TiO_2$, (e) bare $TiO_2$ NP.

522, 559, 595, and 653nm. On protonation, the Soret band position is red shifted to 434 nm (Figure 6.2a). Furthermore, the protonation of porphyrin molecules results in change of symmetry from $D_2h$ to $D_4h$. As a result, Q-band comprises only one strong Q-band at 660nm. TPPcat forms J-aggregates in $HNO_3$ aqueous solution (pH 1.8), which exist in equilibrium with small amount of monomer form. In J-aggregates, Soret band peak intensity decreases at 434nm and a new band appears at 490nm. According to Kasha's exciton theory [6.4], the "in-phase" transition moment in parallel oriented dipole-dipole interaction of J-aggregate, appear in red region of corresponding monomer absorption bands. So, absorption peak at 490 nm is assigned to characteristic Soret exciton band of J-aggregate. Similarly, new peak appearing at 745nm is assigned to Q-exciton band. Thus, the spectral response of J-aggregate increases significantly in 460-500nm and 700-800nm region on account of Soret (2-exciton) and Q-exciton (1-exciton) bands (Figure-6.2c), respectively. On addition of $TiO_2$ NPs in J-aggregates, the relative increment in Soret- and Q-exciton absorption band and remarkable red shift in 800-970nm region can be attributed to exciton coupled CT complex formation (Figure 6.2d). It represents an integrated J-aggregate/$TiO_2$ system where exciton spectral properties can be perceived by charge transfer process at the interface. The presence of exciton coupled $TiO_2$ CT state is reconfirmed by photoluminescence studies and presented in next section (Figure 6.3).

### 6.3.3 CT emission: J-aggregate/$TiO_2$ NPs vs. monomer/$TiO_2$ NPs

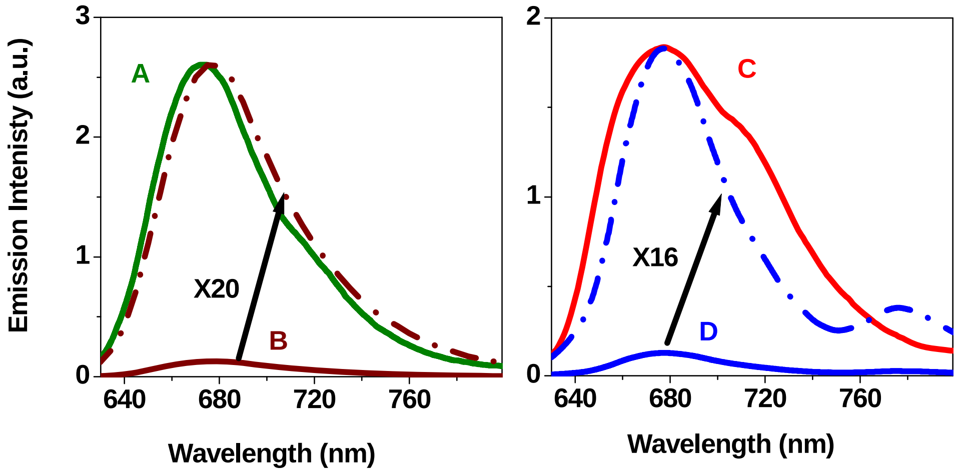

**Fgure-6.3**: Q-band emission spectra of different systems: (A) Monomer, (B) Monomer / $TiO_2$, (C) J-aggregate, (D) J-aggregate / $TiO_2$.

The photoluminescence (PL) of porphyrin occurs from lower energetic Q-excited state since the excitation in Soret- and Q-band region yields identical emission spectrum. Figure-6.3a shows emission spectrum of TPPcat after 460nm excitation at which absorbance of 20µM monomer TPPcat and J-aggregate TPPcat samples are nearly identical. The emission band at 654nm corresponds to $S_1 \rightarrow S_0$ transition and its shoulder at 718nm is assigned to transition to vibrationally excited states of the S$_0$ level. [6.9] It is evident from figure-6.3c that the emission is broadened in J-aggregated-TPPcat samples. The emission broadening is assigned to mixing of low energy Q-exciton emission band of J-aggregates with monomer emission band. The emission intensity decreases by 20folds in presence of TiO$_2$ NPs. For comparison purpose, normalized emission spectrum is shown in figure-6.3. The emission quenching in both the samples are attributed to photoinduced electron transfer on TiO$_2$ NP. However in J-aggregate/TiO$_2$ system, a characteristic red shifted emission is observed at 770 nm and assigned to CT emission.[6.53] Herein, a strong coupling of J-aggregate and TiO$_2$ NP, results in new hybridized states, which are known as CT states. These CT states are low energetic in comparison to exciton states of J-aggregate and are confined over TiO$_2$ surface.[6.54] Therefore, the red shifted emission at 770 nm, corresponds to direct back electron transfer from TiO$_2$ NP to J-aggregates of TPPcat. The Kinetics of CT recombination are investigated by time–resolved emission studies and presented in next section.

### 6.3.4 TCSPC measurements: Exciton coupled CT emission

Figure-6.4 shows transient emission kinetics of monomer TPP-cat, J-aggregate-TPPcat in presence and absence of TiO$_2$ NPs monitored at respective emission peak wavelengths (figure-6.3). The emission kinetics of TPPcat monomer (Figure-6.4a) is best fitted biexponentially with time constants of 2.6ns (74%) and 9.2 ns (26%) whereas J-aggregated porphyrin is best fitted with much shorter 180ps (85%) and 2.3 ns (15%) time constants (Figure-6.4b). The reduced radiative component (180ps) corresponds to exciton coherence (~14 Nc) of S1 states (Q-band). [6.37,6.38] The results are similar to earlier reported Q-exciton life time (150-300ps) and this rule out the exciton-exciton annihilation process for its short decay profile.[6.39-6.41] Also, it infer that though small amount of monomer-TPPcat exist in equilibrium with J-aggregate, photophysical properties are mainly dominated by exciton temporal property of J-aggregates. The transient emission kinetics of monomer- TPPcat/$TiO_2$ system is observed to be instrument response (~ 39ps) limited (~99.8%). However, comparatively slow emission kinetics is observed in J-aggregate/$TiO_2$ NPs where transient emission is monitored in exciton coupled CT emission band at 770 nm (figure-6.4d). The emission kinetics is fitted multiexponentially with 45ps (98.5%), 350ps (1.2%) and ~ns (0.3%) time constants.

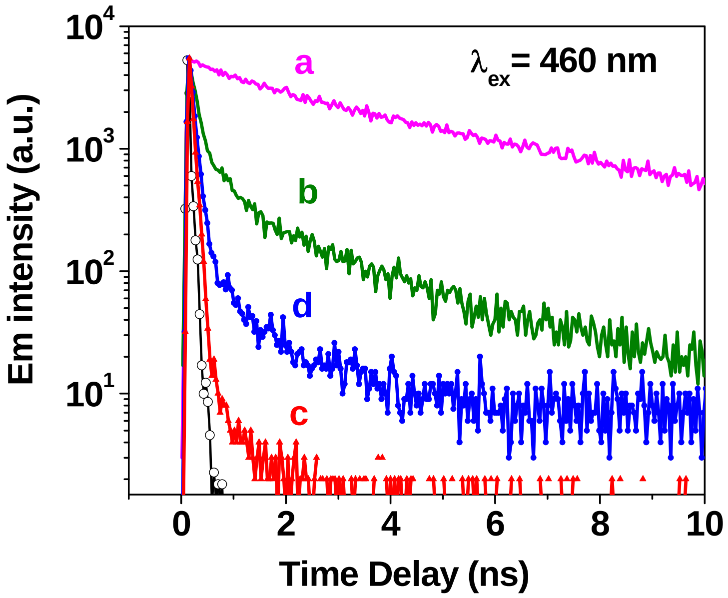

**Figure 6.4:** Emission decay traces for the TPPcat (20μM) using 460nm (~39ps FWHM) excitation wavelength: (a) Monomer, (b) J-aggregate, (c) Monomer/$TiO_2$, (d) J-aggregate / $TiO_2$.

Electron transfer in strongly coupled dye-catechol/$TiO_2$ system occurs in <50 fs time scale.[chapter-4, 5] So the shortest component 45ps (98.5%) cannot be attributed to electron transfer emission quenching. The ultrafast emission decay is attributed to exciton coupled charge recombination. The observance of CT emission confirms direct involvement of exciton coherence to interfacial charge separation phenomena which otherwise sees a diffusion limited loss of exciton states.[6.55] It infers a significant mixing of exciton states of J-aggregate and CT states of terminal TPPcat/$TiO_2$ coupling in J-aggregate/$TiO_2$ system. Therefore, a photo-induced charge separation can follow a dynamic delocalization while relaxing along exciton and CT potential surfaces [6.56]. So, the charge-carrier hopping is expected to be redefined in the system and further investigated by transient absorption (TA) pump-probe spectroscopy.

### 6.3.5 Excited state relaxation dynamics: Monomer vs. J-aggregate TPPcat

Transient emission kinetics revealed rapid (~180ps) relaxation of Q-exciton state. However, relaxation in Soret-exciton state could not be determined due to non-emissive Soret excited state as well as their ultrafast relaxation dynamics which are reported in ~100fs-500fs time scale. So, relaxation in Soret excited state of monomer-TPPcat and J-aggregate-TPPcat are investigated by transient absorption kinetics. Figure-6.5 shows TA spectrum of monomer (left panel) TPPcat and J-aggregate-TPPcat (right panel) after exciting at 400nm in Soret absorption band. The TA spectrum of monomer-TPPcat shows a negative absorption band (bleach) in 630-675 nm region and two excited absorption bands at 480 – 630 nm and 690 – 790 nm regions. The negative absorption is assigned to Q-band bleach and stimulated emission. On 400nm photoexcitation, higher Frank-Condon states of $S_2$ (Soret) state are directly populated. The appearance of pulse width limited Q-band bleach in 630-690n region suggests an ultrafast $S_2 \rightarrow S_1$ internal conversion. This is supported by pulse width limited Q-band excited state absorption in 480-630nm and 690-790nm regions. The transient spectra of J-aggregates exhibits new bleach bands in 470-500 nm and 700-750nm regions as compared to TA spectrum of monomer TPPcat.

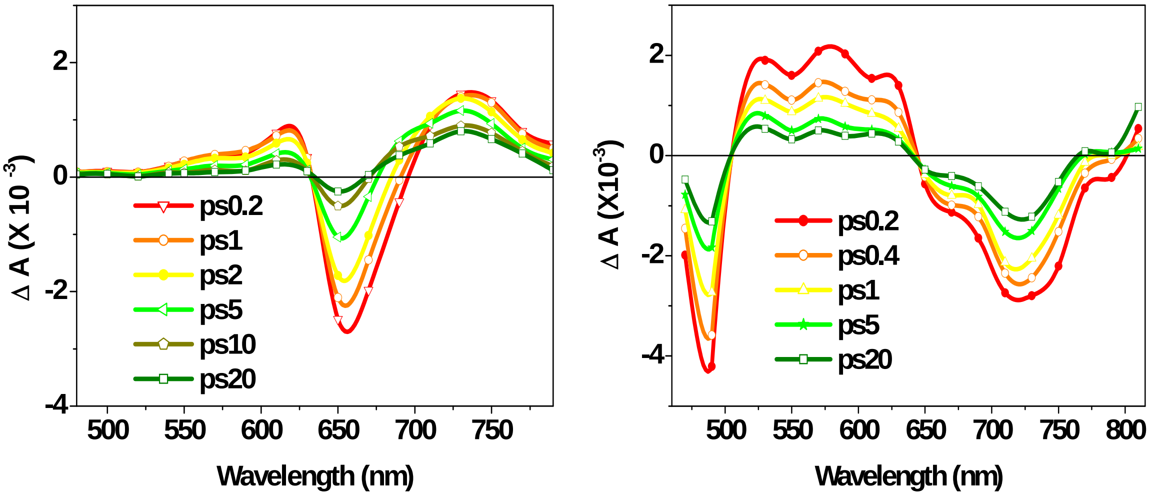

**Figure 6.5**: Transient absorption spectrum of monomer (Left Panel) and J-aggregated (right panel) TPPcat at different time delay after excitation at 400 nm.

The bleach band position at 490nm and 735nm matches well with steady state Soret- and Q-exciton bands, respectively. So, the bleach bands are attributed to $|1, S_2> \leftarrow |0, S_0>$ and $|1, S_1> \leftarrow |0, S_0>$ transitions, respectively. The positive transient absorption of J-aggregate increases in 500-630nm region as compared to that of monomer TPPcat and it is attributed to transient exciton state absorption.

On comparison of TA spectrum, it appears that ESA decay dynamics are faster in J-aggregate-TPPcat as compared to monomer-TPPcat. It is further evident in TA decay kinetics of monomer and J-aggregated TPP-cat as shown in figure-6.6. Figure-6.6a shows Q-band bleach recovery kinetics of monomer TPPcat at 650nm which is multiexponentially fitted with 4±1 ps, 20±5ps & 1ns time constants. Similar decay profile is observed in Q-band ESA at 610nm wavelength. This confirms that internal conversion from photoexcited higher Frank-Condon states of $S_2$ states to $S_1$ state accomplish in pulse width limited time. Earlier, Zewail and co-workers [6.57] have reported biphasic vibrational relaxation (1.5 ps and 15 ps) in TA study of tetraphenyl-poprhyrin ($H_2$TPP) monomer and attributed to intramolecular (solute) and intermolecular (solute-solvent) thermalization of hot $S_1$ state. Later, Kong and co-workers [6.58] have reported $S_2 \rightarrow S_1$ internal conversion within 10 fs time scale. So, in present study, a pulse width limited (< 100 fs) $S_2 \rightarrow S_1$ internal conversion results in vibrationally hot $S_1$ state which undergoes a biphasic (4±1 ps, 20±5ps) vibrational relaxation [6.12,6.29,6.47,6.59] to reach its final long lived $S_1$ state.

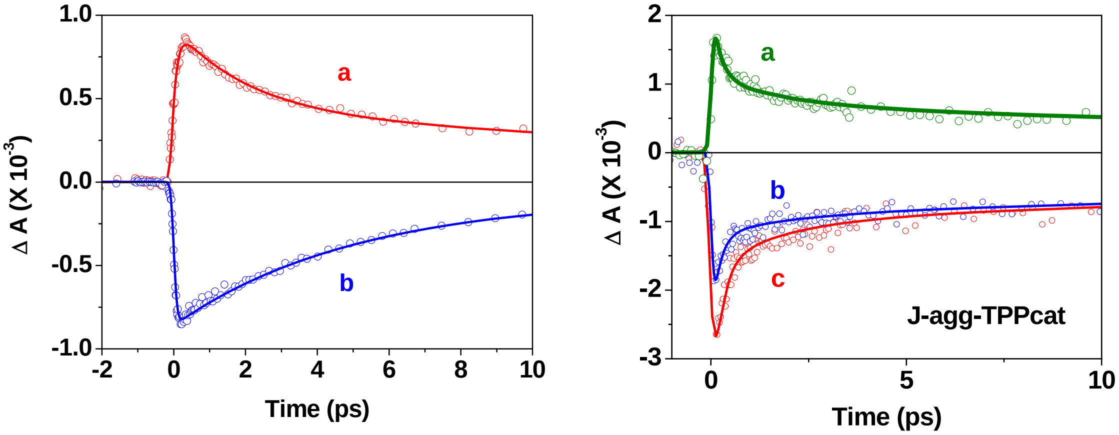

**Figure 6.6**: Left Panel: Normalized TA Kinetic of monomer TPPcat (a) at 610nm and at (b) 650nm; Right Panel: TA Kinetic of J-aggregated TPPcat (a) 610nm, b) 730, c) 490nm.

Figure-6.6 (Right panel) shows Soret- and Q-exciton bleach recovery dynamics and Q-exciton state absorption. The Soret exciton bleach recovery at 490nm is fitted multiexponentially with 200 fs (70 %), 1.5 ps (10%), 15 ps (10%) & > 400 ps (10%). The 610nm TA kinetics is fitted with 200 fs (50 %), 1.5 ps (16.5 %), 15 ps (16.5 %) & > 400 ps (9 %) time constants and observed to be same as that of 730nm Q-exciton-bleach recovery kinetics which is fitted with

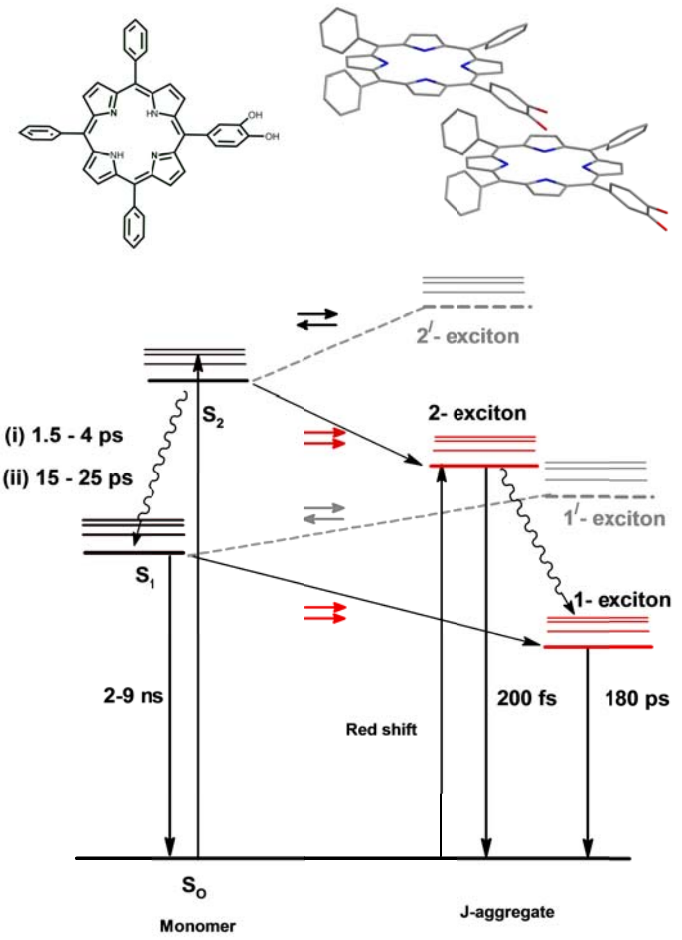

**Scheme-6.3**: Excited and exciton relaxation pathways in monomer and J-aggregated TPPcat.

200 fs (42 %), 1.5 ps (17%), 15 ps (13.5 %) and > 400 ps (13.4 %) time constants. Earlier, Diau and co-workers [6.12] have reported ultrafast (< 100fs) relaxation dynamics in J-aggregated zincporphyrin film. Kobayashi and co-workers [6.13] have observed Soret-exciton relaxation in 380fs using TPPS in solution phase. So, the ultrafast 200fs decay in 490nm bleach recovery dynamics of J-aggregated-TPPcat is assigned to Soret-exciton relaxation. The 1.5ps and 15ps decay components corresponds to biphasic vibrational relaxation in monomer TPPcat. It shows a

small amount of monomer TPPcat molecules exist in equilibrium with J-aggregates. Scheme 6.3 shows excited and exciton relaxation process in monomer and J-aggregate.

### 6.3.6 Interfacial electron transfer dynamics: monomer/$TiO_2$ *vs.* J-aggregate/$TiO_2$

Transient absorption and emission studies revealed an ultrafast ~200fs and 180ps relaxation of Soret and Q-exciton states. The rapid radiative decay of Q-exciton state (~180ps) as compared to Q-excited state (~2.2ns) refers to large exciton coherence (~14Nc) in J-aggregates. So, energy transducing antenna function of J-aggregates can be useful in interfacial electron transfer (IET) dynamics on $TiO_2$ NPs. In view of an ultrafast (~200fs, ~18ps) exciton relaxation, an efficient IET reaction would requires a competitive fast electron transfer dynamics on $TiO_2$ surface. This is evidenced in transient emission studies which indicate dynamic charge carrier delocalization while relaxing along exciton and CT potential surfaces. So, femtosecond time resolved absorption studies are carried out to understand exciton coupled charge transfer dynamics in J-aggregates/$TiO_2$ system in comparison to charge transfer dynamics of monomer TPPcat/$TiO_2$ system.

Figure-6.7 shows TA spectrum of monomer TPPcat/$TiO_2$ NPs (Top panel) and J-aggregate/$TiO_2$ NPs (bottom panel). TA spectra of monomer-TPPcat/$TiO_2$ system consist a broad positive TA band in 800-1000nm which is attributed to injected electron in the conduction band of $TiO_2$. (Chapter -4 and -5) The negative TA band in 670-740nm is assigned to Q-band bleach. The transient absorption due to porphyrin cation radical ($TPPcat^{+\bullet}$ ) appears in 490-650nm region which is confirmed by selective one electron oxidation in pulse radiolysis study. In addition, ESA due to CT interaction is also reported in 490-650nm region.[6.56] So, the broad positive TA band in the 490-650nm region is attributed to both excited state absorption of oxidized TPPcat (TPPcat+•) and ESA arising from CT interaction.

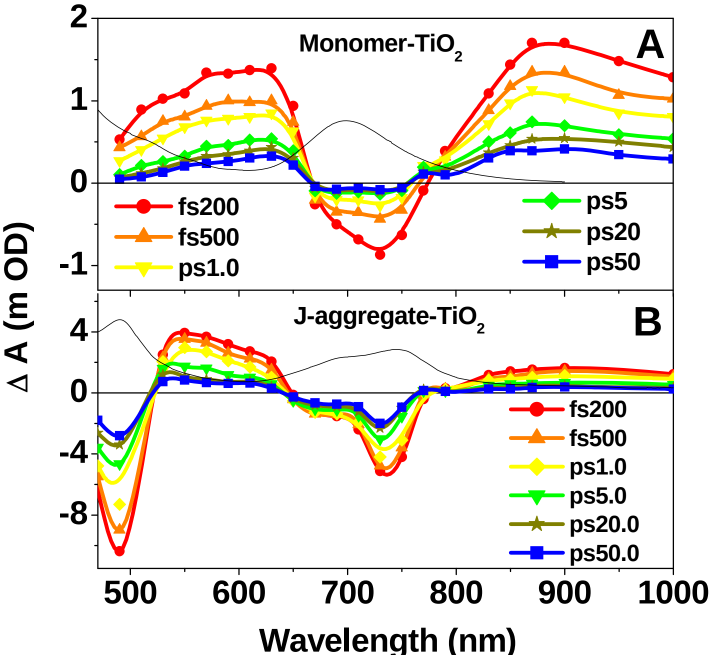

**Figure 6.7**: Transient absorption spectra of Monomer /$TiO_2$ NP (Panel-A) and J-aggregate /$TiO_2$ NP (Panel-B) at different time delay after exciting at 400nm laser light. (Steady state absorption is shown for comparison (thin line)).

TA spectrum of J-aggregate-TPPcat/$TiO_2$ NPs exhibits a new bleach band in 470-520 nm regions and an increased bleach band in 710-770nm regions. These bands are assigned to Soret- and Q-exciton coupled CT absorption band (Figure-6.2d). The positive absorption band in 800-1000nm region is assigned to electron in conduction band of $TiO_2$ NP. The broad TA band in 520-630nm is attributed to oxidized J-aggregate-TPPcat species formed after electron injection from photo excited J-aggregate-TPPcat to $TiO_2$ CB. In J-aggregate/$TiO_2$, the Soret- and Q-exciton bleach recovery (490nm and 730nm respectively) involve surface localized CT states due to strong interaction between catechol moiety and $TiO_2$ NP whereas TA kinetics at 1000nm corresponds to delocalized electron in CB of $TiO_2$ NPs. So, interfacial electron transfer dynamics are explored in bleach recovery (490nm or 730nm) and 1000nm TA kinetics. Figure 6.8 shows the normalized 1000 nm TA kinetics (CB $e^-$ in $TiO_2$) at and normalized 670nm bleach recovery

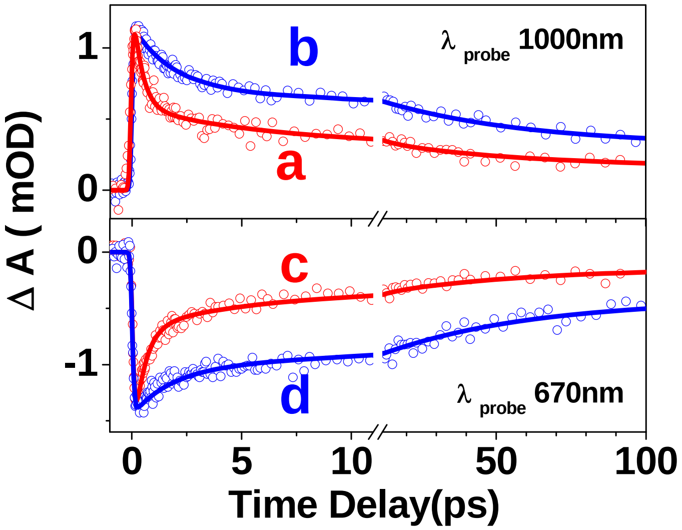

**Figure-6.8**: Normalized Kinetic decay traces of injected electron in CB of $TiO_2$ at 1000nm in (a) Monomer/$TiO_2$, (b) J-aggregate / $TiO_2$ system and normalized bleach recovery kinetics in (c) Monomer/$TiO_2$, (d) J-aggregate / $TiO_2$ at 670nm.

kinetics of monomer and J-aggregate sensitized $TiO_2$ NPs. The rise in TA at 1000 nm corresponds to electron injection which is observed to be pulse-width limited (< 80 fs) in both monomer-TPPcat/$TiO_2$ and J-aggregate/$TiO_2$ system. In chapter-4, -5, a pulse width limited ultrafast electron injection is observed from unthermalized MLCT states in Ru(II)- and Os(II)-complexes sensitized $TiO_2$ NP which is ascribed by strong CT interaction of catecholate moiety and $TiO_2$ NP. Similarly, the strong electronic coupling in monomer-TPPcat/$TiO_2$ NPs facilitates in electron injection from unthermalized excited states. In previous section, the TA study of unbound TPPcat (monomer) has revealed $S_2 \rightarrow S_1$ internal conversion (IC) in a pulse width limited (<100fs) ultrashort time scale. So, the ultrafast electron injection (<100fs) occurs from unthermalized $S_2$ and $S_1$ states. This is further supported by TA kinetics of monomer-TPPcat/TiO$_2$ which does not show any biphasic (4±1 ps, 20±5ps) vibrational relaxations which are characteristic to $S_1$ state thermalization processes (Figure-6.6). Herein, the ultrafast electron injection from unthermalized Soret- or Q- state cease the bi-phasic vibrational relaxation of hot Q-excited state and an instantaneous 670 nm Q-band bleach signal is observed (figure 6.8c).

In J-aggregates, the Soret- and Q-exciton coupling [6.31,6.60] promotes an efficient internal conversion process and its coherence (exciton states) results an ultrafast ~200 fs and ~180 ps decay of $S_2$ and $S_1$ states (figure-6.4 and -6.6). Since, terminal TPPcat of J-aggregates offer strong electronic coupling with TiO$_2$ NPs, than the exciton coupled charge transfer complex should prefer IET reactions over exciton relaxation. The ultrafast electron injection (< 80 fs) is observed in 1000nm TA kinetics. It shows that electron transfer occurs from unthermalized Soret- and Q-exciton states of J-aggregates before onset of its own (intrinsic) exciton relaxation process (~200fs and ~180ps). As a result, the Soret and Q-exciton relaxation (200fs and 180 ps) components are observed to be absent in bleach recovery (490nm, 670nm, 730nm) kinetics of J-aggregate/TiO$_2$ system (Figure -6.8,-6.9, and -6.10). This observation clearly indicates that both the excitonic states are able to inject electron in TiO$_2$ CB while leaving behind a hole on J-aggregate of TPPcat. The charge-separation is subject to recombination in due course of time and finally regenerates the ground state of dye (or J-aggregate)-TiO$_2$ system. In strongly coupled charge transfer (CT) system, the injected electron can localize at the surface due to strong CT interaction or can delocalize in the conduction band (high density of states) of TiO$_2$ NPs.

Therefore, the recombination dynamics is accordingly contributed by localized and delocalized electron very distinctly. The back electron transfer (BET) dynamics involving delocalized electron is determined by monitoring the 1000 nm transient signal or 670 nm bleach recovery kinetics. On comparison of 670nm TA decay kinetics (or 1000nm), the BET dynamic is observed to be slower in J-aggregate/$TiO_2$ system [1.8 ps (27.8%), 50 ps (41.1%), >ns (31.1%)] with respect to monomer TPPcat/$TiO_2$ system [400 fs (63.6%), 5 ps (13.3%), 50 ps (13.3%), > ns (10.8%)].

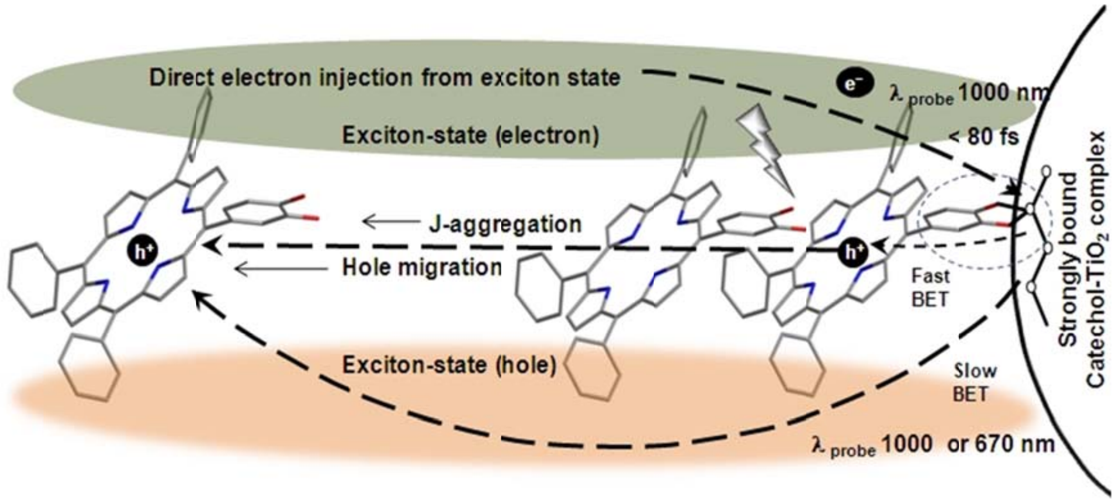

**Scheme 6.4**: Free charge carrier generation in Frenkel exciton coupled J-aggregate-porphyrin / semiconductor ($TiO_2$) composite system accomplish via interfacial exciton dissociation process. The separated hole is delocalized through excitonic coherence of J-aggregate. The immobilized hole is spatially less accessible to electron injected in $TiO_2$ and hence leads to slower back electron transfer.

In monomer TPPcat/$TiO_2$ system, the positive charge (hole) is localized on monomer TPPcat molecule near the $TiO_2$ NP's surface and the catecholate assisted strong electronic coupling leads to fast BET dynamics. However, in case of J-aggregate/$TiO_2$, the local field modification in the TPPcat building units results a highly delocalized Soret- and Q-exciton states whose HOMO (exciton) level is energetically higher than HOMO level of monomer TPPcat.[6.22] The hole produced after electron injection process is no longer bound to terminal TPPcat (closest to $TiO_2$ NP surface) but migrates away from J-aggregate/$TiO_2$ interface via higher lying exciton HOMO of J-aggregate. The hole hopping which is reported in sub-ns time domain for incoherent porphyrin units, can be as fast as sub ps time in J-aggregates due to coherent HOMO-level.[6.55,6.61,6.62] Such an ultrafast hole hopping leads to a better spatial charge separation on sensitized $TiO_2$ interface. As a result the BET process is slowed down in J-aggregate/$TiO_2$ system as compared to monomer-TPPcat/$TiO_2$ system (Scheme-6.4). This is one way the exciton coherence lead to better charge separation at the J-aggregate/$TiO_2$ interface.

In porphyrins, the meso-substituted phenyl rings are perpendicularly oriented which makes an electronically decoupled system. A recent density functional theory (DFT) calculation in TPPcat system,[6.63] shows that catechol moiety is appended near perpendicularly (Dihedral angle = 112.8°) to porphyrin ring. In such geometrical configuration, the catechol moiety remains no longer in full conjugation with porphyrin-π-electron system, and comprises its own HOMO. As a result, it makes a separate molecular interaction with $TiO_2$ NPs. Earlier, Bignozzi *et al* have shown weak electronic coupling between porphyrin and $TiO_2$ NP due to near perpendicular orientation of meso-substituted anchor rings.[6.27] This led to significant catehcol-$TiO_2$ CT character in addition to porphyrin-$TiO_2$ interaction within monomer-TPPcat/$TiO_2$ NPs system. Earlier, Lian and co-worker have reported transient absorption band of catechol/$TiO_2$ CT complex in 490-650nm region where CT dynamics are observed to be as fast as 400fs (contributes 60% in complete charge recombination).[6.56] The ultrafast decay kinetics have

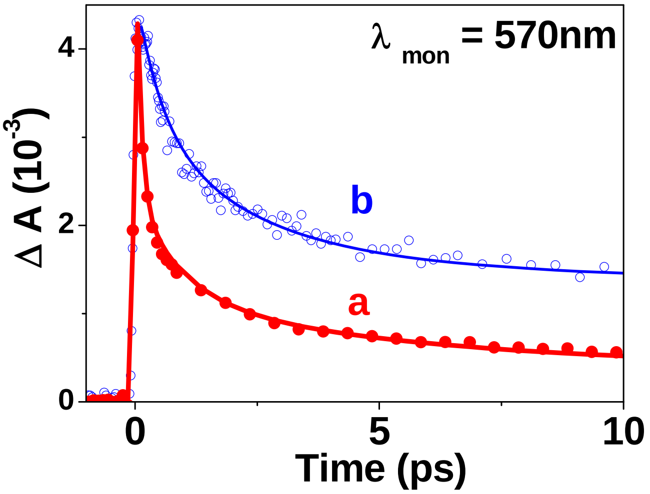

**Figure 6.9**: Kinetic decay traces monitored at 570nm (a) Monomer/TiO$_2$ (b) J-aggregate/TiO$_2$ systems.

been attributed to CT recombination of localized electron and catechol cation. Similar ultrafast decay is evidenced in TA spectrum of monomer-TPPcat/TiO$_2$ NPs in 490-600nm region. Figure-6.9a shows TA kinetics at 570nm of monomer-TPPcat/TiO$_2$ NPs which exhibits an ultrafast ~100fs (~54.4%) decay in addition to other 400 fs (22.7%), 5 ps (9.7%), 50 ps (6.7%) and > 1 ns (6.5%) components. The 400fs to ~ns time constants corresponds to TPPcat$^{+\bullet}$ cation decay as it matched to conduction band electron decay kinetics monitored at 1000nm (figure-6.8). The additional ultrafast decay component (100fs) is attributed to direct charge recombination of localized electron at terminal catechol/TiO$_2$ linkage. However, catechol-TiO$_2$ CT recombination is not observed in TA spectrum of J-aggregate-TiO$_2$ NPs. Figure-6.9b shows TA decay kinetics of J-aggregate-TPPcat/TiO$_2$ NPs at 570nm which is fitted with 500 fs (42.2%), 2 ps (18.8%) and 40 ps (17.8%) and > 1 ns (22.2%) time constants. In case of J-aggregate/TiO$_2$ system, only the terminal TPPcat can inherit the additional CT complex (pure catechol/TiO$_2$) whereas other

TPPcat molecules are stacked in J-aggregate and hence devoid of direct catechol assisted CT complex formation. At the same time, the exciton coherence of J-aggregate involves many TPPcat (coherence length NC ~14) units which facilitates electron injection into TiO$_2$ CB after photoexcitation of any constituent porphyrin unit. Thus, large exciton oscillator strength of J-aggregate in 400-800nm region suppresses the pure catechol/TiO$_2$ CT complex absorption in 400-600nm region. As a result, CT recombination due to ctahecol-TiO$_2$ CT band is absent in 570nm TA kinetics of J-aggregate/TiO$_2$ NPs. In J-aggregate-TPPcat, 570nm TA kinetics shows an additional ~500fs (~42%) decay in comparison to 1000nm decay kinetics (figure 6.9). Transient absorption at 1000nm corresponds to delocalized conduction band electron. So, the ultrafast component ~500fs can be due to exciton coupled CT dynamics in J-aggregate/TiO$_2$ NPs.

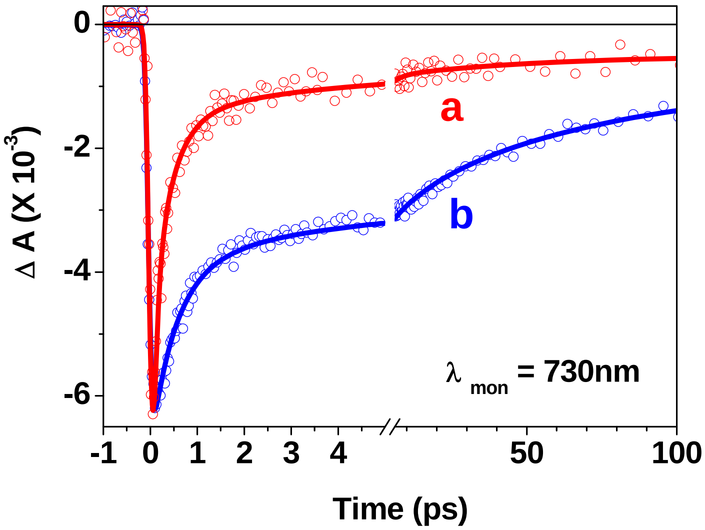

**Figure 6.10**: CT kinetics of (a) Monomer-TPPcat/TiO$_2$, (b) J-aggregate-TPPcat / TiO$_2$ at 730nm.

The exciton coupled charge transfer dynamics of J-aggregate-TPPcat/$TiO_2$ NPs are confirmed in 730nm bleach recovery kinetics as shown in figure-6.10. The bleach recovery at 730nm is fitted multi-exponentially with 500 fs (40%), 2.4 ps (16%), 40 ps (16%), >ns (22%) time constants for J-aggregate/$TiO_2$ and 100 fs (54%), 400 fs (29.1%), 3ps (5.8%), 50 ps (3%), >ns (8.1%) for monomer-TPPcat/$TiO_2$. The ultrafast 100fs bleach recovery represents CT recombination at catechol-$TiO_2$ linkage in monomer-TPPcat/$TiO_2$ NPs whereas 500fs bleach recovery arises from exciton coupled CT recombination in J-aggregateTiO$_2$ NPs. In J-aggregates, the Qx (or Bx) transition moment of many TPPcat units (constituting the "head-to-tail" pattern along J-aggregation axis) interact strongly to produce exciton states with their k (exciton) vector oriented in direction of $TiO_2$ CB acceptor states. The J-aggregates retains these coherent excited states (exciton) on $TiO_2$ NP surface and sensitize it as a single entity via its terminal TPPcat. In previous section, the J-aggregate/$TiO_2$ CT complex is pointed out in steady state absorption and emission studies. So, the shortest component of 500fs in bleach recovery dynamic at 730nm is assigned to the exciton coupled CT transition of J-aggregate-TPPcat/$TiO_2$ system. In this case, the bleach recovery kinetics at 730 nm represents recombination dynamics of localized electron and cation of J-aggregate.

### 6.4. Conclusion:

Charge carrier generation in exciton coupled charge transfer complex J-aggregate-porphyirns/$TiO_2$ NP is explored in transient absorption and emission studies. For this purpose, TPPcat is used as building block for J-aggregation. J-aggregate formation is confirmed by steady state absorption, emission, and circular dichroism studies. Steady state absorption has revealed that spectral response of J-aggregate-TPPcat extends to visible and near IR region due to presence of Soret- and Q-exciton band in addition to Soret- and Q-excited state of monomer-TPPcat absorbing in 400-450nm and 630-700nm regions. Spectral sensitziation of TiO$_2$ NPs is confirmed in steady state absorption and emission studies which revealed exciton coupled CT states in J-aggregate/TiO$_2$ NPs. Transient absorption and emission studies has revealed ultrafast ~200fs and ~180ps lifetime of Soret- and Q-exciton state, respectively. The ultrafast radiative decay of Q-exciton revealed exciton coherence length of ~14 Nc order. Transient absorption studies of J-aggregate/TiO$_2$ system has revealed an ultrafast (<100fs) electron injection dominating over fast exciton (~200fs and ~180ps) relaxation of J-aggregates. The kinetics competition in favor of interfacial electron transfer is attributed to the strong electronic coupling between terminal porphyrin-catechol and TiO$_2$ NP which facilitates an ultrafast electron injection from exciton states well before onset of intrinsic exciton (~200fs, 180ps) relaxation process. The exciton dissociation at interface is gained from large binding energy (> 1.0 eV) for catechol-TiO$_2$ system. The resulting interfacial charge separation is stabilized via hole migration within J-aggregates. The exciton coherence (~14Nc) of J-aggregates helps to immobilize hole in ultrafast time scale which increase the interfacial charge separation. The study shows that the antenna functioning of circular aggregates and primary charge separation at the interface (reaction centre) can be coupled in favor of efficient charge carrier generation (electron/hole) in photon-processing units.

## 6.5 References:

[6.1] F. J. M. Hoeben, P. Jonkheijm, E. W. Meijer, A. P. H. J. Schenning, Chem. Rev. 2005, 105, 1491.

[6.2] M. R. Wasielewski, Acc. Chem. Res. 2009, 42, 1910.

[6.3] A. S. Davydov, Theory of Molecular Excitons; McGraw-Hill, NewYork, 1962,

[6.4] E. G. McRae, M. J.Kasha, in Physical Processes in Radiation Biology, Academic Press, New York, 1964, 23.

[6.5] A. N. Glazer, S. W. Yeh, S. P.Webb, J. H. Clark, Science 1985, 227, 419–423.

[6.6] R. Huber, Angew. Chem. Int. Ed. 1989, 28, 848.

[6.7] M. Shirakawa, S. -I. Kawano, N. Fujita, K. Sada, S. Shinkai, J. Org. Chem. 2003, 68, 5037.

[6.8] K. Kano, K. Fukuda, H. Wakami, R. Nishiyabu, R. F. Pasternack, J. Am. Chem. Soc. 2000, 122, 7494.

[6.9] K. Kano, H. Minamizono, T. Kitae, S. Negi, J. Phys. Chem. A 1997, 101, 6118.

[6.10] L. D. A. Siebbeles, A. Huijser, T. J. Savenije, J. Mater. Chem., 2009, 19, 6067.

[6.11] S. M. Vlaming, E. A. Bloemsma, M. L. Nietiadi, J. Knoester, J. Chem. Phys. 2011, 134, 114507.

[6.12] L. Luo, C.F. Lo, C. Lin, I. Chang, E.W. Diau, J. Phys. Chem. B 2006, 110, 410.

[6.13] H. Kano, T. Kobayashi, J. Chem. Phys. 2002, 116, 184.

[6.14] E. Collini, C. Ferrante, R. Bozio, J. Phys. Chem. C2007, 111, 18636.

[6.15] S. M. Vlaming, R. Augulis, M. C. A. Stuart, J. Knoester, P. H. M. van Loosdrecht, J. Phys. Chem. B, 2009, 113, 2273.

[6.16] D. L. Akins, H.-R. Zhu, C. Guo, J. Phys. Chem. 1996, 100, 5420.

[6.17] Gregg, B. A.; J. Phys. Chem. B 2003, 107, 4688.

[6.18] C.-W. Lee, H.-P. Lu, C.-M. Lan, Y.-L. Huang, Y.-R. Liang, W.-N. Yen, Y.-C. Liu, Y.-S. Lin, E. W.-G. Diau, C.-Y. Yeh, Chem. Eur. J., 2009, 15, 1403.

[6.19] R. Ma, P. Guo, H. Cui, X. Zhang, M. K. Nazeeruddin, M. Grätzel, J. Phys. Chem. A,2009, 113, 10119.

[6.20] H. Imahori, T. Umeyama, S. Ito, Acc. Chem. Res., 2009, 42, 1809.

[6.21] A. Mishra, M. K. R. Fischer, Peter Bäuerle, Angew. Chem. Int. Ed.2009, 48, 2474.

[6.22] D. F.Watson, G. J. Meyer, Annu. Rev. Phys. Chem. 2005, 56,119.

[6.23] Y. He, E. Borguet, Angew. Chem. Int. Ed. 2007, 46, 6098.

[6.24] A. Takai, C. P. Gros, J.-M. Barbe, R. Guilard, S. Fukuzumi, Chem. Eur. J.2009, 15, 3110.

[6.25] A. Huijser, B.M.J.M. Suijkerbuijk, R.J.M.K. Gebbink, T.J. Savenije, L.D.A. Siebbeles, J. Am. Chem. Soc., 2008, 130, 2485.

[6.26] A. Huijser, T.J. Savenije, J.E. Kroeze, L.D. A. Siebbeles, J. Phys. Chem. B, 2005, 109, 20166.

[6.27] F. Odobel, E. Blart, M. Lagré, M. Villieras, H. Boujtita, N. E. Murr, S. Caramoric, C. A. Bignozzi, J. Mater. Chem., 2003, 13, 502.

[6.28] M. Enescu, K. Steenkeste, F. Tfibel, M.-P. Fontaine-Aupart, Phys. Chem. Chem. Phys., 2002, 4, 6092.

[6.29] A. Marcelli, P. Foggi, L. Moroni, C. Gellini, P.R. Salvi, I.J. Badovinac, J. Phys. Chem. A2007, 111, 2276.

[6.30] E. Collini, C. Ferrante, R. Bozio, J. Phys. Chem. C2007, 111, 18636.

[6.31] H. Kano, T. Saito, T. Kobayashi, J. Phys. Chem. A, 2002, 106, 3445.

[6.32] S. M. Vlaming, R. Augulis, M. C. A. Stuart, J. Knoester, P. H. M. van Loosdrecht, J. Phys. Chem. B, 2009, 113, 2273.

[6.33] A. V. Sorokin, I. I. Filimonova, R. S. Grynyov, G. Y. Guralchuk, S. L. Yefimova, Y. V. Malyukin, J. Phys. Chem. C, 2010, 114, 1299.

[6.34] V. Gulbinasa, R. Karpicza, R. Augulisc, R. Rotomskisc, Chem. Phys., 2007, 332, 255.

[6.35] Y. Tachibana, J. E. Moser, M. Gra1tzel, D. R. Klug, J. R. Durrant, J. Phys. Chem. 1996, 100, 20056.

[6.36] C.-W. Chang, L. Luo, C.-K. Chou, C.-F. Lo, C.-Y. Lin, C.-S. Hung, Y.-P. Lee, E. W.-G. Diau, J. Phys. Chem. C, 2009, 113, 11524.

[6.37] M. R. Wasielewski, Chem. Rev., 1992, 92, 441.

[6.38] Sundström, V., Gillbro, T., Gadonas, R. A., Piskarskas, A., J. Chem. Phys., 1988, 89, 2754.

[6.39] P. Persson, R. Bergström, S. Lune, J. Phys. Chem. B, 2000, 104, 10348.

[6.40] T. L. -Villarreal, A. Rodes, J. M. Pérez, R. Gómez, J. Am. Chem. Soc. 2005, 127, 12601.

[6.41] G. Ramakrishna, A. K. Singh, D. K. Palit, H. N. Ghosh, J. Phys. Chem. B, 2004, 108, 1701.

[6.42] O. V. Prezhdo, W. R. Duncan, V. V. Prezhdo, Progress in Surface Science, 2009, 84, 30.

[6.43] L. Gundlach, R. Ernstorfer, F. Willig, Phys. Rev. B, 2006, 74, 035324.

[6.44] S.-C. Li, L.-N. Chu, X.-Q. Gong, U. Diebold, Science, 2010, 328, 882.

[6.45] P. C. Redfern, P. Zapol, L. A. Curtiss, T. Rajh, M. C. Thurnauer, J. Phys. Chem. B2003, 107, 11419.

[6.46] X.-F. Ren, A.-M. Ren, J. -K. Feng, X. Zhou, Organic Electronics, 2010, 11, 979.

[6.47] A. D. Jose, A. D. Shukla, D. Krishnakumar, B. Ganguly, A. Das, G. Ramakrishna, D. K. Palit, H. N. Ghosh, Inorg Chem. 2005, 44, 2414.

[6.48] A. S. R. Koti, N. Periasamy, Chem. Mater., 2003, 15, 369.

[6.49] S.C. Doan, S. Shanmugham, D. E. Aston, J. L. McHale, J. Am. Chem. Soc. 2005, 127, 5885.

[6.50] S. Okada, H. Segawa, J. Am. Chem. Soc., 2003, 125, 2792.

[6.51] M.Y. Choi, J.A. Pollard, M. A. Webb, J. L. McHale, J. Am. Chem. Soc. 2003, 125, 810.

[6.52] X. Li, D. Li, W. Zeng, G. Zou, Z. Chen, J. Phys. Chem. B, 2007, 111, 1502.

[6.53] S. Verma, P. Kar, A. Das, D. K. Palit, H. N. Ghosh, J. Phys. Chem. C 2008, 112, 2918.

[6.54] O. V. Prezhdo, W. R. Duncan, V. V. Prezhdo, Progress in Surface Science, 2009, 84, 30.

[6.55] D. Holten, D. F. Bocian, J. S. Lindsey, Acc. Chem. Res.2002, 35, 57.

[6.56] Y. Wang, K. Hang, N. A. Anderson, T. Lian, J. Phys. Chem. B, 2003, 107, 9434.

[6.57] J.S. Baskin, H. Z. Yu, A. H. Zewail, J. Phys. Chem. A, 2002, 106, 9837.

[6.58] Q. Zhong, Z. Wang, Y. Liu, Q.H. Zhu, F.A. Kong, J. Chem. Phys. 1996, 105, 5377.

[6.59] O.J. Scherer, S. F. Fischer, Chem. Phys. 1984, 86, 269.

[6.60] J. Zimmermann, U. Siggel, J.H. Fuhrhop, B. Ro1der J. Phys. Chem. B2003, 107, 25, 6019.

[6.61] I.-W. Hwang, M. Park, T. K. Ahn, Z. S. Yoon, D. M. Ko, D. Kim, F. Ito, Y. Ishibashi, S. R. Khan, Y. Nagasawa, H. Miyasaka, C. Ikeda, R. Takahashi, K. Ogawa, A. Satake, Y.Kobuke, Chem. Eur. J., 2005, 11, 3753.

[6.62] Y. H. Kim, D. H. Jeong, D. Kim, S. C. Jeoung, H. S. Cho, S. K. Kim, N. Aratani, A. Osuka, J. Am. Chem. Soc. 2001, 123, 76.

[6.63] C. -R. Zhang, Y. -H. Chen, Z. –S. Pu, Z. –Q. Wei, D. –B. Wang, Y. –Z. Wu, H. –S. Chen, Atom. Mol. Phys., 2008, 25, 1241.

# CHAPTER 7

# EMPLOYING A PHOTOSYNTHETIC ANTENNA COMPLEX TO INTERFACIAL ELECTRON TRANSFER ON ZnO QUANTUM DOT.

## 7.1 Introduction:

The light harvesting mechanisms in cyanobacteria have enlightened a very important aspect of energy migration in closely coupled protein-pigments.[7.1] The energy migration in light harvesting pigment -phycobilisome (PBS) takes place with overall efficiency of 95%.[7.2] The multilayer interfacing of phycocyanin (PC) discs in rod region to allophycocyanin (APC) core region makes a large association of light absorbing phycocyanobilin (PCB) chromophores in PBS.[7.3] The excitonic interaction and dipole-dipole interaction between PCB chromophores lay foundation of downhill energy transfer from peripheral PC pigment to APC core in ~100ps time scale.[7.4-7.8] According to structure-function relationship[7.9], αβ polypeptide pair (monomer) assemble in ring symmetry (trimer/hexamer) which expresses the genesis of sub ps energy transfer in coherently aligned PCB-chromophores (α84 and β84 cysteine residue) within PC and APC core pigments.[7.10,7.11] Further, the Förster energy transfer cascade from outer core PCB chromophore (β155) to inner core PCB chromophore (α84) in multitude of PC discs set upper limit of ~100ps for energy transfer in the PBS complex.[7.12] Accordingly, the Förster coupled-chromophores devise subset of "sensitizing (s)" and "fluorescing (f)" chromophores which cover a broad spectral region (visible) on account of gradual energetics shift of PCB chromophores in peripheral to core region of the PBS entity.[7.13]

The PBS complex can formulate antenna function [7.14,7.15] as a result of unique energy directing property and broad spectral response which are suitable for light harvesting devices,

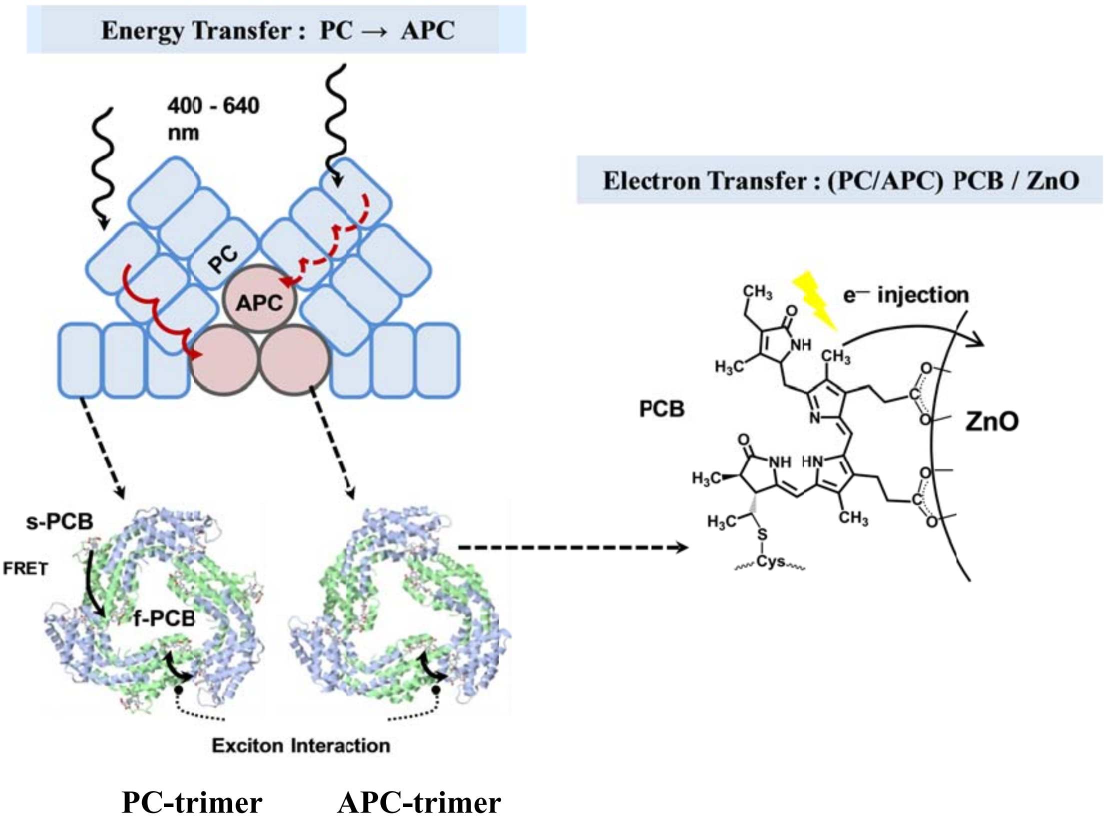

**Scheme-7.1.** A: The ring assembly of PC and APC unit for coherent and incoherent energy transfer. B: Phycocyanobilin-apoprotein sensitization of ZnO.

sensor and photo-catalytic application. Recently, PBS as extracted in native form, are employed in luminescent solar concentrator [7.16] with a function of redirecting captured photon energy onto optically coupled solar cell unit. However, a direct involvement of PBS antenna complex in interfacial electron transfer (IET) process is hindered by multitude of parallel and sequential energy transfer [7.1-7.13] processes in PBS antenna complex. In principle, the pigment-protein has high potential to develop efficient photosensitizer for semiconductor nanocrystal or quantum-dot material due to its high molecular extinction coefficient (~ $10^5$ $M^{-1}cm^{-1}$) and phenomenal unidirectional energy transport property.[7.17] In this chapter, antenna functionality of PC-APC conjugate is used to generate interfacial charge separation on ZnO semiconductor quantum dot (QD) material. Herein, "PC-APC conjugate" term refers to PBS antenna complex extracted from Synechococcus BD1,[7.18] in HEPES buffer solution at pH 8.0. The labeling "PC-APC conjugate" postulates energy transfer function from PC to APC units. The ZnO semiconductor material is selected for its good pH compatibility with PBS-buffer solution (8.0pH) and suitable conduction band (CB ~ -0.45 eV vs. NHE) energetic.[7.19] The carboxylate functionality of PCB chromophore helps in binding on ZnO surface as depicted in scheme-7.1.

In PC-APC conjugate sensitized ZnO system (Scheme-7.1), the electron injection process can initiate first from directly photoexcited PC entity (PCB chromophore, [7.20]). The significant PC-APC coupling can help in getting additional electron transfer pathway from APC unit by receiving captured photo-energy from non-participating PC entity. In this way PBS, antenna functionality may circumvent the loss of non-participating photoexcited states of PC complex and can provide better charge separation. In this chapter, the antenna function of phycocyanin-allophycocyanin (PC→APC) complex is explored by transient emission and absorption spectroscopy. Further, the role of PC-ACP antenna function is aimed at interfacial electron-transfer dynamics of PC→APC complex sensitized ZnO semiconductor quantum dot material in native and denatured conditions

## 7.2 Materials:

Native PC-APC conjugate is extracted from Synechococcus BD1 by following previously reported procedure.[7.18]

### 7.2.1 Preparation of ZnO quantum dots:

ZnO QDs are prepared by controlled hydrolysis of Zinc(II) acetate. In brief, 8 mM Zinc acetate (99.99%, Aldrich) is added to 400ml water (conductivity 18.2 mho/cm) at 70°C and stirred for 20 minutes. 3-Mercaptopropionic acid (MPA) is added as capping agent and the solution is adjusted to 9pH with NaOH. The solution is stirred continuously for 24 hrs. at 90°C. The ZnO QD synthesis is monitored by steady state absorption spectra. Final solution is concentrated using rotavapor and ZnO QD is precipitated using isopropyl alcohol. The white turbid solution is centrifuged immediately and ZnO pallet is redissolved in aqueous solution. After adequate washing, ZnO QDs are used for sensitization study.

## 7.3 Results and discussion

### 7.3.1 Photophysical properties of ZnO QDs:

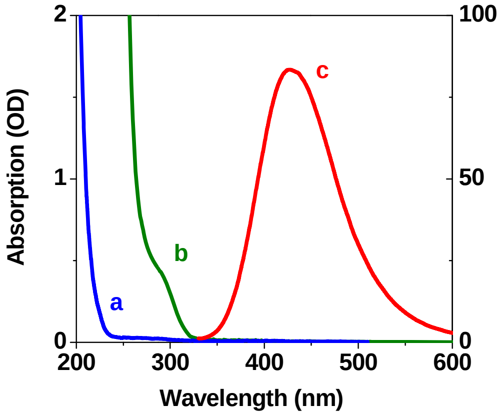

**Figure 7.1:** Absorption spectrum of a) zinc acetate and b) ZnO QD. c) Emission spectra of ZnO QD with photoexcitation at 290nm.

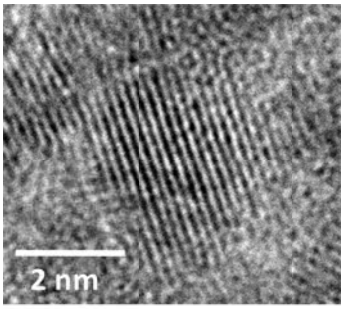

**Figure 7.2**: HR-TEM image of ZnO QD

Figure-7.1 shows optical absorption and emission spectrum of ZnO QDs dispersed in aqueous solution. The exciton absorption peak of ZnO QD is observed at 295nm which suggests particle size of ≤ 2.7 nm (Brus equation, chapter-1) for ZnO QDs. The broad emission peak in 350-600nm region (very large stroke shift >100nm) corresponds to trap states of ZnO QD. Figure 7.2 shows the HRTEM image of ZnO QD.

### 7.3.2 Photophysical properties of native PC-APC complex:

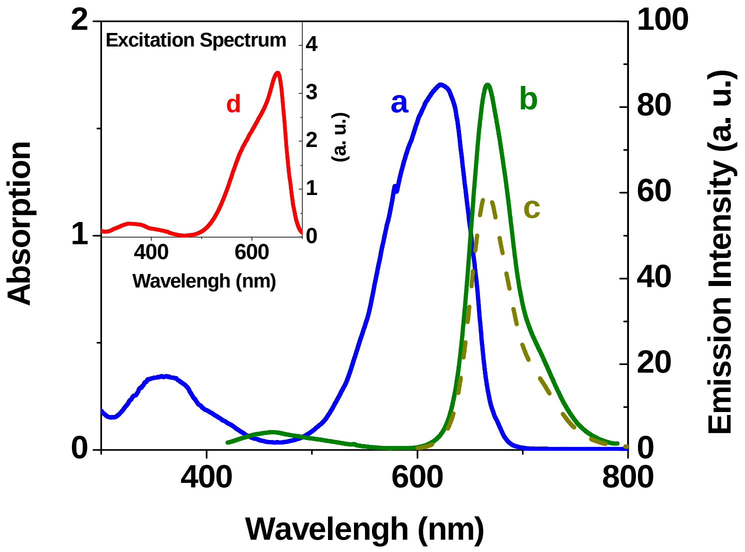

**Figure 7.3:** a) Steady state absorption spectra of PC-APC conjugate (~4.7μM); Emission spectrum of native PC-APC conjugate at b) 400nm excitation and c) 590nm excitation. (Inset: Excitation spectrum at 725nm emission wavelength).

Figure-7.3 shows the steady state absorption, emission and excitation spectra of native PC-APC conjugate in HEPES buffer solution. The absorption spectrum comprises two bands in 300-450nm and in 500-700nm region which correspond to Soret- ($S_2$) and Q- ($S_1$) states of linear tetrapyrrole -PCB chromophores bound in protein matrix.[7.21] The intense band in red region exhibits peak at 623nm with shoulder at 655nm which is assigned to PC and APC units in native complex.[7.1-7.13] The 655nm peak of APC unit is confirmed in excitation spectrum (Figure-7.3; inset). Figure-7.3b and 7.3c show emission spectra of native PC-APC complex at 400nm and 590nm excitation wavelengths ($S_2$ and $S_1$ state, respectively). Both the emission spectra are identical and comprise an intense emission peak at 665nm with a shoulder at 720nm. The excitation spectrum ($\lambda_{em}$ 725nm) of native PC-APC conjugate comprises an intense peak at 655nm which matches to weak absorption band at 655nm. In PC-APC native complex, efficient energy transfer (~95%) from PC to APC results emission from APC units. So, excitation peak at 655nm corresponds to APC units. The weak absorption peak appearing at 655nm represents relatively smaller APC content as compared to PC content (absorbing at 623nm) in native PC-APC conjugate.

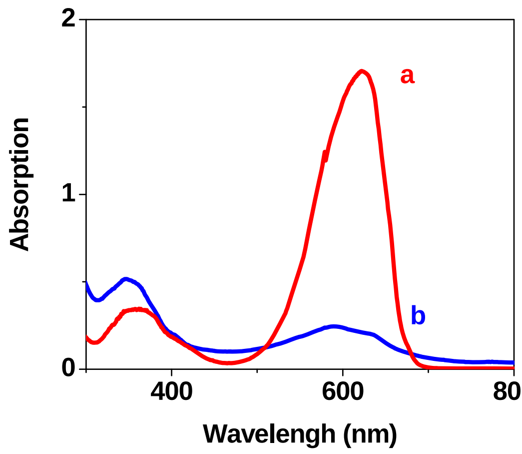

**Figure 7.4:** Absorption spectra of PC-APC conjugate in a) native condition, b) denatured condition. (Concentration is kept same at 4.7μM).

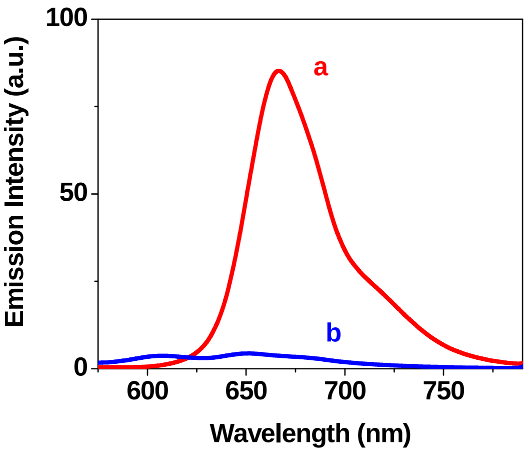

**Figure 7.5:** Emission spectra of PC-APC conjugate in a) native condition, b) denatured condition. (Absorbance is kept same at $\lambda_{ex}$ 400nm).

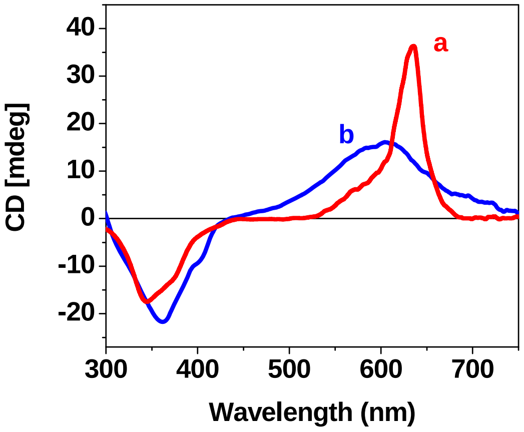

**Figure 7.6**: CD spectra of PC-APC conjugate in a) native condition, b) denatured condition (8M urea).

This is further supported by absorption, emission and circular dichroism (CD) spectrum of PC-APC complex in denatured condition as shown in figure-7.4, figure-7.5 and figure-7.6, respectively. On addition of 8M urea, the absorbance decreases drastically and comprises two bands at 600 and 635nm. Likewise, emission spectrum also quenches drastically and splits into blue shifted 610nm and 654nm broad bands. The appearance of two peaks in absorption and emission spectra corresponds to isolation of PC and APC units. The denaturation is confirmed by CD spectrum of PC-APC complex. The native PC-APC complex exhibits a sharp CD peak at 640nm which is blue shifted to 600nm in presence of 8M Urea. On denaturation, the protein scaffolds open-up which remove the PC-APC conjugation. Thus, reduced and split emission spectrum is result of loss of energy transfer mode from PC to APC units in denatured protein. Conversely, it establishes an efficient PC to APC energy transfer in native condition.

### 7.3.3 Spectral sensitization of ZnO QDs: PC-APC/ZnO QDs:

Spectral sensitization of ZnO QDs are evidenced in absorbance increase and electron transfer emission quenching as shown in figure-7.7 and -7.8, respectively. On addition of ZnO QDs, the absorbance increases significantly throughout 350-800nm regions. This shows that the carboxylate functionality of PCB chromophore (located on both PC and APC units) offer significant binding on ZnO QDs as shown in sheme-1. It forms the basis of electron transfer from photoexcited PC and APC units which are observed in electron transfer emission quenching measurements (figure-7.8). Photoexcitation at 400nm mainly populates the PCB chromophore located on peripheral PC pigment whereas emission is observed from APC units due to efficient PC→APC energy transfer. Therefore, a ~90 % emission quenching in presence of ZnO QDs indicates that energy transfer antenna functioning supports the electron transfer process.

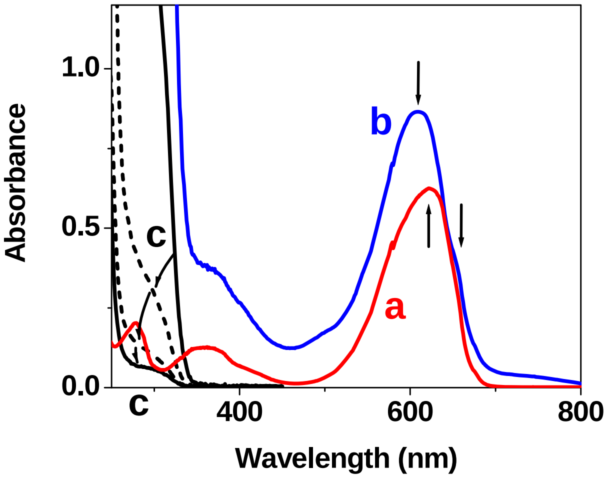

**Figure 7.7.** Optical absorption spectra of a) native PC-APC conjugates b) PC-APC / ZnO QD; c) ZnO QD at different concentration (peak positions are indicated by arrow).

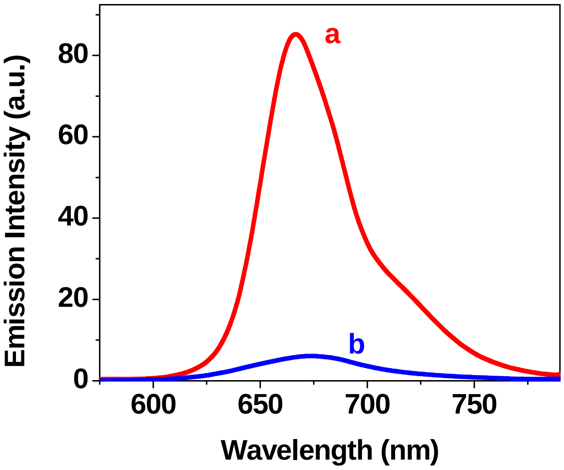

**Figure 7.8:** Emission spectra of PC-APC conjugate in a) absence and in b) presence of ZnO QD after photoexcitation at 400nm.

### 7.3.4 PC→APC energy transfer: Time resolved emission and absorption studies:

In native PC-APC conjugate, an efficient PC→APC energy transfer produces photoluminescence (PL) from APC units on photoexcitation in PC units ($\lambda_{ex}$ 400nm). Thus, the energy transfer is studied by exciting PC-APC conjugate at 400nm and monitoring transient emission in 635-710nm region using streak camera (Instrument response function (IRF) ~6ps).

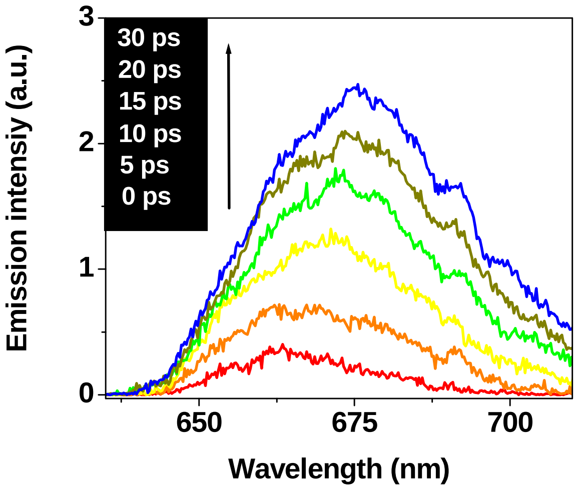

**Figure 7.9:** Transient emission spectra of native PC-APC conjugate in buffer solution at 8.0pH in 0-30 ps time scale by using laser pulse excitation at 400nm.

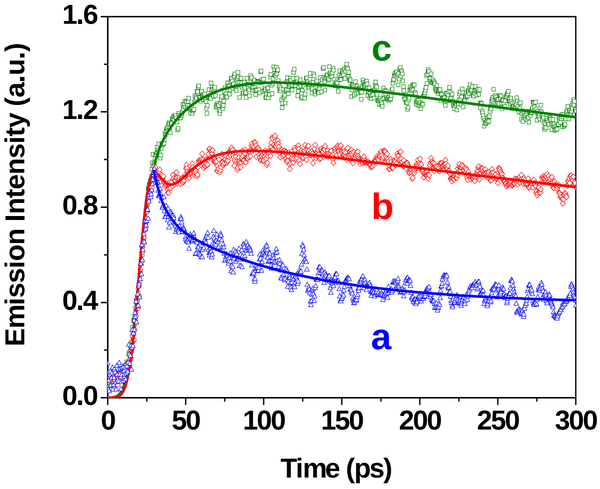

**Figure 7.10:** Transient emission decay kinetics of conjugated PC-APC complex at a) 615nm, b) 655nm and c) 675nm (Normalized for comparison purpose).

Figure-7.9 shows transient emission spectrum of native PC-APC conjugate. Initially, an emission maximum is observed at 663nm which red shifts to 675nm position with increasing intensity in 0-30ps delay time. The transient emission spectrum is assigned to APC trimer. In literature [7.4,7.12], the emission due to pure PC entity is reported in 620-650nm region. In present study, the absence of prominent PC complex emission is sign of efficient PC→APC energy transfer

**Table-7.1**: Fitting parameter for time resolved emission traces of native PC-APC complex.

| 615 nm | 655nm | 675 nm |
|---|---|---|
| IRF (+100%)<br>6.5ps (-25%),<br>82ps (-32%),<br>> 400ps (-43%). | IRF (+85%)<br>6.5ps (-5.7%),<br>8ps (+10.7%),<br>20ps (+4.3%),<br>> 400ps (-94.3%). | IRF (+68%)<br>30ps (+32%),<br>>400ps (-100%). |

process. The 400 nm photoexcitation leads to Förster energy transfer from peripheral s-PCB chromophore (β155) to inner core f-PCB chromophore (β84) of PC pigment. The whole process is traced by leaked emission (low) of s-PCB chromophore in 615-620nm.[7.9-7.13]

Figure-7.10 shows the transient emission decay profile of PC-APC conjugate at 615nm, 655nm and 675nm wavelengths. The fitting time constants are provided in table-7.1. The 6.5ps decay component of 615nm emission kinetics is closely matching to rise of 655nm emission (~8ps) and hence is assigned to s-PCB→f-PCB energy transfer process. The 30ps evolution time in 675 nm emission kinetics, represents solvation (diffusive protein-matrix response) process [7.22] of PC-APC complex which explains the increasing emission intensity during peak-shift (~12nm) in 0-30ps time scale (figure-7.9). The ultrafast (~8-30ps) solvation process inhibits the back energy transfer and thus ensures a unidirectional energy transfer in PC→APC complex. The longer decay component (~80ps) observed only at 615nm, represents the heterogeneous relaxation channel of PC complex. Similar heterogeneous relaxation processes were observed earlier in 40-100ps time scale for PC complex obtained from different cyanobacteria systems and recognized as characteristic of PC complex.[7.5,7.23] The longer component (> 400ps) is assigned to long lived APC complex reported earlier with 1-2 ns lifetime. [7.1-7.13]

Transient emission studies shows PC→APC energy transfer in 6ps time scale which is very close to response function of streak camera used in present study. So, the energy transfer function of native PC-APC conjugate is confirmed by another complementary technique - femtosecond time resolved transient absorption (TA) spectroscopy [7.24] using 400nm pump excitation and 480-900nm probe wavelengths. In addition, TA spectroscopy allows comparison of transient kinetics in native and denatured PC-APC complex which could not be carried out in streak camera due to poor emission yield of denatured PC-APC mixture (figure-7.5).

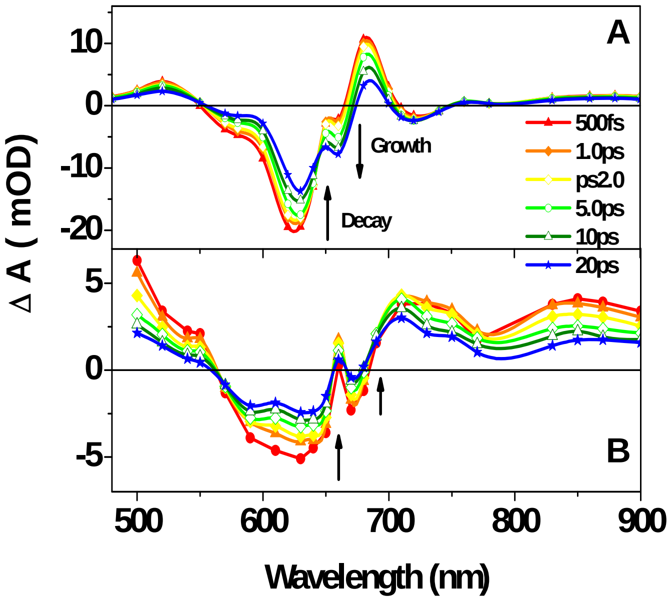

**Figure 7.11.** Transient absorption spectra of native PC-APC conjugate (Panel A) and denatured PC-APC complex (Panel B) recorded at 500 fs, 1 ps, 2 ps, 5 ps, 10 ps and 20 ps delay times after 400nm laser pulse excitation.

Figure-7.11 shows the TA spectrum of PC-APC complex in native (top panel) and denatured (bottom panel) conditions. TA spectrum of native PC-APC conjugate comprises a strong negative band in 600-640nm region in early 500fs time scale. The negative absorption is assigned to photobleach or stimulated emission or both on the ground that absorption and emission of PC complex appears in this region (figure-7.3, [7.4,7.12]). The photobleach/stimulated emission band shows decay of 630nm peak with concomitant growth of 660nm peak in 20ps time window. The presence of an isosbestic point at 645 nm signifies the PC→APC energy transfer process in native PC-APC conjugate. The energy transfer process is further supported by monotonously decaying excited state absorption band (positive band) of PC unit in 480-550nm region and corresponding growth of stimulated emission band of APC unit in 700-750nm region. Such spectral features are not observed in transient absorption spectrum of denatured PC-APC mixture as shown in Figure-7.11; bottom panel-B. In denatured condition, the structured negative transient absorption band (570-650nm and 670-680nm) is attributed to photobleach of isolated PC and APC constituents. Unlike native PC-APC conjugate, the TA spectrum of denatured PC-APC complex does not comprise any isosbestic point (645nm) or stimulated emission in 700-750nm region. This suggests that no energy transfer is occurring between PC and APC in denatured condition.

This is further evidenced in normalized TA kinetics of native and denatured PC-APC complexes monitored at 600and 660nm and shown in figure-7.12. Table-7.2 shows fitting time constants of TA kinetics monitored at selected TA regions. The shortest ~300fs time component of 600nm and 660nm transient absorption kinetics can be assigned to exciton relaxation [7.7,7.8] process in native PC-APC conjugate. Second decay component of 6.5 ps time scale in 600nm photobleach/stimulated emission kinetics of PC segment, matches well with the growth

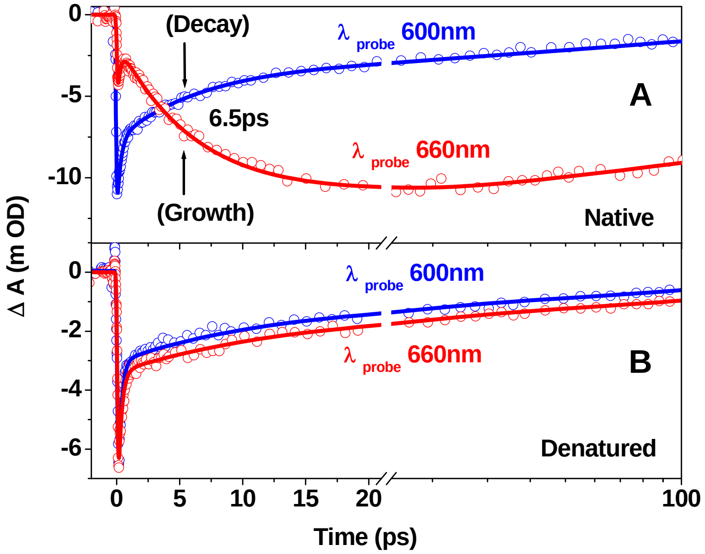

**Figure 7.12.** TA kinetics at 600nm and 660nm which respectively probe i) panel A: the PC and APC entity in native PC-APC conjugate, ii) panel B: denatured PC-APC complex.

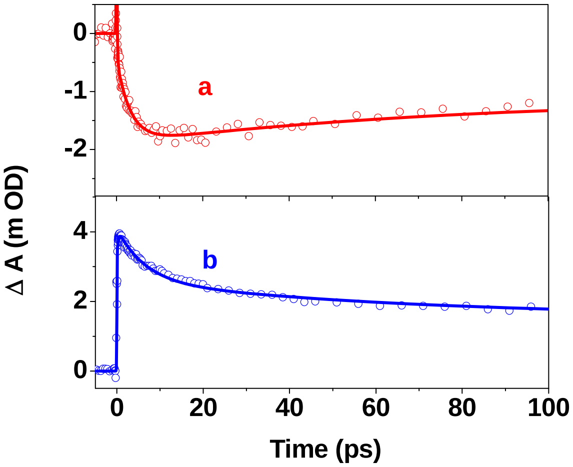

**Figure 7.13.** Transient absorption decay kinetics at 720nm represents A) SE growth of native PC-APC conjugate, B) ESA decay of denatured PC-APC mixture.

component of 660nm photobleach/stimulated emission of APC segment. However, such concomitant growth and decay is not observed in denatured PC-APC mixture (Figure 7.12; bottom panel-B). This reaffirms 6.5ps time domain for PC→APC energy transfer process which is observed earlier in transient emission studies. It is further confirmed by growth of stimulated emission at 720nm in native PC–APC conjugate which is absent in denatured PC-APC mixture as shown in figure-7.13. The longer ~ 70ps and > 1ns time components (table-7.2) which are monitored in transient absorption decay of native PC-APC complex, are assigned to heterogeneous relaxation and natural lifetime of PC and APC segment, respectively.

**Table-7.2:** Fitting parameter for transient absorption kinetics of PC-APC conjugate in native and denatured condition (instrument response function (IRF) ≤100fs).

| | **500nm** | **600 nm** | **660nm** | **720nm** |
|---|---|---|---|---|
| **Native**<br>PC-APC<br>conjugate | IRF (+75.6%)<br>250fs (+24.4%),<br>6.5ps (-36.6%),<br>70ps (-26.3%)<br>> 1ns (-37.1%) | IRF (+100%)<br>300fs (-41.6%)<br>6.5ps (-27.1%)<br>70ps (-18.5%)<br>>1ns (-12.8%) | IRF (+56.4%)<br>300fs (-29%)<br>6.5ps (+72.6%)<br>80ps (-23%)<br>>1ns (-77%) | 3.2 ps (+100%),<br>80 ps (-53.3%)<br>>1ns (-46.7%).<br>***SE** |
| **Denatured**<br>PC-APC<br>mixture<br>(8M Urea ) | IRF (+100%)<br>1.2 ps (-39.1%),<br>13 ps (-34.1%),<br>> 200 ps (-26.8%)<br>**( *ESA)** | IRF (+100%)<br>250 fs (-45%)<br>13ps (-36.7%)<br>> 200ps (-18.3%)<br>**( *PB/SE)** | IRF (+100%)<br>270 fs (-49%)<br>12ps (-37.9%)<br>> 200ps (-13.1%)<br>**( *PB/SE)** | IRF (+78.3%)<br>500 fs (+21.7%)<br>14ps (-43%)<br>> 200ps (-57%)<br>***ESA** |

* PB = photobleach, SE = stimulated emission, ESA = excited state absorption

### 7.3.5 Interfacial electron transfer: Native *vs.* denatured PC-APC sensitized ZnO QDs

The transient absorption and emission studies establish the antenna functioning of PC-APC conjugate in sub ps to ~ 10ps time domain. So, it is appropriate to carry out interfacial electron transfer study of sensitized ZnO QD system which also occurs in same time domain. [7.25]

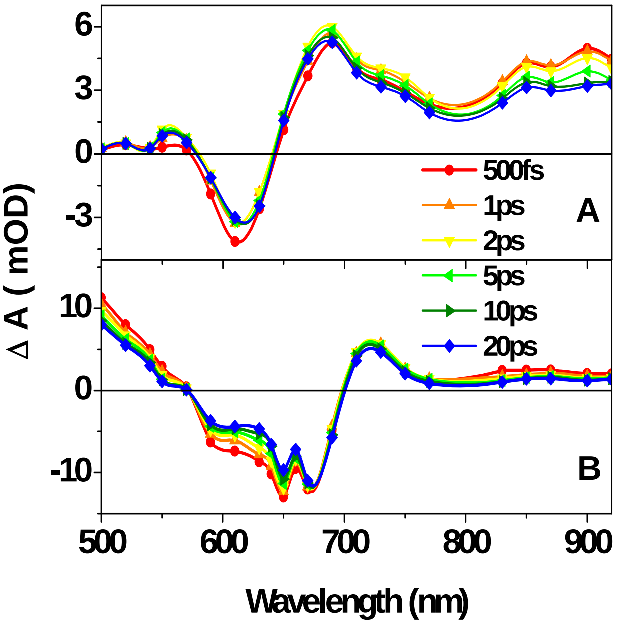

**Figure 7.14.** Transient absorption spectra of native PC-APC conjugate sensitized ZnO QD (Panel A) and denatured PC-APC complex sensitized ZnO QD (Panel B) recorded at 500 fs, 1 ps, 2 ps, 5 ps, 10 ps and 20 ps delay times after 400nm laser pulse excitation.

Figure-7.14A (top panel) shows the transient absorption spectra of conjugated PC-APC complex sensitized ZnO QDs. The prominent difference of transient absorption spectrum of PC-APC conjugates in absence (figure-7.11A) and in presence of ZnO QD (figure-7.14A) corresponds to transient species generated by interfacial electron transfer process. The positive transient absorption band in 650-770nm region resembles to cation $[\text{PC-APC}]^{+\bullet}$ spectrum. The assignment is based on [PC-APC]+• cation spectrum (figure -7.15) ascertained by selective one electron

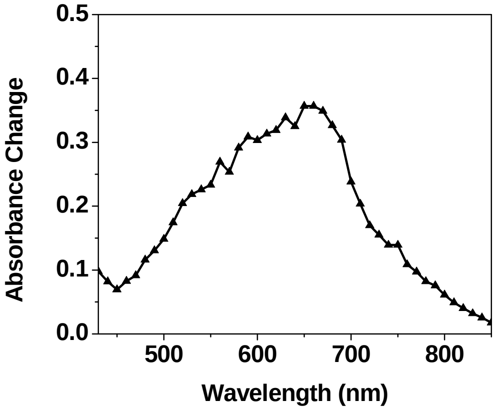

**Figure 7.15:** Transient absorption spectra of [PC-APC conjugate]$^{\bullet+}$ cation.

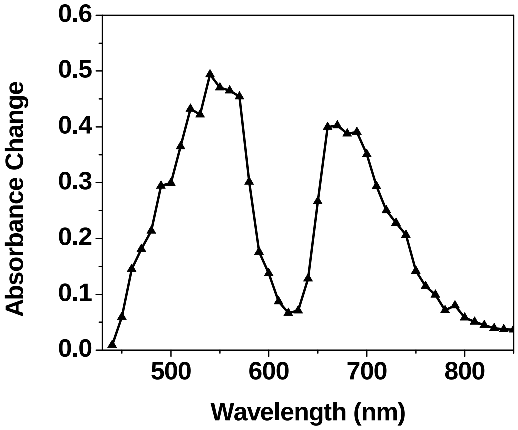

**Figure 7.16:** Transient absorption spectra of [denatured PC-APC mixture]$^{\bullet+}$ cation.

oxidation in pulse radiolysis studies (general radiolysis reactions are given in chapter-4). Another positive transient absorption band in 830-950nm region represents electron injected in conduction band (CB) of ZnO QD.[7.26] The negative transient absorption band in 575-640nm region corresponds to bleach recovery by charge recombination and exciton relaxation processes. However, TA spectrum of denatured PC-APC mixture sensitized ZnO QDs comprises two photobleach bands at 650nm and 670nm which represent unconnected PC/ZnO and APC/ZnO systems. The positive band in 700-760nm is assigned to cation of denatured PC-APC mixture (PC$^{+\bullet}$ and APC$^{+\bullet}$). It does not show two separate cation peaks as observed in transient absorption of [denatured PC-APC] $^{+\bullet}$ cation shown in figure-7.16. This can be attributed to lower electron injection yield of denatured PC-APC mixture which is indicated by low TA signal of CB e$^{-}$ in ZnO QD (compare TA signal in 830-920nm region). The low cation yield or electron injection yield is also supported by extended photobleach band of denatured PC-APC/ZnO system in 575-700nm region as compared to that of native PC-APC/ZnO system in 575-640nm region. In case of native PC-APC/ZnO system, a positive absorption band due to conjugated [PC-APC]$^{+\bullet}$ cation dominates over negative photobleach band caused by ground state recovery of PC-APC in 640-700nm region. However, in denatured condition, the low electron injection yield causes low cation yield which results in low cation absorbance in 640-700nm region and hence an extended photobleach band is observed in this region. Thus, comparisons of TA spectrum of native and denatured PC-APC/ZnO systems reveal an efficient electron injection in former case. The role of PC-APC conjugate function in achieving a better charge separation across the ZnO QD interface is understood by comparing the interfacial electron transfer dynamics (IET) (690nm cation or 850nm $e^{-}$CB (ZnO)) in native and denatured condition. Figure-7.17 shows a comparison of IET dynamics (normalized TA kinetics) in native and denatured condition.

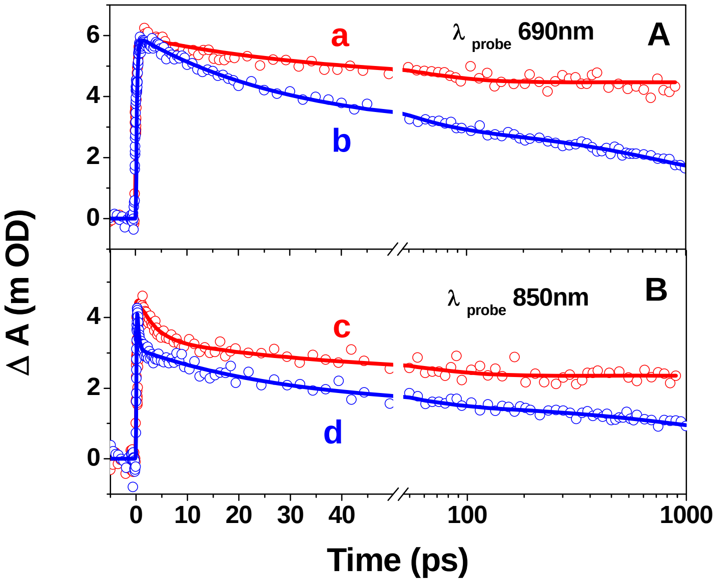

**Figure 7.17.** TA kinetics at 1) Panel A: 690nm probing to (PC-APC)+• cation in a) native PC-APC/ZnO QD, b) denatured PC-APC/ZnO QD system. 2) Panel B: 850nm probing to e— CB (ZnO QD) in c) native PC-APC/ZnO system, d) denatured PC-APC/ZnO system.

**Table-7.3:** Fitting parameter for transient absorption kinetics of PC-APC conjugate in native and denatured condition in presence of ZnO QD (sensitized ZnO QD**).**

| | **690nm** | | **850nm** |
|---|---|---|---|
| Native PC-APC conjugate / ZnO QD | Electron Injection | <80fs (+50%),<br>400fs (+50%), | <80fs (+68.4%),<br>400fs (+31.6%), |
| | BET | 40ps (-25%),<br>> 1ns (-75%). | 3ps (-27.4%),<br>40ps (-23.2%),<br>> 1ns (-49.4%). |
| Denatured PC-APC mixture / ZnO QD | Electron Injection | <100fs (50%),<br>300fs (+ 50%), | <100fs (+100%),<br>300fs (-47.5%), |
| | BET | 30ps (-49%),<br>>1ns (-51%). | 30ps (-27.5%),<br>> 1ns (-25%) |

Table-7.3 shows fitting time constants of TA kinetics, monitored at 690nm (cation$^{\bullet+}$) and 850nm (CB e$^{-}$). The cation formation kinetics (rise of 690nm transient absorption signal) are observed to be multiexponential (<80fs (+50%) and 400fs (+50%)) in both native and denatured PC-APC/ZnO systems. This is attributed to low density of acceptor states (in CB) of ZnO QD. More importantly, the cation decay kinetics (1ps to 1ns) is observed to be slower in the native PC-APC / ZnO QD system (40ps (-25%), > 1ns (-75%)) in comparison to that in denatured PC-APC / ZnO QD system (30ps (-49%), >1ns (-51%)). The trend is further observed in the decay profile of e$^{-}$CB (ZnO) recorded at 850nm.

### 7.3.6 Role of antenna function of PC-APC conjugates on Interfacial electron transfer:

The comparison of native and denatured PC-APC/ZnO system reveals a higher electron injection yield (~ 2.4 times) and a slow BET in native condition. The antenna function of native PC-APC conjugate bestows a higher electron injection yield due to largely associated network of PCB chromophores. In any interfacial electron transfer reaction, the photoexcitation energy of sensitizer molecule is not fully utilized in view of certain energy loss caused by non-radiative or radiative decay to ground state.

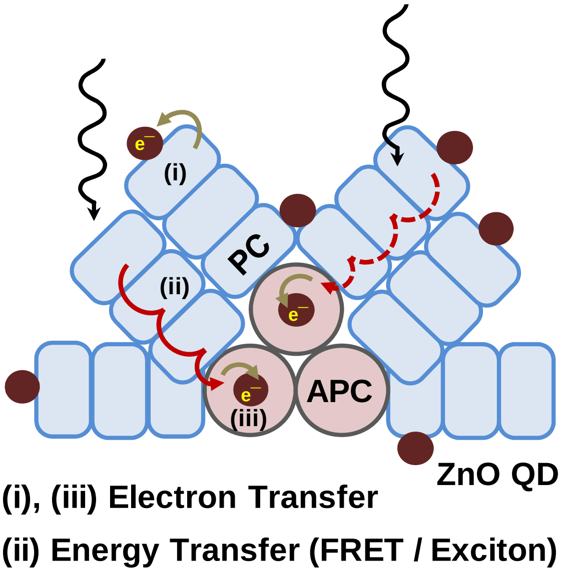

**Scheme-7.2:** Photophysical process in native-PC-APC conjugate/ ZnO system: (i) Primary electron injection from initially photo excited PC species. (ii) Sequential energy transfer directs captured photon energy from non-injecting PC to APC entity. (iii) Secondary electron injection accomplish from APC unit.

In this regard, the conjugate function of PC-APC complex enlightens a way to counterbalance the energy loss by redirecting the excitation energy from non-injecting primary source (PC pigment) to secondary source (APC pigment) (Scheme-7.2). The success relied on the fact that energy transfer process (6.5ps in PC-APC conjugate) is faster enough to compete with heterogeneous relaxation channel (~80ps for PC pigment) but slower than the interfacial electron transfer process (≤ 400 fs) related to either of electron injecting source (PC pigment or APC pigment). The importance of the antenna function is further realized when breaking of long-range association (denatured PC-APC mixture) causes fast back electron transfer process. In native PC-APC conjugate, the cation ([conjugate PC-APC] +•) is stabilized by large network of electron donor units (associated PCB chromophores). So, the back electron transfer process is accordingly slowed down in conjugated system (native PC-APC complex) in comparison to non-conjugated system (denatured PC-APC mixture). Thus, antenna functioning of PC-APC conjugates favours an improved charge separation across the semiconductor interface.

## 7.4 Conclusion:

Photosynthetic antenna complexes exhibit unidirectional energy transport phenomena which make them potential photosensitizer in interfacial electron transfer process. The antenna function of phycocyanin-allophycocyanin (PC-APC) complex is explored by transient emission and absorption spectroscopy. The interfacial electron transfer in PC-APC complex sensitized ZnO semiconductor quantum dot material is compared in native and denatured conditions. The downhill sequential energy transfer from peripheral phycocyanin disc to core allophycocyanin disc opens a new electron injection pathway from allophycocyanin disc in addition to primary electron injection from directly photoexcited phycocyanin disc. Further, the large association of phycocyanobilin chromophores in PC-APC conjugates stabilizes the positive charge within the sensitizer which leads to slower charge recombination in comparison to that in denatured condition. This study reveals the antenna function of energy efficient biomolecules which favours a better charge separation across the semiconductor interface.

## 7.5 References:

[7.1] A. N. Glazer, C. Chan, R. C. Williams, S. W. Yeh, J. H. Clark, Science, 1985, 230, 1051.

[7.2] A. N. Glazer, S. W. Yeh, S. P. Webb, J. H. Clark, Science, 1985, 227, 419.

[7.3] A. N. Glazer, Ann. Rev. Microbiol., 1982, 36, 173.

[7.4] I. Yamazaki, N. Tamai, T. Yamazaki, A. Murakami, M. Mimuro, Y. Fujita, J. Phys. Chem., 1988, 92, 5035.

[7.5] W. F. Beck, K. Sauer, J. Phys. Chem., 1992, 96, 4658.

[7.6] M. P. Debreczeny, K. Sauer, J. Zhou, D. A. Bryant, J. Phys. Chem.1995,99, 8420.

[7.7] J. M. Womick, A. M. Moran, J. Phys. Chem. B, 2009, 113, 15747.

[7.8] J. M. Womick, S. A. Miller, A. M. Moran, J. Chem. Phys., 2010, 133, 024507 (1-10).

[7.9] R. Huber, Angew. Chem. Int. Ed. Engl., 1989, 28, 848.

[7.10] R. MacColl, J. Str. Biol.,1998, 124, 311.

[7.11] M. D. Edington, R. E. Riter, W. F. Beck, J. Phys. Chem., 1996, 100, 14206.

[7.12] G. W. Suter, A. R. Holzwarth, J., 1987, 52, 673.

[7.13] A. N. Glazer, J. H. Clark, Biophys. J.1986, 49,115.

[7.14] G. D. Scholes, J. Phys. Chem. Lett., 2010, 1, 2.

[7.15] R. Das, P. J. Kiley, M. Segal, J. Norville, A. Amy Yu, L. Wang, S. A. Trammell, L. E. Reddick, R. Kumar, Nano Lett., 2004, 4, 1079.

[7.16] C. L. Mulder, L. Theogarajan, M. Currie, J. K. Mapel, M. A. Baldo, M. Vaughn, P. Willard, B. D. Bruce, M. W. Moss, C. E. McLain, Adv. Mater.2009, 21, 3181.

[7.17] A. N. Glazer, J. Biol. Chem., 1989, 264,1.

[7.18] A. Gupta, J. K. Sainis, J. Appl. Phycol., 2010, 22, 231.

[7.19] C. G. Van de Walle, J. Neugebauer, Nature, 2003, 433, 626.

[7.20] Z. Liu, J. Mol. Str. : Theochem, 2008, 862, 44.

[7.21] M. Gouterman, The Porphyrins. Dolphin, D, Ed.; Academic Press, New York, 1978, Vol. III, p 1.

[7.22] R. R. Riter, M. D. Edington, W. F. Beck, J. Phys. Chem., 1996, 100, 14198.

[7.23] M. P. Debreczeny, K. Sauer, J. Zhou, D. A. Bryant, J. Phys. Chem., 1995, 99, 8412.

[7.24] S. Verma, P. Kar, A. Das, H. N. Ghosh, Chem. Euro. J., 2011, 17, 1561.

[7.25] R. Katoh, A. Furube, K. Hara, S. Murata, H. Sugihara, H. Arakawa, M. Tachiya, J. Phys. Chem. B,2002, 106, 12957.

[7.26] C. Bauer, G. Boschloo, E. Mukhtar, A. Hagfeldt, J. Phys. Chem. B, 2001, 105, 5585.

## CHAPTER 8

# INTERFACIAL ELECTRON TRANSFER DYNAMICS ON $TiO_2$ NP SURFACE SENSITIZED WITH POLYNUCLEAR Ru/Os POLYPYRIDYL COMPLEX: A MOLECULAR ANTENNA EFFECT ON EFFICIENT CHARGE SEPARATION.

### 8.1 Introduction:

The energy efficient light transducing function of natural photosynthetic pigments originates from long range energy and electron transfer reactions.[8.1,8.2] The multicomponent light absorption and then sequential energy transfer enhances the primary charge separation at reaction center.[8.3] In addition, the secondary electron donating groups stabilize the charge separated (CS) states and produce multi-cation center.[8.4] Thus, molecular functions are added in cohesive manner to perform several distinct acts in series.[8.5,8.6] The biomimetic systems designed for such antenna function can be very useful in molecular charge storage devices.[8.7-8.10] With recent advancement in supramolecular chemistry, it has become possible to synthesize polynuclear complexes that exhibit vectorial energy transfer and also absorbs light throughout visible and near IR region [8.11-8.15] In this regard, Ru(II)- and Os(II)- polypyridyl complexes are suitable choice for antenna fragments as the nonreactive “metal-to-ligand charge-transfer” (MLCT) states serves optimum gradient for vectorial energy transfer.[8.16- 8.18] In addition, the use of “electron donor” or “π-acceptor” multidentate bridging ligands enables electronic crosslinking between redox asymmetric M(+2)/M′(+3) ion pairs (M/M′= Fe, Ru, Os *etc.*) which stabilizes higher oxidation states through intervalence charge transfer reactions (*i.e.* $d^6 \leftrightarrow d^5$ exchange reactions).[8.19-8.21] Thus, the multinuclear complexes offer novel intramolecular energy and electron transfer pathways which can be used in solar energy conversion, molecular switches and sensors applications.[8.9, 8.22-8.27]

The "complexes as ligands/complexes as metals" synthetic strategy allows wide range of shapes and sizes in growing generations of polynuclear-dendrimer.[8.14,8.15,8.28] The spectral response improves with subsequently increasing generations *viz.* 0th (n=3), 1st (n=6), 2nd (n=12) *etc.* generations of dendrimer. Hence, such large functional arrays can be suitable for light harvesting schemes as shown in scheme-8.1.[8.29] However in larger dendrimer (n>6), the "peripheral-to-core" energy transfer efficiency decreases due to energy barrier of intermediate generations.[8.30] Since, the electronic communication is maximum between adjacent coordinating complexes, the energy transfer is very efficient in tri- and tetra- nuclear complexes.

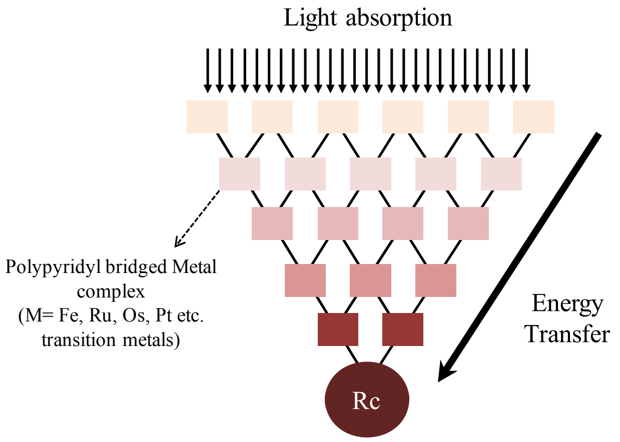

**Scheme-8.1**: Photoexcitation of chromophoric array followed by vectorial energy transfer towards reaction center (Rc).

For photovoltaic application such as dye-sensitized solar cell (DSSC), trinuclear complexes are well adapted in functionalized core activity (reaction center). The concept of remote sensitization was first shown in cyano bridged $[Ru(bpy)_2(\mu\text{-}CN)_2]_2Ru(bpy(COO)_2)_2^{-2}$ trinuclear complex /$TiO_2$ film.[8.25] In such system, the central unit get excited either by direct photoexcitation or by energy transfer from peripheral units. The directional energy transfer in cyano bridged M(μ-CN)M' (M/M' = Fe, Ru, or Os ) complexes arises from non-symmetric electronic distribution at cyano bridge itself.[8.15] However, the electronic asymmetry also renders localized oxidation states on cyano bridged metal centers.[8.31] So, polyazine bridging ligand- 2,3-bis(2'-pyridyl)pyrazine (dpp) are used for its symmetrical electronic properties. [8.14,8.30,8.32] The dpp ligands (represented by ^ in this chapter) are also suitable for its photo-inert electronic transitions and non-ligand/metal scrambling.[8.14,8.33]

In dpp bridged complexes, the unidirectional energy transfer is ascribed by π-donor/acceptor properties of heterometallic ion pairs.[8.14,8.20,8.21,8.34-8.37] The redox asymmetry of heterometallic Ru(II)-(μ-dpp)-Os(II) ion pair leads to ~100% energy transfer as observed in $Ru_3$^$Os_1$ complex ($Os^{II}[(\mu\text{-dpp})Ru^{II}(bpy)_2]_3$).[8.38,8.39] The strong electronic communication through π-acceptor dpp ligand causes partial hole (positive charge) delocalization along Ru(II)-(μ-dpp)-Os(II) channel which stabilizes higher oxidation states ($M^{+2/+3}$).[8.40] The ground state (GS) hole delocalization is determined from comproportionation constant (Kc) [8.41] which is defined as;

$$\mathbf{K_c = 10^{\Delta E/59mV}} \tag{8.1}$$

$$\underset{\textbf{(Red)}}{[L_xM^n(\mu\text{-BL})\,M^nL_x]} \;\underset{E_1}{\underset{+e^-}{\overset{-e^-}{\rightleftharpoons}}}\; \underset{\textbf{(Int)}}{[L_xM^n(\mu\text{-BL})\,M^{n+1}L_x]} \;\underset{E_2}{\underset{+e^-}{\overset{-e^-}{\rightleftharpoons}}}\; \underset{\textbf{(Ox)}}{[L_xM^{n+1}(\mu\text{-BL})\,M^{n+1}L_x]}$$

The Kc constant of $Ru_3$^Os tetranuclear complex (~100,000) is significantly higher than that of uncoupled bimetallic center (Kc ~4). [8.14, 8.21] Thus, trinuclear $Ru_2$^Os complex can be good photosensitizer in DSSC on account of very large spectral response, "peripheral-to-core" energy transfer and GS charge delocalization.[ 8.34-8.37, 8.42,8.43]

In sensitization process, the complexes are immobilized on $TiO_2$ nanoparticle (NP) surface through functional groups such as carboxylate, phosphate, catecholate *etc.*[8.44] The spectral sensitization by catechol functionalized Ru(II)- and Os(II)- complexes have been described in chapters -3, -4 and -5. The use of similar molecular fragments can help to understand the photophysical changes which are sought after trimerization.

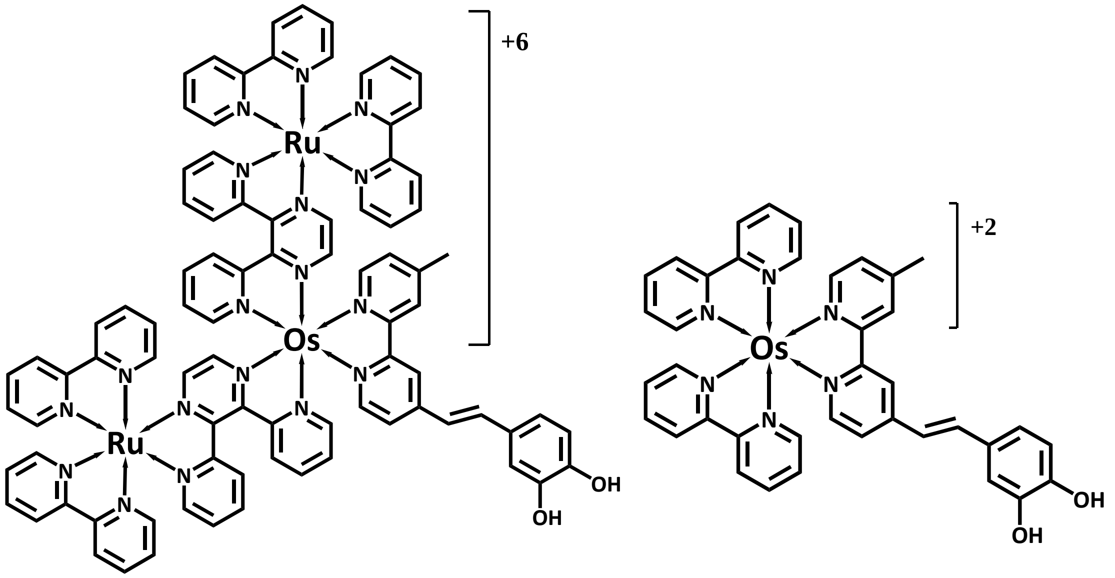

**Scheme-8.2**: Left: Trinuclear “$Ru_2$^Os” complex **(-1)** ($[Ru(bpy)_2(dpp)]_2Os$(bpy-CH=CH-catechol)); Right: Mononuclear “$Os_1$” complex **(-2)** ($Os(bpy)_2$(bpy-CH=CH-catechol)).

Scheme-8.2 shows structure of catechol functionalized trinuclear $Ru_2$^$Os_1$ and its mononuclear core $Os_1$ complexes which are used in ES energy and electron transfer studies. Further, their structural analogues $Ru_2$^$Ru_1$ and $Ru_1$ complexes are used to understand the role of redox asymmetry in vectorial energy transfer. Femtosecond transient absorption spectroscopy is used to study “Ru(II)-complex → Os(II)-complex” energy transfer and then its effects on interfacial electron transfer (IET) dynamics. This study provide fundamental information on how interfacial electron transfer dynamics changes on inclusion of individual component ($M^{II}$-complex) into larger assembly.

## 8.2 Materials:

(4-[2-(4'-methyl-2,2'-bipyridinyl-4-yl)vinyl]benzene-1,2-diol) (**L1**) ligand, complex-**2** ($Os_1$) and $TiO_2$ NPs were used same as reported in chapter 3. $Ru^{II}(bpy)_2Cl_2$ were synthesized following reported procedure.[8.45].

### 8.2.1 Synthesis of trinuclear $Ru_2$^$Os_1$ complex:

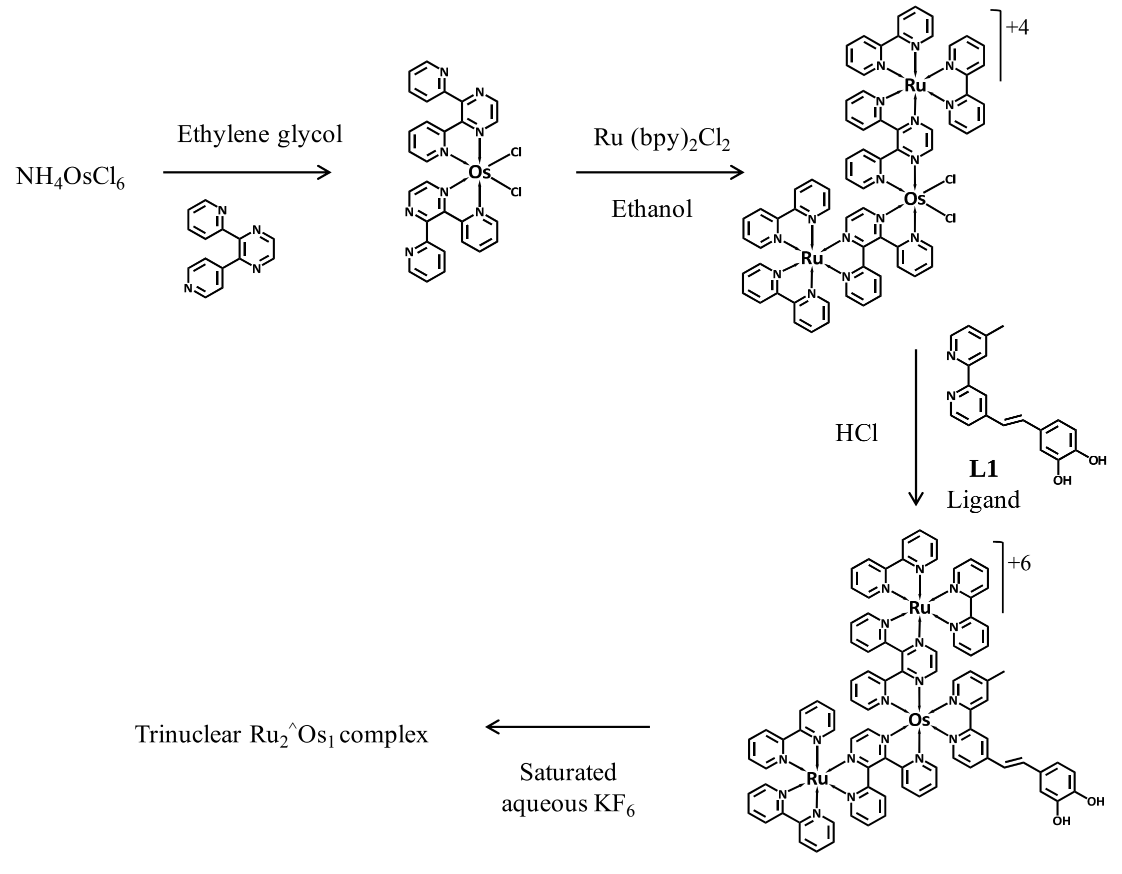

**Scheme-8.3:** Synthetic methodology adopted for the synthesis of trinuclear $Ru_2$^$Os_1$ complex

**8.2.1a Synthesis of [Os(2,3-dpp)$_2$Cl$_2$] :** A solution of ammonium hexachloroosmate (200 mg, 0.46 mmol) is dissolved in 30 ml of ethylene glycol. 2,3-dpp (217 mg, 0.92 mmol) is added to this solution and heated at 100 °C for 5 hours. The reaction mixture is then cooled to room temperature. 5 ml of saturated sodium dithionite solution is added and the reaction mixture is kept inside a refrigerator overnight. The purple black precipitate formed is then filtered through a grade 4 sintered glass crucible, washed with large volumes of water and then dried in a vacuum desiccator to give the desired compound. Yield: 240 mg (72.3 %). ESI-MS (m/z): Calculated for $C_{28}H_{20}Cl_2N_8Os$ - 729.65, Observed – 729.75.

**8.2.1b Synthesis of {[(bpy)$_2$Ru(μ-2,3-dpp)]$_2$OsCl$_2$}Cl$_4$ :** [Os(2,3-dpp)$_2$Cl$_2$] (100 mg, 0.13 mmol) is dissolved in hot ethanol. To this Ru(bpy)$_2$Cl$_2$.2$H_2O$ (136 mg, 0.26 mmol) is added and the resulting solution is refluxed for 24 hours. Ethanol is then evaporated completely and the resulting crude solid is used for the next step without further purification. Yield: 230 mg.

**8.2.1c Synthesis of {[(bpy)$_2$Ru(μ-2,3-dpp)]$_2$OsL$_2$}(PF$_6$)$_4$:** {[(bpy)$_2$Ru(μ-2,3-dpp)]$_2$OsCl$_2$}Cl$_4$ (230 mg, 0.115 mmol assuming 100 % purity) is dissolved in ethanol. To the resulting solution, **L1** (35 mg, 0.115 mmol) is added followed by a drop of 4N hydrochloric acid. The reaction mixture is then refluxed for 24 hours. Ethanol is then evaporated completely and the solid so obtained is dissolved in 10 ml of water. Saturated aqueous potassium hexafluorophosphate (10 mole equivalents) is then added and the resulting mixture is kept in a refrigerator to precipitate the crude complexes. The precipitate is then filtered through a grade 4 sintered glass crucible, washed with large volumes of water and finally dried in a vacuum desiccator to obtain the crude compound. This is then purified by column chromatography using silica as the stationary phase and acetonitrile as the eluent to obtain the desired compound in pure form. Yield: 89.3 mg (25

%). ESI-MS (*m/z*): Calculated for $C_{87}H_{71}F_{24}N_{18}O_2OsP_4Ru_2^{2+}$ [$(M - 2PF_6^{-})^{2+}$] - 1186.07, Observed – 1168.5 $(M - 2PF_6^{-} - H_2O)^{2+}$. $^1$H NMR ($CD_3CN$, ppm): δ 8.7–7.2 (m, 62H).

## 8.3 Results and discussion:

**8.3.1 Cyclic voltammetry:** Electrochemical studies of trinuclear $Ru_2$^$Os_1$ complex reveals 1e¯ and 2e¯ oxidation peaks at +1.28V and +1.53V (*vs*. SCE), respectively. However, trinuclear $Ru_2$^$Ru_1$ complex comprises single oxidation (2 e¯) peak at +1.50V and no other oxidation peak is observed till +1.8V. The oxidation potential of mononuclear $Os_1$ complex and $Ru(bpy)_2(dpp)^{2+}$ complex are observed to be +1.12V and +1.33V, respectively.[ chapter-3; 8.46] 1st oxidation (+1.28V) peak of trinuclear $Ru_2$^$Os_1$ complex is assigned to Os(II) core metal ion due to its higher dπ level than that of peripheral Ru(II) metal ion.[8.21] The 2nd oxidation peak (+1.53V) is assigned to peripheral Ru(II) metal ion which is observed to be more positive than that of $Ru(bpy)_2(dpp)^{2+}$ complex (+1.33V). This is attributed to increase in π-acceptor behaviour of dpp ligand after 1st oxidation of Os(II) core metal ion. The Kc constant is observed to be $\sim 10^{4.2}$ which suggest a moderate Ru/Os metal-metal interaction in $Ru_2$^$Os_1$ complex. It also suggest a partial hole delocalization in monooxidized $Ru_2$^$Os_1$ (+7) complex.

### 8.3.2 Spectral sensitization of $TiO_2$ NP: UV-vis absorption spectra

The spectral sensitizations of $TiO_2$ NPs by using $Os_1$ and $Ru_2Os_1$ complexes are studied by steady state absorption spectroscopy. Figure 8.1 show absorption spectra of mononuclear $Os_1$ and trinuclear $Ru_2Os_1$ complexes in absence and in presence of $TiO_2$ NPs. The $Os_1$-complex exhibits two absorption bands in 400-550nm and 550-750nm regions which are attributed to singlet and triplet "$t_{2g} \rightarrow \pi^*_{bpy}$" MLCT transitions, respectively.[8.47] The $Ru_2Os_1$-complex exhibits absorption spectrum that extends far beyond red region of visible and near IR region. It shows that spectral response improves enormously after substituting ancillary ligand- bpy of Os$_1$ complex with coordinating (μ-dpp)Ru$^{II}$(bpy)$_2$ fragments.

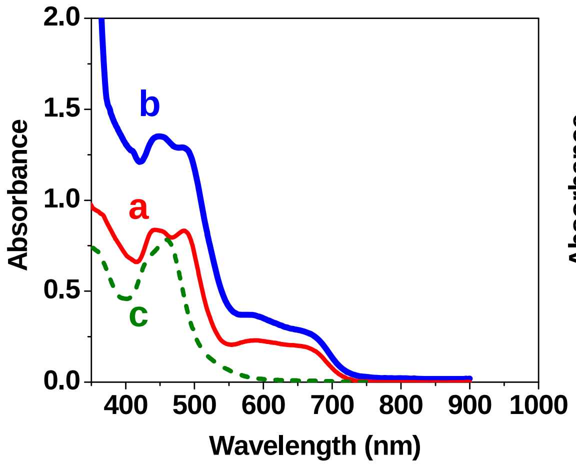

**Figure 8.1**: Optical absorption spectra of ~30 μM Os$_1$ a) in water, b) on TiO$_2$ nanoparticle surface, c) Normalized absorption spectra of Ru$_1$ in water.

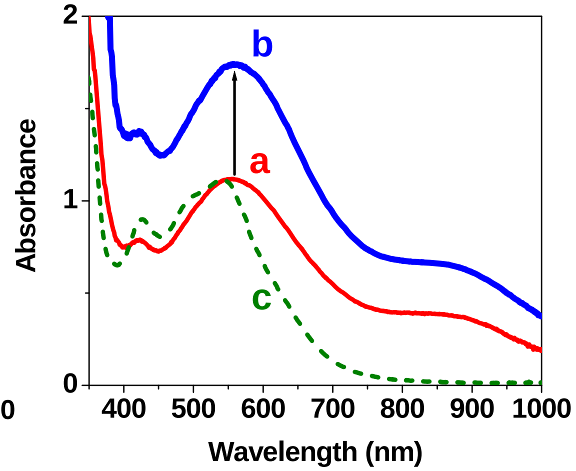

**Figure 8.2**: Optical absorption spectra of ~ 17μM Ru$_2$^Os a) in water, b) on TiO$_2$ nanoparticle surface, c) Normalized absorption spectra of Ru$_2$^Ru$_1$ in water.

The broad absorption of Ru$_2$^Os$_1$ complex is the contributed by several MLCT transitions of Ru(II)- and Os(II)- complex fragments. The “$t_{2g}\rightarrow\pi^*_{bpy/L1}$” $^1$MLCT transitions occur in 400-550nm region as observed in absorption spectra of mononuclear Ru$_1$ and Os$_1$ complexes (figure -8.1a and -8.1c). Since, the dpp (bridging) ligand is stronger π-acceptor than bpy (ancillary) ligand, than the “$t_{2g}\rightarrow\pi^*_{dpp}$” $^1$MLCT transitions are lower energy transitions as compared to “$t_{2g}\rightarrow\pi^*_{bpy}$” $^1$MLCT transitions. [8.20,8.21,8.34,8.36] Therefore, the broad absorption band in 450-750nm region is assigned to “$t_{2g}\rightarrow\pi^*_{dpp}$” $^1$MLCT transitions of Ru(II)- and Os(II)- complex fragments. Likewise, the broad band in 750-1000nm region is assigned to “$t_{2g}\rightarrow\pi^*_{dpp}$” $^3$MLCT transitions of Os(II)- complex fragment. These assignments are further supported by absorption spectrum of $Ru_2$^$Ru_1$ complex in which “$t_{2g}\rightarrow\pi^*_{dpp}$” $^3$MLCT transitions occur in 450-700nm region and $S_0\rightarrow^3$MLCT transitions are not observed (figure 8.2c). The red shift of $^1$MLCT absorption band of $Ru_2$^$Os_1$ complex than that of $Ru_2$^$Ru_1$ complex corresponds to redox asymmetry of heterometallic Ru/Os ions pair as observed in electrochemical study.

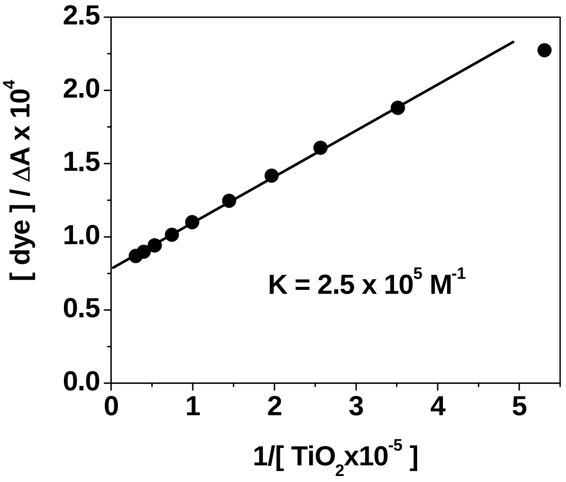

**Figure 8.3**: Benesi-Hildebrandt plot of $Os_1/TiO_2$ system monitored at 530 nm.

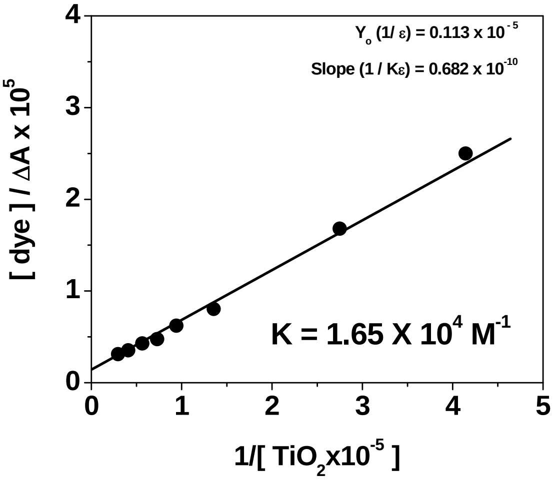

**Figure 8.4:** Benesi-Hildebrandt plot of $Ru_2$^$Os_1/TiO_2$ system monitored at 600nm.

On addition of $TiO_2$ NPs, the absorbance increases significantly in trinuclear $Ru_2$^$Os_1$ and mononuclear $Os_1$ complexes (Figure -8.1 to -8.4). Similar, results are observed for $Ru_2$^$Ru_1$ and $Ru_1$ complexes. This represents significant complex binding on $TiO_2$ NP’s surface. The binding constants are measured in BH plot analysis of $Os_1$ and $Ru_2Os_1$ complexes. Figure-8.3 and -8.4 show the BH plot of $Ru_2$^$Os_1$/ $TiO_2$ NPs and $Os_1$/ $TiO_2$ NPs. The binding constant of $Ru_2$^$Os_1$

complex (1.6 X$10^4$ $M^{-1}$) is observed to an order less than that of $Os_1$ complex (2.5 X $10^5$ $M^{-1}$). This may be due to bulky nature of trinuclear complexes.[8.48] Nonetheless, the binding constant of catecholate functionalized trinuclear complex is comparable to that of phosphate or carboxylates functionalized mononuclear complexes (~$10^4$ $M^{-1}$) which are commonly used in DSSC.[8.49] Thus, catecholate functionalized trinuclear $Ru_2$^$Os_1$ complex binds sufficiently strong on $TiO_2$ NPs that an efficient sensitization could be achieved in entire visible and near IR region.

### 8.3.3 Intramolecular energy transfer in $Ru_2$^$Os_1$ complex: Transient Absorption study

The "peripheral to core" energy transfer properties of trinuclear $Ru_2$^$Os_1$ complex is explored by transient absorption (TA) studies of $Ru_2$^$Os_1$, $Ru_2$^$Ru_1$ and $Os_1$ complexes. Figure-8.5 and -8.6 show TA spectrum of $Os_1$ and $Ru_2$^$Os_1$ complexes in acetonitrile solvent after photoexcitation at 400nm. The TA spectral features of $Os_1$ complex are found to be same as observed earlier in TA study of $Os^{II}(bpy)_2$(bp-catechol) complex (chapter-4). The negative band in 490-550nm and 550-700nm regions are assigned to $S_0 \rightarrow {}^1$MLCT and $S_0 \rightarrow {}^3$MLCT ($t_{2g} \rightarrow \pi^*_{bpy/\mathbf{L1}}$) bleach bands, respectively. Since $^1$MLCT→$^3$MLCT crossover occurs in <50 fs timescale,[8.50,8.51] the positive absorption band in 700-1000nm is assigned to excited state absorption (ESA) of $^3$MLCT states. The ESA of $^3$MLCT state (Frank-Condon states) overlaps with $^3$MLCT bleach in 550-700nm region. So, a small growth in bleach region (550-700nm) can be assigned to ESA decay of unthermalized $^3$MLCT states (vibrational cooling).

The TA spectrum of $Ru_2$^$Os_1$ complex comprises utterly different TA spectral features which are not observed in mononuclear $Os_1$ and $Ru_1$ complexes (Figure-8.5, chapter-4, [8.52]). It comprises broad bleach in 550-1000nm region which recovers completely in ≥20ps time scale and then a positive ESA band appears. Interestingly, the bleach recovery and then growth of ESA band (550-1000nm region) matches well with decay of ESA and then growth of bleach in 490-540nm region. The congruous changes of TA spectrum (490-540nm *vs.* 550-1000nm regions) occur with an isosbestic point at 545nm which indicates excited state energy transfer.

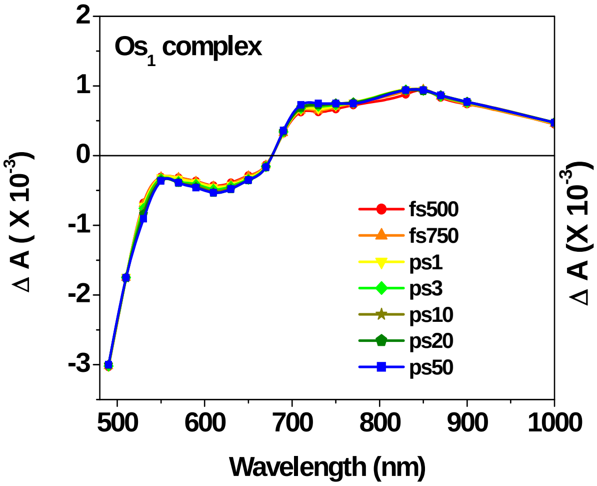

**Figure 8.5**: TA spectra of $Os_1$ complex in acetonitrile at different time delay after excitation at 400nm laser pulse.

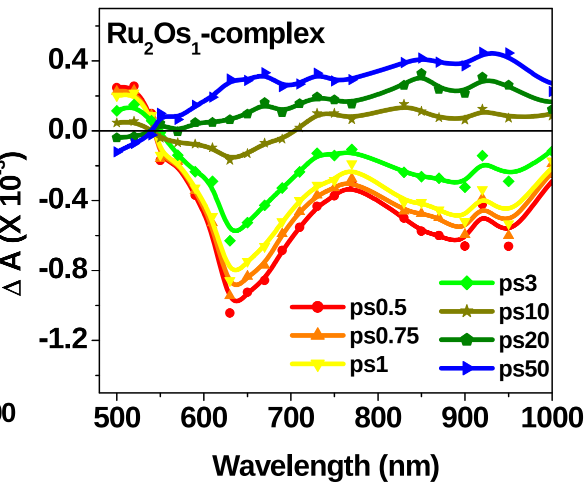

**Figure 8.6**: TA spectra of $Ru_2$^$Os_1$ complex in acetonitrile at different time delay after excitation at 400nm laser pulse.

In $Ru_2$^$Os_1$ complex, the "$t_{2g} \rightarrow \pi^*_{bpy}$" $^1$MLCT transitions (400-450nm) of peripheral Ru(II)-complex fragments are higher energy transition than "$t_{2g} \rightarrow \pi^*_{dpp}$" transitions (450-750nm) of core Os(II)-complex fragment.[8.29,8.32,8.36] Further, the strong π-donor character of Os(II) metal ion decreases the excited state energy (π*) of strong π-acceptor bridging dpp ligand more than that by Ru(II) metal ions.[8.14,.8.20,8.21,8.34-8.37] On 400nm photoexcitation, "$t_{2g} \rightarrow \pi^*_{bpy}$" transition directly populates $^1$MLCT states of peripheral Ru(II)-complex fragment. The $^1$MLCT→$^3$MLCT intersystem crossing (ISC) occurs in a pulse width limited time (<100fs) which lead to $^3$MLCT ($t_{2g} \rightarrow \pi^*_{bpy}$) states. Therefore, the positive absorption band in 490-540nm is assigned to ESA of $^3$MLCT states of Ru(II)-complex fragment. A complete decay of ESA (490-540nm) represents empty $^3$MLCT ($\pi^*_{bpy}$) states which can be due to ~100% energy transfer from peripheral to core units [$(Ru^{II})\pi^*_{bpy} \rightarrow \pi^*_{dpp}(Os^{II})$]. It corresponds to excited state filling of core Os(II)-complex fragment which results ESA of filled $\pi^*_{dpp}$ states in 550-1000nm regions (≥20ps). The excited state energy transfer is further supported by presence of an isosbestic point at 545nm.

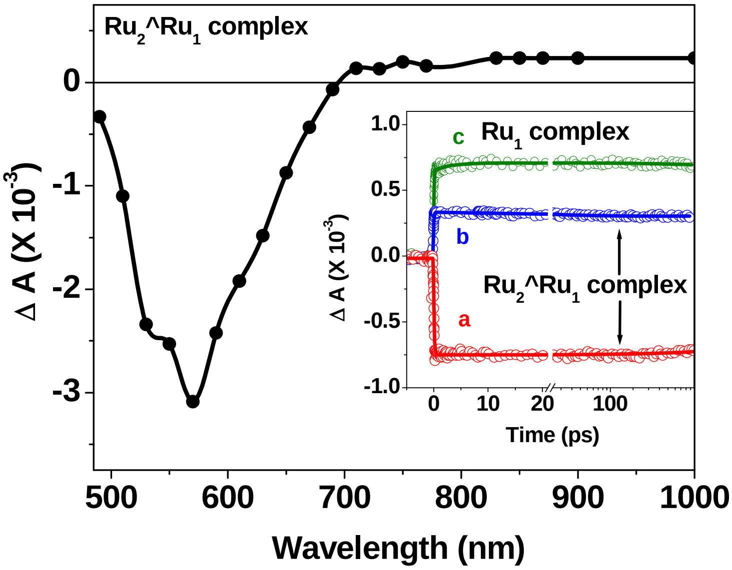

**Figure 8.7**: TA spectrum of $Ru_2$^$Ru_1$ complex at 20ps delay time [Inset: a) Bleach recovery kinetics (630nm), b) ESA kinetics (1000nm) of $Ru_2$^$Ru_1$ complex, c) ESA kinetics at 630nm for $Ru_1$ complex]

The vectorial energy transfer is result of redox asymmetry of heterometallic Ru/Os ion pair. This can be confirmed by TA studies of homo-metallic trinuclear $Ru_2$^$Ru_1$ complex. Figure 8.7 shows TA spectrum of trinuclear $Ru_2$^$Ru_1$ complex which comprises broad negative and positive absorption bands in 490-700nm and 700-1000nm regions, respectively. The negative and positive absorption bands are assigned to bleach ($S_0 \rightarrow {}^1$MLCT) and ESA of $^3$MLCT states, respectively. Unlike $Ru_2$^$Os_1$ complex, the ESA and bleach of trinuclear $Ru_2$^$Ru_1$ complex remain unchanged even up to 1ns time scale (figure-8.7; inset). Moreover, the TA kinetics of trinuclear $Ru_2$^$Ru_1$ complex are alike to that of mononuclear $Ru_1$-complex (figure-8.7; inset). It clearly shows that energy transfer does not occur in homo-metallic $Ru_2$^$Ru_1$ complex. This is supported by earlier photophysical studies of tetranuclear $Ru_3$^$Ru_1$ complex which has shown a reverse "core-to-peripheral" energy gradient.[8.37,8.45] The electrochemical study of $Ru_2$^$Ru_1$ complex reveals that peripheral Ru(II)-complex fragment (+1.53V) oxidizes before core Ru(II)-complex fragment (> +1.8V). The raised dπ level stabilizes the LUMO of bridging dpp ligand more on peripheral Ru(II)-complex fragment than towards core Ru(II)-complex fragment. Therefore, the energy of lowest energy excited state ($*^3\pi_{dpp}$) of peripheral Ru(II)-complex fragment is lower than that of lowest energy excited state of core Ru(II)-complex fragment. Thus, 400nm photoexcitation directly populates "$t_{2g} \rightarrow \pi^*_{bpy}$" $^1$MLCT state of peripheral Ru(II)-complex fragment which remain localized due to reverse "core to peripheral" energy gradient. This confirms that redox asymmetry of Ru/Os ion pair is responsible for an efficient "peripheral to core" energy transfer in trinuclear $Ru_2$^$Os_1$ complex.

The vectorial energy transfer in $Ru_2$^$Os_1$ complex are monitored by TA kinetics at 500nm, 630nm and 900nm and shown in figure-8.8. The bleach recovery kinetics are fitted multiexponentially with 400 fs (73 %), 8 ps (23 %), 40ps (4 %), > 1ns (-100%) at 630nm and 400 fs (50%), 8 ps (40.5%), 40ps (9.5%), > 1ns (-100%) at 900nm. The ESA decay (500nm) is fitted with 400 fs (42%), 8 ps (45.3%), 40ps (12.7%), > 1ns (-100%) time constants. The TA decay or growth kinetics are not observed in mononuclear $Os_1$ complex even up to 1ns (figure-

8.9. In Ru$_2$^Os$_1$ complex, the "peripheral to core" energy transfer causes excited state filling of core $^3$MLCT ($\pi^*_{dpp}$) states and decay of peripheral $^3$MLCT ($\pi^*_{bpy}$) states, simultaneously. As a result, the ESA (500nm) of peripheral $^3$MLCT ($\pi^*_{bpy}$) depletes in congruence to the ESA growth of core $^3$MLCT ($\pi^*_{dpp}$) states (900nm). Thus, both 500nm and 900nm TA kinetics corresponds to vectorial energy transfer. The ESA at 630nm (≥20ps) probes. $^3$MLCT ($\pi^*_{dpp}$) states of both core Os(II)- and peripheral Ru(II)- complex fragments. The ESA growth due to core Os(II)-complex fragment is reduced by the ESA decay due to peripheral Ru(II)-complex fragments. As a result, the amplitude of 630nm ESA decreases with respect to 900nm TA signal but the kinetics could be fitted with 400fs, 8ps and 40ps time constants

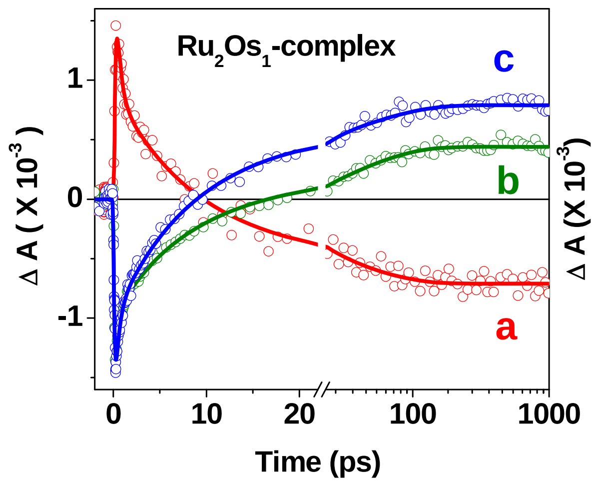

**Figure 8.8**: TA kinetics of Ru$_2$^Os$_1$ complex a) 500nm, b) 630nm and c) 900nm.

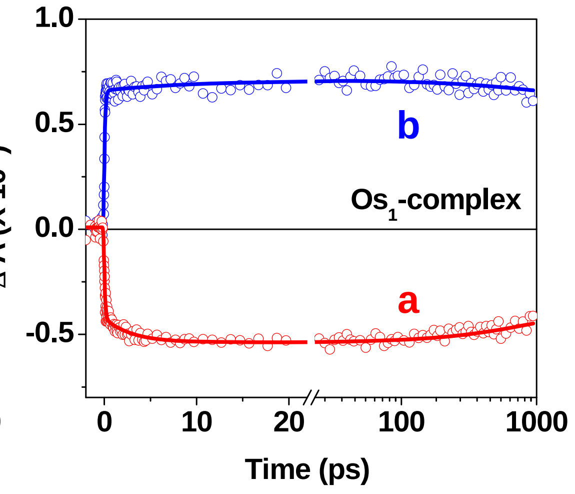

**Figure 8.9**: TA kinetics of Os$_1$ complex a) 610nm and b) 710nm.

The 400fs, 8ps and 40ps time constants are assigned to "peripheral to core" energy transfer in trinuclear Ru$_2$^Os$_1$ complex after comparing the TA kinetics of mononuclear- Ru$_1$, Os$_1$, trinuclear- Ru$_2$^Ru$_1$ and Ru$_2$^Os$_1$ complexes. Previously, the kinetics studies of (L)$_2$Ru$^{II}$-(μ-dpp)-$Os^{II}(L)_2$ complexes have also shown vectorial energy transfer as fast as <200fs time scales.[8.54,8.55] Thus excited state energy transfer initiates before vibration cooling of $^3$MLCT states.[8.50,8.52] Therefore, resonant energy transfer (Förster) model ($k_{en} \sim 10^7$ -$10^8$ $s^{-1}$) can be excluded in such system.[8.17] The ultrafast energy transfer can be attributed to "superexchange" mechanism in which higher energy dπ orbital of $Os^{II}$ metal ion mixes with LUMO of dpp ligand and promotes two electron transfer process *i.e.* $Os^{+2} \rightarrow Ru^{+3}$ and ($Ru^{II}$-dpp)$^3\pi^* \rightarrow {}^3\pi^*$(dpp-$Os^{II}$).[8.21,8.34] On replacing central $Os^{II}$ metal ion with $Ru^{II}$ metal ion ($Ru_2$^$Ru_1$ complex), the gradient for energy transfer is reversed as higher dπ level are now located at peripheral Ru units. Thus, "superexchange" mechanism could be responsible for ultrafast energy transfer in trinuclear $Ru_2$^$Os_1$ complex.

### 8.3.4 Interfacial electron transfer dynamics in $Ru_2$^$Os_1$/$TiO_2$ system: Antenna effect

Femtosecond TA studies has revealed an efficient vectorial energy transfer in $Ru_2$^$Os_1$ complex which can be used in remote sensitization of $TiO_2$ NPs. The effects of electronic communication between adjacent heterometallic complexes on interfacial electron transfer (IET) dynamics are further explored in TA studies of $Ru_2$^$Os_1$ complex, $Ru_2$^$Ru_1$ and $Os_1$ sensitized $TiO_2$ NPs. Since, the IET reactions of $Os^{II}(bpy)_2$(bpy-catechol)/$TiO_2$ NPs have already been discussed in earlier TA studies(chapter-4), only the 20ps delay time TA spectrum of $Os_1$-complex/$TiO_2$ system is therefore shown in figure-8.10. Figure 8.10 also shows a comparison of TA spectrum of $Os_1$-complex in absence and in presence of $TiO_2$ NPs. On addition of $TiO_2$ NPs, the bleach band disappears and a new positive TA band appears in 550-850nm region. Furthermore, the positive TA band increases significantly in 700-1000nm region. The positive TA band in 550-650nm can be assigned to $Os_1$-complex$^{\bullet+}$ cation spectrum. The assignment is supported by

$[Os^{II}(bpy)_2(bpy\text{-}catechol)]$ complex$^{\bullet+}$ cation spectrum (530-650nm region) as observed in earlier pulse radiolysis studies (chapter-4). The TA band of $Os_1$-complex$^{\bullet+}$ cation overlaps with $S_0 \rightarrow {}^3MLCT$ bleach of $Os_1/TiO_2$ system in 530-650nm region and hence a small positive absorption band is observed in 550-850nm region. The increase of positive absorption band in 700-1000nm region is assigned to TA band of conduction band (CB) electron (injected in $TiO_2$ NPs).

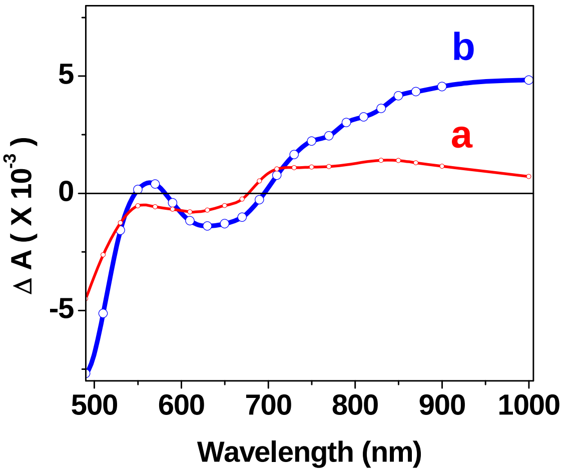

**Figure 8.10**: TA spectra of $Os_1$ complex a) in absence of $TiO_2$ NPs b) in presence of $TiO_2$ NPs at 20ps time delay after excitation at 400nm laser pulse.

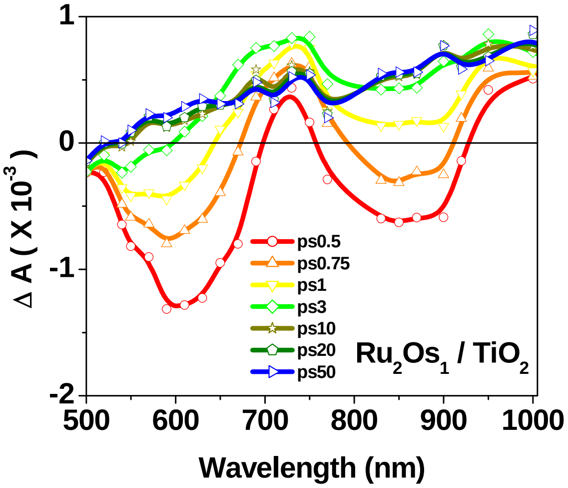

**Figure 8.11**: TA spectra of $Ru_2$^$Os_1$ /$TiO_2$ NPs at different time delay after excitation at 400nm laser pulse.

Figure-8.11 shows TA spectrum of $Ru_2$^$Os_1$ complex/$TiO_2$ system at different time delays. Unlike TA spectrum unbound $Ru_2$^$Os_1$ complex which comprises bleach in entire 550-1000nm region (< 10ps), the TA spectrum of $Ru_2$^$Os_1$ complex/$TiO_2$ NPs comprises new positive absorption bands in 700-750nm and 920-1000nm regions (>200fs). Also, new bleach appears in 490-540nm region and bleach band blue shifts at 600nm after addition of $TiO_2$ NPs. The positive absorption band in 700-750nm can be assigned to $[Ru_2$^$Os_1]^{+\bullet}$ complex cation. It shows a red shift in absorption spectrum of trinuclear $[Ru_2$^$Os_1]^{+\bullet}$ complex cation as compared to that of mononuclear $Os_1$-complex$^{\bullet+}$ cation (530-650nm). In $Ru_2$^$Os_1$ complex/$TiO_2$ NPs system, photoexcitation at 400nm leads to electron injection from core Os(II)-complex fragment to $TiO_2$ NPs which generates $[(\mu$-**dpp**$)_2Os^{II}$(bpy-CH=CH-catechol)$]^{\bullet+}$ cation. Hence, its absorption spectra is red shifted (700-750nm) as compared to that of $[($**bpy**$)_2Os^{II}$(bpy-CH=CH-catechol)$]^{\bullet+}$ cation (530-650nm). Like $Os_1/TiO_2$ NPs system, absorption of $[Ru_2$^$Os_1]^{+\bullet}$ complex cation also overlaps with bleach band of $Ru_2$^$Os_1$ complex/$TiO_2$ NPs system in 630-770nm region. As a result, the bleach band appears to be blue shifted at 600nm. Likewise, the positive absorption band in 920-1000nm is assigned to TA band of conduction band (CB) electron (injected in $TiO_2$ NPs).

TA study of $Ru_2$^$Os_1$ complex/$TiO_2$ NPs system shows an overlapping bleach and cation absorption band in 600-770nm region. It also shows an overlapping bleach and CB electron absorption band in 770-950nm region. Therefore, the IET dynamics is determined from TA kinetics at 1000nm. The rise and decay of 1000nm TA kinetics represents electron injection and back electron transfer (BET) reactions, respectively. Figure- 8.12 shows 1000nm TA kinetics of $Os_1$-complex/$TiO_2$ NPs and $Ru_2$^$Os_1$-complex/$TiO_2$ NPs systems. The electron injection from mononuclear $Os_1$-complex to $TiO_2$ NPs is observed to be biexponential with <100fs (+61.3%), 1.5ps (+38.7%) time constants. In this regards, the $Os_1$-complex comprises catechol functionality which binds strongly on $TiO_2$ NP's surface and form a strong electronic coupling between complex and $TiO_2$ NPs. The strong electronic coupling should facilitates a single exponential electron injection from unthermalized $S_1$ (or $^1$MLCT) states as observed in earlier TA studies of catechol-dyes/$TiO_2$ NPs systems.[8.52,8.53] However, the $^1$MLCT→$^3$MLCT ISC process is very efficient in Os(II)-complexes (large spin-orbit coupling matrix) and hence competes with electron injection reactions.[8.17,8.56] Therefore, the biexponential electron injection is assigned to electron injection from unthermalized $^1$MLCT and thermalized $^3$MLCT states.

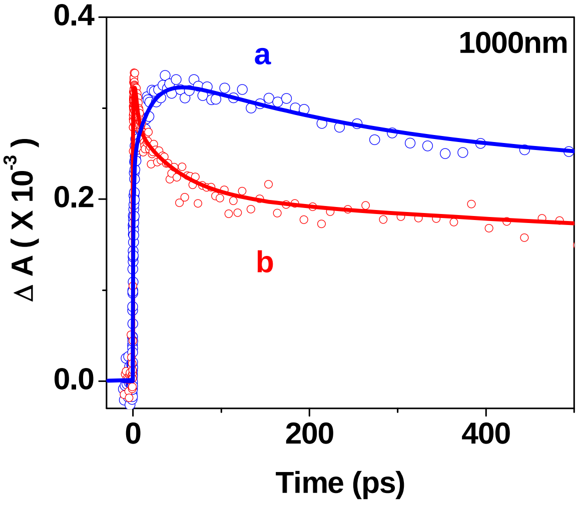

**Figure 8.12**: TA kinetics at 1000nm a) $Ru_2$^$Os_1$/$TiO_2$ NPs, b) $Os_1$/$TiO_2$ NPs.

Figure-8.12a shows a multiexponential electron injection in $Ru_2$^$Os_1$/$TiO_2$ system which is best fitted with <100fs (+22.8%), 1ps (+45.7%), 20ps (+31.5%) time constants. In $Ru_2$^$Os_1$/$TiO_2$ system, the 400nm photoexcitation leads to electron injection from core Os(II)-complex fragment ($t_{2g}\rightarrow\pi^*_{bpy\text{-}CH=CH\text{-}catechol}$) to $TiO_2$ NPs and the process is still comparable to mononuclear $Os_1$/$TiO_2$ system. However, the vectorial energy transfer gradually (in relative to ultrafast electron injection; <100fs) populates low energetics $^3$MLCT ($\pi^*_{dpp}$) states of core Os(II)-complex fragment which leads to multiexponential electron injection in $Ru_2$^$Os_1$/$TiO_2$ system. Alternatively, the multiexponential electron injection may also arises from remote sensitizing ability of peripheral Ru(II)-complex fragments in addition to core Os(II)-complex fragment.[8.22-8.27] The possibility of remote electron injection process is examined in IET study of $Ru_2$^$Ru_1$/$TiO_2$ NPs system.

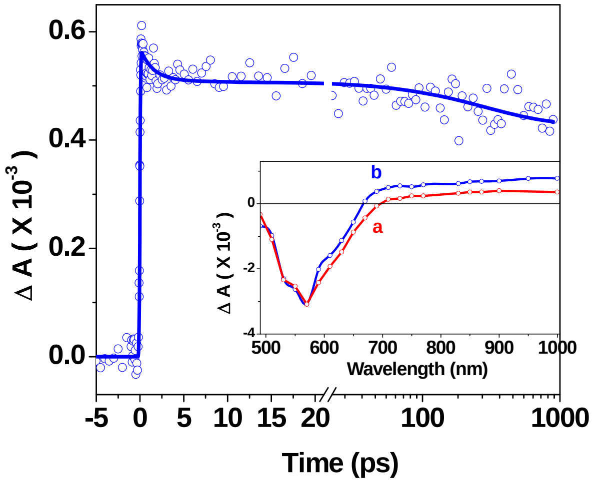

**Figure 8.13**: TA kinetics of $Ru_2$^$Ru_1$/$TiO_2$ NPs at 950nm. (Inset: TA spectrum of $Ru_2$^$Ru_1$ complex a) in absence of $TiO_2$ NPs, b) in presence of $TiO_2$ NPs).

Figure-8.13 shows 1000nm TA kinetics of $Ru_2$^$Ru_1$/$TiO_2$ NPs. Unlike $Ru_2Os_1/TiO_2$ system, the electron injection kinetics is observed to be single exponential (< 100fs) in $Ru_2$^$Ru_1$/$TiO_2$ NPs. The 400nm photoexcitation populates $^1$MLCT states of peripheral and core Ru(II)-complex fragments ($t_{2g}\rightarrow\pi^*_{bpy}$ and $t_{2g}\rightarrow\pi^*_{bpy\text{-}CH=CH\text{-}catechol}$). The electron injection from core Ru(II)-complex fragments occurs single exponentially as observed in mononuclear $Ru_1$-complex/$TiO_2$ system. The multiexponential electron injection due to peripheral Ru(II)-complex fragments is not observed in $Ru_2$^$Ru_1$/$TiO_2$ NPs system. Thus, it rules out the possibility of remote sensitization in $Ru_2$^$Os_1$/$TiO_2$ NPs system.

The back electron transfer dynamics of $Os_1/TiO_2$ NPs and $Ru_2$^$Os_1/TiO_2$ NPs systems are observed by decay of 1000nm TA kinetics. It is observed to be very slow in $Ru_2$^$Os_1/TiO_2$ NPs systems [300ps (-30%), > 1ns (-70%)] as compared to $Os_1/TiO_2$ NPs system [2.8ps (-18.7%), 50ps (-21.8%), 300ps (-12.5%), >1ns (-47%)]. The slow charge recombination in $Ru_2$^$Os_1/TiO_2$ system is assigned to partial hole delocalization in mono-oxidized [$Ru_2$^$Os_1$-complex]$^{+\bullet}$ cation radical. This is supported by moderate value of $K_c$ constant ~$10^{4.2}$ (trinuclear $Ru_2Os_1$ complex).[8.21,8.40] A partial hole delocalization decrease the driving force of BET reaction in $Ru_2Os_1/TiO_2$ system. As a result, BET reactions are very slow in $Ru_2$^$Os_1/TiO_2$ system as

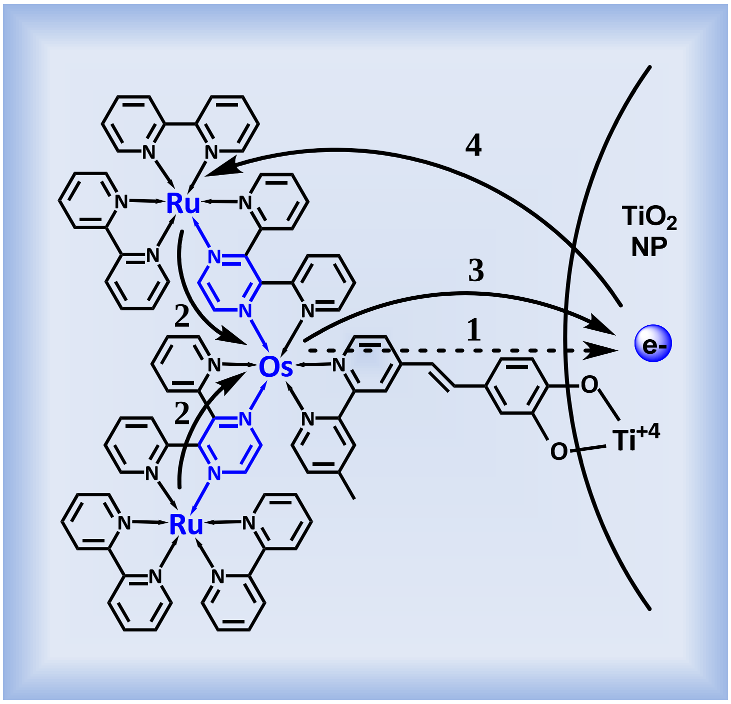

**Scheme-8.4** : Interfacial electron transfer mechanism in $Ru_2$^$Os_1/TiO_2$ system: (i) Primary electron injection from directly photoexcited core Os center, (ii) Vectorial energy transfer from peripheral Ru to Os center, (iii) Slow electron injection through space, (iv) Slow back electron transfer through space.

compared to $Os_1/TiO_2$ system. Scheme-8.4 shows IET mechanism $Ru_2$^$Os_1/TiO_2$ system. On photoexcitation, electron injection occur from core-Os(II)-complex fragments. The "peripheral to core" energy transfer leads to multiexponential electron injection and establish a long lived charge separation at complex/$TiO_2$ interface.

## 8.4. Conclusion:

The "vectorial energy transfer" of photosynthetic antenna complex is mimicked in trinuclear $Ru_2Os_1$ complex by using "$(bpy)_2Ru^{II}(\mu\text{-dpp})$ complex as ligand/"$(\mu\text{-dpp})_2Os^{II}(bpy)$ complex as metal" strategy. The electronic interaction between peripheral Ru(II)-complex fragment and core Os(II)-complex fragment improves the spectral response of $Ru_2Os_1$ complex enormously in entire visible and near IR region (400-1000nm). The redox asymmetry of heterometallic Ru(II)/Os(II)-complex fragments leads to a very efficient "peripheral to core" energy transfer which has been observed clearly in transient absorption (TA) studies. A comparison of TA kinetics of $Ru_2Os_1$- , $Ru_2Ru_1$-, $Os_1$- complexes has revealed an ultrafast (400fs, 8ps, 40ps) vectorial energy transfer in $Ru_2Os_1$ complex. The large spectral response and vectorial energy transfer properties makes $Ru_2Os_1$ complex -a potential photosensitizer for $TiO_2$ semiconductor material. The B-H plot reveals that catechol functionalized core binds ($K_a$~ $10^4$ $Mcm^{-1}$) strongly on $TiO_2$ surface. A comparison of TA kinetics of $Ru_2Os_1$- and $Os_1$- complexes sensitized $TiO_2$ NPs has revealed a multiexponential electron injection (100fs, 1ps, 20ps) in $Ru_2Os_1$ complex/$TiO_2$ system that shows "peripheral to core" energy transfer in favour of interfacial charge separation. In addition, TA studies have also revealed a slow back electron transfer in $Ru_2Os_1$ complex/$TiO_2$ system that shows intercomponent electronic interaction in support of hole (positive charge) stabilization. This study provide fundamental information on how interfacial electron transfer dynamics changes on inclusion of individual component ($Ru^{II}$/$Os^{II}$ complex) into larger assembly. It shows that large functional array of multicomponent "energy/electron" donor entities can be very useful in photosensitizations.

## 8.5 References:

[8.1] G. H. Krause, E. Weis, Annu. Rev. Plant Physiol. Plant Mol. Biol. 1991, 42, 313.

[8.2] Tõnu Pullerits, Villy SundströM, Acc. Chem. Res. 1996, 29, 381.

[8.3] P. Horton, A. V. Ruban, R. G. Walters, Annu. Rev. Plant Physiol. Plant Mol. Biol. 1996, 47, 655

[8.4] M. R. Wasielewski, J. Org. Chem. (perspective) 2006, 71, 5051.

[8.5] D. Gust, T. A. Moore, Science, 1989, 244, 35.

[8.6] D. Gust, T. A. Moore, A. L. Moore, Acc. Chem. Res. 1993, 26, 198.

[8.7] S. Karlsson, J. Boixel, Y. Pellegrin, E. Blart, H. –C. Becker, F. Odobel, L. Hammarström, J. Am. Chem. Soc. 2010, 132, 17977.

[8.8] M. R. Wasielewski, chem. Rev. 1992, 92, 435

[8.9] Kenneth D. Karlin, ed. Progress in Inorganic Chemistry: Molecular Level Artificial Photosynthetic Materials, Volume 44.

[8.10] D. Gust, T. A. Moore, A. L. Moore, Acc. Chem. Res. 2001, 34, 40.

[8.11] V. Balzani, P. Ceroni, M. Maestri, V. Vicinelli, Current Opinion in Chemical Biology 2003, 7, 657.

[8.12] D. Kuciauskas, P. A. Liddell, S. Lin, T. E. Johnson, S. J. Weghorn, J. S. Lindsey, A. L. Moore, T. A. Moore, D. Gust, J. Am. Chem. Soc. 1999, 121, 8604.

[8.13] P. V. Kamat, J. Phys. Chem. C 2007, 111, 2834.

[8.14] V. Balzani, A. Juris, M. Venturi, Chem. Rev. 1996, 96, 759.

[8.15] D. M. D'Alessandro, F. R. Keene, Chem. Rev. 2006, 106, 2270.

[8.16] A. Juris, V. Balzani, F. Barigelletti, S. Campagna, P. Belser, A. von Zelewsky, Coord. Chem. Rev., 1988, 84, 85.

[8.17] Photochemistry and Photophysics of Coordination Compounds: Ruthenium (Volume-280, p.117), Osmium (Volume 281, p.101), Editors: V. Balzani, S. Campagna, Springer, Topics in Current Chemistry Series, 2007.

[8.18] Y. Fuchs, S. Lofters, T. Dieter, W. Shi, R. Morgan, T. C. Strekas, H. D. Gafney, A. D. Baker, J. Am. Chem. Soc. 1987, 109, 2691.

[8.19] K. J. Brewer, W. R. Murphy, Jr., J. D. Petersen, Inorg. Chem. 1987, 26, 3376.

[8.20] W. Kaim, G. K. Lahiri, Angew. Chem. Int. Ed. 2007, 46, 1778.

[8.21] M. M. Richter, K. J. Brewer, Inorg. Chem. 1993, 32, 2827.

[8.22] R. Argazzi, C. A. Bignozzi, T. A. Heimer, G. J. Meyer, Inorg. Chem., 1997, 36, 2.

[8.23] R. Argazzi, N. Y. M. Iha, H. Zabri, F. Odobel, C. A. Bignozzi, Coord. Chem. Rev., 2004, 248, 1299.

[8.24] C. A. Bignozzi, R. Argazzi, C. J. Kleverlaan, Chem. Soc. Rev., 2000, 29, 87.

[8.25] R. Amadelli, R. Argazzi, C. A. Bignozzi, F. Scandola, J. Am. Chem. Soc. 1990, 112, 7099.

[8.26] J. Otsuki, T. Akasaka, K. Araki, Coord. Chem. Rev., 2008, 252, 32.

[8.27] B. Gholamkhass, K. Koike, N. Negishi, H. Hori, T. Sano, K. Takeuchi, Inorg. Chem., 2003, 42, 2919.

[8.28] V. Balzani, S. Campagna, G. Denti, A. Juris, S. Serroni, M. Venturi, Coord. Chem. Rev., 1994, 132, 1.

[8.29] V. Balzani, S. Campagna, G. Denti, A. Juris, S. Serroni, M. Venturi, Acc. Chem. Res. 1998, 31, 26.

[8.30] S. Campagna, C. D. Pietro, F. Loiseau, B. Maubert, N. McClenaghan, R. Passalacqua, F. Puntoriero, V. Ricevuto, S. Serroni, Coord. Chem. Rev., 2002, 229, 67.

[8.31] C. A. Bignozzi, R. Argazzi, J. R. Schoonover, K. C. Gordon, R. B. Dyer, F. Scandola, Inorg. Chem. 1992, 31, 5260.

[8.32] K. Kalyanasundaram, Md. K. Nazeeruddinm, Chem. Phys. Lett., 1989, 158, 45.

[8.33] S. Serroni, S. Campagna, F. Puntoriero, C. D. Pietro, N. D. McClenaghan, F. Loiseau, Chem. Soc. Rev., 2001, 30, 367.

[8.34] G. Denti, S. Campagna, S. Serroni, M. Ciano, V. Balzani, J. Am. Chem. Soc. 1992, 114, 2944.

[8.35] C. N. Fleming, K. A. Maxwell, J. M. DeSimone, T. J. Meyer, J. M. Papanikolas, J. Am. Chem. Soc. 2001, 123, 10336.

[8.36] S. Serroni, A. Juris, M. Venturi, S. Campagna, I. R. Resino, G. Denti, A. Credi, V. Balzani, J. Mater. Chem., 1997, 7, 1227.

[8.37] S. Campagna, G. Denti, L. Sabatino, S. Serroni, M. Ciano, V. Balzani, Chem. Commun., 1989, 1500.

[8.38] G. Denti, S. Serroni, S. Campagna, V. Ricevuto, and V. Balzani, Coord. Chem. Rev., 1991, 111, 227.

[8.39] G. Denti, S. Serroni, S. Campagnab, A. Juris; V. Balzani, Mol. Cryst. Liq. Cryst. 1993, 234, 79.

[8.40] M. M. Richterf, K. J. Brewer, Inorg. Chem. 1993, 32, 5762.

[8.41] D. M. D'Alessandro, F. R. Keene, Dalton Trans., 2004, 3950.

[8.42] N. Hirata, J.-J.Lagref, E. J. Palomares, J. R. Durrant, M. K. Nazeeruddin, M. Grätzel, D. D. Censo, Chem. Eur. J. 2004, 10, 595.

[8.43] J. N. Clifford, E. Palomares, Md. K. Nazeeruddin, M. Grätzel, J. Nelson, X. Li, N. J. Long, J. R. Durrant, J. Am. Chem. Soc. 2004, 126, 5225.

[8.44] J. Moser, S. Punchihewa, P. P. Infelta, M. Grätzel, Langmuir 1991, 7, 3012.

[8.45] B.P. Sullivan, D.J. Salmon, T.J. Meyer, Inorg. Chem. 1978, 17, 3334.

[8.46] W. R. Murphy, Jr., K. J. Brewer, G. Gettliffe, J. D. Petersen, Inorg. Chem. 1989, 28, 81.

[8.47] S. Verma, P. Kar, A. Das, D. K. Palit, H. N. Ghosh, J. Phys. Chem. C, 2008, 112, 2918.

[8.48] E. Galoppini, Coord. Chem. Rev., 2004, 248, 1283.

[8.49] K. Kilså, E. I. Mayo, B. S. Brunschwig, H. B. Gray, N. S. Lewis, J. R. Winkler, J. Phys. Chem. B 2004, 108, 15640.

[8.50] N. H. Damrauer, J. K. McCusker, J. Phys. Chem. A, 1999, 103, 8440.

[8.51] A. C. Bhasikuttan, M. Suzuki, S. Nakashima, T. Okada, J. Am. Chem. Soc., 2002, 124, 8398.

[8.52] G. Ramakrishna, D. A. Jose, D. KrishnaKumar, A. Das, D. K. Palit, H. N. Ghosh, J. Phys. Chem. B 2005, 109, 15445.

[8.53] G. Ramakrishna, D. A. Jose, D. K. Kumar, A. Das, D. K. Palit, H. N. Ghosh, J. Phys. Chem. B, 2005, 109, 15445.

[8.54] J. Andersson, F. Puntoriero, S. Serroni, A. Yartsev, T. Pascher, T. Polívka, S. Campagna , V. Sundström, Chem. Phys. Lett., 2004, 386, 336.

[8.55] H. B. Baudin, J. Davidsson, S. Serroni, A. Juris, V. Balzani, S. Campagna, L. Hammarström, J. Phys. Chem. A, 2002, 106, 4312.

[8.56] D. Kuciauskas, J. E. Monat, R. Villahermosa, H. B. Gray, N. S. Lewis, J. K. McCusker, J. Phys. Chem. B 2002, 106, 9347.

# CHAPTER 9

# SUMMARY AND OUTLOOK.

## 9.1 Summary

The main aim of these studies is to understand the mechanism of interfacial electron transfer (IET) reactions of various dye molecules sensitized wideband gap semiconductor nanomaterials *viz*. $TiO_2$ and ZnO. Different molecular level modifications are used to improve the optical response and interfacial charge separation of dye/$TiO_2$ NPs systems. The molecular amendments are employed to Ru(II)/Os(II)-polypyridyl complexes and porphyrin dyes which are well known photosensitizer in DSSC. In addition, the vectorial energy transfer function of light harvesting antenna complexes are explored and then mimicked in polynuclear complexes. The key aspects of IET dynamics are discussed in this thesis. The experimental findings are applicable to DSSC and also help in exploration of new biomimetic systems. Important conclusions summarized in various chapters are sequentially presented here.

The synthesis and photophysical properties of catechol functionalized Os(II)-polypyridyl complexes, $TiO_2$ NPs and $ZrO_2$ NPs are described in chapter-3. The optical studies has revealed that catechol moiety of Os(II)-polypyridyl complex binds strongly on $TiO_2$ and $ZrO_2$ NP's surface which led to charge-transfer (CT) interaction. The $TiO_2$ NPs are efficiently sensitized through charge transfer absorption band in 400-800nm region. The electron transfer emission quenching experiments has revealed new CT photoluminescence (PL) (750-870nm region) which has made it possible to assess the IET reactions by transient emission measurements. A comparison of PL kinetics of Os(II)-complex sensitized $TiO_2$ and $ZrO_2$ NP's has revealed a slow back electron transfer (BET) dynamics on $ZrO_2$ NP's surface that shows charge recombination through surface states. The contribution of surface states are also rationalized in PL kinetics after photoexcitation in $^1$MLCT and $^3$MLCT absorption bands. This study has confirmed the surface state mediated charge recombination on $TiO_2$ NPs surface.

The heavy atom effects on IET dynamics of M(II)-polypyridyl complex (M=Ru/Os) sensitized $TiO_2$ NPs are described in chapter-4. A replacement of Ru(II)- ion with Os(II)- ion in $M^{II}(bpy)_2$(bpy-catechol) complex extends the spectral sensitization of $TiO_2$ NPs in visible region(*i.e.* 400-750nm). The IET dynamics are studied by femtosecond transient absorption (TA) spectroscopy. The TA has revealed that strong catecholate binding of Ru(II)-complex on $TiO_2$ NP's surface facilitates single exponential (<100fs) electron injection from unthermalized $^1$MLCT (metal to ligand charge transfer) states of Ru(II)-complex to $TiO_2$ NP. Since, the spin-orbit coupling matrix is very large for Os(II)-complex, the $^1$MLCT→$^3$MLCT states intersystem crossing (ISC) therefore competes with ultrafast electron injection process in Os(II)/$TiO_2$ system. As a result, biexponential electron injection kinetics is observed on account of unthermalized $^1$MLCT and thermalized $^3$MLCT states. In addition, the TA study has also revealed a slow BET dynamics in Os(II)-complex/$TiO_2$ system which is attributed to strong π-donor character of Os(II) ion. It suggests that appropriately designed Os(II)-polypyridyl complexes can be a good photosensitizer owing to broad absorption spectrum and slow charge recombination.

The photophysical properties of "ligand-to-ligand charge transfer (LLCT)" states and its effect on IET dynamics are described in chapter-5. A derivatization of ancillary bipyridyl (bpy) ligand with "N, N' –dimethylaminophenyl" electron donating group introduces LLCT states to MLCT manifold of $Ru^{II}$(bpy)(bpy-ph-$NMe_2$)(bpy-CH=CH-catechol) complex. The optical studies *viz.* absorption, PL, PL-kinetics at different pH and temperatures has revealed that LLCT states are lower energy states than MLCT states. Photoexcitation at 400nm directly populates

LLCT states or else through internal conversion from MLCT states. In LLCT states, the electron and hole (positive charge) are localized on bpy-CH=CH-catechol and bpy-ph-$NMe_2$ ligands, respectively. The TA study reveals that intramolecular charge separation due to LLCT states helps in interfacial charge separation in Ru(II)-complex/$TiO_2$ system. The electron injection from MLCT state to $TiO_2$ NP leaves hole on oxidized Ru(III) ion which is then transferred to electron donor -$NMe_2$ moiety. The electron injection from LLCT states results similar interfacial charge separation in a diffusion less process. The increased spatial charge separation led to slower BET reactions in derivatized Ru(II)-complex/$TiO_2$ film than that in unmodified system. The results have great significance in DSSC as all the transient studies are carried out on $TiO_2$ film phase.

The effects of aggregation on IET dynamics of porphyrin/$TiO_2$ NPs system are described in chapter-6. A mono-catechol derivative of tetraphenylporphyrin is used in J-aggregate formation. The J-aggregation improves the spectral response of porphyrin throughout 400-800nm region on accounts of Frenkel exciton bands. The PL-kinetics have revealed exciton coherence of ~14 molecules in J-aggregate ensemble. The large exciton coherence causes ultrafast decay (~200fs, 180ps) of J-aggregate excited states. In view of improved spectral response but ultrafast exciton decay dynamics, the photosensitization ability of porphyrin J-aggregate is examined by TA studies. The TA studies has revealed that interfacial exciton dissociation leads to an ultrafast electron injection (<100fs) into $TiO_2$ NP. The large binding energy of catechol functionality on $TiO_2$ surface facilitates interfacial exciton dissociation prior to natural exciton decays process. The hole (positive charge) is delocalized in J-aggregate which results a slow BET dynamics in porphyrin-J-aggregate/$TiO_2$ system as compared to monomer-porphyrin/$TiO_2$ system. This study shows that the antenna functionality of circular aggregates and primary charge separation at the interface (reaction centre) can be coupled in favor of efficient charge carrier generation (electron/hole) in photon-processing units.

The "peripheral to core" energy transfer of natural light harvesting "phycocyanin-allophycocyanin (PC-APC)" protein pigments and its effects on IET of sensitized ZnO quantum dots (QDs) are described in chapter-7. In native PC-APC conjugates, the protein scaffolds serve as template for strong excitonic interaction and long range dipole-dipole interaction of carboxylate functionalized phycocyanobilin (PCB) chromophores which causes unidirectional PC→APC energy transfer. Transient emission and absorption studies have revealed an efficient PC→APC energy transfer in ~6.5ps time scale. The photophysical study has shown that carboxylate functionality of PC-APC units binds strongly on ZnO QDs. A comparison of IET dynamics (TA studies) of PC-APC/ZnO system in native and denatured condition has revealed that the downhill sequential energy transfer from peripheral PC discs to core APC discs opens a new electron injection pathway from allophycocyanin disc in addition to primary electron injection from directly photoexcited phycocyanin disc. Further, the large association of phycocyanobilin chromophores in phycocyanin-allophycocyanin conjugates stabilizes the positive charge within the sensitizer which led to slower charge recombination in comparison to BET in denatured condition. This study displays the antenna function of energy efficient biomolecules in favor of better charge separation across the semiconductor interface.

The "vectorial energy transfer" of photosynthetic antenna complex is mimicked in trinuclear $Ru_2Os_1$ complex by using "$(bpy)_2Ru^{II}(\mu\text{-dpp})$ complex as ligand/"$(\mu\text{-dpp})_2Os^{II}(bpy)$ complex as metal" strategy in chapter-8. The electronic interaction between peripheral Ru(II)-complex fragment and core Os(II)-complex fragment improves the spectral response of $Ru_2Os_1$ complex enormously in entire visible and near IR region (400-1000nm). The redox asymmetry of heterometallic Ru(II)/Os(II)-complex fragments leads to a very efficient “peripheral to core” energy transfer which has been observed clearly in transient absorption (TA) studies. A comparison of TA kinetics of $Ru_2Os_1$- , $Ru_2Ru_1$-, $Os_1$- complexes has revealed an ultrafast (400fs, 8ps, 40ps) vectorial energy transfer in $Ru_2Os_1$ complex. The optical studies have revealed that catechol functionalized core binds ($K_a \sim 10^4$ $Mcm^{-1}$) strongly on $TiO_2$ surface. A comparison of TA kinetics of $Ru_2Os_1$- and $Os_1$- complexes sensitized $TiO_2$ NPs has revealed a multiexponential electron injection (100fs, 1ps, 20ps) in $Ru_2Os_1$ complex/$TiO_2$ system that shows “peripheral to core” energy transfer in favour of interfacial charge separation. In addition, the intercomponent electronic interaction stabilizes the hole (positive charge) which leads to slow BET in $Ru_2Os_1$ complex/$TiO_2$ system. This study provide fundamental information on how interfacial electron transfer dynamics changes on inclusion of individual component ($Ru^{II}$/$Os^{II}$ complex) into larger assembly. It shows that large functional array of multicomponent “energy/electron” donor entities can be very useful in photosensitizations.

## 9.2 Outlook

The investigations presented in this thesis work principally engross upon interfacial electron transfer reactions between molecular adsorbate and wide bandgap semiconductor nanomaterial. It also offers an understanding of various strategies that are executed at molecular level to improve the optical response and kinetics control of interfacial charge separation. The photosensitizers are gradually progressed from monomer to supramolecular assemblage in pursuit of prolific charge separation in strongly coupled system. The kinetic models which have drawn the feasibility of such systems can be incorporated in the futuristic studies of primary photoconversion processes.

The crucial role of surface states in interfacial electron transfer reaction is identified from charge transfer emission in Os(II)-complex sensitized $TiO_2$ and $ZrO_2$ nanoparticles. The CT emission is not very common in sensitized $TiO_2$ NPs and its revelation in catecholate/$TiO_2$ system should be thoroughly examined. A reevaluation of charge transfer emission is possible by using surface modified $TiO_2$ NPs. The surface passivation of $TiO_2$ NPs using molecular adsorbate such as oleic acid, dodecylbenzenesulfonate (DBS) *etc*. has already been implemented and efforts are underway to comprehend the surface state mediated CT dynamics.

The strong binding of dye/$TiO_2$ system owes CT interaction for an instantaneous interfacial charge separation. It essentially accelerates both forward- and back- electron reactions at dye/$TiO_2$ interface. This situation can leads to kinetics redundancy of photoinduced charge separation if oxidized states are left unattended. Present experimental findings indicates that the use of different transition metal ion (dπ donor strength of $Ru^{II}$ vs. $Os^{II}$), secondary electron donor groups (-ph-$NMe_2$) or multicomponent association (porphyrin aggregation, PC-APC conjugation, trinuclear complex) in sensitizer entity retains the driving force for forward electron transfer but reduces it for back electron transfer reactions. It is one the important outcome of present investigations. Varieties of electron donor groups such as -$NR_2$, -SR, -OR, $SCN^{-}$, $CN^{-}$ *etc*. are available, different metal ion such as $Ru^{II}$, $Os^{II}$, $Co^{II}$, $Mn^{II}$, $Pt^{II}$ *etc.* can be incorporated, molecular fragments can be conjoined with different bridging ligands such as $CN^-$, $SCN^-$, pyrazine and its derivatives like triazoles, hexaazatriphenylene (HAT) *etc.* Thus, myriads of possibility are there and a fundamental knowledge about prototype electron transfer reactions certainly projects a step closer to future initiatives.

The antenna function of molecular assemblage gives a glimpse of large spectral coverage. The porphyrin-J-aggregate, phycocyanin-allophycocyanin pigment, trinuclear metal polypyridyl complexes, all have shown a very large spectral response in 400-800nm region. In fact, mononuclear Ru(II)-complex with secondary electron donor group (-ph-$NMe_2$) have shown better molar extinction coefficient than that of unmodified Ru(II)-complex. Thus, the antenna complexes have significant potential to evolve as panchromatic sensitizer and needs further study in this direction.

An extension of electronic communication between molecular fragments offers efficient energy/electron transfer functions in molecular assembly. The electronic interactions such as dipole-dipole interactions (PC-APC complex), super-exchange interactions ($Ru_2$^$Os_1$ complex), exciton interactions (J-aggregates and PC-APC complex) *etc*. are controllable by chemical nature of substituent groups, molecular geometry and relative configurations. An advanced study on different aggregation pattern, a careful inclusion of different substituents groups, a theoretical support for ligand localized states, selectivity among diastereoisomers are further needed for complete gain of vectorial and kinetic control over intramolecular energy/electron transfer reactions.

In future, transient absorption studies of surface electron transfer reactions which have been carried out in visible region will be extended in infrared region. This would offer an in depth knowledge of surface electron transfer and coupled vibrational modes of photosensitizer molecules. Besides this, a solvatochromic effects on surface electron transfer are impending and will be addressed in future. The effects of size-quantization of quantum dot semiconductor materials such as ZnO, CdS, CdSe, CdTe, ZnS, ZnSe, ZnTe *etc*. will be included in surface electron transfer reactions.

The aforementioned archetype studies are helpful to speculate new energy efficient photoconversion processes and will contribute in the regulatory momentum towards advanced and more sophisticated systems.

## Publication List: Included in Thesis

1. Interfacial Electron-Transfer Dynamics on $TiO_2$ and $ZrO_2$ Nanoparticle Surface Sensitized by New Catechol Derivatives of Os(II)-polypyridyl Complexes: Monitoring by Charge-Transfer Emission.

   **Sandeep Verma**, Prasenjit Kar, Amitava Das, Dipak K. Palit, Hirendra N. Ghosh

   **J. Phys. Chem. C 2008, 112, 2918.**

2. Ultrafast Exciton Dynamics of J- and H-Aggregates of the Porphyrin-Catechol in Aqueous Solution.

   **Sandeep Verma** and Hirendra N. Ghosh

   **Ultrafast Phenomena, Chem. Phys., Springer, 2008, 328.**

3. Ultrafast Exciton Dynamics of J- and H-Aggregates of the Porphyrin-Catechol in Aqueous Solution.

   **Sandeep Verma**, Amrita Ghosh, Amitava Das, Hirendra Nath Ghosh

   **J. Phys. Chem. B 2010, 114, 8327.**

4. The Effect of Heavy Atoms on Photoinduced Electron Injection from Nonthermalized and Thermalized Donor States of M(II)–Polypyridyl (M=Ru/Os) Complexes to Nanoparticulate $TiO_2$ Surfaces: An Ultrafast Time-Resolved Absorption Study.

   **Sandeep Verma**, Prasenjit Kar, Amitava Das, Dipak K. Palit, Hirendra N. Ghosh

   **Chem. Eur. J. 2010, 16, 611.**

5. Efficient Charge Separation in $TiO_2$ Films Sensitized with Ruthenium(II)–Polypyridyl Complexes: Hole Stabilization by Ligand-Localized Charge-Transfer States.

   **Sandeep Verma**, Prasenjit Kar, Amitava Das, Hirendra N. Ghosh

   **Chem. Eur. J. 2011, 17, 1561**

6. Exciton-Coupled Charge-Transfer Dynamics in a Porphyrin J-Aggregate/$TiO_2$ Complex.

   **Sandeep Verma**, Amrita Ghosh, Amitava Das, Hirendra Nath Ghosh

   **Chem. Eur. J. 2011, 17, 3458.**

7. Employing a Photosynthetic Antenna Complex to Interfacial Electron Transfer on ZnO Quantum Dot.

   **Sandeep Verma**, Alka Gupta, Jayashree K. Sainis, and Hirendra N. Ghosh

   **J. Phys. Chem. Lett. 2011, 2, 858.**

8. Photophysical Study of Ligand Localized Excited State in Ruthenium (II) Polypyridyl Complexes: A Combined Effect of Electron Donor-Acceptor Ligand.

   **Sandeep Verma**, Prasenjit Kar, Amitava Das, Hirendra N. Ghosh

   **Dalton Trans., 2011, 40, 9765.**

9. Sequential Energy and Electron Transfer in Polynuclear Complex Sensitized $TiO_2$ Nanoparticle.

   **Sandeep Verma**, Prasenjit Kar, Amitava Das, Hirendra N. Ghosh.

   **J. Phys. Chem. Lett., 2012 (Accepted; dx.doi.org/10.1021/jz3005305)**

10. Exciton Energy and Charge Transfer in Porphyrin Aggregate / Semiconductor ($TiO_2$) composites.

    **Sandeep Verma** and Hirendra N. Ghosh.

    **J. Phys. Chem. Lett. *(Perspective)*, 2012 (*Submitted by Invitation*)**

**Publication List: Associated in research work**

1. Interfacial Electron Transfer Dynamics Involving a New Bis-Thiocyanate Ruthenium(II) Polypyridyl Complex, Coupled Strongly to Nanocrystalline $TiO_2$, through a Pendant Catecholate Functionality

   Prasenjit Kar, **Sandeep Verma**, Amitava Das, and Hirendra N. Ghosh

   **J. Phys. Chem. C 2009, 113, 7970.**

2. Evidence of Multiple Electron Injection and Slow Back Electron Transfer in Alizarin-Sensitized Ultrasmall $TiO_2$ Particles.

   Sreejith Kaniyankandy, **Sandeep Verma**, Jahur A. Mondal, Dipak K. Palit, Hirendra N. Ghosh

   **J. Phys. Chem. C, 2009, 113, 3593.**

3. Interfacial Electron Transfer Dynamics in Quinizarin Sensitized ZnS Nanoparticles: Monitoring Charge Transfer Emission.

   Sachin Rawalekar, **Sandeep Verma**, Sreejith Kaniyankandy, Hirendra N. Ghosh.

   **Langmuir, 2009, 25, 3168.**

4. Sensitization of Nanocrystalline $TiO_2$ Anchored with Pendant Catechol Functionality Using a New Tetracyanato Ruthenium(II) Polypyridyl Complex.

   Prasenjit Kar, **Sandeep Verma**, Anik Sen, Amitava Das, Bishwajit Ganguly, Hirendra Nath Ghosh.

   **Inorg. Chem. 2010, 49, 4167.**

5. Ultrafast Charge Carrier Relaxation and Charge Transfer Dynamics of CdTe/CdS Core-Shell Quantum Dots as Studied by Femtosecond Transient Absorption Spectroscopy.

   Sachin Rawalekar, Sreejith Kaniyankandy, **Sandeep Verma**, Hirendra N. Ghosh

**J. Phys. Chem. C 2010, 114, 1460.**

6. Charge carrier dynamics in thiol capped CdTe quantum dots

   Sreejith Kaniyankandy, Sachin Rawalekar, **Sandeep Verma**, Dipak K. Palit, Hirendra N. Ghosh.

   **Phys. Chem. Chem. Phys., 2010, 12, 4210.**

7. Effect of Surface States on Charge-Transfer Dynamics in Type II CdTe/ZnTe Core–Shell Quantum Dots: A Femtosecond Transient Absorption Study.

   Sachin Rawalekar, Sreejith Kaniyankandy, **Sandeep Verma**, Hirendra N. Ghosh.

   **J. Phys. Chem. C, 2011, 115, 12335.**

8. Ultrafast Hole Transfer in CdSe/ZnTe Type II Core-Shell Nanostructure.

   Sreejith Kaniyankandy, S. Rawalekar, **Sandeep Verma**, Hirendra N. Ghosh.

   **J. Phys. Chem. C 2011, 115, 1428.**

9. Surface-State-Mediated Charge-Transfer Dynamics in CdTe/CdSe Core–Shell Quantum Dots.

   Sachin Rawalekar, Sreejith Kaniyankandy, **Sandeep Verma**, Hirendra N. Ghosh.

   **Chem. Phys. Chem. 2011, 12, 1729.**

10. Effect on the Role of Hydrogen Bonds in Photoinduced Electron-Transfer Dynamics between 9-Fluorenone and Amine Solvents.

    Hirendra N. Ghosh, Katrin Adamczyk, **Sandeep Verma**, Jens Dreyer, Erik T. J. Nibbering.

    **Chem. Eur. J. 2012, 18, 4930.**